Modelling the microstructure and simulation of progressive fracturing in brittle granular materials

Von der Fakultät Luft- und Raumfahrttechnik und Geodäsie
der Universität Stuttgart zur Erlangung der Würde eines Doktors der
Ingenieurwissenschaften (Dr. Ing.) genehmigte Abhandlung

vorgelegt von

Rainer Andreas Dattke

aus Bruchsal

Hauptberichter:	Prof. Dr.-Ing. habil. Bernd Kröplin
Mitberichter:	Prof. Dr.-Ing. Christian Miehe
Mitberichter:	Priv.Doz. Dr.-Ing. Ioannis Doltsinis

Tag der mündlichen Prüfung: 1. August 2003

Institut für Statik und Dynamik der Luft- und Raumfahrtkonstruktionen
der Universität Stuttgart

2003

Für Simon

This manuscript was prepared with LaTeX 2ϵ under Linux 2.2.18.

Contents

Abstract

The present thesis is concerned with the initiation and extension of microcracks in brittle, granular materials, particularly in porous ceramics, and with the effect of this microsopic damage on the macroscopic material properties. For an investigation of the damage behaviour, a two-dimensional geometric model of the microstructure and a physical model of its elastic and strength properties is developed.

The emerging computer algorithm represents a novel approach to the simulation of microscopic damage since it combines elements of the purely analytical 'micromechanical' models, and ideas of the rather numerical 'mesh models'. The numerical parts are due to the discretization of the actual structure into a grid of grain boundaries, which is seen as a network of potential cracks; the disorder immanent to the microstructure is accounted for via random numbers during the grid generation. The analytical parts are involved in the stress analysis: elementary analytical solutions for the single cavities (cracks, pores) are employed to determine the local stress disturbances; crack interactions are explicitly taken into consideration. The fracture criterion at the microscale relies on an energy balance estimation for the individual grain boundaries ('facets').

This semi-numerical simulation model serves as a tool for investigation of progressive damage under various loading conditions, in particular external compression and internal pore pressure. Crack closure resulting from normal compression, internal friction between sliding crack faces, and structural changes due to microcracking give rise to nonlinear effects which are properly described in the formalism.

Exemplary simulations reproduce the various types of damage (unstable crack growth, distributed microcracking, localization) and demonstrate their dependence on the loading modes and on the level of structure heterogeneity. Under internal compression, microcracks grow to connect pores, thus building chains or networks of defects.

In the investigations, high interest is focused on the statistical fluctuations of the observables due to the microstructural disorder. The studies span the whole range between nucleation of single microcracks and material failure.

Zusammenfassung

Die vorliegende Arbeit beschäftigt sich mit der Entstehung und Ausbreitung von Mikrorissen in spröden, granularen Medien, insbesondere in porösen Keramiken, und mit den Auswirkungen dieser mikroskopischen Schädigung auf die makroskopischen Materialeigenschaften. Zur Untersuchung dieses Schädigungsverhaltens wird ein zweidimensionales geometrisches Modell der Mikrostruktur und ein physikalisches Modell ihrer elastischen Eigenschaften und ihrer Festigkeit entwickelt.

Der hieraus hervorgehende Computer-Algorithmus stellt einen neuartigen Ansatz zur Simulation der Schädigung von Mikrostrukturen dar, denn er vereinigt Konzepte der rein analytischen 'mikromechanischen' Modelle und Konzepte der überwiegend numerischen 'Gitternetz'-Modelle. Die numerischen Anteile ergeben sich aus der Diskretisierung der tatsächlichen Struktur in ein Gitter aus Korngrenzen, welches als ein Netzwerk potenzieller Risse aufgefasst wird. Der natürlichen mikrostrukturellen Unordnung wird durch die Verwendung von Zufallszahlen bei der Gittergenerierung Rechnung getragen. Die analytischen Anteile rühren von der Spannungsanalyse her: die lokalen Spannungsfelder werden mittels elementarer analytischer Lösungen für die einzelnen Kavitäten (Risse, Poren) berechnet; Wechselwirkungen zwischen den Rissen werden explizit berücksichtigt. Das mikroskopische Bruchkriterium gründet auf eine Energieabschätzung für die einzelnen Korngrenzen ('Facetten').

Mit diesem semi-numerischen Simulationsmodell wird die fortschreitende Schädigung der Mikrostruktur insbesondere unter externen kompressiven Kräften und internem Porendruck untersucht. Das Schließen der Riss-Flächen unter Druckbelastung, interne Reibungskräfte sowie Strukturänderungen verursachen nichtlineare Effekte, die im Formalismus adäquat beschrieben werden.

Exemplarische Simulationen reproduzieren die unterschiedlichen Schädigungs-Typen (instabiles Risswachstum, verteilte Mikrorisse, Lokalisierung) und zeigen deren Abhängigkeit von den Belastungsformen und vom Grad der Struktur-Heterogenität auf. Unter Innendruck bilden die Mikrorisse Verbindungen zwischen den Poren, so dass Ketten oder Netzwerke von Defekten entstehen.

Ein wichtiges Thema bei den Untersuchungen sind die statistischen Schwankungen der Resultate aufgrund der mikrostrukturellen Unordnung. Die durchgeführten Studien erstrecken sich über die gesamte Bandbreite vom Entstehen einzelner Mikrorisse bis hin zum Materialversagen.

Zusammenfassung (Langform)

Modellierung der Mikrostruktur und Simulation fortschreitender Schädigung in spröden, porösen Keramiken

Die vorliegende Arbeit beschäftigt sich mit der Entstehung und Ausbreitung von Mikrorissen in spröden, granularen Medien, insbesondere in porösen Keramiken, und mit den Auswirkungen dieser mikroskopischen Schädigung auf die makroskopischen Materialeigenschaften. Zur Untersuchung dieses Schädigungsverhaltens wird ein zweidimensionales geometrisches Modell der Mikrostruktur und ein physikalisches Modell ihrer elastischen Eigenschaften und ihrer Festigkeit entwickelt; diese Modelle dienen als Grundlage für Computersimulationen, mit denen verschiedene Fragestellungen aus dem Bereich der Schädigungsmechanik bearbeitet werden.

Angelehnt an die maßgeblichen Struktureigenschaften eines heterogenen, dreiphasigen Materials konzentriert sich das Strukturmodell auf die festen, granularen Bestandteile und die Poren. Die Auflösungslänge des Modells ist demnach die Größe der Körner. Unter Verwendung von 'globalen' Strukturinformationen, die aus stereologischen Auswertungen elektronenmikroskopischer Bilder hervorgehen, sowie 'lokalen' Strukturinformationen, die aus empirischen Beobachtungen hervorgehen, erzeugt ein Computeralgorithmus numerische Repräsentanten der Kornstruktur. Hierbei werden Zufallszahlen eingesetzt, so dass diese Strukturmodelle als Stichproben des tatsächlichen Materials zu verstehen sind.

Anhand dieser konkreten Strukturbilder wird dann mit dem physikalischen Modell die Mikroriss-Bildung und der Mikroriss-Fortschritt unter vorgegebenen Belastungen simuliert. Die Belastungsmodi sind angelehnt an die Situation beim industriellen Einsatz des Materials als Filterträger, wo externe, kompressive Kräfte und interne Belastungen (Flüssigkeitsdruck in den Poren) dominieren. Das physikalische Modell geht von einem spröden Bruchverhalten der Korngrenzen (Facetten) aus. Das Modellgitter der Korngrenzen dient als ein Netzwerk potenzieller Risse, in dem die Simulation des Rissfortschritts nicht kontinuierlich, sondern in diskreten Schritten abläuft. Als Ergebnis der Berechnungen erhält man schließlich makroskopische elastische Parameter (z.B. effektive Steifigkeit, Gesamtdehnung), statistische Angaben für die Festigkeit, Strukturparameter (z.B. Rissdichte) und topologische Rissmuster.

Das hier vorgestellte und ausgearbeitete Computermodell stellt einen neuartigen Ansatz zur Simulation der Schädigung von Mikrostrukturen dar, denn es vereinigt Konzepte der 'mikromechanischen' Modelle, die auf analytischen Beschreibungen beruhen, und Konzepte der 'Gitternetz'-Modelle, die in erster Linie numerisch sind. Die numerischen Anteile ergeben sich hier aus der Diskretisierung der tatsächlichen Struktur in ein Gitter aus Korngrenzen; über diese Diskretisierung ist eine gewisse Verwandtschaft mit dem bekannten Konzept des Voronoi-Gitters gegeben. Anders als bei konventionellen Gitternetz-Methoden, z.B. Finite-Elemente-Methoden, ist das Korngrenzengitter jedoch nicht konzipiert, um Lasten zu übertragen. Die Bestimmung der Spannungen und Dehnungen im Material erfolgt hier nicht über die festen Strukturteile, sondern vielmehr über die Defekte, d.h. die Poren und Risse: Es werden elementare analytische Lösungen für die durch einzelne Kavitäten eingebrachten Störungen des lokalen Spannungsfeldes in den festen Materialphasen verwendet. Die Wechselwirkungen zwischen den Rissen werden

explizit berücksichtigt mittels Transmissionsfaktoren, einer Superpositions-Technik und Lösen eines selbst-konsistenten Gleichungssystems. Effektive, d.h. makroskopische, Parameter wie z.B. die Flexibilitätsmatrix werden durch explizites Aufsummieren der Beiträge der einzelnen Kavitäten berechnet.

Durch die Kombination von Gitternetz-Struktur und mikromechanischer Spannungsanalyse entsteht ein semi-numerisches Modell. Zu den Vorteilen dieses alternativen Konzepts zählt zunächst, dass die Spannungsanalyse aus der Perspektive der Kavitäten einen umfassenden, kompakten Formalismus ermöglicht, der anwendbar sowohl unter Zug- als auch unter Druckbelastungen ist. Gerade unter kompressiven Kräften, wo sich zusätzlich zu den Mikroriss-induzierten Strukturänderungen weitere nichtlineare Effekte durch das Schließen der Rissflächen und die Reibung beim Verschieben der Rissflächen ergeben, erweist sich die mikromechanische Beschreibungsweise als vorteilhaft. Aber im Unterschied zu durchgehend mikromechanischen Modellen berücksichtigt der vorgestellte Ansatz auch die räumlichen Korrelationen der Defekte und ist somit nicht-lokal. Andererseits ist im Vergleich zu Finite-Elemente-Methoden der rechnerische Aufwand (Finite-Elemente-Darstellung der Mikrodefekte, Matrixinversion etc.) gering, da das wechselwirkende System hier das Ensemble der Defekte und nicht die Gesamtzahl der Verbindungselemente im Materialnetz ist. Zudem ergibt im vorgestellten Konzept die Diskretisierung der festen Materialphasen ein ungeordnetes Korngrenzengitter; dieses erscheint hinsichtlich der Schädigungs-Simulation realitätsnäher und flexibler als die geordneten Gitternetze in standardisierten Finite-Elemente-Techniken.

Der semi-numerische Ansatz bringt freilich auch gewisse Nachteile mit sich. So erfordert die analytische Implementierung der verfügbaren Spannungslösungen eine sehr grobe Näherung für die Kavitäten-Formen, beispielsweise elliptische Porengeometrien oder geradlinige Risse. Insbesondere müssen Netzwerke aus Poren und Rissen durch elementare, eher 'glatte' Körper ersetzt werden. Eine weitere Schwäche des Modells ergibt sich aus der Tatsache, dass die analytischen Spannungslösungen nur für gleichförmig angreifende Einheitskräfte zur Verfügung stehen: die Belastungskräfte müssen deshalb entlang der Risslinien gemittelt werden. Diese Technik ist am besten vertretbar für verteilte Risse vergleichbarer Länge, wird bisweilen aber unklar bei Lokalisierung der Risse und bei stark unterschiedlichen Riss-Formen.

Zentrales Element in einem solchen Simulationsmodell für fortschreitende Schädigung ist das mikroskopische Bruchkriterium. Bei dem vorgestellten Konzept handelt es sich im Wesentlichen um ein Kriterium für die Energiebilanz, mit dem die Stabilität des Korngitters während des Belastungspfads kontrolliert wird: Spontanes Versagen einer Facette ist erst möglich, wenn die elastische Dehnungsenergie, die beim Trennen der Korngrenze freigesetzt wird, die Erhöhung der freien Oberflächenenergie kompensiert. Auf der Grundlage dieses Energiekriteriums und einzelner Ergänzungen berücksichtigt das Simulationsmodell neben der Entstehung neuer Risse auch die Vergrößerung und das Zusammenwachsen schon vorhandener Defekte (Risse und Poren) sowie das Entstehen von Pore-Riss-Netzwerken. Eine Verzweigung von Rissen wird allerdings nicht behandelt.

Ein wichtiger Gesichtspunkt im Modell und bei den durchgeführten Untersuchungen ist auch die Berücksichtigung natürlicher statistischer Schwankungen: Während die makroskopischen Strukturparameter gewissermaßen unveränderlich sind, unterscheidet sich die Mikrostruktur eines Werkstücks von Probe zu Probe, und dies hat Auswirkungen auf deren elastisches und bruchmechanisches Verhalten. Im Modell wird eine Monte

Carlo Simulations-Strategie angewandt, um — im Rahmen vorgegebener Verteilungsfunktionen — durch zufälliges Streuen der Körner und Poren mikroskopisch verschiedene Materialausschnitte zu erzeugen. Deterministische Simulationen an einer großen Anzahl solcher makroskopisch identischen Modellstrukturen liefern dann Daten, anhand derer mit einer statistischen Analyse die wesentlichen Trends des Schädigungsprozesses und die Varianz der beobachteten Größen ermittelt werden.

Kapitel 1 der vorliegenden Dissertationsschrift führt in wichtige Begriffe aus dem Bereich der Schädigungsmechanik ein und bietet einen Überblick über die aus der Literatur bekannten Berechnungsmodelle. Der neue, semi-numerische Ansatz wird vorgestellt und zwischen den traditionellen Modellen eingeordnet.

Im zweiten Kapitel wird das Verfahren zur Generierung von geometrischen Mikrostruktur-Bildern erläutert. Hinsichtlich der benötigten Eingabe-Informationen wird verdeutlicht, dass die aus der stereologischen Analyse von elektronenmikroskopischen Aufnahmen gewonnenen Daten die Mikrostruktur nicht ausreichend charakterisieren. In Bezug auf die 'lokalen' Struktureigenschaften, z.B. die Form und Größe der individuellen Strukturelemente, sind daher zusätzliche Annahmen erforderlich. Letztendlich weisen die mit dem zweidimensionalen Strukturmodell erzeugten Bilder aber eine beachtliche visuelle Ähnlichkeit zu den experimentellen Strukturbildern auf.

Kapitel 3 beschäftigt sich mit dem Einfluss von Kavitäten auf die effektiven elastischen Materialeigenschaften und auf die lokale Spannungsverteilung. Nach einer kurzen Einführung in die Theorie der Homogenisierung werden die traditionellen mikromechanischen Ansätze zur Berechnung der makroskopischen Steifigkeit bzw. Flexibilität, wie etwa das selbst-konsistente Schema, skizziert. Anschließend werden die aus der Literatur verfügbaren analytischen Spannungslösungen für einzelne Kavitäten ausgewertet und visualisiert. Für Strukturen mit zahlreichen, beliebig verteilten Rissen und/oder Poren wird dann ein Formalismus zur Berechnung der lokalen Spannungen und Verschiebungen entwickelt, der diese analytischen Lösungen numerisch verarbeitet. Über ein Homogenisierungsverfahren können somit auch die Flexibilitätsmatrix und die Gesamtdehnung des betrachteten Materialausschnitts bestimmt werden. Aufgrund der bereits erwähnten nichtlinearen Effekte (Schließen der Riss-Flächen, Reibung, Strukturänderungen) entsteht eine Abhängigkeit des Materialverhaltens vom vorangegangenen Belastungspfad; dieser Rolle der *Vergangenheit* wird durch Inkrementierung im Computer-Algorithmus und durch eine Reihe von Fallunterscheidungen Rechnung getragen. Von großer Bedeutung sind hier zwei physikalische Größen, die den momentanen Zustand eines Risses kennzeichnen: seine Aktivitätsfaktoren und die Fehlanpassung seiner Scherungsöffnung ('shear mismatch').

Als erste Anwendung dieses *nicht-lokalen* Formalismus' wird die Bedeutung der Wechselwirkungen zwischen den Kavitäten untersucht. Hinsichtlich der makroskopischen Parameter wie Steifigkeit und Gesamtdehnung ist der Einfluss der Wechselwirkungen so lange vernachlässigbar wie die Kavitäten zufällig verteilt sind. Sobald die Orientierung der Kavitäten eine Vorzugsrichtung aufweist und die gegenseitige Positionierung der Kavitäten eine Tendenz zur Stapel- oder Kettenform andeutet, haben die Wechselwirkungen jedoch entweder verstärkende oder abschwächende Wirkung. Eine spezielle Untersuchung unter Einsatz des Computermodells verdeutlicht, dass die mikroskopischen Spannungskonzentrationen durch die Wechselwirkungen in jedem Fall verstärkt werden, auch bei zufälliger Verteilung der Kavitäten.

Im vierten Kapitel wird die Entstehung und Ausbreitung von Mikrorissen in einem kompakten (d.h. nicht-porösen) Material untersucht. Mit exemplarischen Simulationen werden die unterschiedlichen Schädigungs-Typen (instabiles Risswachstum, verteilte Mikrorisse, Lokalisierung) reproduziert und deren Abhängigkeit von der Belastungsform (Zug, Druck, laterale Kräfte) und dem Grad der Struktur-Heterogenität aufgezeigt. Die Untersuchungen erklären, dass das Lokalisierungsphänomen, also das 'kooperative' Verhalten vieler Einzelrisse, eine Folge der verwinkelten Korngrenzen und der lokalen Störungsfelder der Risse ist. Die verwinkelten Korngrenzen wirken als Energie-Barrieren für den Rissfortschritt. Bei instabilem Risswachstum, das zu spontanem Versagen führt, sowie bei Lokalisierung ist eine Homogenisierung der mikroskopischen Daten nutzlos; hier kann der Übergang von mikroskopischer Schädigung zu makroskopischem Versagen ausschließlich anhand der Rissmuster analysiert werden.

Weitergehende Simulationsrechnungen unter externem Druck illustrieren, wie sich durch Mikrorisse die Steifigkeit des Materials verringert und eine Anisotropie entwickelt. Aufgrund ihrer Abhängigkeit vom Aktivitätszustand der Risse ist die Steifigkeit jedoch kaum geeignet, den Schädigungsgrad des Materials zu charakterisieren. Stattdessen bietet sich hier die skalare Rissdichte als Kenngröße an, da diese in den Simulationen eine enge Korrelation zu den Komponenten ϵ_{xx} and ϵ_{yy} der Gesamtdehnung aufweist und dem Formalismus leicht zugänglich ist. Testreihen an statistischen Materialproben verdeutlichen, wie die Unordnung im Korngitter die Resultate beeinflusst. Die absolute Streuung des Schädigungsparameters erhöht sich mit zunehmender Schädigung, während der Variationskoeffizient (d.h. die relative Streuung) mit zunehmender Schädigung abnimmt.

Wie die Untersuchungen bestätigen, wird die Schädigung im Material gefördert durch die von den Rissen und ihren Wechselwirkungen induzierten lokalen Spannungsfelder. Dagegen hat die Berücksichtigung interner Reibungskräfte in den Simulationen eine hemmende Wirkung auf die Ausbreitung der Schädigung.

Kapitel 5 ist einem speziellen Belastungs-Modus gewidmet, der beim industriellen Einsatz von porösen keramischen Filterträgern dominiert, nämlich der Druckbelastung innerhalb der Poren. Das Simulationsmodell wird hierbei dem Umstand angepasst, dass die höchsten Spannungskonzentrationen in der Umgebung der Poren auftreten und die Mikrorisse daher von den Poren ausgehen. Da jedoch schon die elementare Geometrie einer Pore-Riss-Kombination zu kompliziert für eine analytische Beschreibung des umgebenden Spannungsfeldes ist, werden im Energie-Bruchkriterium nun Spannungs-Intensitätsfaktoren eingesetzt. Zudem erweist es sich als notwendig, das Energiekriterium durch weitere Bedingungen zu ergänzen. Unter dem Einfluss des Innendrucks werden die Poren nun durch Mikrorisse verbunden, und es ergeben sich somit *Netzwerke* von Defekten. Für die Simulationsrechnungen müssen solche Defekt-Agglomerate durch einfache Kavitäten ersetzt werden, die vergleichbare Spannungskonzentrationen hervorrufen; in den hier vorliegenden Berechnungen sind dies Ellipsen.

Simulationen an einfachen porösen Strukturen zeigen unter Innendruck ein plötzliches, instabiles Ausbreiten der Defekte zu willkürlich orientierten, nahezu geradlinigen Fehler-Ketten, die die Materialproben schließlich durchtrennen (*Perkolation*). Dieses spröde Verhalten legt einen Vergleich mit statistischen 'weakest-link'-Theorien (Theorien des schwächsten Bindeglieds) nahe, insbesondere mit der Weibull-Theorie. Folglich wird die Verteilung der kritischen Belastungen, die sich aus Simulationen an einer Reihe statistischer Strukturproben ergibt, entsprechend der Weibull-Theorie analysiert. Für vorgegebene Größe des Materialausschnitts stimmen die Testergebnisse mit der Weibull-Theorie gut

überein. Simulationen an unterschiedlich großen Proben zeigen hingegen einen deutlichen Skalierungseffekt sowohl für den Mittelwert als auch für die Varianz der kritischen Belastung: In Übereinstimmung mit dem Größeneffekt der 'weakest-link'-Hypothesen sinkt die kritische Belastung bei zunehmender Probengröße. Während aber im Skalierungsgesetz der Standard-Weibull-Theorie die kritische Belastung asymptotisch gegen null strebt, ist der berechnete asymptotische Grenzwert von null verschieden. Das Skalierungsgesetz der Standard-Weibull-Theorie ist hier deshalb nicht anwendbar, weil das Material sich nicht *perfekt* spröde verhält. (Ursache ist, dass bei der Modellierung die Porengröße begrenzt ist.) Deshalb wird ein alternatives Skalierungsgesetz formuliert, welches die für verschiedene Probengrößen berechneten Resultate gut beschreibt und für ein Extrapolieren der kritischen Belastung hin zu größeren Probendimensionen hilfreich erscheint.

Die Auswertung der darauf folgenden Simulationsreihen berücksichtigt das Skalierungsverhalten der Materialproben. Die Rechnungen bestätigen, dass die Größe des repräsentativen Volumenelements mit der Maximalgröße der maßgeblichen Strukturelemente wächst: wichtig sind hier die statistischen Extreme, beispielsweise die größten Poren. Bei annähernd monodispersen Poren-Größenverteilungen sinkt die mittlere kritische Belastung mit dem spezifischen Poren-Umfang, d.h. sie steigt mit zunehmender 'Feinheit' der Phase. Die kritische Belastung sinkt dagegen mit zunehmender Porosität, und sie ist bei elliptischer Porenform geringer als bei kreisrunden Poren. Ähnlich wie im Fall der Poren hat auch eine höhere Feinheit der Körner eine stärkende Wirkung auf die Materialstruktur; die mikromechanischen Gründe sind allerdings verschieden.

Wie erwartet, ist die Varianz der kritischen Belastung in einem statistischen Proben-Ensemble umso größer, je ungeordneter die Struktur ist; diese Unordnung wächst mit der Anzahl der Freiheitsgrade im Strukturmodell (z.B. beliebige Position, Größe, Form, Orientierung der Poren). Gleichzeitig sinkt der Mittelwert der kritischen Belastung mit zunehmender Unordnung.

Als Fazit gilt festzustellen, dass der vorgestellte semi-numerische Ansatz selbstverständlich nicht alle in der Literatur beschriebenen Modelle zur Schädigungssimulation ersetzen kann. Wie die vorliegende Dissertation zeigt, ist dieser Ansatz jedoch eine nützliche Alternative, die für ganz unterschiedliche Problemstellungen gute Ergebnisse liefert. Dies betrifft wesentliche Aspekte der spröden und quasi-spröden Schädigung, der internen Reibung, oder der statistischen Unordnung in der Mikrostruktur. Bemerkenswert ist, dass die gesamte Bandbreite vom Entstehen einzelner Mikrorisse bis hin zum Materialversagen abgedeckt wird.

Obwohl die hier durchgeführten Modellrechnungen weitgehend auf eine Aluminiumoxid/Titandioxid-Struktur abgestimmt sind, können viele Teile der dargestellten Theorie und der Resultate auch auf andere mehrphasige (kompakte oder poröse) spröde Stoffe übertragen werden, seien es Keramiken, keramische Komposite, Gesteine oder Beton. Wie im letzten Kapitel der Dissertation skizziert, können durch Erweiterungen des Modells neben den rein mechanischen Belastungsformen auch thermische Restspannungen, Spannungskorrosion oder Ermüdungsrisse berücksichtigt werden. Obwohl das vorgestellte Modell auf vorgegebene Spannungen zugeschnitten ist, ist eine Kopplung mit makroskopischen Untersuchungen (z.B. Finite-Elemente-Modellen), die eher von Verschiebungen ausgehen, gut denkbar.

Die Vorteile und Möglichkeiten des semi-numerischen Modellansatzes bei der qualitativen Untersuchung von Schädigungsprozessen können jedoch nicht darüber hinweg-

täuschen, dass mit dem Modell in seiner gegenwärtigen Form die *quantitative* Beschreibung des Material-Bruchverhaltens mitunter noch sehr unzulänglich ist. Dies wird deutlich am Beispiel des kritischen Innendrucks, der zur Schädigung der porösen Strukturen aufgewandt werden muss: Während für die Modellstrukturen Schwellwerte oberhalb von 100 MPa berechnet werden, beobachtet man in industriellen Anwendungen schon bei einem Flüssigkeitsdruck zwischen 1 und 5 MPa signifikante Schädigungen. Diese hohe Diskrepanz ist nicht allein auf die Vernachlässigung thermischer, chemischer und zyklischer Einflüsse oder die Beschränkung auf nur eine Korn-Phase (Titandioxid) bei den Modell-Simulationen zurückzuführen. Die Gründe liegen auch auf einer tieferen, konzeptionellen Ebene:

Zum einen ist das Modell durch seine sehr grobe Näherung für die Kavitäten-Geometrien eingeschränkt. Reelle Poren sind weniger glatt und rund, sondern vielmehr kantig und spitz; deshalb bewirken sie höhere Spannungskonzentrationen im Material, die das Entstehen der Mikrorisse beträchtlich erleichtern. Um diese Spannungs-Spitzen im Modell zu berücksichtigen, wäre eine künstliche Variation der Spannungs-Intensitätsfaktoren erforderlich. Außerdem ist für eine quantitativ gültige Rechnung eine wesentlich breitere Streuung der Porengrößen bei der Struktur-Modellierung nötig — in den Materialproben wird nämlich eine 'offene' Porosität beobachtet, die sich in den zweidimensionalen Querschnitten durch vereinzelte sehr lange, schmale Poren bemerkbar macht.

Eine weitere konzeptionelle Einschränkung ergibt sich durch die zweidimensionale Betrachtungsweise. Die Beschränkung auf zwei Dimensionen kann für eine quantitative Simulation nur in gewissen Sonderfällen genügen, aber sie hat ihre Berechtigung insofern, als ein Verständnis der Probleme im zweidimensionalen Raum hilfreich für die Bewertung der wesentlich komplexeren Situationen im dreidimensionalen Raum ist. (Prinzipiell sind wesentliche Teile des Formalismus auch auf Situationen im Dreidimensionalen anwendbar, jedoch wäre die praktische Umsetzung sehr aufwändig und kaum lohnenswert.) Eine kurze Diskussion am Ende des letzten Kapitels macht deutlich, dass die auf den zweidimensionalen Raum beschränkte Sicht zwei gegensätzliche Konsequenzen hat: eine 'reduzierte' Wahrnehmung der Defekt-Geometrien einerseits, und eine Überschätzung der Einflüsse der Defekte auf die elastischen Materialeigenschaften andererseits. Inwieweit diese beiden konträren Effekte sich gegenseitig aufheben, dürfte wohl vom Einzelfall abhängen.

Hinsichtlich ihrer quantitativen Gültigkeit sind die in Kapitel 4 vorgestellten Ergebnisse generell realistischer einzuschätzen als die Ergebnisse von Kapitel 5. Denn Kapitel 4 beschränkt sich auf kompakte Materialien, während die oben genannten konzeptionellen Einschränkungen in erster Linie mit den Poren zur Geltung kommen. Aber bereits die Modellierung des kompakten Materials kann durch besser angepasste Eingabe-Informationen optimiert werden — die Strukturparameter (genaue Korngrößen, Eigenschaften der Korn-Grenzflächen etc.), die Materialparameter (z.B. spezifische Oberflächenenergie, elastische Konstanten) oder auch die Randbedingungen der Materialausschnitte gehen nämlich bisher nur in sehr grober Näherung ins Modell ein. Ein exaktes Abbild der Realität zu schaffen, ist jedoch kein vielversprechendes Ziel eines Computermodells. Die Vorzüge des hier ausgearbeiteten Modells liegen in der Klarheit, mit der es die wesentlichen Phänomene qualitativ wiedergibt, und nicht etwa in einer quantitativen, numerischen Genauigkeit. Davon abgesehen gewinnt man ein Verständnis für die mikromechanischen Schädigungsprozesse nicht erst mit dem Einsatz des 'fertigen' Modells in Simulationsrechnungen, sondern bereits mit der Entwicklung des Modells selbst.

List of Symbols

symbol	meaning
a, b	lengths of ellipse semiaxes
a_k^{n}, a_k^{s}	crack activity factors
A	area
$\mathbf{b}_k$	crack opening displacement
$\mathbf{C}$	elastic compliance (tensor resp. matrix)
d	damage parameter / diameter
D	specimen size (volume or area)
E	Young's modulus
$\boldsymbol{\epsilon}$	elastic strain tensor
G	energy release rate
γ	specific surface energy
$\mathbf{I}$	unit matrix
K	stress intensity factor
L_A	specific perimeter (perimeter per unit area)
l_k	crack length
λ	size factor (Weibull theory)
$\mathbf{\Lambda}_{ki}$	traction transmission factor
m	Weibull shape parameter
μ_y	population mean
μ_m	sliding friction coefficient
μ_s	static (sticking) friction coefficient
N_A	number density (number per unit area)
$\mathbf{n}_k$	unit normal vector
$\mathbf{N}_\theta$	projection matrix
ν	Poisson ratio
p	porosity / probability density
P	internal (fluid) pressure

symbol	meaning
Π	cumulative failure probability
q	shape factor
r	radius / fitting parameter (scaling law)
r_{kl}	correlation coefficient
ρ	scalar crack density
ρ, θ	curvilinear coordinates
s_y	sample standard deviation
$\mathbf{S}$	elastic stiffness (tensor resp. matrix)
σ_y	population standard deviation
$\boldsymbol{\sigma}$	stress tensor
S_V	specific surface (surface per unit volume)
$\mathbf{t}_k$	traction acting on a crack
$t_{k,\mathrm{mism}}^{\mathrm{s}}$	shear traction mismatch
τ, T	time
θ_k	crack orientation angle
Θ	temperature
U	cumulative survival probability
V	volume
V_V	specific phase volume (phase volume per unit volume)
W	energy
x, y	Cartesian coordinates
y	observable
$\bar{y}$	sample mean of y
y_s	characteristic strength (Weibull theory)

Chapter 1

Introduction

The present dissertation has emerged from the BRITE-EURAM project N^0 BE-3109 *Extend-Nanofilters* which run in the years 1997 to 2000. Essential parts of the work have been developed and written in the bounds of the project, others have been motivated by questions raised during that time, and have been elaborated later on. The context of the European project and the cooperation with international partners suggested the English language for the writing.

The project, fully named "Improvement of porous ceramic substrate for the extension of nanofiltration", addressed two main points of basic industrial and economical interest: Firstly, the applicability of certain membranes to filtering nanoscale particles, and their performance with respect to the separation rates; secondly, the reliability and lifetime of the porous, multiphased ceramic supports on which the membranes are deposited.

The present work contributes to the second point. The objective was the geometrical modelling of the structural properties and the simulation of damage evolution in the filter support material at the microscale. These studies supplement the efforts of the project partners for a better understanding of the filter support behaviour at the macroscopic level, which included experimental measurements and loading tests on industrial components as well as numerical simulations of the fabrication process and of service conditions via finite element methods. Vice versa, the present account is supported and partially confirmed by micrographic analyses of actual specimens performed by a project partner.

The computational model established and employed here represents a new approach on the simulation of microcracking and irreversible structural changes, which combines elementary analytical solutions, numerical meshing and statistical investigations. It is attached to the essential characteristics of the micro-heterogeneous filter support material: a granular microstructure consisting of several solid-phase constituents (Al_2O_3, TiO_2) and pores, and a brittle or quasi-brittle rupture behaviour. It concentrates on the special industrial service conditions, which comprise remote as well as internal loading modes. Nevertheless, the model is applicable to other multi-phased, compact or porous ceramics subjected to mechanical stresses, and is extendable with respect to the impact of thermal residual stresses and corrosion.

The computer programs for the numerical calculations have all been written in *FORTRAN 90* in the course of the project. The computations have been performed under a *UNIX* operating system running on a Silicon Graphics "*O2*" workstation. Visualization of the results has been done in the framework of the *MATLAB* engineering software. The administration of data and of the different software modules has been supported by *Perl*

scripts. Advantage has been gratefully taken of several further software tools running under the *GNU* public license.

This introductory chapter will first outline the basic modes of damage and failure from a general, rather phenomenological point of view (section 1.1.1), then review the common concepts of modelling in damage mechanics (section 1.1.2), and finally describe the objective and characteristics of the present approach (section 1.2 and 1.3).

1.1 Micromechanics and damage mechanics

Damage in materials is usually considered from three fundamental observation levels:

At the *macroscopic* scale, the corresponding scientific discipline is called 'fracture mechanics'; it deals with macroscopic cracks and notches. The resolution length of models at the macroscale is the size of the 'representative volume element' (RVE) of the material. Elementary fracture mechanics deals with the solid phases at the continuum level, i.e. it neglects the heterogeneous character of the material at the microscale.

In many cases, failure of structural parts at the macroscale follows from irreversible processes at the *microscale*. The corresponding scientific discipline is called 'damage mechanics'; it is concerned with microscopic defects, and microcracks in particular. A typical resolution length of related models is the grain size or the size of the inclusions in a ceramic material. Transition from considerations at the macroscopic level to models at the microscopic level requires a procedure called 'discretization' [48][1], while the inverse process is called 'homogenization'.

At the *molecular* level, damage is expressed in ruptured inter-molecular bonds and atomic dislocations. The resolution length is the atomic distance.

The present investigation must be attributed to the intermediate observation scale (the microscale), and to the field of damage mechanics in brittle solids.

1.1.1 Microscopic damage from a general point of view

Generalizing, one may distinguish two basic 'modes' of damage evolution at the microscopic level: nucleation of new microcracks resulting in distributed microcracking, on the one hand, and propagation (growth) of already existing microcracks, on the other hand. Accordingly, failure of a material may be ultimately dominated by unstable growth of a singular crack or by the 'collective' impact of a number of cracks. The latter phenomenon is called *localization*; it may be categorized in between the two limiting mechanisms of unstable crack growth and randomly distributed microcrack nucleation.

The present thesis does not account for any plastic deformation, but consider an idealization of the fracture process.

Distributed microcracking. A damage evolution dominated by microcrack nucleation and stable propagation of existing microcracks requires a heterogeneity or a strongly disordered structure of the material at the microscale: in this case, grain boundaries and inclusions provide energy barriers which trap the nucleated microcracks and arrest their

[1] Alternatively, the macro-micro transition is often called 'localization' [56], but the present thesis will use this term to describe a damage phenomenon (see p. 19).

growth. Nucleation of new microcracks and the arising patterns of distributed cracks result in a *quasi-brittle* response of these 'damage tolerant solids'.

Crack nucleation is rather an *intrinsic* phenomenon depending on the constitutive material properties and the micro-defect density, i.e. on effective (macroscopic, averaged) parameters. Compressive loads, high temperatures, or corrosive effects of the environment are further conditions favouring the distributed damage. A moderate lateral compression renders the growth of microcracks stable by decreasing their stress intensity factors.

For example, a material under triaxial compression may keep hardening at the specimen scale while it is progressively crushing into smaller fragments; under these conditions, the microcrack densities may reach and exceed the percolation limit without clearly affecting the current macroscopic response of the material. The connectivity failure becomes obvious only after removal of the confinement (and application of a minute tensile load).

Unstable crack growth. Unstable growth of a single crack is encountered in solids with a rather homogeneous, ordered microstructure. Such materials are called 'defect-sensitive', 'damage-intolerant', or 'perfectly brittle', and break without warning: in simple terms, the first crack arising will immediately grow to divide the specimen into two or more parts.

The exhibited sudden (*brittle*) failure does hardly depend on the effective material parameters, on the density of the accumulated damage, or on overall stresses; the failure threshold rather depends on the size, location and orientation of the largest defect, i.e. on the statistical extremes, not on the averages.

The probability of finding such a critical defect in a specimen depends on the size and shape of the specimen and on the loading conditions. The failure threshold is an *extrinsic* (structural) parameter and a statistical variate; the scatter of the experimental data is substantial.

The possibility of unstable crack growth is favoured in uncompressed specimens. Otherwise, stable evolution of damage may cross over into unstable evolution if one of the microcracks reaches its critical length.

Localization.[2] If in a material "microcracks both nucleate and grow and the growth is dependent on the direct interaction of microcracks", then a cooperative phenomenon may occur: closely spaced small microcracks tend to self-organize into long and thin clusters where the cracks are roughly parallel and the interaction amplifies their stress intensity factors and the elastic energy release rate. The short range correlation "crosses over to a long range correlation which thereafter dominates the macro response". This "threshold of the short to long range correlation transition" is called *localization*.

The crack clusters form a narrow 'band' where the microcrack density is much higher than in the rest of the volume. One may speak of a 'shear band mode' in case of compressive loads, and of a 'split' (or 'cleavage') mode in case of tensile loads. A shear band is nearly parallel (spanning a small angle in the range between 15 and 25 degrees) to the compression axis and exhibits a very small shear resistance (1 to 5 % of the pristine value) in the direction of the band tangent, whereas the split mode extends perpendicular to the direction of tensile load. As soon as the shear band is formed, the undamaged material domains undergo elastic unloading. The material is stable only under displacement

[2]The quotations in the current section refer to [48].

controlled conditions.

In polycrystalline solids, the width of a localized band may typically span several grains. The width of the band where the microcracks are correlated represents a characteristic length, and the material must therefore be described by a *non-local* theory.

After the onset of localization, the material cannot be considered statistically homogeneous any more. "The material in the exterior of the band remains statistically homogeneous in contrast to the material in the band interior".

The localization phenomenon is essentially non-deterministic, so "the role of the disorder and dynamic nature of the localization cannot be overestimated".

1.1.2 Review of model approaches in the literature

An immense variety of publications is available in the context of computational damage mechanics; the present section is to give a coarse review of the multitude of model approaches. In order to reach some clarity, it establishes several classes of models, each based upon a different fundamental concept, relating to a different viewpoint on the underlying physical processes. Figure 1.1 shows a chart of the model classes and their relationships.

It is, however, significant that such a categorization is always too simplifying, since the transition between the classes is smooth; they are "complementary (not competing)" [48]. A rational model must integrate several of them: for example, a micromechanical approach is never complete without accounting for the statistical aspects.

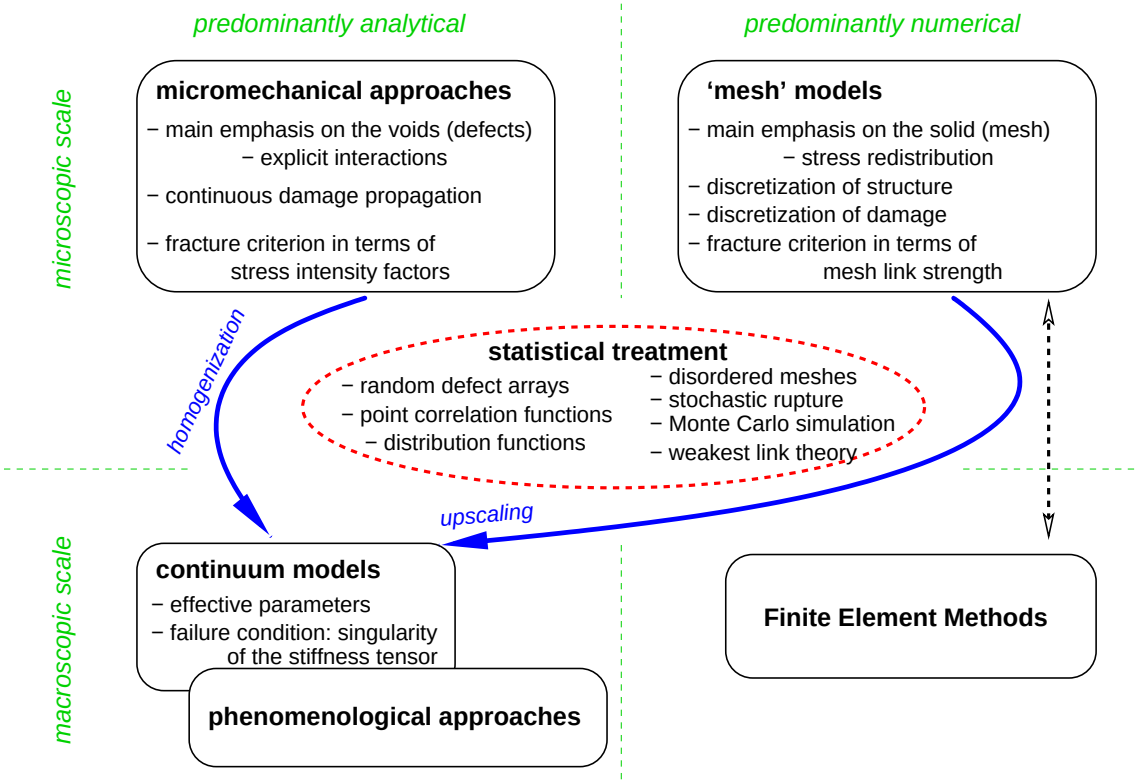

Figure 1.1: Fundamental model approaches in the field of damage mechanics.

1.1.2.1 Micromechanical approaches

Micromechanical approaches are based upon elementary considerations in elasticity theory and fracture; they establish and apply *analytical* terms and solutions for local stress concentrations (in particular stress intensity factors), crack opening displacements, or cavity compliances.

Conceptually, the impact of the *defects or inclusions* on the solid phases is the central part of a micromechanical description. On the other hand, the emphasis of the defects usually comes along with a neglection of the microscopic properties of the matrix material (e.g., the grain structure), even though these are fundamental for microcracking. The solid material phases are considered as a continuum, so that the micromechanical models often are applicable to macroscopic problems as well. Vice versa, solutions from fracture mechanics (e.g., stress intensity factors for macrocracks: [75], [44], [7]) are standard tools employed in micromechanical studies (using the stress intensity factors for microcracks: e.g., [67], [83]). In other words, the present class of models is not really specified to micro- or macromechanical situations. Also those studies which are in close contact to experiments, getting their input informations (typically the defect-size distribution) from micrographic and fractographic studies of actual specimens, focus nevertheless on the defects, not on the solid phases (e.g., [6], [35]).

Another essential characteristic of the micromechanical approaches is the analytical formulation of the basic laws. As a matter of course, an analytical model must restrict to simple geometries and thus involves rough approximations of the defect shapes: circular pores, straight cracks etc. (see [43], [41] for a review). The important issue of connected defects, e.g. cracks emanating from pores, necessitates a further reduction of the geometry: the configuration of two equal cracks emanating axially from a circular pore is conveniently approximated by an ellipse of equal overall extent ('elliptical holes model') or by superposition of a circular pore and a *separate* long crack ('hole and crack model') [83]. In three dimensions, there are approaches which replace the configurations of cracks emanating from a circular pore by a spheroid (e.g., [46]). For the description of stresses at arbitrarily shaped pores with rounded (not sharp) borders, the 'equivalent ellipse concept' [51] is a prominent representative: the local stress concentration at a rounded pole of the pore is substituted by the stress concentration of an ellipse with the same linear extent and an equal radius of curvature. In the study of [6], a three-dimensional defect is approximated by the smallest envelopping disk (penny-shaped crack). A common feature of these reduced configurations is that they are suitable for a prediction of effective elastic material properties and for an elementary comprehension of basic cracking mechanisms, but they are not sufficient for a quantitative simulation of damage evolution from the complex defect shapes encountered in actual materials. Statistical evaluations with appropriate size distributions of the simple defects (see, e.g. [6]) may assist to account for the fact that failure is governed by the extremes.

Studies on single defects or dilute defect concentrations can demonstrate the significance of defect orientation, shape, size and loading conditions for the material response. Due to the defect-centered approach, the description of correlations requires an explicit modelling of the defect interactions. Even in a two-dimensional model, exact analytical solutions must naturally be limited to very few defects (e.g., two cracks) or to periodical arrays.

A higher number of defects, or arbitrary defect arrangements, necessitates transition

from the purely analytical to semi-numerical formalisms: The loading conditions on the individual defects are replaced by 'pseudotractions', and the interactions in the multi-defect array result in complex equation systems to be solved by numerical means ([42], [5]). The even simpler 'dipole asymptotics model' [25] is another example for these semi-numerical concepts which can manage configurations of hundreds and thousands of cracks with the aid of modern computer facilities.

Alternatively, many approaches are founded on ensembles of identical defects centered at the nodes of a perfectly periodic lattice, and thus ignore the fact that defects in reality form clusters and other anomalous patterns. The assumption of periodicity (perfect order) in these 'cell models' reduces the problem associated with the interactions to the consideration of a single defect located in a cell of regular geometry. The boundary conditions at the cell surfaces result easily from the periodicity. The assumption of periodicity reduces the computational efforts significantly, but is seldom a good recipe to describe the physical reality at the microstructural level. On the other hand, exact solutions are available for certain periodic arrays of defects; semi-numerical model approaches may be applied to the same periodic arrays, and the results may be compared with the exact ones for an assessment of the model approaches, see [25] as an example. For an extended discussion of solids with a periodic microstructure, see [62].

As for the damage evolution, micromechanical models predominantly deal with the continuous growth of existing cracks or cavities. Rupture criteria are classically based on Griffith's model, which compares the stress intensity factor at a crack tip with the fracture toughness (cohesive strength) of the material [76]. For prediction of the propagation of elliptical notches (which have – in contrast to cracks – a finite radius of curvature and thus cause no stress singularity), a simple stress criterion is often used ([58], [35]). The present dissertation will show that simulation of defect *nucleation* is more challenging, requiring different methods and further assumptions.

The vast majority of the approaches in the literature addresses systems subjected to tensile or shear loads. Approaches on systems under compression are rather rare, even though brittle materials, such as rock, concrete and ceramics, are primarily used in applications subjected to compressive tractions. Modelling compressive loading conditions requires to account for the variating state (passive/active) of the microcracks [62]. Simple models ([84]) neglect the effect of friction between the closed crack faces. A special case is the longitudinal splitting of specimens under uniaxial compression: cracks emanating from pores in the axial direction are in fact under tension [83].

1.1.2.2 'Mesh' techniques

Whereas the micromechanical approaches work from the perspective of the defects and cavities, the mesh models ('lattice' models) focus main attention on the solid phase of the material. The mesh models rely on a discretization of the solid structure into a finite element mesh, which is assigned to contain the material and structural properties and to carry the externally applied loads. The model simulations aim at the determination of loads and displacements on each individual mesh node as a function of the boundary conditions, involving extensive linear or nonlinear equation systems. Since closed-form analytical solutions for the stresses and strains are not applicable to discretized structures, the simulations make use of numerical techniques instead. Deterministic computational algorithms of elementary structural mechanics can be applied, and available finite element

algorithms (standard software) may be employed to facilitate the calculations.

The characteristic length (resolution length) in lattice models is the size of the links (bonds) in the mesh. The discretization may be done on different resolution scales: At the microscale, *disordered* meshes may correspond to certain properties of the solid structure, e.g. to the network of grain boundaries, whereas 'macroscopic' finite element models veil the microscopic characteristics and usually work on regular meshes. For special considerations, the meshes sometimes are chosen to be even finer than the dimension of the microscopic heterogeneities.

In lattice models, the discretization of the structure comes along with a discretization of the damage evolution. Damage evolution can be simulated simply by a sequential removal of links. The local load sharing effects are incorporated in a natural way: after failure of a link, the algorithm computes the stress redistribution within the mesh structure — an explicit consideration of the defect interactions is not necessary.

In that manner, both defect growth and defect *nucleation* are naturally incorporated: damage is where the local stresses or strains exceed the rupture strength of the links. Rupture criteria attributed to the links refer either to energy [45] or force considerations. It is self-evident that the strength of the links is easier defined in terms of a critical tensile load, whereas the more complex conditions of compressive loads are often left aside.

Simple lattices. The simplest examples from the class of lattice models are represented by the one-dimensional *parallel bar models* (see, e.g., [48]). They consist of loose or interconnected bundles of beams attributed with an axial stiffness and strength. They exhibit no characteristic length, but suffice to illustrate the effect of stress redistribution: Damage, i.e. removal of some of the beams, disturbes the orderly transfer of the forces through the lattice structure; the imbalance of the forces in the beams increases with the accumulation of damage.

In the two- or three-dimensional space, a classical and often applied example for a lattice model is the Delaunay network. The Delaunay network consists of a number of distributed points (nodes) which are connected to the neighboring points by straight lines, respectively. In the simplest realization, the resulting cells are triangles (in 2-D, see fig. 1.2) or tetrahedra (in 3-D). The links between the nodes may be axial, transverse, rotational, or combinations of them.

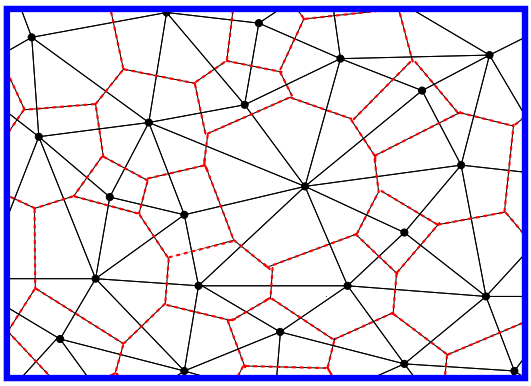

Figure 1.2: Sketch of a Delaunay network (solid) and the dual Voronoi lattice (dashed).

The dual to the Delaunay network is the Voronoi lattice [28]: the edges of the Voronoi polyhedra (also called 'Poisson cells' [50]) intersect the links of the Delaunay network in

the perpendicular direction. Thus, the two-dimensional space may be tiled with polygons (fig. 1.2), and the three-dimensional space may, correspondingly, be filled with polyhedra. If the Voronoi polyhedra are considered as the grains of a polycrystalline ceramic [45], then the sides of the Voronoi polyhedrons correspond to the grain boundaries, and the links in the Delaunay lattice correspond to the cohesive strengths of the grain boundaries. A missing Delaunay link then corresponds to an intergranular crack.

Finite element method (FEM). The standardized finite element method (see, e.g. [85]), which relies on libraries of sophisticated numerical algorithms for solving the extensive linear and non-linear equation systems, is a popular technique employed by engineers for product design, structural analysis and strength computation. The specimens under consideration are modelled by a regular-type mesh; for reasons of economy and accuracy, those regions in the material which will receive larger amounts of stress are covered by a higher node density than those which experience little or no stress. The generation and adaptive modification of the meshes is usually supported by commercial software packages.

As for the simulation of damage progression, FE-techniques are traditionally applied to macroscopic cracks [58], but they may also be used for computational studies at a lower (microscopic) level. Macroscopic criteria for modelling crack extension may refer to a 'contour integral' ('J-integral': an energy density expression is integrated along a closed path surrounding the crack tip), to the tearing modulus, or to the crack tip opening angle. The increment of rupture is given by the element size, which is usually much smaller than the crack [58]. Introduction of new crack surfaces into the mesh requires to double the node at the center of the respective element (e.g., [45]).

The approach in [80] concerns the propagation and coalescence of microcracks preexisting around the granulates in a concrete structure. The propagation is controlled by stress-intensity factors of linear elastic fracture mechanics; elastic behaviour is assumed everywhere in the structure except at the crack tip. Typical for this class of approaches, the analysis restricts to tensile stresses, and the finite element mesh is significantly finer than the dimension of the (microscopic) heterogeneities. Remeshing is required to catch the changes in the specimen topology.

A more distinct treatment of crack initiation and propagation is facilitated by introducing zero-thickness interface elements along the expected crack paths within the standard continuum finite element mesh (which is considered linear elastic) [10]. The interface elements are associated with rather extensive, constitutive energy laws for cracking, which may account for a fracture process zone (elastoplastic behaviour) in quasi-brittle materials as well as rather complex loading modes such as shear/compression (see [11], which also includes an extensive review of cracking models in the context of FE-methods).

The above mentioned approaches are applied to two-dimensional studies only. An attempt on crack evolution in three dimensions is described by Kamiya et al. [45], but it relies on very coarse approximations for the fracture criterion, and borders quickly on restrictions imposed by computer facilities.

1.1.2.3 Approaches to the continuum

The ultimate goal of the considerations at the microscopic level is to obtain a general, applicable, efficient model at the *macroscopic* observation scale, where the microscopic

details become blurred. The transition to these *continuum* models is achieved by homogenization techniques.

Continuum models address volume averages and effective parameters of the material; ideally, they provide constitutive equations for macroscopic stresses and strains. The latter are nonlinear in the presence of damage evolution, and singular conditions along the constitutive paths indicate failure of the material. Therefore, the failure condition in continuum models claims a vanishing of the determinant (zero eigenvalue) of the tangent stiffness tensor (see, e.g. [83]): the uniaxial stress-strain curve must reach a turning point.

Deduction from the microscale. Homogenization starting from the micromechanical models often relies on simplifying assumptions for the defects at the microscopic level — e.g., a dilute concentration, an 'effective environment' (see section 3.2 of the present dissertation), or a periodic array ([83], [46], [25]). To mention an example, the continuum model presented in [65] accounts for defect interactions in a way motivated by the micromechanical approach by Mark Kachanov ([42], see section 3.4.3 of the present thesis) and the periodic cell model. Concerning the class of mesh models, the linear size of the microscopic specimens may enter a continuum model as the resolution length.

Phenomenological approaches. Phenomenological approaches lead to a special, but very convenient kind of continuum models which are not necessarily motivated by micromechanical studies but may directly emanate from considerations at the macroscopic level. They focus in "constitutive relations in which the mechanical effect of cracking and void growth is introduced with internal state variables which act on the elastic stiffness of the material" [65].

According to the literature, the origin of the continuum damage approaches is attributed to L. M. Kachanov [40] who established a scalar theory focusing on uniaxial problems. The extent of damage in a material is combined to a damage parameter d which defines the loss of stiffness, entering the stress-strain relation as follows:

$$\sigma = \underbrace{E(1-d)}_{E_d}\,\epsilon \tag{1.1}$$

The parameter d may assume values between 0 and 1; a value of 1 refers to total damage, but failure generally occurs when a somewhat lower critical value is reached. Following this simple approach, the evolution of the damage parameter can be determined experimentally by measuring the easily accessible effective Young's modulus E_d of the material.

The mathematical nature of the internal state variable is different among the various continuum models. It may be a scalar (for isotropic damage, e.g. the porosity), a vector or a tensor. One or more damage parameters may be involved. The continuum damage model illustrated in [65] incorporates two scalar damage parameters, and accounts for crack interactions, damage localization and a characteristic length. The non-local description of the material is realized by introducing a local weight factor for the damage variable in the constitutive relation of the model. The approach in [29] uses an orthotropic damage tensor which results in a fourth order compliance matrix (instead of the scalar $1/E_d$ in eq. 1.1); the model is further extended by distinguishing damage variables under tension and compression, and expressing the evolution of damage parameters in terms of a thermodynamic damage force. Anyway, many continuum mechanics models are based

on thermodynamical approaches which describe the irreversible rearrangements of the microstructure in the process of deformation by kinematic variables; energy dissipation is reflected here in the evolution of an energy potential (Gibb's energy density, see, e.g., [73], which also contains an extended review of the concepts of continuum damage mechanics).

Attempts have been undertaken to extend the phenomenological damage models to deactivation and reactivation of the damage effects. The approach presented in [30] introduces smoothed Heaviside functions to account for the transition between active and inactive states; it is elaborated with respect to elastoplasticity effects, but the phenomenological level does hardly allow for a consideration of delicate effects such as frictional sliding.

All in all, "phenomenological modelling is a mixture of science, skill and experience" [48]. The elegant, closed formalism of many continuum damage models comes along with physical clarity and tractability and renders this class suitable for reflecting certain basic aspects of material behaviour. Expecting quantitatively realistic results from this kind of models is, however, too much. In order to apply a continuum model in further studies, such as (macroscopic) finite element calculations, the damage state variables are sometimes *fitted* to macroscopic parameters from experiments [29].

1.1.2.4 Statistical considerations

The original micromechanical models and mesh models refer to deterministic defect arrangements and structures, thus ignoring the inevitable stochastic disorder at the microscale. However, "randomness is the most prominent feature of a polycrystal" [50]. An opening up of the above concepts to the actual stochastic nature may be accomplished by a widening or a variation of the input informations. Usually, the introduction of statistics concerns the microstructure modelling, while the calculation of elastic parameters and the simulation of damage evolution remain deterministic.

Analytical methods. In an analytical framework, statistical input information may be provided in terms of n-point correlation functions, which result from integration of n-point probability density functions or may be determined by experimental methods. n-point correlation functions have a macroscopic character, since the statistical fluctuations at the microscopic level are averaged ([50], [49], [35]).

These functions firstly refer to elastic parameters such as the stiffness, or stress or strain. Strictly speaking, the n-point correlation functions and probability density functions describe the local values of these parameters at n specified points within a statistical ensemble ('ensemble averaging'), but the *ergodic hypothesis* [50] says that there is an equivalence to averaging between n arbitrary points within a single member of the ensemble. Via the local values of the considered elastic parameters, the functions reflect the statistical properties of the structure, e.g. the distribution of grain shapes and orientations. The full set of n-point correlation/probability functions contains the whole statistical information, but "in many cases, it is satisfactory to work with correlations up to order 3" [50]: the one-point correlation function represents the mean value (of the modulus, or of the stress or strain); the two-point correlation function indicates the anisotropy of the grain shapes ("mean value of the grain diameters, taken in the various directions"); the three-point correlation function describes lengthy grains also if they are not aligned, i.e. in an isotropic arrangement [49].

The correlation functions allow for a determination of the tensors of effective elastic moduli of macro-homogeneous polycrystals to within any desired accuracy, depending on the available order n of the functions [50].

In a *local* approach where the correlations are disregarded, it is sufficient to consider simple distribution functions or probability density functions of the structure elements. Section 4.4 of the present thesis will demonstrate how such input information, representing the distribution of grain boundary lengths and orientations, may be utilized to predict the evolution of the effective moduli for the progressively fracturing system.

Numerical methods. In numerical approaches, especially mesh models, a statistical treatment is executed by the introduction of *randomness*. For example, the strengths of the links in a parallel bar model or in a Delaunay lattice may be randomly distributed in space. Or the grain boundaries in a structure model may have random specific surface energies. Or the inhomogeneities, e.g. pores, are randomly positioned across the model image.

While most of the models are characterized by a random, disordered structure and a deterministic analysis, it should be mentioned that other models start from ordered systems and continue with stochastic rupturing processes or a random dilution of the lattice.

The randomness introduced into single specimens often necessitates analyses of a large number of physical realizations. The same kind of experiment should be performed on many specimens which are prepared alike such that they appear to be macroscopically equal though different in the microscopic details. The so-called *Monte Carlo methods* can approximate expectation values and estimate errors where analytical methods do not work. Depending on the computational power, the results are systematically improvable by using larger samples and extended systems.

An extreme case is the study by Ju and Chen ([38], [39]) where the observations are averaged over 'all' possible realizations of a random crack distribution (see section 3.2.2.4 in Chapter 3 and section 30 in Chapter 4).

Methods at the macroscopic scale. In defect-sensitive (perfectly brittle) materials, the least resistant element is decisive: failure of the weakest element entails the fracture of the whole solid. Up-scaling of the failure probability of small specimens to the failure probability of larger specimens may then be accomplished by weakest-link theories assuming a Weibull distribution ('algebraic law'/power law dependence on the applied load, see section 5.5.1.2 of the present dissertation) or a Gumbel distribution (exponential law dependence on the applied load), or even simpler laws for the distribution of small specimen failure thresholds. The proper choice of the distribution of rupture strengths is the crucial point in these models.

Weibull theory may be classified as a 'phenomenological' approach since it does not account for the explicit microstructure or the stress fluctuations at the microscopic level. Instead, macroscopic stresses are considered. If the distribution of defects systematically varies within certain batches or areas in the material, then standard Weibull theory fails to predict the results and must be replaced by a 'multiscale' approach [6].

The weakest-link theory does not apply to materials under compressive load and to situations where the microcracks are stopped by microscopic heterogeneities [29]. As outlined above, the latter situation represents a typical quasi-brittle behaviour.

1.2 Objective and scope of the present study

The present thesis considers brittle sintered solids exhibiting a heterogeneous granular structure, either compact or including pores, with ceramic materials as an application. The materials are subjected to special loading conditions such as externally applied compression, or fluid pressure acting inside the pores. The applied loads are high enough to cause irreversible changes (damage) inside the specimens.

The scope is to gain a better comprehension of the macroscopic behaviour and resistance of these materials by modelling the responsible processes on a finer, microscopic level of the material structure. To this end, the facilities provided by a modern computer system are to be employed, for computer simulations can deal with specimens that are hardly obtainable and conditions that are not easily accessible to experimental analysis.

These special requirements suggest to establish a novel model approach which takes advantage of the existing concepts outlined in the previous section 1.1.2, but goes beyond them. The efforts in establishing and employing the model should particularly address the following issues:

- identification of the microstructural parameters and characteristics relevant for initiation of damage
- investigation of statistical effects due to the microstructural disorder
- inspection of the significance of certain micromechanical correlations (e.g., defect interactions) for the evolution of damage
- considerations on the appropriate damage parameter/observable
- estimation of the macroscopic response of the system (homogenization)

The model should serve as a tool for the determination of universal trends and qualitative attributes of the brittle rupture processes; it does not aim at exact quantitative results. The essential modes of damage as portrayed in section 1.1.1 should be reproduced.

1.3 Principle and characteristics of the present approach

The present approach emanates from a concept by Doltsinis that investigates microcracking in brittle materials in conjunction with the microstructure. Following early preparatory steps ([21], [20]), the theoretical constitutive framework was established in [15]. Essential extensions have been outlined in [16], which concern the nonlinear effects associated with crack closure and friction. The theoretical background is elaborated here to a computational model procedure, the characteristics of which are compiled in the following:

Resolution scale. The resolution length of the present model is the average size of the smallest grains. Below this discretization level, details of the material texture and fluctuations of stress and strain are smeared and summarized in empirical parameters (for example, specific surface energy). The choice of this resolution length follows the numerous observations that the heterogeneity between grains is fundamental for microcracking, and

that the grains are a "natural choice for the discrete elements" in the case of polycrystalline solids [48].

Classification. The present approach combines essential characteristics of both the class of mesh models and the class of micromechanical models, and must therefore be categorized somewhere intermediate:

- The microstructure model is discretized at the level of the grains. Accordingly, the simulation of progressive damage is not performed in a continuous way, but in discrete steps: the model grid of grain boundaries (*facets*) represents a network of potential microcracks, and each grain boundary may only fail instantaneously with the full dimension. The discretization of the model establishes a certain relationship with the Voronoi lattice described in section 1.1.2.2. The resulting model images are closer to the actual microstructures than common mesh models, and the same holds for the simulation of damage.

- On the other hand, these facet meshes are not designed to carry any load — the stress and strain analysis in the present approach is not founded on the solid parts of the structure, but rather focuses on the defects (cracks, pores). A deterministic analysis of the local stress field is performed with the aid of elementary, analytical solutions for the disturbances induced by singular defects. The interactions between the defects are directly accounted for via transmission factors and a superposition technique. These concepts are borrowed from the class of micromechanical models (section 1.1.2.1).

Microscopic rupture criterion. Fracturing of facets in the respective loading state is decided by an energy estimation: the elastic strain energy released by separating facets must exceed the associated increase in free surface energy. The energy criterion requires the calculation of the actual local stress condition on each facet. (This is accomplished by superposition of the tractions from external load, and those tractions 'transmitted' by cracks and pores.) In case that the facet emanates from an existing defect, the shape and size of the possibly growing defect must be accounted for in the calculation of the strain contribution.

The specific surface energy may be individually adjusted to the boundaries between the various grain phases.

Algorithm. The *computer algorithm for generation of artificial geometrical microstructure images* requires input informations on certain morphological parameters from actual microstructures. The *computer algorithm for simulation of microcracking* requires input informations on the elastic properties and certain material properties (such as the specific surface energy) of the grain phases, and on the macroscopic loading conditions (stress or internal pressure).

The simulation of progressive fracturing starts with a stable state of fracturing (usually the undamaged state) in the model images. Afterwards, the loading state is incrementally modified, and the current tractions on each facet are determined. The most critical facet is singled out and – if the rupture criterion is fulfilled – 'removed', i.e. replaced by a crack. Appearance of defect growth and coalescence of defects is recognized and approximately accounted for:

- If a new cracked facet touches an existing crack, then no additional crack is allocated but the old one is extended; a kinked crack arising from this procedure is subsequently approximated by a straight line.

- The spatial extent of chains and networks of connected pores and cracks is permanently recorded; regarding the stress analysis, the flaw clusters are approximated by large cavities of simple shape.

Then, a quasi-static redistribution of local stresses is calculated for the surviving network. This procedure is repeated incrementally for each change of applied load. The analysis ultimately ends when the final load is reached or a localization of damage (percolation, failure) is observed.

The main instructions of the crack formation algorithm are presented in Table 1.1.

The model accounts for the different behaviour of cracks under tension and compression, and the constrained shear displacement of compressed crack faces due to static friction.

The output of the damage simulation algorithm comprises effective elastic parameters such as stiffness and overall strain, structural parameters such as the crack density, and the topological microcrack pattern in the damaged microstructure.

loading loop	**start:** zero load
	• advance state of applied external stress $\boldsymbol{\sigma}$ or internal pressure P along prescribed loading path • calculate loading conditions on each unbroken facet; determine potential defect cluster and strain energy release in case of facet failure • calculate overall energy release in case of failure of any facet; allocate a cracked facet if energy release is positive • update cracks, facets, defect clusters • in case of defect percolation or localization: stop loading loop • determine current strain state $\boldsymbol{\epsilon}$ and effective compliance $\mathbf{C}$ resp. stiffness $\mathbf{S}$ for the current structure
	end: final load (input value)

Table 1.1: Scheme of the microcrack evolution algorithm to be employed on a given model specimen.

Statistical treatment. The model images attributed to a certain kind of material are macroscopically almost 'identical', but are different at the microstructure level. A Monte Carlo sampling strategy is employed which leads to microscopically different specimens of a material structure by each time randomly distributing the individual constituents. Fluctuations of the averaged structure parameters from specimen to specimen may be allowed as well.

The damage simulations, which are deterministic for a given model structure, are employed in a statistical procedure by successively performing tests on a large number of such macroscopically identical specimens.

Then, a statistical analysis of the results identifies universal trends of the deformation process and of the scatter of the observables.

Restrictions. The present approach is designed with respect to two-dimensional considerations. Thus, the stress analysis assumes plane stress or plane strain conditions. The restriction to two dimensions is at the expense of the generality of the model, but it yields a manageability and applicability with respect to numerical calculations. Compared to this, the applicability of any three-dimensional model for simulation of damage would be limited to the very basics.

Anyway, one should be aware that detailed information on the actual three-dimensional structural properties of the addressed materials is not available.

1.4 Organization of the present thesis

An appealing model study in the field of damage mechanics must cover four essential points: description of the material structure, stress analysis, simulation of damage initiation, and failure. The present thesis comprises four substantial chapters (2 to 5) which are roughly dedicated to these stages:

The immediately following Chapter 2 is concerned with the properties of the actual material structures in question, and the generation of geometrical model images reflecting the essential characteristics.

Then, Chapter 3 deals with the stress fields around cavities and cracks, and with the effective elastic properties and overall strains of structures containing such defects. After reviewing some popular local continuum models, the *non-local* micromechanical formalism is established which may be seen as the theoretical backbone of the present work. At present, the formalism is rather general with respect to the loading conditions, involving uniaxial or biaxial stresses and internal pressure. Micromechanical details are discussed, and homogenization to the continuum level is demonstrated.

Different from Chapter 3, which refers to structures of a given, fixed state, the subsequent Chapters 4 and 5 pursue the issues of damage evolution and statistical fluctuations in the microstructure — it is here where the discretization of the structure into a granular mesh becomes important. Chapter 4 addresses the *nucleation* and growth of microcracks under various loading conditions, with a focus on compressive loads. It introduces the theoretical ideas for simulation of fracturing, and presents computer simulations illustrating various points, from the modes of fracturing to the friction coefficients. For practical reasons, the studies are restricted to compact material structures, and to rather small crack densities.

The subject of Chapter 5 is the progressive damage in porous structures under internal pressure. These particular conditions require a modification of the formalism, which is outlined and illustrated first. The computational simulations then show how microcracks emanate from the existing pores and thus connect the cavities to form large, growing defect clusters. The simulations are continued until the failure of the specimens is recognized in terms of percolation.

Finally, Chapter 6 provides a concluding assessment of the presented investigations, a summary of the insights and results of each previous chapter, and an outlook at possible extensions and further discussions.

Chapter 2

Modelling of porous granular microstructures

The evolution of damage is simulated on two-dimensional geometrical 'images' (i.e., numerical representations) of the microstructure (see fig. 2.1, right, as an example). At the time of generation, no microcracks are present in the model images.

The morphological characteristics of the artificial two-dimensional model images are specified by stereological analysis data from actual material structures (see fig. 2.1, left, as an example[1]). The materials under consideration comprise three individual phases: pores, and grains of different constitution. In the context of the present approach, the grains are attributed to a titanium oxide (TiO_2) phase and an aluminum oxide (Al_2O_3) phase, but the model applies to different materials as well. The explicit geometry and topology of the microstructure are statistical entities.

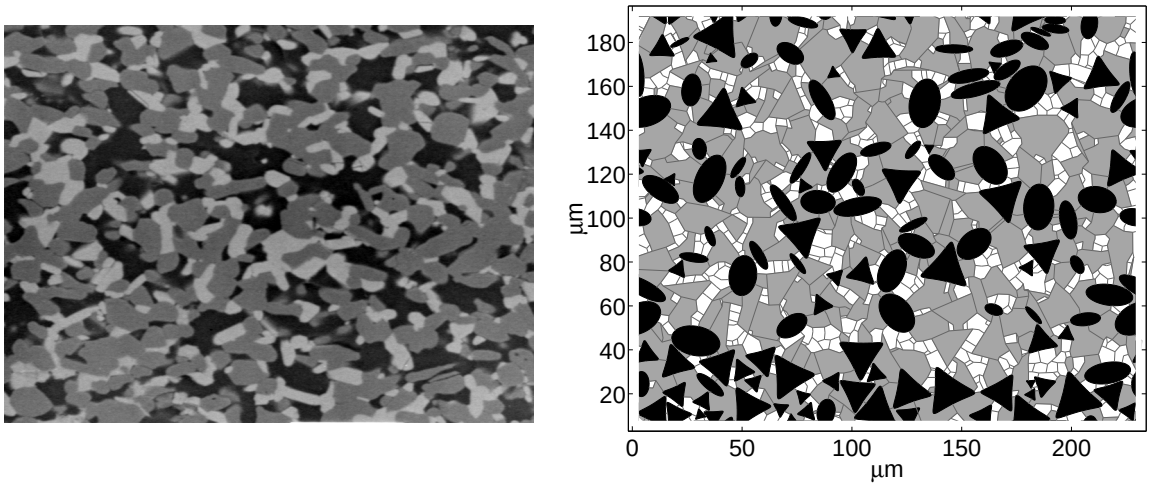

Figure 2.1: Left: Scanning Electron Micrograph (SEM) of an aluminum oxide based filter support with 28 % porosity. The size of the image is 170 μm $\times$ 230 μm. *Right: model structure. In both figures, black areas refer to pores, while the gray-coloured grains represent the* Al_2O_3 *phase, and the white grains represent the* TiO_2 *phase. In the model, the grid of gray strokes represents the network of potential cracks along grain facets.*

[1]The Scanning Electron Micrographs presented in the current chapter have been provided by Olivier Vansse [63].

Section 2.1 outlines the basics and features of the model generation algorithm, section 2.2 discusses the available input parameters and the additional assumptions required. Section 2.3 presents some exemplary model specimens, which are assessed with the aid of image analysis methods, and are compared with micrographs of actual material structures. The chapter closes with some reflections on three-dimensional structures (section 2.4).

2.1 Computer generation of two-dimensional microstructure images

Artificial two-dimensional microstructure images with specified characteristics are generated by a computer algorithm. First steps reported in [19] have been considerably extended in order to generate rather realistic images of observed microstructures containing several phases. The modelling algorithm essentially comprises four stages, which are illustrated in fig. 2.2, and are elucidated in the following.

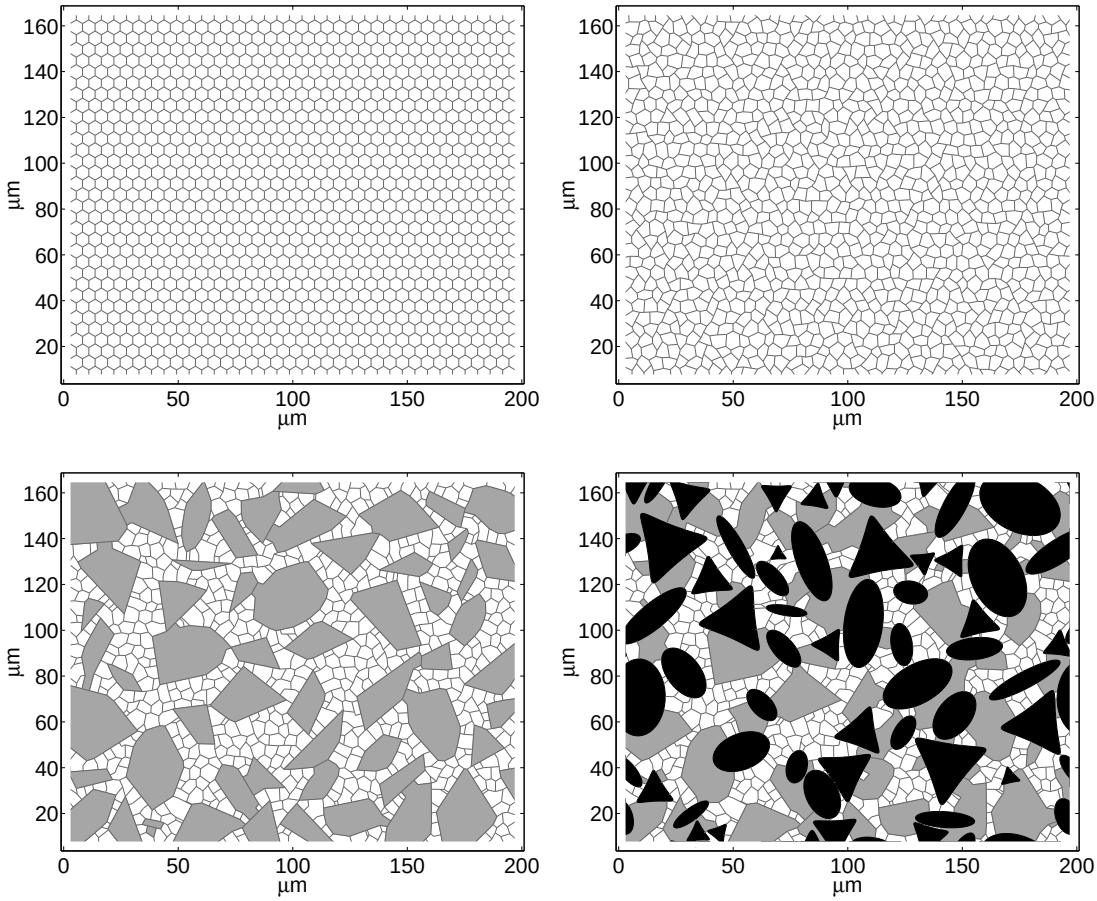

Figure 2.2: Various stages in modelling, exemplified for a TiO_2/Al_2O_3 *porous structure: 1) Undistorted regular hexagonal lattice; 2) Distortion of the regular hexagonal lattice, thus getting a basic grid of (*TiO_2*) grain boundaries; 3) Implanting the second grain phase (*Al_2O_3*) and adjustment of the basic grain boundaries; 4) Implanting pores of simple geometrical shapes and adjustment of first and second grain phase boundaries.*

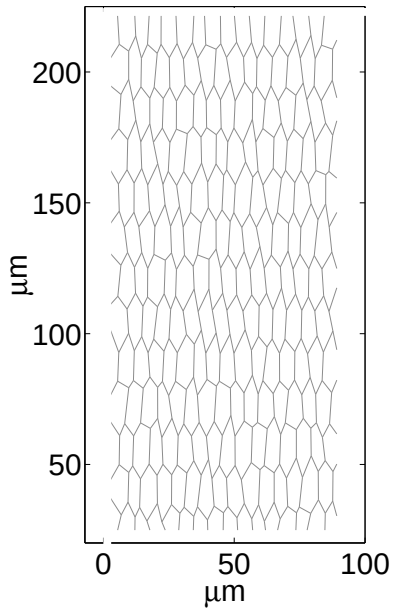

Figure 2.3: Anisotropic grain model structure.

- For the present purpose, an essential constituent of the microstructure model is a network of potential cracks. Assuming *intergranular* fracture, the network is identical to the grid of grain boundaries (facets) in the ceramic material. The standard algorithm allows for a two-phase mixture of grains:

  – Generation of the first, basic grain phase starts with a regular hexagonal lattice ('honeycomb structure'); the cells are then subjected to random distortions by displacing triple points. The general extent of distortion may be adjusted. Anisotropic structures, consisting of elongated grains oriented in a preferred direction, might be created by re-scaling of this lattice along a certain linear axis (fig. 2.3).

  – A second phase of grains, different in shape and of larger size, may be implanted into this basic lattice. The individual second-phase grains are created as polygons with corners located on the boundary of imaginable ellipses; the aspect ratio[2] of the respective ellipse and the number of polygon corners are specified by input parameters.

- For a representation of porosity, various cavities, differing in their effect on the stiffness, can be distributed between the grains. These cavities are of simple geometrical shape, since the local stress analysis in the model is based upon analytical stress solutions for the cavities (see Chapter 3). The distribution of size and orientation of the cavities may be adjusted individually for the various shapes.

  Available are 'elastically isotropic' and 'elastically anisotropic' cavities: circular pores and pores with (approximately) regular triangular shape, on the one hand, and elliptical pores as well as cracks, on the other hand. For elliptical pores, a

[2]aspect ratio: ratio of the semiaxis lengths

discrete summation yields for the porosity (area fraction)

$$p = \frac{1}{A}\pi \sum_k a_k b_k \ , \tag{2.1}$$

whereas the shape factor ('eccentricity') is defined as

$$q = \frac{1}{A}\pi \sum_k (a_k - b_k)^2 \ , \tag{2.2}$$

with a_k and b_k denoting the semiaxis lengths of pore k, and A being the area of the material section. Special cases are circular pores: $p = \frac{1}{A}\pi \sum_k (a_k)^2$ and $q = 0$, and cracks (length $l_k = 2a_k$): $p = 0$ and $q = \frac{1}{A}\pi \sum_k (l_k/2)^2$.

The shape factor q of cracks is closely related to the scalar *crack density*[3] ρ:

$$\rho = \frac{1}{A} \sum_k \left(\frac{l_k}{2}\right)^2 \tag{2.3}$$

$$q = \pi\rho \tag{2.4}$$

Regarding the effective elastic properties, ellipses represent a good approximation for rectangles, too [41]. Modelling the actual 'jagged' contours of the pores by ellipses (or, in 3-D, ellipsoids) represents a proper simplification since the inscribed and circumscribed ellipses generate lower and upper bounds for the effective properties (for references, see [71]).

Optionally, small triangular cavities can be implanted to represent triple point voids between grains in sintered ceramics.

Due to the two-dimensional formulation, the approximation of *open porosity* is rather poor: strictly speaking, open pore channels are assumed to extend in the third dimension. The porosity in the modelling plane is of a closed type.

Shapes and sizes of the individual second-phase grains and pores are either fixed at computation time or read from a data file in advance; the individual objects are then successively implanted into the current structure. Apart from the constraint that pores must neither touch nor overlap and second-phase grains may touch but must not overlap too high, the location of second-phase grains and pores is generally random. The orientation of second-phase grains and pores may be chosen individually or statistically, thus attaining isotropy or certain anisotropies.

The adjustment of the previous structure to the presence of an implanted new object (second-phase grain, pore) requires an extensive algorithm: grain boundaries located completely inside the new object need to be eliminated, grain boundaries crossing the border or located close to the border of the new object need to be shifted towards the border, etc.

[3] Under certain conditions, the scalar crack density is an important parameter for characterization of the damage state (see Chapter 4).

In the ultimate model structure, the individual grains (first phase, second phase) are identified and related to unique numbers (see fig. 2.4). This procedure enables to assign special properties to the grain elements, e.g. orientation angles of the crystalline planes. The latter will be important if a micromechanical description of thermal residual stresses ([77], [54]) is to be added to the simulation algorithm.

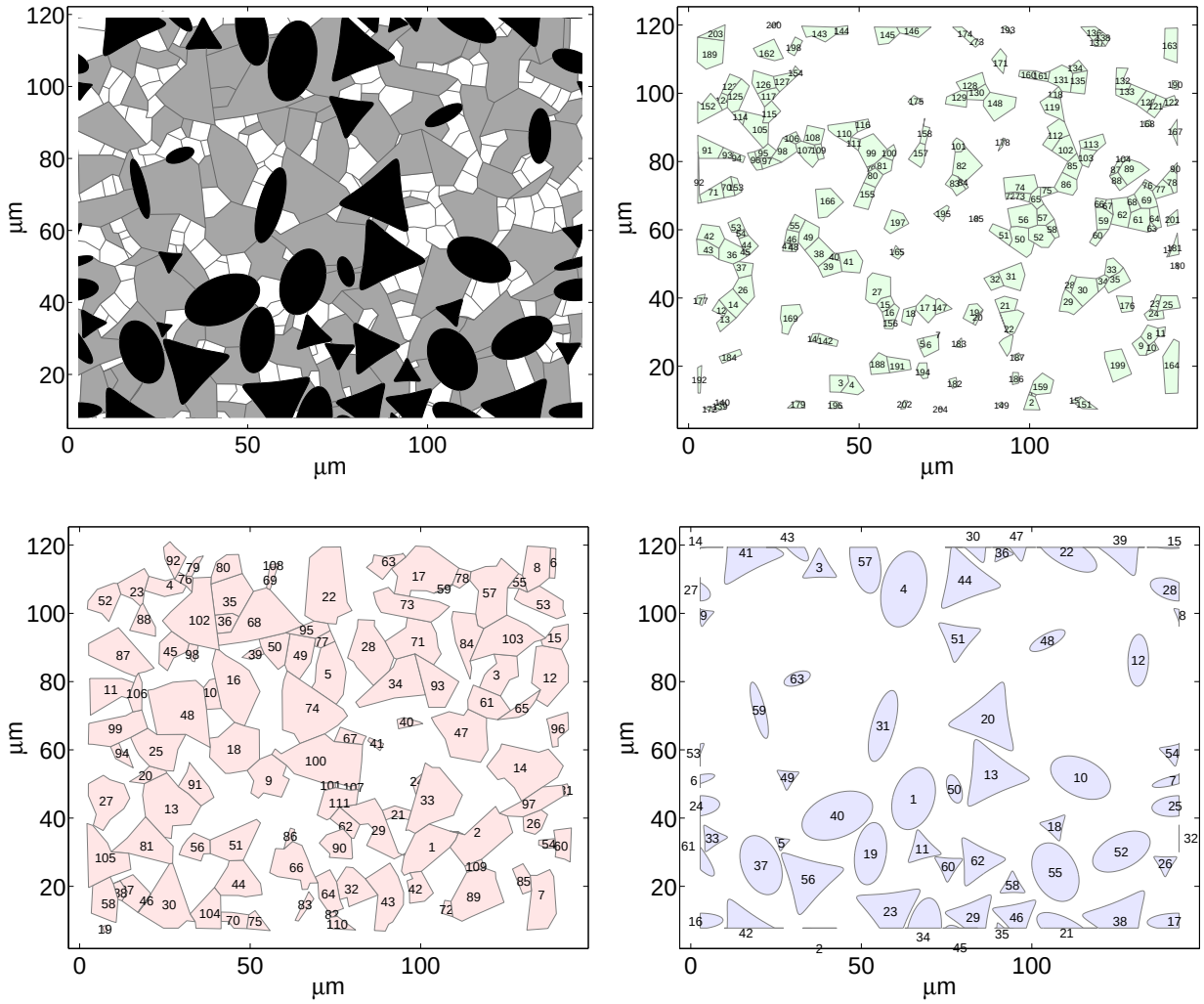

Figure 2.4: Three-phase microstructure image, and identification of the individual elements belonging to the first grain phase, second grain phase, and pore phase, respectively. Main axis orientations are (randomly) assigned to the individual grains, a prerequisite for consideration of thermal residual stresses.

In order to account for the effect of the surrounding material, the borders of the specimen are designed such that the structure can be duplicated with respect to all four sides. Thus, the specimen can be extended periodically (fig. 2.5). The presence of pores located outside, but in close vicinity to the specimen border (red margin in fig. 2.5) is recorded and accounted for in the stress analysis (Chapter 5).

Different specimens of a material structure are obtained by selecting different distributions of the individual constituents (pores, second-phase grains). Usually, a random positioning will be chosen since informations on the explicit spatial correlations are not available. The random-number generator of the computer is extensively used for the

generation of sizes, shapes, positions and orientations of the material constituents.

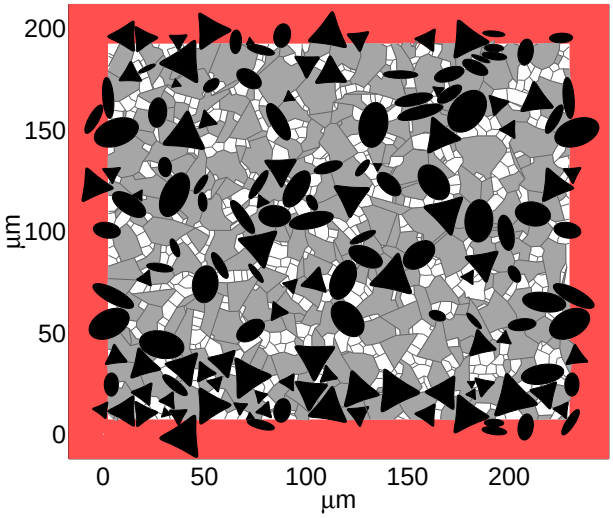

Figure 2.5: Accounting for the material surrounding the specimen. The pore pattern along the borders allows periodic continuation of the specimen as an option: pore parts outside the specimen (red margin) are continued inside at the opposite border.

2.2 On the input parameters applied in the model

Stereological parameters from experiment. In order to generate a realistic microstructure image, morphological data of the actual material are required. These may be supplied by analysis of Scanning Electron Micrographs. A pertinent tool in this context is quantitative stereology, a branch of geometry employed for numerical characterization of points, lines, surfaces and volumes from observations on two-dimensional sections in three-dimensional specimens ([48], [78]). It takes advantage of the Euler-Poincaré characteristic, which is suitable for studying n-dimensional structures (R^n) from measurements of connectivity numbers in lower-dimensional spaces (R^{n-1}) (see [70] for details). The most fundamental parameters provided here may serve as input parameters for the modelling program: the specific area (area fraction) A_A and specific perimeter (perimeter per unit area) L_A of the different grain and pore phases. In the following, it is presumed that the considered stereological parameters actually *exist*, which means that the scatter of these parameters in a statistical sample tends towards zero when the specimen size increases towards infinite, or that the observed parameters in fact *have* a mean. (The existence of the stereological parameters is not at all a general property of materials, see [52]).

Although obtained from a *local* analysis of the medium, quantities such as area fraction and specific perimeter are, in effect, *global* parameters: they refer to properties of a phase (a 'collective') from a 'global' point of view. The global parameters forge links between experiment and model, but the modelling of the individual structure elements ('individual analysis', e.g. size and shape of the pores) still comes along with some arbitrariness.

It is therefore useful to discuss the limits of the information provided by the stereological parameters, and to explain the additional assumptions underlying the present

generation of microstructure images:

Additional assumptions. Given the specific area and specific perimeter of a certain phase, one may first assume a simple case where the individual elements of that phase conform to a monodisperse size and shape distribution. Then the global parameters are directly related to the properties of the individual elements — the conversion factor is N_A, the number density of the elements —, and it can be stated:

- For a given specific area, the specific perimeter of the phase is a measure for the 'fineness' or the granularity of the phase. If a certain shape is prescribed, too, then the size of the elements is a unique function of the specific perimeter (see fig. 2.6, left, for illustration).

- For elements of an elliptical shape type and given size (length a of large semi-axis), the exact shape (specified by length b of small semi-axis) is unique, i.e. a unique function of (specific) area and (specific) perimeter (see fig. 2.6, right, for illustration). This fact is of some importance since the largest linear extent of an element (which corresponds to $2a$) is rather easily accessible by image analysis.

- For elements of an elliptical shape type and given area, the exact shape (aspect ratio a/b) of the elements is unique as well (see fig. 2.7, for illustration).

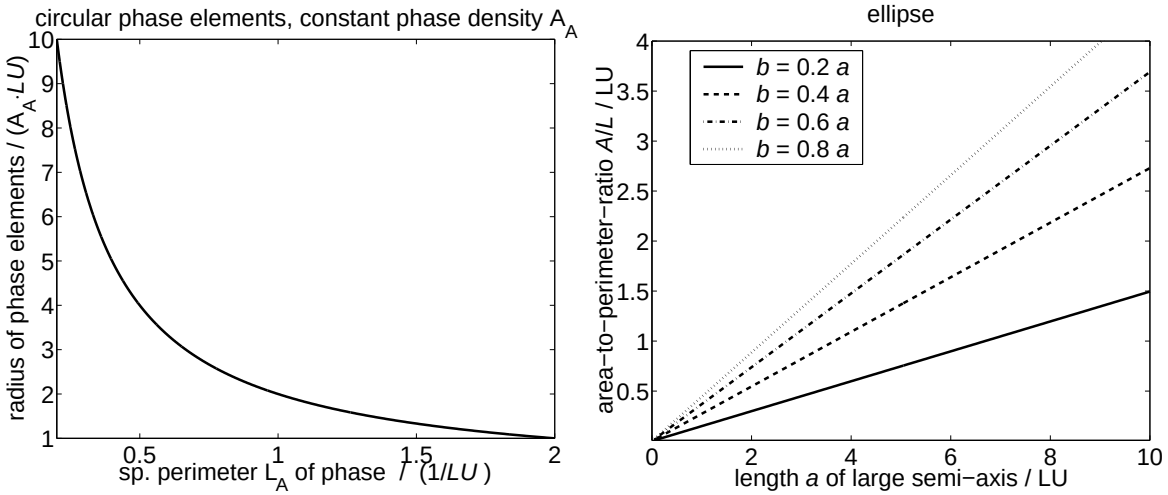

Figure 2.6: Left: For a monodisperse distribution of circular phase elements with given area fraction A_A, the specific perimeter L_A is a measure for the fineness (radius r) of the elements: $r = 2\ A_A/L_A$. (LU: length unit). Right: For an ellipse, there is a unique relation between area, perimeter, length a of large semi-axis, and length b of small semi-axis.

If a monodisperse shape distribution, but a polydisperse size distribution is given, then the explicit size distribution cannot be deduced from area fraction and specific perimeter. For the general case of polydisperse shape and size distributions, the properties of the individual elements are even more vague.

The main point to emphasize here is that the above three items apply to polydisperse size distributions in an approximate way, provided that the range of element sizes is

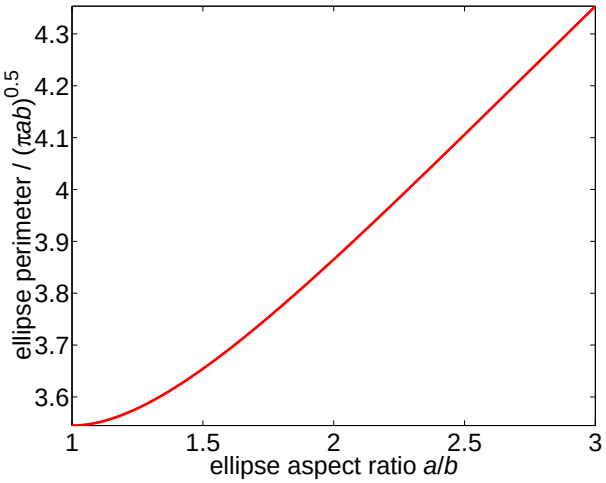

Figure 2.7: Perimeter of an ellipse as a function of aspect ratio at constant ellipse area: For an elliptical pore of given area, there is a unique (in the shown range: approximately linear) relation between pore perimeter and pore shape (aspect ratio).

rationally bounded (not too small and not extremely large) — an assumption which typically holds for the actual microstructures.

Finally, the present way of modelling is based on additional assumptions regarding the type of the size distribution (Gaussian normal distribution, uniform distribution), the range of the sizes, and the shapes. All the parameters involved here are chosen to fit to primitive observations on micrographs.

Remarks on the specimen size. Another important input parameter is the size (area) of the specimens. It is obvious that the analysis of a heterogeneous microstructure should preferably be performed on specimens large enough to be *representative*. In that context, it is essential to introduce the common term '*R*epresentative *V*olume *E*lement' (RVE).

As a rule, the RVE relates to a certain observable, and its size depends on the desired accuracy of the observation. It is defined as the smallest material section for which the distribution of the observable among a sufficient number of specimens conforms to the corresponding distribution within a very large section. This means that the distribution is the same (to within the defined accuracy), no matter how large the material section is if only larger than the RVE. Thus, the RVE is statistically homogeneous: the properties are invariant (or at least approximately invariant) with respect to translations of the RVE; "any RVE at a specific point looks very much like any other RVE taken at random at another point" [56]. In micromechanical models with a deterministic, periodic structure, the basic cell is a paradigm of a RVE, representing the characteristic pattern. In random structures, the RVE is much larger than the source of the heterogeneity, and may be called a *micro-continuum* [69].

The structural parameters such as porosity are *intrinsic* material properties for which a representative volume element usually exists [48]. While the mean μ_y of such stereological parameters y is expected not to depend on the specimen size D,

$$\mu_y(D) = \text{const.}, \tag{2.5}$$

the situation is different for the standard deviation σ_y of the estimate[4]: For sizes below RVE, the variance decreases with increasing specimen size D as follows [52]:

$$\sigma_y(D) \propto \frac{1}{\sqrt{D}}, \tag{2.6}$$

tending to zero for D exceeding RVE. D denotes the area (in 2-D) or the volume (in 3-D) (or, in 1-D, the length) of the specimen [37].

In the case that RVE-specimens are too large for the experimental analysis, eq. (2.6) suggests to use nevertheless the maximum specimen size accessible. This will yield more precision in the results, and a reduction of effort.

For the RVE in metals and ceramics, a characteristic magnitude of $(0.1\text{mm})^3$ has been suggested (see [73]). Boundary effects are not present in the context of stereological structure parameters.

2.3 Suiting the model to real microstructures

Stereological information from image analysis of scanning electron micrographs is a valuable input for the microstructure modelling, but an *exact* reproduction of these values in the model images is not possible. The reason is that the procedure of successively implanting the second-phase grains and the pores gives no perfect control on the global parameters, which are coupled to one another in a complex way. One may be tempted to variate certain individual input parameters in order to improve the results, but the computer algorithm should rather be based upon input from physical observations than from a try-and-error strategy.

The current section shows several exemplary results for microstructure images which have been generated exclusively from experimental input: Figure 2.8 refers to a material with a majority of titanium oxide grains, fig. 2.9 refers to a material with a majority of aluminum oxide grains at high porosity, and fig. 2.10 refers to a material with a majority of aluminum oxide grains at lower porosity. It should not be forgotten that the model images shown in these figures are no reproductions of the scanning electron micrographs, but single realizations of the statistical sampling.

For an assessment of the quality of the modelling, it suggests itself to apply here the same image analysis techniques which are otherwise applied to the scanning electron micrographs. The image analysis comprises two steps: The first step is a separate presentation of the three structure phases, as included in figures 2.8 to 2.10. A qualitative, visual comparison of the separation images from SEM and modelling already reveals a satisfactory agreement. As expected from the rough modelling with elementary geometrical shapes, the poorest correspondence is seen for the porous phase. The second step of the image analysis applies stereological methods to the separation images, thus providing data for a quantitative comparison. Some results are compiled in table 2.2 (p. 46).

All in all, the two-dimensional modelling approach seems to sufficiently reflect the properties of the considered microstructures.

The typical structural input parameters of the model approach, as well as the elastic/energetic material parameters attributed to the specimens throughout the present work, are compiled in table 2.1 (p. 45).

[4]For a detailed description of the statistical quantities, see section 4.3.1.1, p. 107.

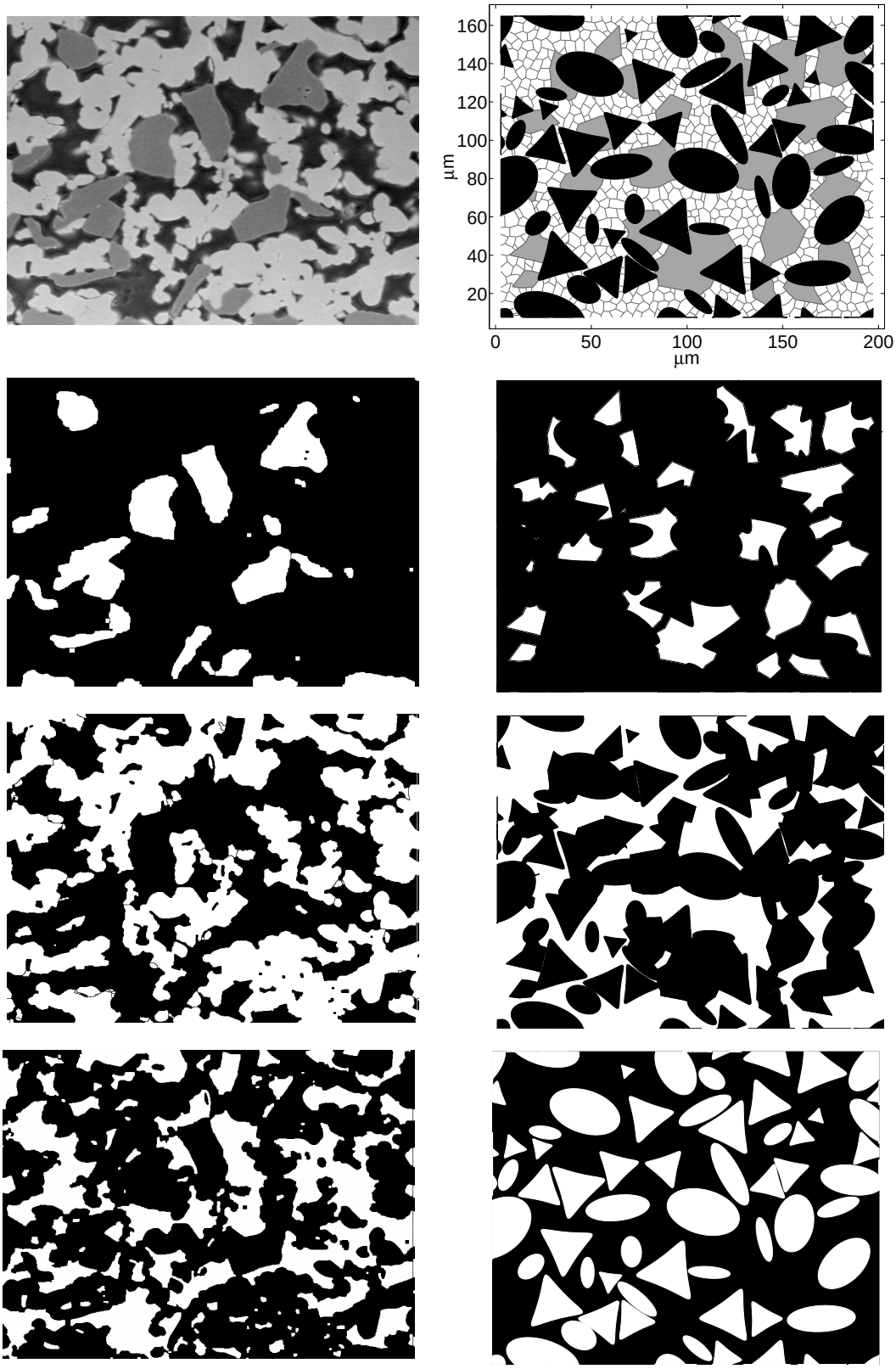

Figure 2.8: Left: Scanning electron micrograph of a TiO_2 *based microstructure (upper row), and image analysis (below). Right: corresponding model specimen, and separate presentation of the three phases in there. Second row:* Al_2O_3 *phase in white (*$A_A(\mathrm{Al}) = 0.17$, $L_A(\mathrm{Al}) = 36$ mm/mm^2*). Third row:* TiO_2 *phase in white (*$A_A(\mathrm{Ti}) = 0.43$, $L_A(\mathrm{Ti}) = 116$ mm/mm^2*). Fourth row: pores in white (*$A_A(\mathrm{po}) = 0.41$, $L_A(\mathrm{po}) = 105$ mm/mm^2*).*

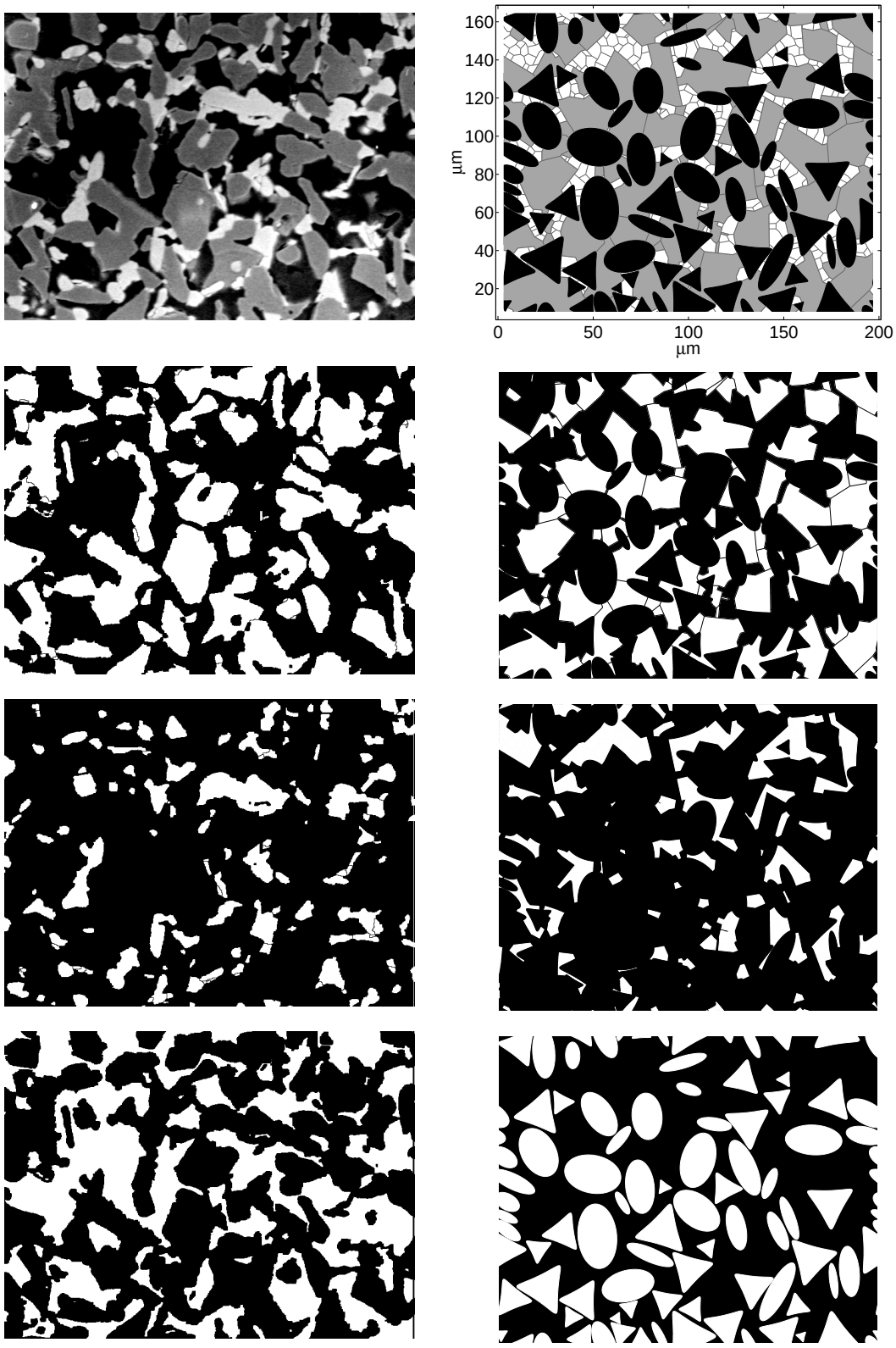

Figure 2.9: Left column: Scanning electron micrograph (SEM) of an aluminum oxide based microstructure with 40 % porosity (upper row), and image analysis (below). Right column: corresponding model specimen, and separate presentation of the three phases in there. Second row: Al_2O_3 *phase in white. Third row:* TiO_2 *phase in white. Fourth row: porous phase in white.*

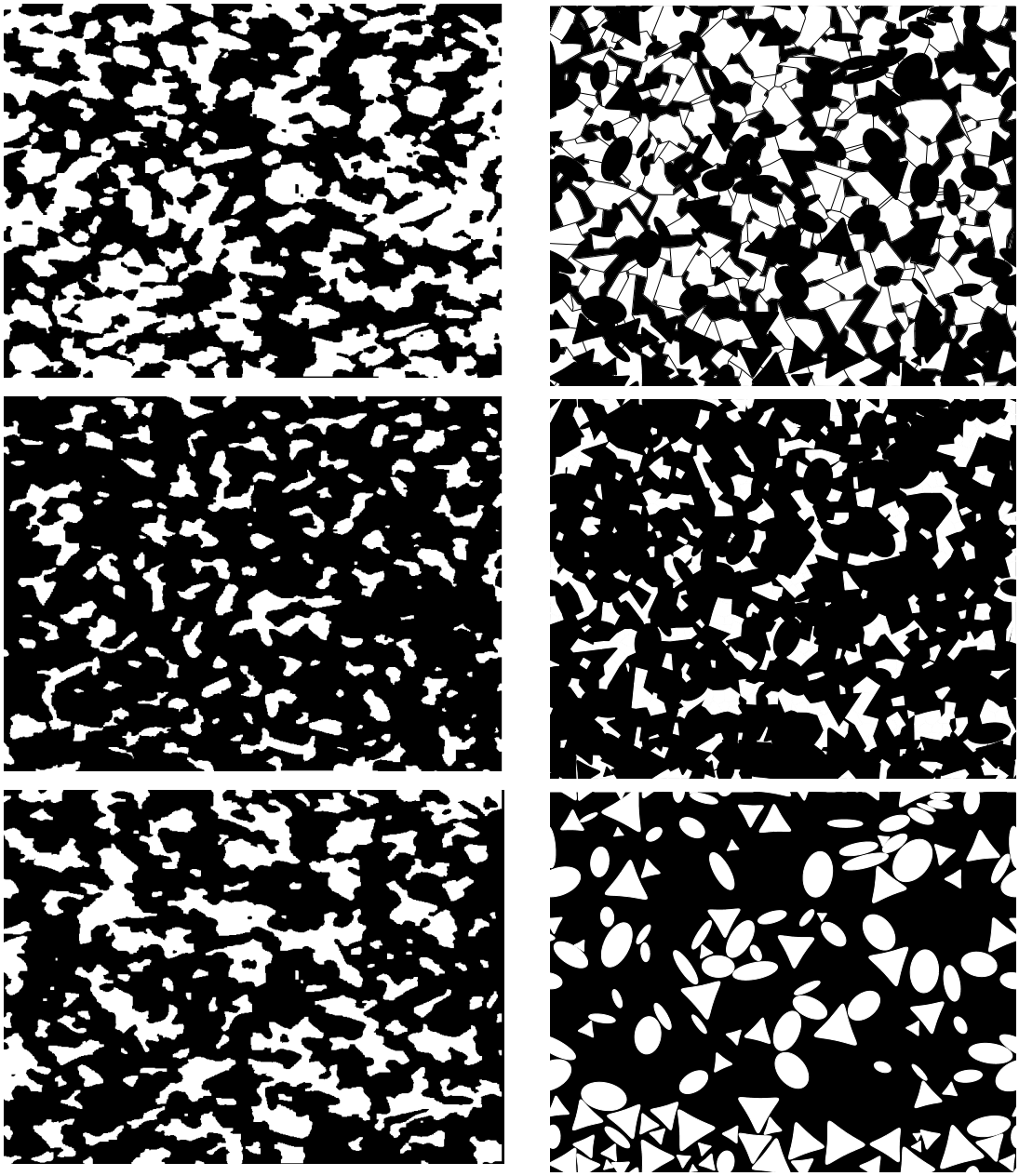

Figure 2.10: Left column: image analysis of the SEM of an aluminum oxide based filter support with 28 % porosity (fig. 2.1, left). Right column: separate presentation of the different phases in the model image (fig. 2.1, right). Above: Al_2O_3 *phase. Middle:* TiO_2 *phase. Below: porous phase.*

structural parameters		
specimen size	D	(variating)
volume fraction of grains and pores	A_A(Ti) A_A(Al) A_A(po)	(variating)
specific perimeter of grains and pores	L_A(Ti) L_A(Al) L_A(po)	(variating)
average diameter of grains and pores	d (Ti) d (Al) d (po)	5.4 μm (variating) (variating)
size distribution of grains and pores		Gaussian normal distr. or uniform distr. (with bounds); monodisperse
shape of grains		hexagonal (TiO_2), polygonal (Al_2O_3), randomly distorted
shape of pores		circular, elliptical, triangular
location and orientation of grains and pores		(random, uniform distr.)

elastic material parameters		
Young's modulus of compact grain phases	E	270 GPa
Poisson ratio of compact grain phases	ν	0.15

miscellaneous		
specific surface energy between grain boundaries	γ(Ti/Ti) γ(Al/Al) γ(Ti/Al)	2.00 Jm^{-2} 1.00 Jm^{-2} 0.50 Jm^{-2}
static friction coefficient	μ_s	(0.7)
sliding friction coefficient	μ_m	(0.6)

Table 2.1: Basic input parameters for modelling the microstructure, stress analysis, and simulation of microcracking. Right column: respective values or assumptions as chosen for the present studies.

fig. 2.9		SEM	model image
volume fraction of porous phase,	A_A(po)	0.39	0.42
volume fraction of Al_2O_3 phase,	A_A(Al)	0.43	0.41
volume fraction of TiO_2 phase,	A_A(Ti)	0.18	0.17
specific perim. of porous phase,	L_A(po) [mm/mm^2]	137.6	129.33
specific perim. of Al_2O_3 phase,	L_A(Al) [mm/mm^2]	134.3	128.92
specific perim. of TiO_2 phase,	L_A(Ti) [mm/mm^2]	92.3	95.89

fig. 2.10		SEM	model image
volume fraction of porous phase,	A_A(po)	0.28	0.31
volume fraction of Al_2O_3 phase,	A_A(Al)	0.50	0.45
volume fraction of TiO_2 phase,	A_A(Ti)	0.23	0.22
specific perim. of porous phase,	L_A(po) [mm/mm^2]	116.6	116.
specific perim. of Al_2O_3 phase,	L_A(Al) [mm/mm^2]	154.2	157.
specific perim. of TiO_2 phase,	L_A(Ti) [mm/mm^2]	112.9	129.

Table 2.2: Comparison of basic structural parameters of the Al_2O_3-based SEM and model images in fig. 2.9 and in fig. 2.10, respectively.

2.4 Deducing three-dimensional information from two-dimensional analysis

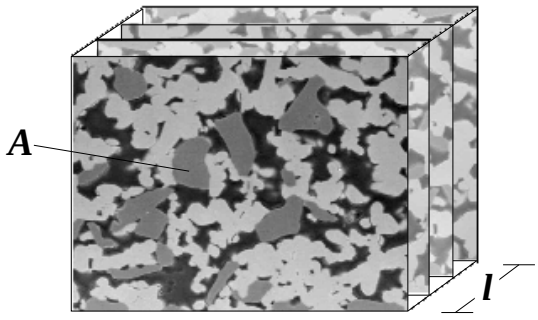

Figure 2.11: Illustration of cross-section analysis in a 3-D material specimen.

For an estimation of the volume content of phase ϕ ($\phi = 1, \ldots, n$) from cross-section analysis, consider the volume element $V = A\ l$ in fig. 2.11.[5] Denoting by $A(\phi)$ the area of the phase in the cross section, the respective volume $V(\phi)$ is obtained by integration along the z–axis:

$$V(\phi) = \int_0^l A(\phi) \mathrm{d}z \tag{2.7}$$

[5] Some parts of section 2.4, section 3.3.3, and sections 5.1 to 5.4.2 have already been published in [17] and [18].

The volume fraction of the phase is then

$$V_V(\phi) = \frac{V(\phi)}{V} = \frac{1}{l}\int_0^l \frac{A(\phi)}{A}\mathrm{d}z = \frac{1}{l}\int_0^l A_A(\phi)\mathrm{d}z, \tag{2.8}$$

and it can be determined as the average over the distance l of the area fraction $A_A(\phi) = A(\phi)/A$. The extremum values of $A_A(\phi)$ along l represent bounds of the volume fraction:

$$\min[A_A(\phi)] \leq V_V(\phi) \leq \max[A_A(\phi)] \tag{2.9}$$

Following [13], the above thoughts have already been presented in [14].

The assumption of the material being isotropic and statistically homogeneous simplifies the situation in so far as the analysis may be restricted to a single, arbitrary 2-D cross-section. In other words, the smaller the variation between cross-sections, the more accurately the volume fraction is approximated by the area fraction of a single cross-section. If the cross-section is sufficiently large to represent the phase content, the volume fraction of a phase ϕ (in 3-D) is equal to the corresponding area fraction (in 2-D):

$$V_V(\phi) = A_A(\phi) \tag{2.10}$$

A similarly straight relation holds for the specific perimeter $L_A(\phi)$ (in 2-D) and its equivalent in 3-D, the specific surface $S_V(\phi)$ (surface area of ϕ per unit volume, "surface-to-volume-ratio") [34]:

$$S_V(\phi) = \frac{4}{\pi}L_A(\phi) \tag{2.11}$$

Since $4/\pi > 1$, the specific perimeter of a phase is *under*estimated in a 2-D consideration. Equation (2.11) may be transferred to cracks: if the size of a crack k is defined as its length l_k (in 2-D) or its area extent A_k (in 3-D), then the sum of crack sizes is underestimated in a 2-D section:

$$\frac{1}{V}\sum_{k\in V} A_k = \frac{4}{\pi}\,\frac{1}{A}\sum_{k\in A} l_k \tag{2.12}$$

Regarding the shapes of the individual elements of a phase, one may consider the simple case of (randomly oriented) spheroidal pores in 3-D, which reduce to elliptical pores in 2-D (planar) sections. The studies in [53] confirm that the sum of the aspect ratios per area resp. volume is lower in 2-D than in 3-D, in fact much more for prolate spheroids (approximately logarithmic relation between 2-D and 3-D) than for oblate spheroids (approximately linear relation). Thus, the average 3-D aspect ratio of the phase elements is underestimated in a 2-D analysis, a fact which fits to the message of eq. (2.11) if one recalls that the perimeter is related to the aspect ratio (fig. 2.7, p. 40). However, deducing relations for properties of the individual elements from relations for global parameters such as eq. (2.11) is, as already discussed in section 2.2, only possible under very confined assumptions.

Chapter 3

Elastic properties and stress analysis of solids with cavities

The impact of the micro-cavities on the effective elastic properties is of considerable interest for both the constitutive modelling from the microscopic level, and for an assessment of the material state from macroscopic observations. The scope in modelling is to determine macroscopic parameters such as the stiffness (Young's modulus in particular) and the overall strain of the heterogeneous material from the elastic parameters of its solid constituents, from informations on the incorporated cavities (pores and cracks), and from the loading conditions. The present chapter will first outline some general points in the associated topic of *homogenization* (section 3.1).

Micromechanical models explicitly account for the reduction of the stiffness (of an otherwise compact material) by the presence of the cavities, or sum up the contributions of the cavities to the strain of the material. Among the common micromechanical approaches, two fundamentally different categories should be distinguished: A great deal has been published on *local* theories which do not consider the mutual positions of the cavities. These local approaches result in simple and thus very popular continuum models, which are reviewed in section 3.2 and are very instructive with respect to the successive accounts.

The second category is represented by *non-local* models which focus on explicit complex and deterministic arrangements of cavities, especially of microcracks. The micromechanical way of modelling is based upon analytical stress solutions for the isolated individual cavities (section 3.3), which may be superposed to get a full description of the stress field in a model specimen. Section 3.4 outlines the versatile method established by Mark Kachanov [42], which is extended in section 3.5 with respect to normal compression and frictional sliding of the crack faces, and to structural changes. The deduced expressions essentially relate macroscopic stresses and macroscopic strains and serve as the theoretical fundamentals for the elastic analysis of microstructures in the present thesis.

A useful application of the non-local micromechanical model addresses the stress-strain response of specimens under tension-shear-compression loading cycles. The results presented in section 3.7 clearly illustrate the nonlinear behaviour of solids with cracks.

It should be emphasized that the granular (i.e., discrete) structure of the material is neglected in the present chapter. For the determination of effective moduli, the solid phases are assumed to be linear elastic continua with constant, isotropic elastic moduli. This implies that the elastic properties of both grain phases are equal, and that the grain

interfaces are infinitely thin [50].

3.1 Remarks on homogenization and discretization

Micro-macro transition. The transition from a model on a fine scale to a model on a coarser scale is referred to as *homogenization* (also called 'coarse graining' or simply 'averaging'). Just as in the present work, this transition typically takes place between the microscale and the macroscale, but it should be noted that the properties of the elements at the microscale (grains, facets) result from homogenization of the physical phenomena at an even lower level. From the viewpoint of damage, "the untold number of ruptured bonds [at the atomic/molecular level] are replaced by tens of thousands of microcracks [at the microscopic level] which are subsequently approximated by damage tensors [at the macroscale]" [48].

Homogenization is the modelling of a statistical ensemble of micro-systems with a heterogeneous, discrete, piece-wise continuous microstructure by means of a unique, idealized, continuous medium, where the size of the heterogeneities is very small compared to the characteristic length of this scale. The many body statistical mechanics problem is reduced to simple, deterministic formulae and effective parameters, resulting in effective continuum models or effective field models (see section 1.1.2.3). Homogenization reduces the number of degrees of freedom and enhances the tractability of the model. Features on the lower level are smeared out: details of the micro-defects as well as the local stress and strain field fluctuations are neglected at the macroscale.[1]

"Homogenization assumes that we are able to solve a problem at the macroscopic scale" [56]. It is justified only if the representative volume element (RVE) exists, i.e. if the micro-systems are statistically homogeneous (see section 2.2, p. 40). Determining effective elastic or damage parameters requires the band-width of the distribution of the heterogeneities to be limited.

The formalism of homogenization can easily be demonstrated for the stresses and strains in a linear-elastic material: The macroscopic stresses $\bar{\boldsymbol{\sigma}}$ and macroscopic strains $\bar{\boldsymbol{\epsilon}}$ at a point $\mathbf{X}$ of the macro-continuum are evaluated by the unweighted mean values of the microscopic stresses $\boldsymbol{\sigma}$ and microscopic strains $\boldsymbol{\epsilon}$ ($\langle \dots \rangle$ is the averaging operator) [56]:

$$\bar{\boldsymbol{\sigma}}(\mathbf{X}) = \langle \boldsymbol{\sigma} \rangle \equiv \frac{1}{V} \int_V \boldsymbol{\sigma}(\mathbf{X}, \mathbf{x}) \, \mathrm{d}\mathbf{x} \tag{3.1}$$

$$\bar{\boldsymbol{\epsilon}}(\mathbf{X}) = \langle \boldsymbol{\epsilon} \rangle \equiv \frac{1}{V} \int_V \boldsymbol{\epsilon}(\mathbf{X}, \mathbf{x}) \, \mathrm{d}\mathbf{x} \tag{3.2}$$

The integration is extended over all points $\mathbf{x}$ within the volume V of the RVE ("micro-continuum" [69]) which is associated to the point $\mathbf{X}$ of the macro-continuum. Equations (3.1) and (3.2) yield the elastic fields for the macro-continuum.

[1] A number of methods also provides *bounds* for the macroscopic elastic moduli: Classical examples are the Voigt and Reuss bounds (see [59], [50], or [1] for a review). Assuming that the strain throughout the heterogeneous material is uniform, the Voigt approximation represents upper bounds of the true effective moduli, whereas the Reuss approximation assumes a uniform stress and represents lower bounds. These bounds, however, "are of practical significance only for small volume fractions and slight mismatch of elastic moduli" of the material phases [1].

Macro-micro transition. Modelling at the microscale requires a process which is inverse to the homogenization procedure, and is called *discretization* or 'localization'. Such a macro-micro transition addresses, for example, the determination of $\boldsymbol{\sigma}(\mathbf{X}, \mathbf{x})$ and $\boldsymbol{\epsilon}(\mathbf{X}, \mathbf{x})$ from $\bar{\boldsymbol{\sigma}}(\mathbf{X})$ and $\bar{\boldsymbol{\epsilon}}(\mathbf{X})$. A particular point here concerns the boundary conditions at the microscale. With div $\boldsymbol{\sigma} = \mathbf{0}$, i.e. an equilibrium state of the microscopic stresses, the volume integral is equivalent to a surface integral along the boundary ∂V of the RVE (Gauss theorem). If the RVE is sufficiently large compared to the size of the heterogeneities, then the boundary conditions can be approximated by the value of the macroscopic field at the considered point $\mathbf{X}$; this means that the fluctuations at the boundary of the micro-continuum are neglected. At the same time, the RVE should be chosen small enough so that the macroscopic field may be considered uniform along the boundary.

As already mentioned in section 2.2 (p. 40), the size of the RVE is sometimes — especially in periodic structures — reduced to the scale of the microscopic heterogeneities. In this case, the micro- and macro-scale are "well separated" [55], so that the values of the macroscopic field represent no permissible approximation for the boundary conditions, and the task is more challenging:

The problem is firstly that there are no boundary conditions defined, and secondly that the load is only given by the *averaged* value of a field. The boundary conditions to be introduced "must, in some way, reproduce the internal state of the RVE in the most satisfactory manner" [56]. Possible boundary conditions may be derived from the *Hill-Mandel relation between micro- and macro-scales* ('Hill-Mandel principle of macro-homogeneity', 'Hill's condition'), which reads in a simplified notation:

$$\langle \boldsymbol{\sigma} : \boldsymbol{\epsilon} \rangle = \langle \boldsymbol{\sigma} \rangle : \langle \boldsymbol{\epsilon} \rangle \tag{3.3}$$

Provided that the microscopic displacement and stress fields are "admissible" ([56], [69]), this important relation allows to describe the volume average of a work-like expression at the microscale as a product of the corresponding macroscopic tensorfields, and thus establishes the 'equality of macroscopic and microscopic work'. In statistical theories, this condition is considered as an *ergodic hypothesis*. For details and references, see e.g. [56].

The Hill-Mandel relation induces three possible conditions for the boundary ∂V of the micro-continuum ([56], [69]):

1. *uniform strains:* displacement boundary conditions (Dirichlet bound. conditions)
2. *uniform stresses:* traction boundary conditions (Neumann boundary conditions)
3. *local periodic stresses and strains:* the local microscopic strains consist of the macroscopic mean $\langle \boldsymbol{\epsilon} \rangle$ and a superposed, periodic displacement fluctuation whose mean vanishes; the local microscopic stresses are antiperiodic, i.e. tractions are opposite on opposite faces of ∂V

Uniform-load boundary conditions (1 and 2) do not apply to periodic structures when the RVE is chosen small so that the size of the RVE is of the order of the defects. This fact is underlined by studies on a periodic model structure under large strains, as presented in [69]: assuming traction boundary conditions (2), the deformed microstructure is "kinematically incompatible" for differently chosen (but equivalent) RVE sections; assuming deformation boundary conditions (1), a wrong anisotropic material response is obtained from the numerical computations. In this context, only periodic boundary conditions (3)

supply consistent and correct results, and it is concluded that "the periodic boundary condition offers due to their little constraints the most advantageous formulation for the micro-macro transition" [69].

Examples in the present thesis. Regarding the structure properties, questions of *discretization* have already been discussed in section 2.2 of the previous chapter. Regarding the elastic properties, the model specimens are supposed to be large enough so that the approximation of uniform stress boundary conditions is justified (Chapter 4). More precisely, the traction acting on the boundary of a model specimen is assumed to be equal to the average load in the macroscopic material. Chapter 5 is concerned with internal pressure, a particular loading mode which renders the question of boundary conditions negligible.

The process of *homogenization* is, first of all, carried out with respect to the structural parameters, e.g. porosity (see eq. 2.1, p. 36) or crack density (see eq. 2.3, p. 36). More importantly, the overall strains and effective moduli are obtained from a summation of the discrete crack and pore contributions, see sections 3.4.2 and 3.5.5 of the present chapter. Homogenization starting from a continuous distribution function for the micro-elements is demonstrated in section 4.4 of the following chapter.

It is worth mentioning that homogenization has no meaning where the material behaviour is governed rather by the *extreme* statistical moments than by the mean values: In contrast to the effective stiffness of a fixed-state material, which is governed by averaged values such as porosity and crack density, the brittle rupture strength is sensitive to the size of the *largest* individual defect — see Chapter 5.

3.2 Continuum approaches to the effective stiffness

A customary way of the estimation of macroscopic elastic properties is to apply cavity compliance tensors deduced from complex potential theory ([68], [60], see section 3.3) or from Eshelby's *equivalent inclusion method* [2] ([27], [59]), and to treat the cavities as single inclusions in an otherwise homogeneous medium. These effective continuum theories (as reviewed in [62], [59], [41], [48]) do not account for spatial correlations of the cavities and for the particular cavity sizes; they make no distinction between a small number of large defects and a large number of small defects. Due to the absence of a characteristic length, the models are strictly *local*.

The popularity of the continuum approaches can be attributed to their tractability and elegance. The simplicity of these models, however, excludes the consideration of delicate effects such as crack closure and friction, and it comes along with the disadvantage that their range of applicability is not defined and that there is no rational set of criteria to choose the best suited analytical model for a particular situation [48]. The models differ considerably from each other at moderate to higher cavity densities (as illustrated

[2] The Eshelby method assumes that the material properties of both the inclusion and the matrix are equal but the inclusion contains eigenstrains, which create tractions at the boundary of the inclusion resulting in a disturbance of the stress field in the matrix. The eigenstrains are related to the Eshelby tensor. In contrast to the complex potential theory, the Eshelby method may be applied to three-dimensional problems also.

in fig. 3.2, left). It must be supposed that the validity of all the approaches is limited to 'low' cavity densities.

3.2.1 Approximation of non-interacting cavities

In the limit of a very low concentration of cavities, the individual cavities may be so widely spaced that the direct interactions between them can be neglected. Then, the stress field acting on each microscopic cavity is equal to the average (macroscopic) stress in the material. In a statistically homogeneous material, spatial correlations of the cavities are remote, and the exact positions and orientations of cracks and pores are of no importance. The effective elastic properties of the material are derived simply by superimposing the contributions of all individual cavities, and a subsequent volume averaging.

As for the impact of the cavities on the effective stiffness, the following general statements can be made (the formulae refer to prescribed external stress[3]):

- Cavities with concave borders and sharp corners have lower stiffness (i.e. higher 'strain response', 'contribution to strain', 'compressibility') than cavities with convex borders and smooth corners. Consequently, triangular cavities have lower stiffness than circular cavities (and ellipses with moderate aspect ratio, see also fig. 3.3). This fact can be clearly seen by comparing the formula for Young's modulus E of a material containing non-interacting circular cavities:

$$E = \frac{E_0}{1+3p} \ , \tag{3.4}$$

  and Young's modulus of a material containing non-interacting cavities with approximately triangular shape (see section 3.3.2, p. 65):

$$E = \frac{E_0}{1+4.143\ p} \ , \tag{3.5}$$

  where p denotes the porosity (volume fraction of the cavities), and E_0 denotes Young's modulus for the compact matrix material. (See fig. 3.1 for illustration.)

- The stiffness of elliptical cavities is lower for the more 'elongated' ones. Especially, the stiffness of elliptical cavities is lower than the stiffness of circular cavities: The circle is the stiffest cavity of a given area (fig. 3.2, right). These facts are reflected in the formula for the effective Young's modulus of a material with randomly oriented elliptical cavities:

$$E = \frac{E_0}{1+3p+q}, \tag{3.6}$$

  where q is the shape factor ('eccentricity parameter') of the elliptical cavities (see eq. 2.2, p. 36).

- The *orientation* of triangular or approximately triangular cavities and, of course, circular cavities, has no influence on its contribution to the effective stiffness matrix: Triangles (as well as regular polygons with five or more sharp or smooth corners [41]) and circles are elastically isotropic.

[3]The approximation of non-interacting cavities yields considerably different results depending on whether external stress or strain is prescribed [62].

The formulae show that — for a given porosity and given shape of the cavities — the size (or, equally, the number) of the individual cavities has no impact on the strain contribution of the cavities.

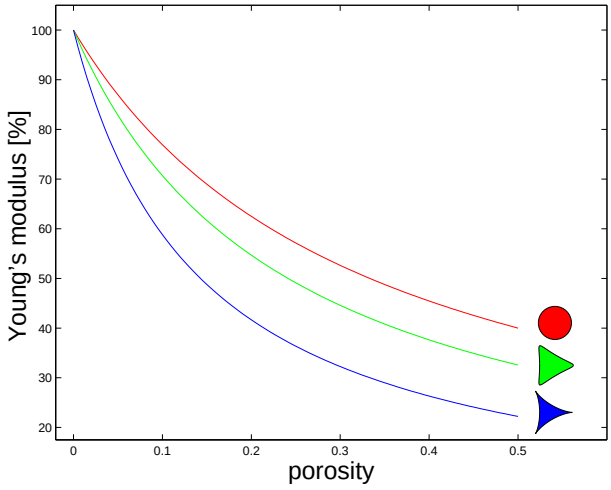

Figure 3.1: Decrease of effective Young's modulus as a function of porosity for different 'isotropic' cavity shapes (approximation of non-interacting cavities).

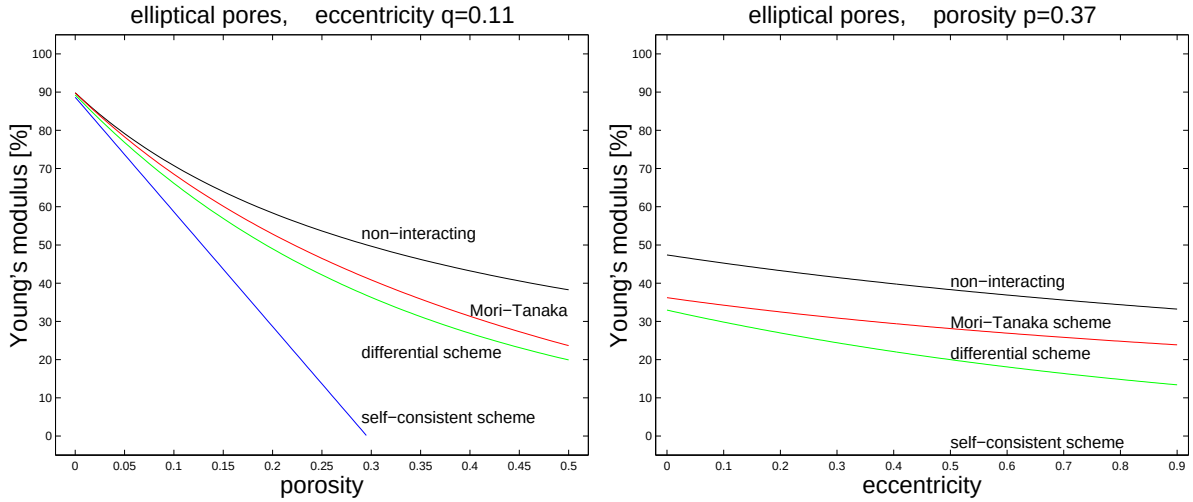

Figure 3.2: Left: Decrease of Young's modulus as a function of porosity in a material with randomly oriented elliptical cavities of fixed eccentricity. Right: Decrease of Young's modulus as a function of eccentricity in a material with randomly oriented elliptical cavities and fixed porosity.

3.2.2 Interacting cavities: effective environment theories

At higher concentrations of microscopic cavities, the importance of direct interactions on the effective stiffness can become substantial. The most frequently used theories for estimating the effective elastic moduli account for interactions by placing representative cavities into some 'effective environment' which combines the effect of all cavities. The effective environment is an effective matrix material in *effective continuum models* such as the self-consistent scheme and the differential scheme, or it is an effective stress field in *effective field models* such as Mori-Tanaka's scheme. These approaches smooth the local fluctuations of stress/strain fields. The considered materials must be statistical homogeneous, and the cavity correlations should be weak.

In the self-consistent and differential scheme (which is an incremental form of the self-consistent scheme), the impact of interactions on a given cavity is simulated by a *reduced stiffness of the surrounding material* [43]. The self-consistent and the differential scheme do not take into account the actual mechanisms of interaction and predict that the effect of interactions is *always* a *softening* of the overall moduli (which is quite strong in the self-consistent scheme). In general, they substantially overestimate the impact of cracks on the effective stiffness.

The prediction that the effective stiffness always reduces with the increase of the micro-defect density is common to all effective continuum and effective field models [48].

3.2.2.1 Self-consistent scheme

The self-consistent scheme predicts for a material containing randomly oriented elliptical cavities:

$$E = [1 - 3p - q)]\ E_0\ , \tag{3.7}$$

and for a material containing triangular cavities:

$$E = [1 - 4.2p]\ E_0 \tag{3.8}$$

Following Krajcinovic [48], "the self consistent model provides very good estimates at surprisingly large concentrations of micro defects".

The self-consistent method results in a unique effective stiffness/compliance tensor, no matter if external stress or external strain is prescribed [62].

3.2.2.2 Differential scheme

In contrast to the self-consistent scheme, where the representative cavity is put into the effective matrix all at once, this process can be performed incrementally: starting from $\rho = 0$ and $E = E_0$, the cavity density is increased by small steps $\Delta\rho$, and the moduli of the effective matrix are recalculated at each step.[4] The differential scheme predicts for a material containing randomly oriented elliptical cavities:

$$E = [\exp(-3p - q)]\ E_0 \tag{3.9}$$

[4]Vice versa, the self-consistent scheme can be deduced from the differential scheme by a linearization: Expanding the exponential function in eq. (3.9) into a power series and truncating to the first-order term yields eq. (3.7).

Different from the self-consistent scheme, there is no 'cut-off point' where the stiffness vanishes. Just as the approximation of non-interacting cavities, the differential scheme predicts that the stiffness vanishes only if the defect density (or damage parameter) tends to infinity.

Following Krajcinovic [48], the "widely held opinion that the differential model provides more accurate results for large defect concentrations [than the self-consistent scheme] has never been documented by compelling arguments".

3.2.2.3 Approximation of the average stress field (Mori-Tanaka's scheme)

Mori-Tanaka's scheme is the simplest method among the effective field models, but it appears to be a reasonable approximation when the mutual positions of the defects are random. With this scheme, experimental data have been successfully described; it seems to be accurate in both limits of small and high porosities [41]. The essential of this scheme is to account for interactions by placing each cavity into the stress field averaged over the solid phase (matrix). This average stress $\boldsymbol{\sigma}$ is expressed in terms of a remotely applied stress $\boldsymbol{\sigma}_0$ as

$$\boldsymbol{\sigma} = \frac{\boldsymbol{\sigma}_0}{1-p} \ . \tag{3.10}$$

For a material with randomly oriented elliptical cavities (pores and/or cracks), Young's modulus is found to be

$$E = \frac{E_0}{1+\frac{3p+q}{1-p}} \ . \tag{3.11}$$

The factor $1/(1-p)$ accounts for the interactions. Since $p = 0$ for cracks, Mori-Tanaka's scheme coincides with the approximation of non-interacting cracks. This is not an inconsistency, but properly reflects the actual situation: Provided *tractions* are prescribed on the material boundaries, introduction of cracks does not change the average stress in the matrix, so there is no reason to expect any impact of interactions on the effective moduli as long as the cracks are located randomly [43]. Different from the self-consistent scheme and differential scheme (which ignore the impact of the shielding mode of interaction and therefore substantially underestimate the stiffness of the cracked material), Mori-Tanaka's scheme apparently remains valid up to high crack densities.

Mori-Tanaka's scheme predicts that the impact of cavities with larger area (and higher contribution to total porosity) on cavities with smaller area is higher than vice versa. In particular, cavities affect cracks, but cracks do not affect cavities — as far as the effective elastic properties are concerned.

Further details of Mori-Tanaka's scheme are described in [4].

The influence of porosity and eccentricity of elliptical cavities in the different effective environment models is graphically displayed in fig. 3.2 (p. 54).

3.2.2.4 Statistical second-order model based on ensemble averaging and pairwise crack interactions

In order to exemplify models based upon micro-defect distribution statistics, mention can be made of the approach by Ju and Chen [38]. The general model manages systems with arbitrary crack densities and arbitrary distributions of crack lengths, crack locations and orientations. It claims to be valid even at higher crack densities and stronger crack

interactions. The core theory is of the micromechanical type, and has some similarities to the approach by Mark Kachanov [42] (see section 3.4 below). Crack interactions are treated in a pairwise way, which means a coarse reduction. On the other hand, crack closure is rudimentarily accounted for.[5]

Ju and Chen treat the interacting microcracks within the framework of the 'ensemble-average approach': The local constitutive relation at a typical point within a statistical RVE is "obtained by averaging over the ensemble of all statistical realizations, including the locations, orientations, lengths, and relative configurations of randomly distributed microcracks". Given the first microcrack, the spatial location of the second microcrack is random.

With the ensemble-average approach, the micromechanical model can be employed in extensive numerical calculations to yield explicit closed-form ('analytical') solutions for the overall moduli and the constitutive equations. Ju and Chen present results for simple, idealized structures. More realistic structures, including cracks with non-uniform lengths, or even crack length distributions, would involve considerably higher efforts.

For a material containing randomly distributed cracks of equal length, Ju and Chen deduced the following formula where the effect of the cracks is reflected through the scalar crack density ρ:

$$E = \frac{1}{1 + \pi(\rho + 0.373\ \rho^2)}\ E_0 \tag{3.13}$$

This is a local effective continuum formula of second order in crack density. The second-order term (quadratic in ρ) can be traced back to the crack-crack interactions; it becomes significant at 'larger' crack densities (e.g., $\rho = 0.5$). For 'extremely large' crack densities, even higher-order terms should be included [39]. Neglection of the second-order term leads to the approximation of non-interacting cracks ('first-order microcrack contributions', eq. (3.6)).

According to this model, the effect of interactions (focusing on the numerical value "0.373") is a further reduction of effective stiffness, but not as strong as in the self-consistent scheme. In contrast to the self-consistent scheme, there is no 'cut-off point' where the stiffness vanishes.

The results of this approach seem questionable since the effects of crack interactions are expected to cancel each other out in the case of a perfectly random crack distribution (see section 3.6, p. 81), so that the second-order term should vanish.

[5] Using the nomenclature of section 3.4 and section 3.5, 'pairwise interaction' means that the effective traction $\mathbf{t}_k$ on a crack k is calculated from the single equation

$$\langle \mathbf{t}_k \rangle = \mathbf{t}_k^0 + \mathbf{\Lambda}_{ki,\mathrm{open}} \langle \mathbf{t}_i^{ki,\mathrm{eff}} \rangle \tag{3.12}$$

in contrast to the extensive equation systems eq. (3.41) resp. eq. (3.60) below (p. 73, p. 77). In eq. (3.12), $\langle \mathbf{t}_i^{ki,\mathrm{eff}} \rangle$ is the effective traction on crack i for the two-crack system comprising cracks i and k. Nevertheless, $\langle \mathbf{t}_k \rangle$ is seen as the effective traction on crack k in the all-crack system. This approximation reduces the problem to a two-microcrack interaction problem. The 'transmission factors' $\mathbf{\Lambda}_{ki,\mathrm{open}}$ in eq. (3.12) take into account that closed microcracks do not contribute. Thus, the first step in Ju and Chen's model is to determine the 'open microcrack angle domain' to restrict the calculation to those cracks which actually contribute to the effective compliance. This involves an extensive set of case differentiations.

3.2.3 Further concepts and reflections

3.2.3.1 Non-random cavity distributions

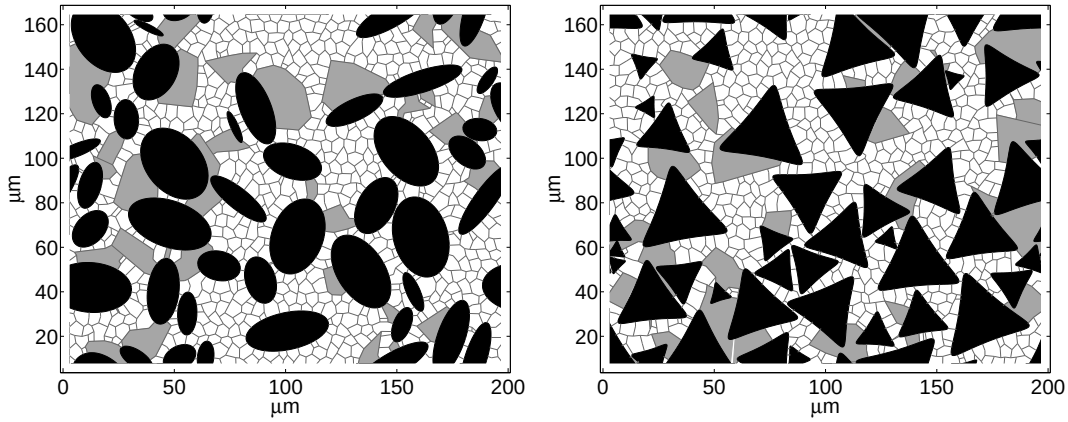

Figure 3.3: Two microstructure model images with identical porosity ($p = 0.41$), but different pore shapes. The structure containing triangular pores has a significantly lower Young's modulus ($E/E_0 = 0.366$) than the structure containing elliptical pores ($E/E_0 \approx 0.403$). The explicit modelling of the individual cavities (using cavity compliance tensors, approximation of non-interacting cavities) enables to adjust or detect anisotropies: For the specimen on the left, $E_x/E_0 = 0.394$ whereas $E_y/E_0 = 0.411$ GPa (E_x: horizontal stiffness, E_y: vertical stiffness).

Crack density tensors and cavity compliance tensors. The simple effective continuum models presented so far apply to randomly oriented cavities, i.e. when the continuum is isotropic. An elastic anisotropy due to a non-isotropic distribution of cavity orientations can be approximately accounted for by using a higher order *cavity density tensor* (for *crack density tensors*, see [43] or [48]) instead of the scalar cavity density, but the simplicity of the models would be lost at the same time. Alternatively, the full fourth-order *cavity compliance tensors* (see [41], [48]) can be employed in an explicit modelling of the cavity arrangements (as in the present account, see fig. 3.3).

Point correlation functions. Some approaches, aiming at the effect of direct defect interactions, employ *two- and four-point correlation functions* as an input information for the structure geometry. These functions — which are typically obtained from analysis of actual structure images — describe the spatial correlation between the defects. For example, two neighboring cracks may be considered as correlated if their stress singularity fields overlap (to some extent). In other words, two objects are correlated if their behaviour depends on their exact relative positions (i.e., distance and orientation). An interaction length may be defined as the maximum distance between two cracks so that the direct interaction provides a contribution to their singularity fields which is large enough to affect their growth and stability. The interaction length must be represented in the form of a distribution, for the crack sizes are generally not uniform. In order to catch the interaction effect between two cracks on their stress fields, two-point correlation functions

summarizing the distances between centers or tips are not sufficient; since the orientations are important as well, a full description requires even four scalar parameters for the geometry (see [48]).

Correlation functions often are expressed as statistical quantities to sum up morphological information; then, the correlation function gives the probability of finding the objects (particles, cracks, defects) at certain positions. The pair (two-point) correlation function gives the probability of finding an object at a certain distance r from any other object [28].

3.2.3.2 Percolation limit

Percolation arises when a cluster of interconnected (i.e., touching or overlapping) cavities emerges to split the specimen into at least two parts. At the same time, the specimen loses its capability to carry or transmit load — the effective stiffness in a certain direction vanishes.

In percolation studies, the range of statistical homogeneity is trespassed, and volume averages are meaningless, so the validity of critical porosities or 'cut-off points' deduced from schemes like the self-consistent model is very restricted ([43], [48]). At least, they may serve as upper limits: For a material containing randomly distributed and oriented cracks, the self-consistent scheme predicts a critical crack density of $\rho_c = 1/\pi = 0.32$ (see eq. (3.7), setting 'porosity' $p = 0$, 'eccentricity' $q = \pi\rho$). The differential scheme yields no finite values for the critical defect density.

In contrast, a class of models has been developed which explicitly addresses the percolation limit (see [48]). The so-called *continuum percolation theories* provide estimates of the critical micro-defect density to which the effective continuum models should tend as the defect concentration increases. Different from the wide class of *lattice percolation models* (see section 1.1.2, p. 20) or to the studies in Chapter 5 of the present thesis, the continuum percolation models deal with micro-defects which can nucleate but not grow. The micro-defects are successively implanted into the structure until the connectivity threshold is reached. For a material containing randomly distributed and oriented cracks, the continuum percolation models yield non-unique values for the critical crack density: e.g., $\rho_c = 0.25$, $\rho_c = 0.20$. The critical porosity of an elastic plate containing elliptical or circular cavities is determined as $p_c = 0.45$ ([48]). Solutions for the critical density are far easier to find for defects of equal size than for problems with polydisperse defect size distributions.

3.2.3.3 Specimen size and boundary-condition effects

In the context of an explicit micromechanical modelling of the defects, the issues of specimen size and boundary conditions become significant. Again, the term of the representative volume element (RVE) is of some importance here. The effective elastic moduli usually are *intrinsic* material properties for which the RVE exists.[6] The RVE must include a sufficient number of micro-defects, but must be much smaller than the scale over which the macroscopic stresses fluctuate: a homogeneous stress and strain state is required. As an alternative to the definition of the RVE in section 2.2 (p. 40), a more

[6] In special materials with cavities or other unloaded defects, however, it is possible that the RVE does not exist at all [32].

specific and strict formulation claims that the RVE represents certain macroscopic material properties independently from the current boundary conditions, and that no scatter of these properties is allowed from one RVE specimen to another [32].

With respect to the effective stiffness/compliance, this means that the effective stiffness ($\mathbf{S}$) of an RVE obtained under displacement control (Dirichlet boundary conditions, subscript ϵ) must be equal (within a small enough error) to the effective stiffness calculated from the inverse of the effective compliance ($\mathbf{C}$) measured under load control (Neumann boundary conditions, subscript σ) (see [62], [48]):

$$\mathbf{S}_\epsilon = \mathbf{S}_\sigma \qquad \text{with} \qquad \mathbf{S}_\sigma = (\mathbf{C}_\sigma)^{-1} \tag{3.14}$$

Size effects and boundary-condition effects on the overall elastic properties of heterogeneous materials with cavities are apparent in specimens smaller than the RVE. The elements of the effective elastic stiffness and compliance tensors of a specimen smaller than the RVE under displacement control, load control and mixed (subscript m) boundary conditions, respectively, are related as follows [32]:

$$S_\sigma \leq S_\mathrm{m} \leq S_\epsilon \tag{3.15}$$

$$C_\epsilon \leq C_\mathrm{m} \leq C_\sigma \tag{3.16}$$

The statistical effects of the specimen size, accompanied by strong scatter of the individual results, are strongly coupled to the boundary condition effects. This fact is reflected in the following two sets of hierarchical order relationships [32]:

$$S_{\sigma,\mathrm{small}} \leq S_{\sigma,\mathrm{large}} \leq S_{\epsilon,\mathrm{large}} \leq S_{\epsilon,\mathrm{small}} \tag{3.17}$$

$$C_{\epsilon,\mathrm{small}} \leq C_{\epsilon,\mathrm{large}} \leq C_{\sigma,\mathrm{large}} \leq C_{\sigma,\mathrm{small}} \tag{3.18}$$

where subscripts 'small' and 'large' indicate sets of smaller-sized specimens and sets of larger-sized specimens, respectively, taken from the same material. Obviously, the trend of the size effect is reversed when passing from load-controlled boundary conditions to displacement-controlled boundary conditions. (The size effect can be non-monotonic in the mixed case [32].)

3.3 Local stress analysis: Analytical stress solutions for various single cavities

A detailed analysis of stresses below the continuum level is essential for the identification of critical locations for microcracking, and will be founded here on analytical solutions for stress fields around individual cavities. The stress solutions available in the literature are restricted to simple geometrical shapes, a fact which enforces the rough geometrical approximation of the porous phase in the microstructure model images. The exact solutions refer to the idealized situation of a single cavity embedded in an infinite, elastic plate under uniform stress applied at infinity.

The first and most popular formalism is the method of complex stress functions, which is assigned to Kolosov [47] and Muskhelishvili [60]. The stress (and displacement) components are treated as functions of the complex variable $z = x + \mathrm{i}y$ which is composed

of the plane coordinates x and y. Since real part and imaginary part of these functions are harmonic, the Cauchy-Riemann equations hold and the biharmonic functions can be expressed in terms of two analytical functions $\phi(z)$ and $\psi(z)$ of one complex variable z. The plain stress components can be deduced from these complex stress functions with the aid of the *Kolosov's formulae*:

$$\sigma_{xx} + \sigma_{yy} = 2\,[\phi'(z) + \overline{\phi}'(\overline{z})] \tag{3.19}$$

$$\sigma_{xx} - \sigma_{yy} + 2\mathrm{i}\sigma_{xy} = -2\,[z\overline{\phi}''(\overline{z}) + \overline{\psi}'(\overline{z})] \tag{3.20}$$

Thus, the problem is reduced to the determination of the functions $\phi(z)$ and $\psi(z)$. The complex stress functions must be specified in accordance with the boundary conditions. The situation is considerably facilitated if the Kolosov-Muskhelishvili method is applied to derive the stress (and displacement) fields around a unit circle, and if a conformal mapping rule is found to transform these fields into the curvilinear orthogonal coordinate system matched to the shape of the particular cavity (see [60]).

The present approach employs analytical stress solutions for elliptical and circular cavities deduced from [74], and for cavities with approximately triangular shape deduced from [68]. None of the original solutions could be utilized without further elaboration in order that the ultimate implementations exactly fulfil the differential equations of elastic equilibrium as well as the respective boundary conditions. The differential equations of elastic equilibrium read in the absence of body forces:

$$\frac{\partial \sigma_{xx}}{\partial x} + \frac{\partial \sigma_{xy}}{\partial y} = 0 \tag{3.21}$$

$$\frac{\partial \sigma_{yy}}{\partial y} + \frac{\partial \sigma_{xy}}{\partial x} = 0, \tag{3.22}$$

whereas the boundary conditions require that superposition of the individual stress disturbance fields to the macroscopic, homogeneous loading field must result in traction-free cavity boundaries.

The figures in the present section reflect the well-known fact that the stress-concentration coefficients[7] depend on the radius of curvature of the cavity. The highest local stresses appear where the curvature is highest, in the limit near tips or corners.

3.3.1 Stress fields around elastically anisotropic cavities

The most versatile cavity shape considered here is the ellipse. The conformal transformation rule mapping the interior of the circle of radius R in the $\zeta = \rho\exp(\mathrm{i}\theta)$ plane on the exterior of the elliptical cavity in the complex $z = x + \mathrm{i}y$ plane is

$$z(\zeta) = R\left(\frac{1}{\zeta} + c\zeta\right), \tag{3.23}$$

where $R = (a+b)/2$ and $c = (a-b)/(a+b)$ (a and b denote the length of the major and the minor semi-axis, respectively).

The curvilinear coordinates ρ and θ matched to the elliptical cavity shape are displayed in the z plane in fig. 3.4.

[7] The 'stress-concentration coefficient' is defined as the ratio of any component of the stress tensor at any point in the vicinity of the cavity to the stress tensor component at the same point in the cavity-free material, when the external forces acting on the material are equal in both cases.

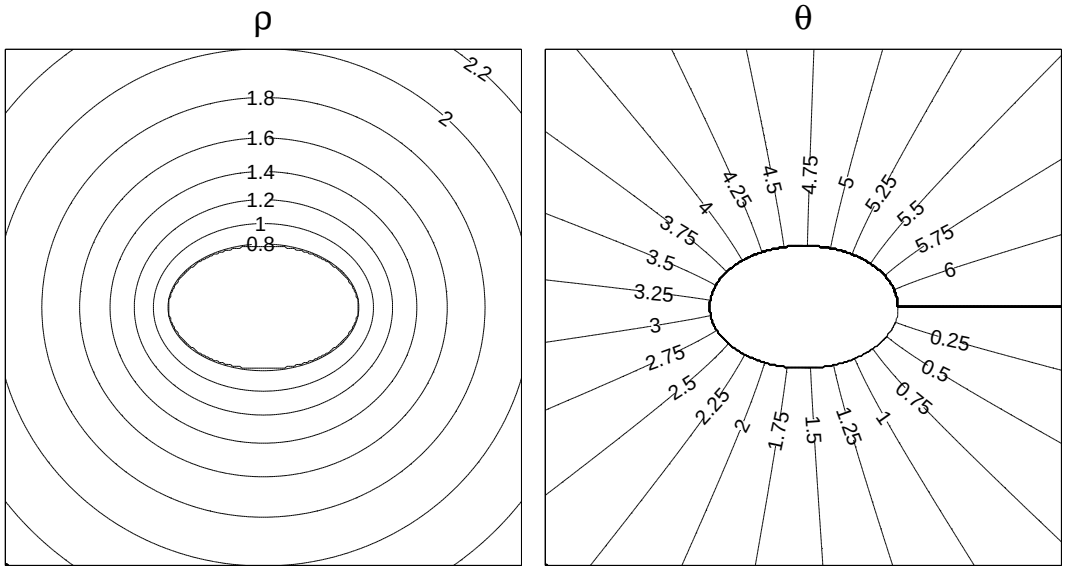

Figure 3.4: Representation of curvilinear coordinates matched to the elliptical cavity shape. Left: 'radial' coordinate ρ (reaching from ∞ to R, where R depends on the ratio of the semi-axes lengths); right: 'polar' ('angular', 'circumferential') coordinate θ (reaching from 0 to 2π).

In the computer algorithm, the stress solutions employed for elliptical cavities follow the analytical results by Stevenson [74]. Stevenson has developed a method of complex stress functions independently from Kolosov at about the same time (1940/1941). Fig. 3.5 shows the disturbance of the local stress field components due to the presence of an elliptical cavity in a material under external tensile and shear stresses of unit intensity.

Fig. 3.6 shows the corresponding stress field disturbances around a crack, which may be regarded as a degenerated ellipse and therefore described by the same formalism [74]. However, the numerical model uses analytical solutions presented by Benveniste ([5]) which provide identical results but are specified to cracks and therefore reduce the analytical and computational effort. Benveniste's solutions are based upon the original Kolosov-Muskhelishvili method.

It is instructive to see that for the elastic plane containing an elliptical cavity under uniaxial tension σ_0 perpendicular to the major semi-axis, the stress concentration σ/σ_0 at the ends of the ellipse is given by a simple formula [61]:

$$\frac{\sigma}{\sigma_0} = \left(1 + \frac{2a}{b}\right) \tag{3.24}$$

Introducing the smallest radius of curvature, $r_c = b^2/a$, and assuming flat ellipses ($b \ll a$), one can distinguish the effects of cavity size (a) and local curvature (r_c):

$$\frac{\sigma}{\sigma_0} = 2\sqrt{\frac{a}{r_c}} \tag{3.25}$$

Equation (3.25) leads to a stress singularity when the ellipse reduces to the limiting case of a crack ($b = 0$).

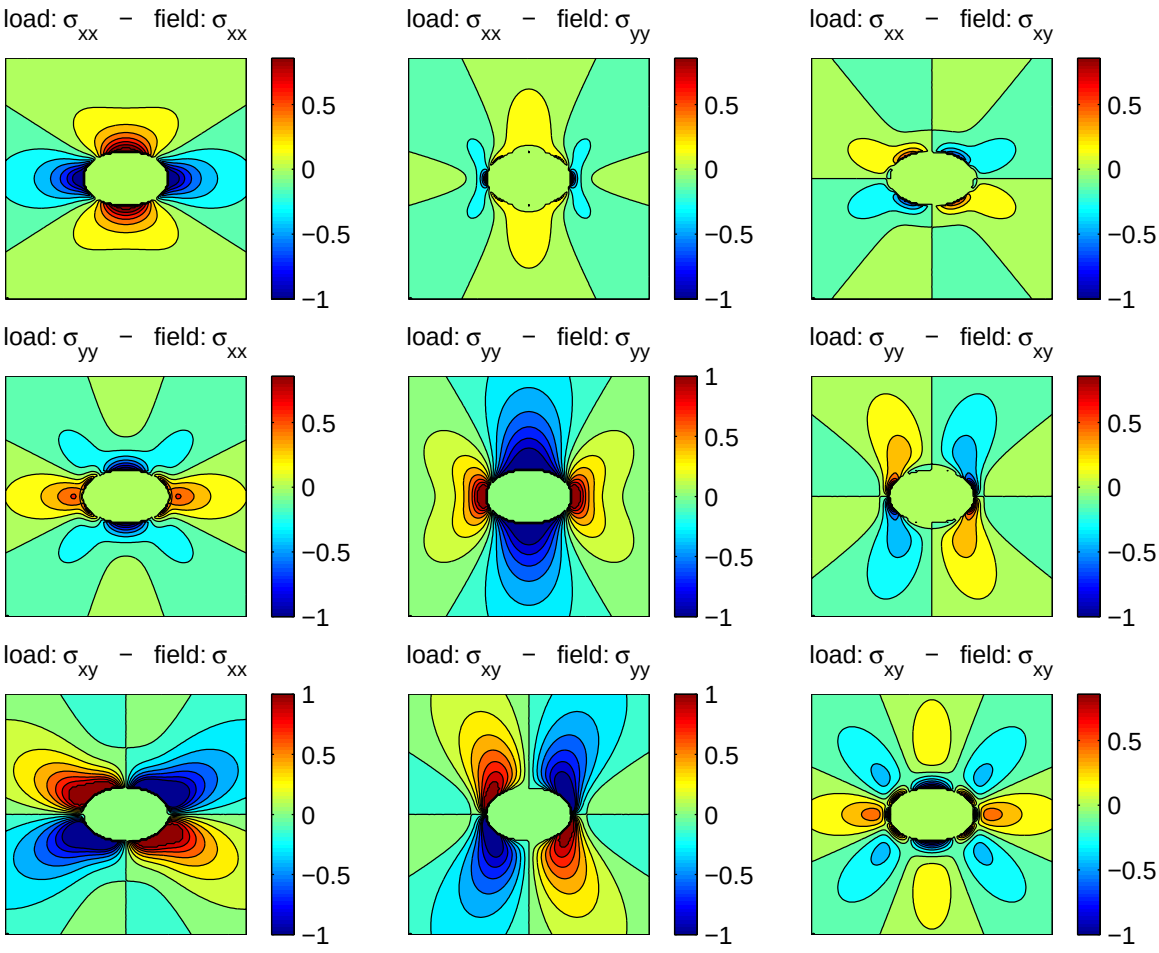

Figure 3.5: Stress field components in Cartesian coordinates around an elliptical cavity under unit tension and shear. The stress field components due to compressive load correspond to the fields displayed in the upper two rows if multiplied by (-1).

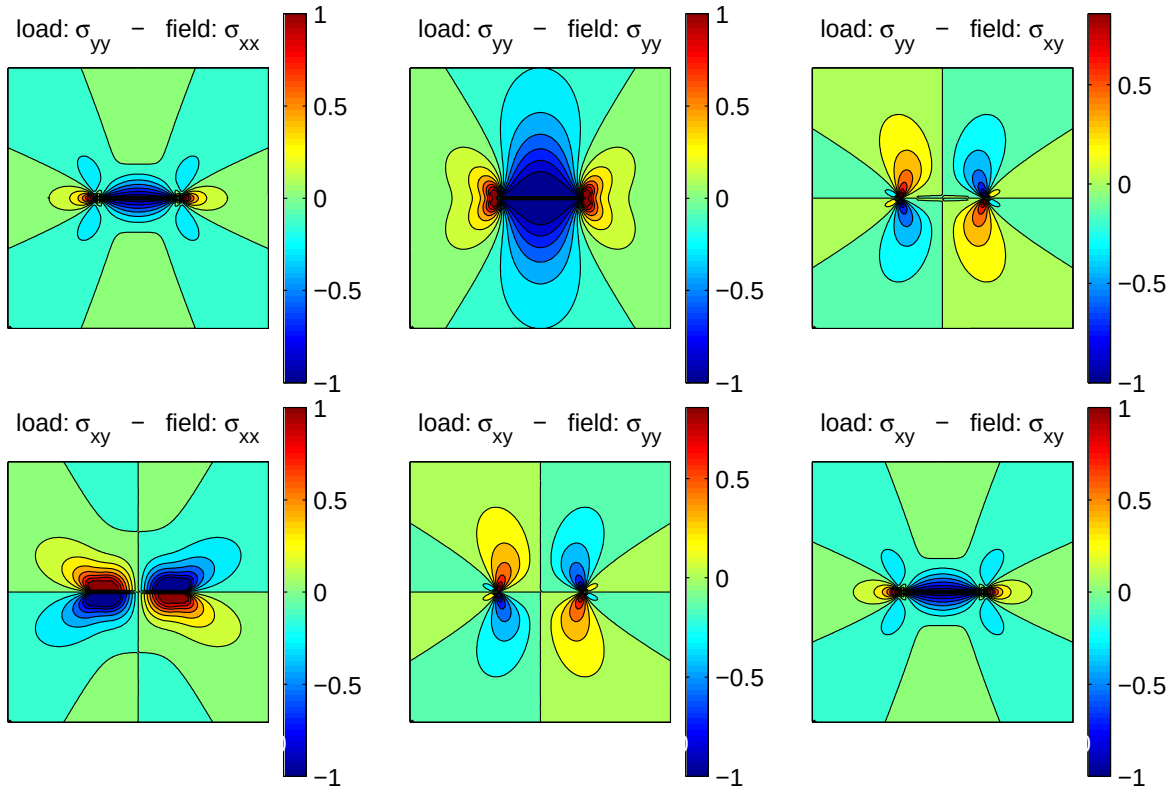

Figure 3.6: Stress field components in Cartesian coordinates around a crack under unit tension and shear. Due to crack closure, the stress field components under compressive load are naturally not simply given by multiplying the fields displayed in the upper row by (-1).

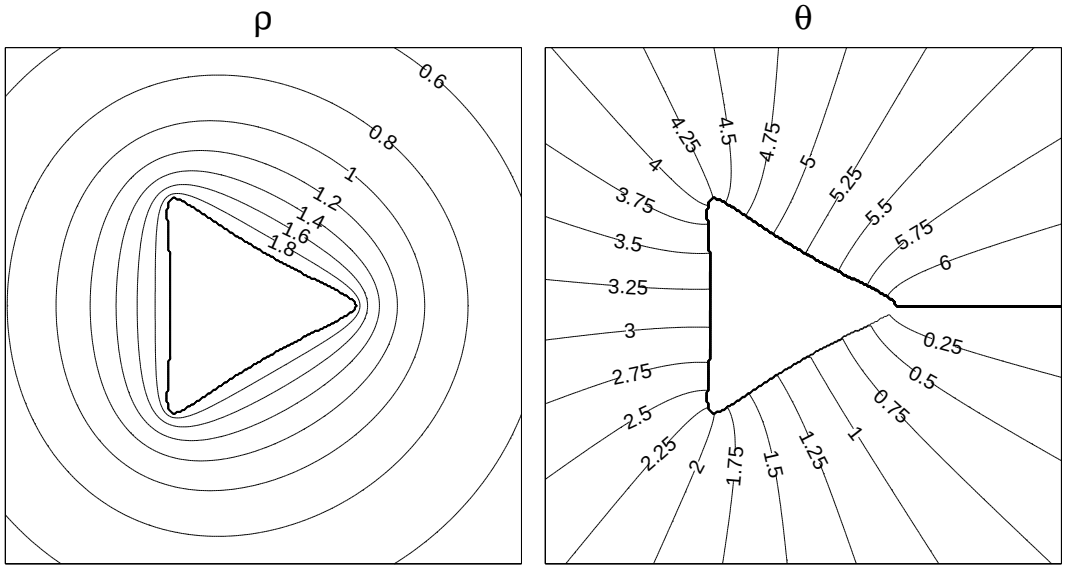

Figure 3.7: Representation of curvilinear coordinates matched to the approximately triangular cavity shape. Left: 'radial' coordinate ρ *(reaching from* ∞ *to* 0*); right: 'polar' coordinate* θ *(reaching from* 0 *to* 2π*).*

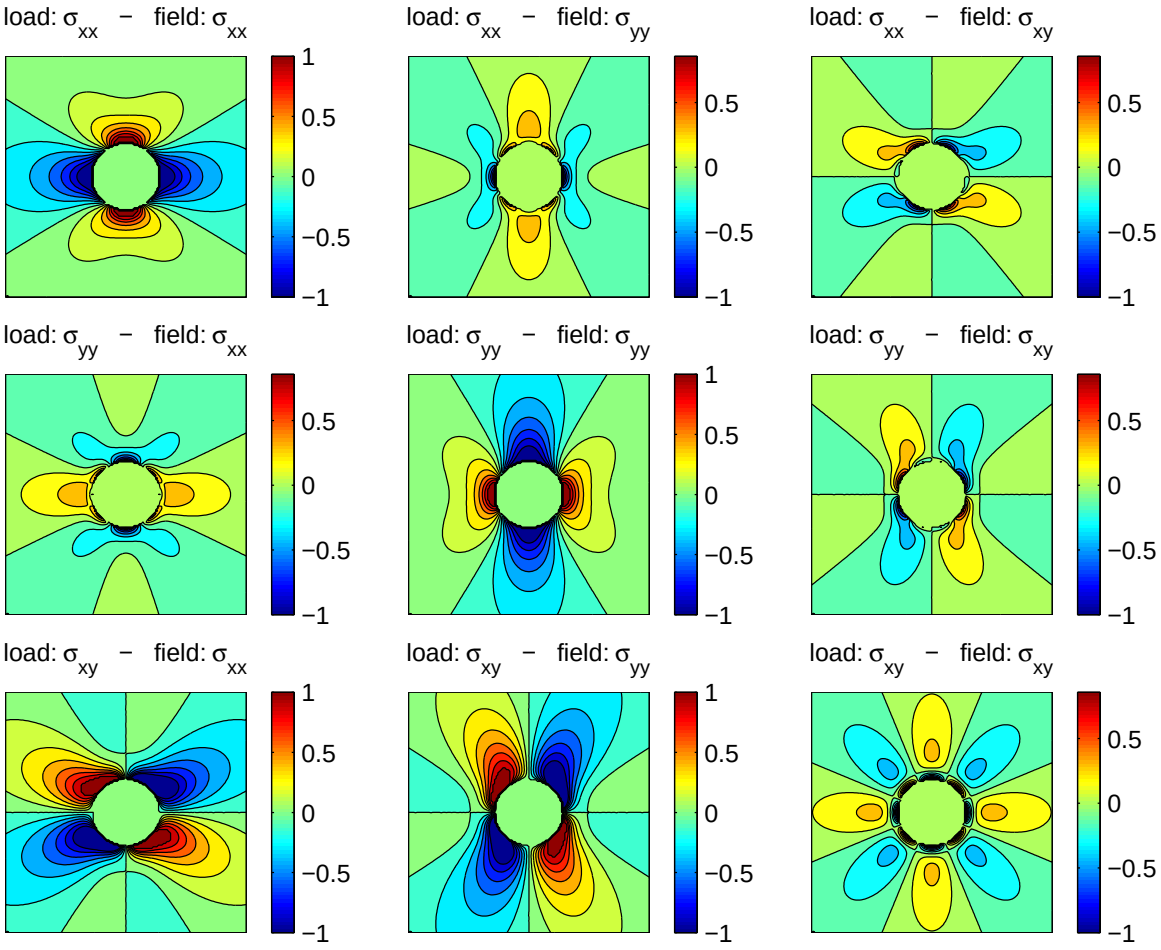

Figure 3.8: Stress field components in Cartesian coordinates around a circular cavity under unit tension and shear. The analytical solutions applied here are those for the elliptical shape [74], with (nearly) equal ellipse semiaxes.

3.3.2 Stress fields around elastically isotropic cavities

Elastically isotropic cavities are exemplified by circular pores and pores with regular triangular shape. The local stress fields for circular pores result from the Stevenson solutions [74] in the special case $a \approx b$ and are illustrated in fig. 3.8.

The triangular cavities are approximated by regular (equilateral) polygons with side number 3 as obtained by conformal transformation mapping the interior of a circle (of radius a) in the $\zeta = \rho \exp(\mathrm{i}\theta)$ plane on the exterior of the cavity in the complex $z = x + \mathrm{i}y$ plane. The transformation rule

$$z(\zeta) = R\left(\frac{1}{\zeta} + \frac{1}{3}\zeta^2\right) \tag{3.26}$$

yields triangles showing rounded-off angles. The corners of the triangle would become sharper by including a third or more terms into the transformation rule; however, the mathematical and computational effort in handling the elastic fields around this geometry

would increase considerably, whereas the increase of accuracy – at least with respect to the strain contribution of the cavity — would be minimal (below 4 % according to [48]).

The curvilinear coordinates ρ and θ matched to the 'triangular' cavity shape are displayed in the z plane in fig. 3.7 (p. 64).

The determination of local stresses in the present thesis is managed with the solutions by Savin ([68], based upon the Kolosov-Muskhelishvili method), which are originally represented in the curvilinear ζ plane. The applicability of the solutions in the numerical model requires their transformation from curvilinear (fig. 3.9) into Cartesian coordinates (fig. 3.10).

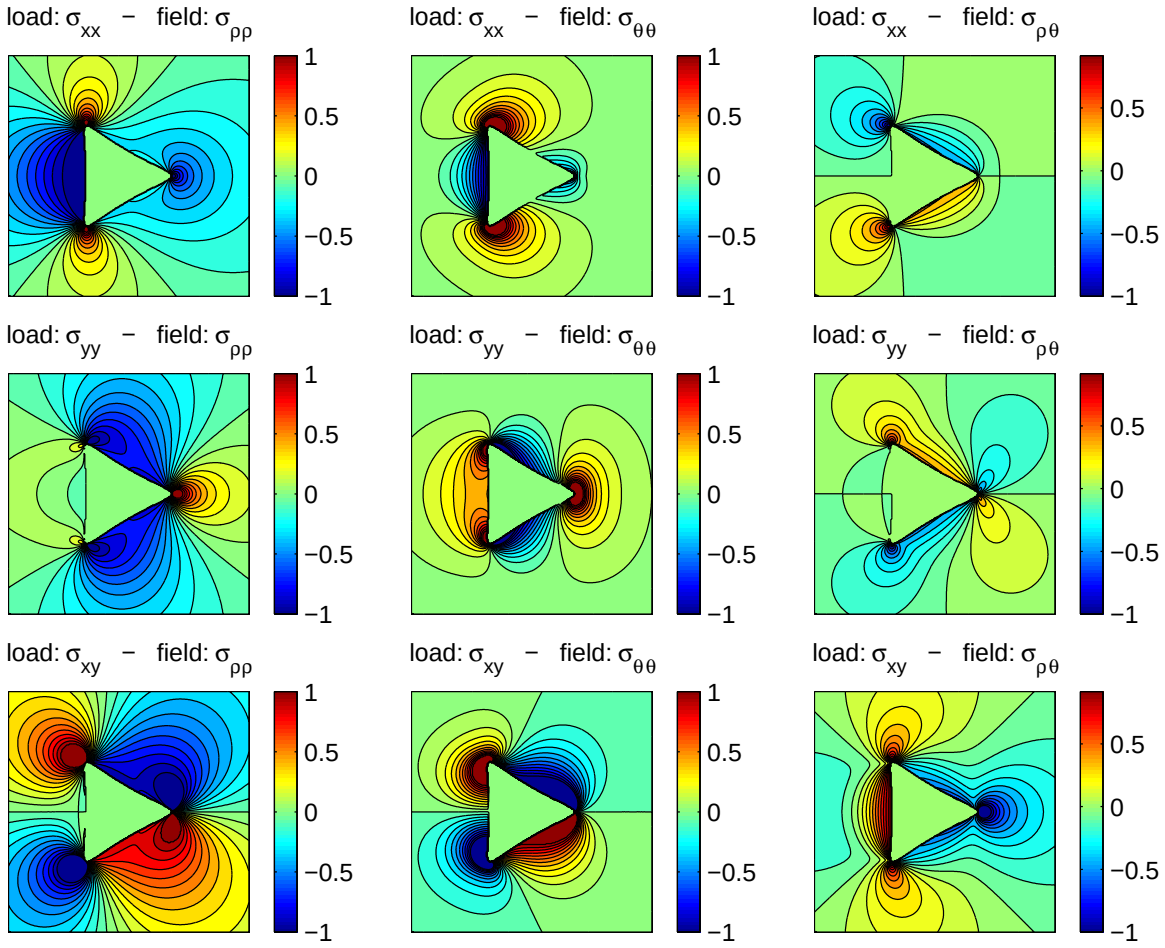

Figure 3.9: Stress field components around approximately triangular cavity under unit tension and shear. Representation in curvilinear coordinates.

In fig. 3.11, the local stress at a triangular cavity 'tip' is confronted with the corresponding field at an elliptical cavity 'tip'. The stress field plots illustrate that the near-field stress distribution qualitatively depends on the local curvature of the cavity boundary. (The quantitative level of the stresses, on the other hand, is essentially a function of the cavity size.)

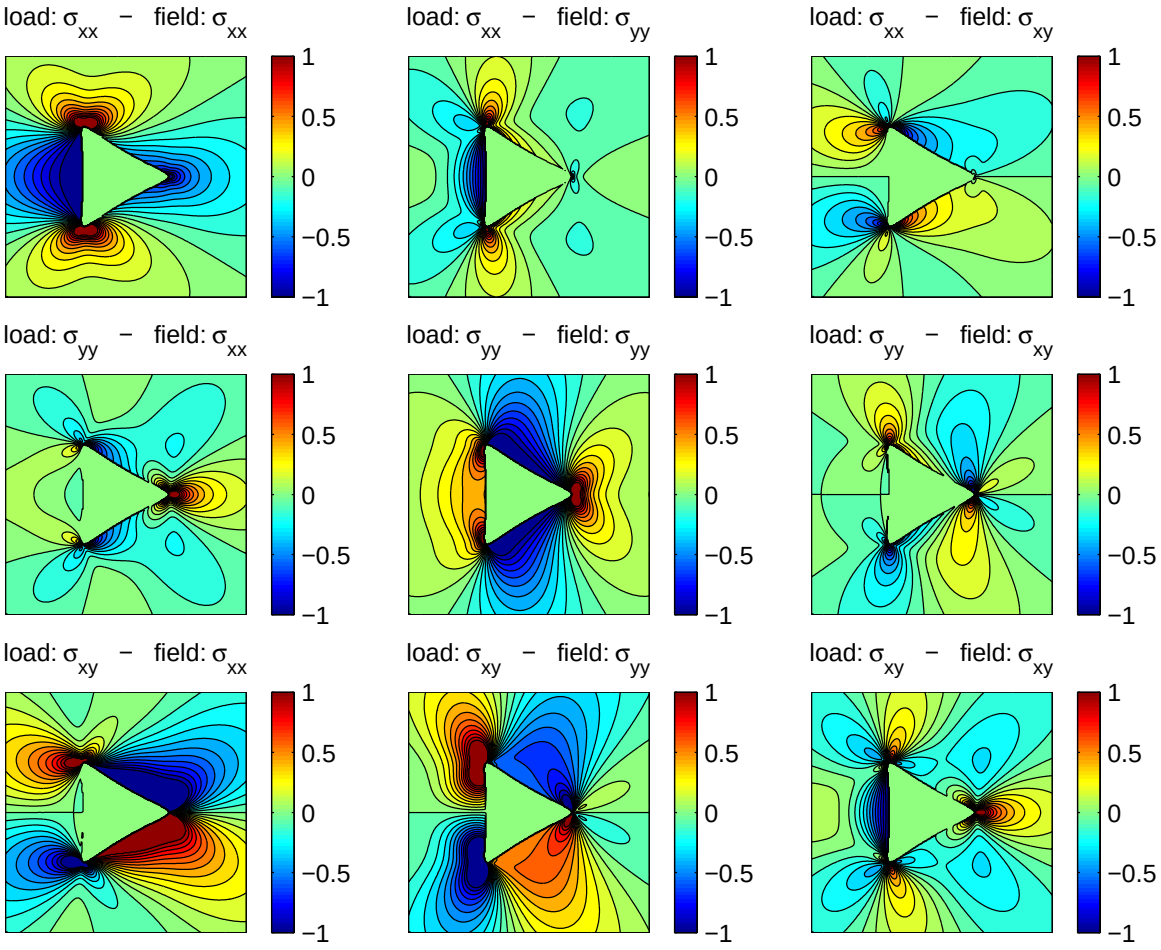

Figure 3.10: Stress field components around approximately triangular cavity under unit tension and shear. Representation in Cartesian coordinates. The stress field components due to compressive load are equal to the fields displayed in the upper two rows multiplied by (-1).

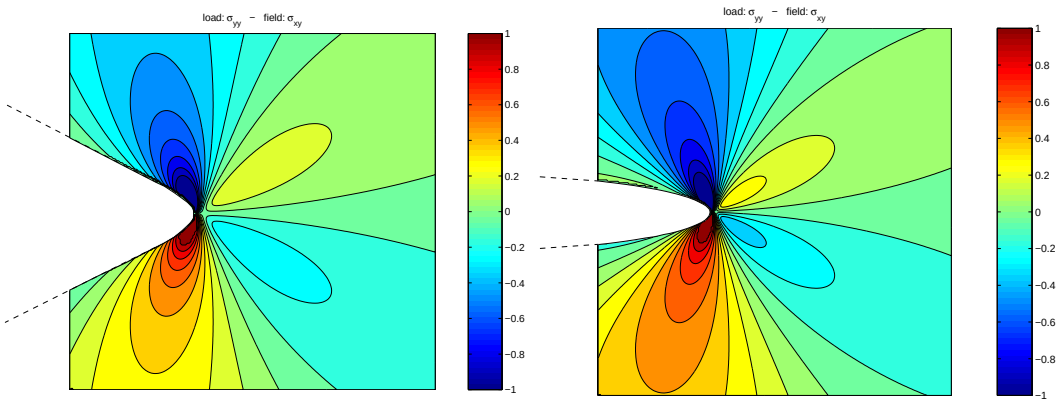

Figure 3.11: For comparison: stress field component σ_{xy} *close to a 'tip' of an approximately triangular cavity (above) and of an elliptical cavity (below) under* σ_{yy} *tension.*

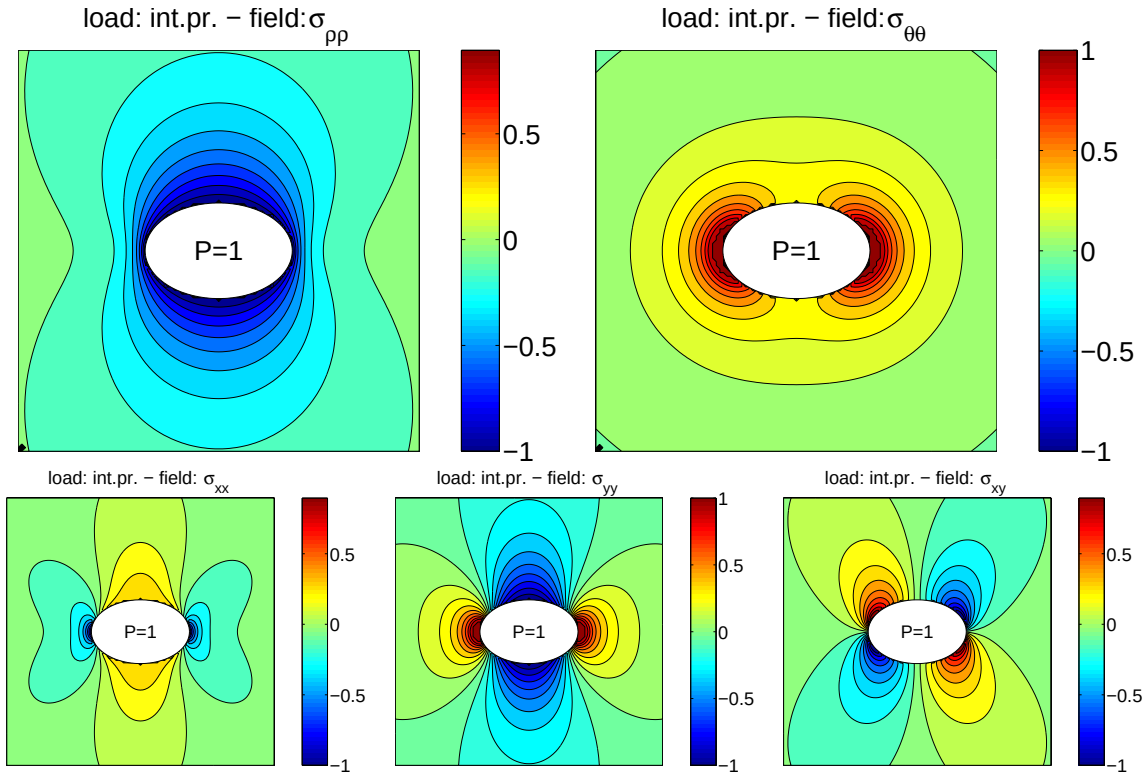

Figure 3.12: Stress field components around an elliptical cavity under unit internal pressure. Above: representation in curvilinear coordinates. Below: representation in Cartesian coordinates.

3.3.3 Stress fields around cavities under internal pressure

The stress distributions on the elastic solid induced by the (fluid) pressure in the cavity have been obtained from the respective analytical solutions for remote all-round tension P (which is equal to the superposition of two orthogonal tensile tractions $\sigma_{xx} = \sigma_{yy} = P$) by superposing the homogeneous stress state $\sigma_{xx} = \sigma_{yy} = -P$. This eliminates the remote loading and introduces the pressure P within the cavity.

The stress fields in a plate with an elliptical cavity are illustrated in fig. 3.12 in curvilinear and Cartesian coordinates. The special case of a circular cavity is illustrated in fig. 3.13 in curvilinear coordinates. For the circular cavity of radius a, the radial and circumferential stress components are simply given by

$$\sigma_{\rho\rho} = -\frac{a^2}{r^2}\, P \tag{3.27}$$

and

$$\sigma_{\theta\theta} = \frac{a^2}{r^2}\, P \tag{3.28}$$

as a function of distance r from the cavity centre [76].

The local stress field components around a triangular cavity under internal pressure are represented in fig. 3.14 in both curvilinear and Cartesian coordinates.

The resulting 'radial' field component $\sigma_{\rho\rho}$ due to the cavity has been proved to be exactly $\sigma_{\rho\rho} = -\sigma_{xx} = -\sigma_{yy}$ at every location on the surface (i.e., $\rho = 1$): the applied

solutions *exactly* satisfy the boundary conditions. This is illustrated in fig. 3.15, which shows enlarged sections of the stress fields.

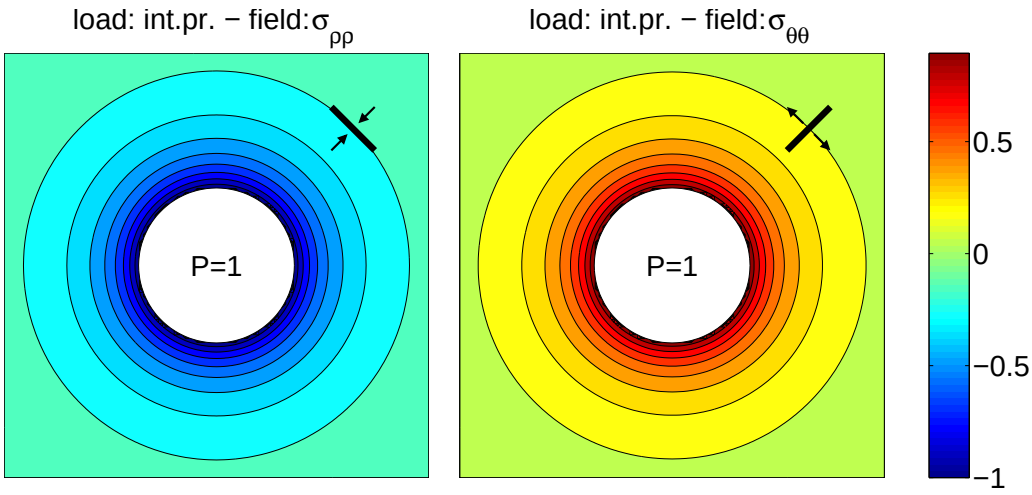

Figure 3.13: Stress field components in curvilinear coordinates around a circular cavity under unit internal pressure.

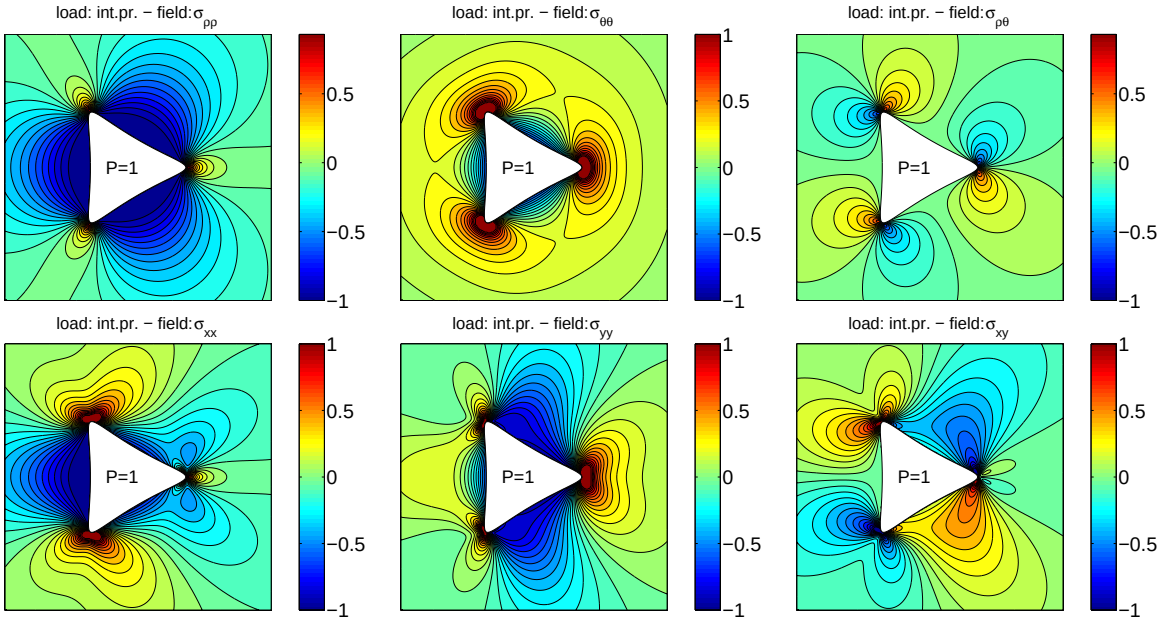

Figure 3.14: Stress field components around approximately triangular cavity under internal pressure. Upper row: representation in curvilinear coordinates; lower row: representation in Cartesian coordinates.

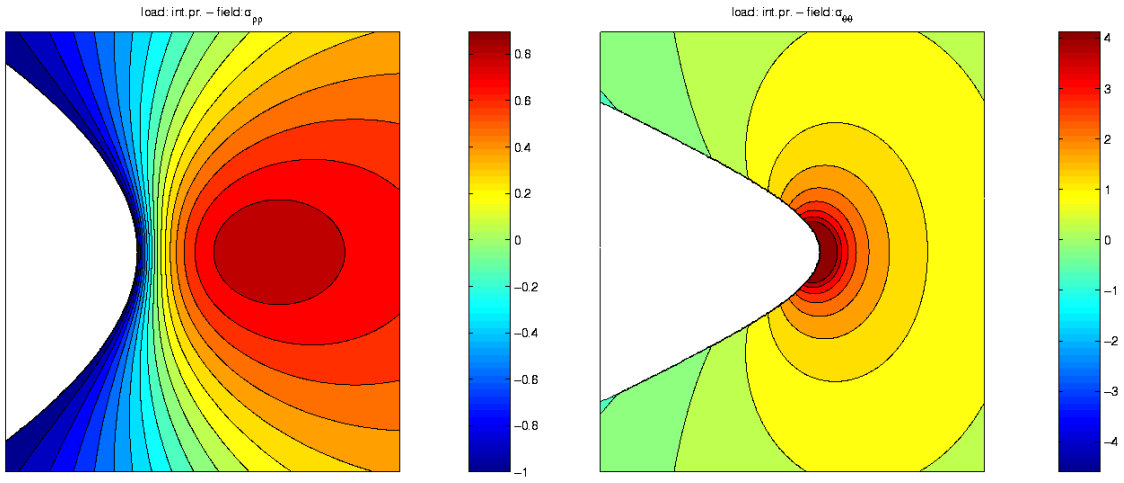

Figure 3.15: Radial stress field (left) and circumferential stress field (right) in the vicinity of a 'tip' of the (approximately) triangular cavity under pressure. The radial stress field representation shows that the boundary condition at the cavity surface is fulfilled.

3.4 Micromechanical description of deterministic crack configurations: linear formalism

The formalism to be developed in the following relies on the micromechanical description of the crack behaviour and a superposition technique for the ensemble of cavities present in a material section. A prominent part is assigned here to the 'transmission coefficients', which can be determined with the aid of the analytical stress solutions from the previous section 3.3.

3.4.1 Crack opening displacement

In general, a crack is characterized by two identical surfaces (the so-called *crack faces*) which are separated by the *crack opening displacement* (COD). The crack opening displacement and the corresponding stresses (tractions) along the crack faces are the main mechanical variables for the crack. Both sets of variables may be decomposed into normal components (superscript "n") and tangential (shear) components (superscript "s").

In the present work – which restricts to two-dimensional configurations – the cracks are assumed to be straight and the tractions are assumed to be uniform over the length of the cracks. The displacement vector at a certain position on the crack denotes the relative displacement of the corresponding points on the two crack faces, which is a function of the local stresses and the elastic parameters of the matrix. It is assumed here that the displacement is a linear function of the applied stresses.

For a crack k in the isotropic elastic plane, the familiar linear relation (see [42], [43], [15]) between the averaged crack opening displacement $\langle \mathbf{b}_k \rangle = \{ \langle b_k^{\mathrm{n}} \rangle \ \langle b_k^{\mathrm{s}} \rangle \}$ and the effective

crack traction[8] $\mathbf{t}_k = \{t_k^{\mathrm{n}}\ t_k^{\mathrm{s}}\}$ reads

$$\langle \mathbf{b}_k \rangle \approx \frac{\pi l_k}{2E'} \mathbf{t}_k \ , \tag{3.29}$$

where l_k denotes the length of the crack, and E' is Young's modulus of the compact surrounding material.[9] The normal component $\langle b_k^{\mathrm{n}} \rangle$ refers to an opening of the crack faces, whereas the shear component $\langle b_k^{\mathrm{s}} \rangle$ refers to a slip of the crack faces. The term $\pi l_k / 2E'$ may be called the scalar *crack compliance*.

3.4.2 Determination of macroscopic elastic properties

The properties of the discrete defect arrays at the microscopic level are to be homogenized in order to get effective material parameters. The essential point in the homogenization procedure is the determination of the average (macroscopic) strain $\boldsymbol{\epsilon}$ over a representative area A. The strain $\boldsymbol{\epsilon}$ generally is related to the remotely applied (macroscopic) stress $\boldsymbol{\sigma}$ via the effective elastic compliance $\mathbf{C}$ of the heterogeneous material:

$$\boldsymbol{\epsilon} = \mathbf{C}\ \boldsymbol{\sigma} \tag{3.30}$$

In a tensor notation[10], the compliance $\mathbf{C}$ is a fourth rank tensor. The overall strain may be decomposed into a contribution $\boldsymbol{\epsilon}_0$ of the solid parts of the material, and contributions $\boldsymbol{\epsilon}_k$ of each individual crack k (see [42], [43], [48]):

$$\boldsymbol{\epsilon} = \underbrace{\mathbf{C}_0\ \boldsymbol{\sigma}}_{\boldsymbol{\epsilon}_0} + \sum_k \underbrace{\frac{1}{2A}\ l_k\ (\mathbf{n}_k \langle \mathbf{b}_k \rangle + \langle \mathbf{b}_k \rangle \mathbf{n}_k)}_{\boldsymbol{\epsilon}_k}, \tag{3.31}$$

where $\mathbf{C}_0$ denotes the compliance of the compact matrix material, and the summation extends over all cracks located within the considered area A. Equation (3.31) involves a *dyadic* multiplication of the unit normal vector $\mathbf{n}_k$ on crack k and the average crack opening displacement $\langle \mathbf{b}_k \rangle$. The $\boldsymbol{\epsilon}_k$ terms are equivalent to surface integrals of the displacement discontinuity $\mathbf{b}_k$ over the cracks.

The crack opening displacements can be substituted by eq. (3.29):

$$\boldsymbol{\epsilon} = \mathbf{C}_0\ \boldsymbol{\sigma} + \frac{\pi}{2AE'} \sum_k l_k^2\ (\mathbf{n}_k \mathbf{t}_k + \mathbf{t}_k \mathbf{n}_k), \tag{3.32}$$

so that the problem of the macroscopic strain is reduced to the determination of the (average) load $\mathbf{t}_k$ on the cracks, an issue which is the subject of the following section 3.4.3.

Corresponding to the decomposition of the macroscopic strain, the effective elastic compliance can be decomposed into a contribution $\mathbf{C}_0$ of the compact matrix material, and a contribution $\mathbf{C}_k$ of each individual crack k:

$$\mathbf{C} = \mathbf{C}_0 + \sum_k \mathbf{C}_k \tag{3.33}$$

[8] overall traction on the crack line *in the absence of the crack*

[9] $E' = E/(1-\nu^2)$ for plane strain conditions, whilst $E' = E$ for plane stress conditions

[10] tensor notation in two dimensions:

$$\begin{bmatrix} \epsilon_{xx} & \epsilon_{xy} \\ \epsilon_{yx} & \epsilon_{yy} \end{bmatrix} = \mathbf{C} \begin{bmatrix} \sigma_{xx} & \sigma_{xy} \\ \sigma_{yx} & \sigma_{yy} \end{bmatrix}$$

The components of the crack contribution $\mathbf{C}_k$ to the compliance tensor relate the macroscopic stress components to the strain contribution of the crack. They can be found from eq. (3.32) if the tractions are expressed in terms of the macroscopic stress $\boldsymbol{\sigma}$. If the interaction between the cracks is neglected, then the relation between stress and traction along a crack line is a simple projection:

$$\mathbf{t}_k = \boldsymbol{\sigma}\ \mathbf{n}_k \tag{3.34}$$

Denoting the orientation angle of the crack with respect to the x-axis of the Cartesian coordinate system by θ_k, the components of the normal unity vector are $\mathbf{n}_k = \{-\sin\theta_k \ \ \cos\theta_k\}$, and eq. (3.34) yields

$$t_k^{\mathrm{n}} = \sigma_{xx}\sin^2\theta_k + \sigma_{yy}\cos^2\theta_k - 2\sigma_{xy}\sin\theta_k\cos\theta_k \tag{3.35}$$

$$t_k^{\mathrm{s}} = (\sigma_{yy} - \sigma_{xx})\sin\theta_k\cos\theta_k + \sigma_{xy}(\cos^2\theta_k - \sin^2\theta_k). \tag{3.36}$$

In a matrix notation (Voigt notation)[11], the contribution of the cracks to the compliance matrix reads thus:

$$\mathbf{C}_{\mathrm{cracks}} \equiv \sum_k \mathbf{C}_k = \frac{\pi}{2AE'}\sum_k l_k^2 \underbrace{\begin{bmatrix} \sin^2\theta_k & 0 & -\sin\theta_k\cos\theta_k \\ 0 & \cos^2\theta_k & -\sin\theta_k\cos\theta_k \\ -\sin\theta_k\cos\theta_k & -\sin\theta_k\cos\theta_k & 1 \end{bmatrix}}_{\mathbf{N}_k}, \tag{3.37}$$

where the 'projection matrix' $\mathbf{N}_k$ takes into account that the contribution of a crack depends on its projection in the direction of loading.

In contrast, the relation is much complexer for interacting cracks (see eq. 3.38 below), resulting in very extensive expressions for the crack compliance.

3.4.3 Determination of the effective load on a crack

The traction on each individual crack and, therefore, the displacement discontinuity along its faces depend not only on the 'externally' applied, homogeneous load, but also on the location, orientation and geometry of the neighboured cracks. Since exact solutions for the interactions of two or more cracks are not available, numerical estimations are needed instead. In order to account for the complex system of crack-crack interactions, the simplifying self-consistent approach introduced by Mark Kachanov [42] is used in the following: The unknown traction $\mathbf{t}_k$ on crack k is the superposition of the traction $\mathbf{t}_k^0$ induced from the external stress $\boldsymbol{\sigma}$ and the tractions 'transmitted' by all other cracks i:

$$\mathbf{t}_k(\xi_k) = [\boldsymbol{\sigma} + \sum_{i\neq k}\boldsymbol{\sigma}_{ki}(\xi_k)]\ \mathbf{n}_k \tag{3.38}$$

$$\mathbf{t}_k(\xi_k) = \mathbf{t}_k^0(\xi_k) + \sum_{i\neq k}\mathbf{t}_{ki}(\xi_k) \tag{3.39}$$

[11] Voigt notation in two dimensions:

$$\begin{bmatrix} \epsilon_{xx} \\ \epsilon_{yy} \\ \epsilon_{xy} \end{bmatrix} = \mathbf{C}\ \begin{bmatrix} \sigma_{xx} \\ \sigma_{yy} \\ \sigma_{xy} \end{bmatrix}$$

Here ξ_k is a current point on crack k.

The basic simplifying assumption of Kachanov's approach is that the 'transmitted' load $\boldsymbol{\sigma}_{ki}$ resp. $\mathbf{t}_{ki}$ is taken as generated by a *uniform average* traction $\langle \mathbf{t}_i \rangle$ on crack i. That means, the impact on crack k of traction non-uniformities $(\mathbf{t}_i(\xi_i) - \langle \mathbf{t}_i \rangle)$ along each crack $i \neq k$ is neglected. The unknown traction $\mathbf{t}_k$, averaged along the crack line ξ_k, is thus obtained as follows:

$$\langle \mathbf{t}_k \rangle = \mathbf{t}_k^0 + \sum_{i \neq k} \langle \mathbf{t}_{ki} \rangle \tag{3.40}$$

One may now set $\langle \mathbf{t}_{ki} \rangle = \mathbf{\Lambda}_{ki} \langle \mathbf{t}_i \rangle$, where $\mathbf{\Lambda}_{ki}$ denotes the 'crack-crack transmission factors', i.e. the 'standard' stress fields generated by uniformly loaded cracks i averaged along the lines of cracks k [42]. (The transmission factors can be determined with the aid of the analytical stress solutions presented in the previous section 3.3 (fig. 3.6). Note that $\mathbf{\Lambda}_{kk} = 0$.) Then, eq. (3.40) can be re-written as follows:

$$\langle \mathbf{t}_k \rangle = \mathbf{t}_k^0 + \mathbf{\Lambda}_{ki} \langle \mathbf{t}_i \rangle \ , \tag{3.41}$$

where a summation over $i = 1, ..., N$ (N: total number of cracks) is implicitly assumed. Taking eq. (3.41) for each crack k establishes a system of N linear algebraic equations ("self-consistency" equations) for the average tractions[12]:

$$(\delta_{ki}\mathbf{I} - \mathbf{\Lambda}_{ki})\langle \mathbf{t}_i \rangle = \mathbf{t}_k^0 \ , \tag{3.42}$$

which can be solved by numerical methods, namely numerical matrix inversion:

$$\langle \mathbf{t}_i \rangle = (\delta_{ki}\mathbf{I} - \mathbf{\Lambda}_{ki})^{-1} \mathbf{t}_k^0 \tag{3.43}$$

Kachanov's method of approximating the traction on a crack by its average over the crack length corresponds to expanding the traction, which may actually be a rapidly varying function of the position ξ on the crack, into a power series and truncating to the zero-th order term. Other models have been proposed which account for higher-order terms (see, e.g. [5]) and different series of orthogonal functions. While these approaches gain some accuracy, they lose at the same time a lot of tractability. It is obvious that the simplest approximation by Kachanov suffices to illustrate the essential aspects of the effects of direct crack interactions.

3.5 Micromechanical description of deterministic crack configurations: nonlinear formalism

The complexity of the formalism is considerably enhanced if nonlinear effects such as crack closure, friction of the sliding crack faces, and irreversible changes of the microstructure (as will be the subject of Chapter 4) occur. The material response then exhibits a path-dependence which necessitates incrementation of the loading process and of the constitutive equation. The present section outlines the corresponding formalism, which is fundamental for the numerical simulations. The incremental theory is supplemented by the effects of pores and of pressure acting inside the cavities.

[12] In fact, it is a system of $2N$ equations, since each traction vector involves two scalar components.

3.5.1 Accounting for crack closure and frictional sliding

The formalism for the cracked solid presented in section 3.4.3 refers to opening and free sliding conditions for all cracks. If the loading system induces compressive stresses on individual cracks, the displacement discontinuity is suppressed in the normal direction ('damage deactivation'), whilst the tangential motion may be prohibited by the appearance of friction. The instantaneous response of the cracked solid to an incremental change of load then depends on the current state of the microstructure, which results from the entire history of loading and the associated irreversible changes and rearrangements in the microstructure. In other words, there is a *path-dependence* of the material response.

The simplest illustrative example for the history dependence refers to a crack under normal load: if uniaxial *tension* is applied first (leading to an active state of the crack), then the change of material stiffness due to a superimposed incremental tension or compression will have a different value than in the case when uniaxial *compression* is applied first (leading to a passive state of the crack). A different example, referring to mixed loading conditions (shear load and normal load), is illustrated in fig. 3.16. The description of frictional cracks involves a complex set of conditions, as will be elaborated below.

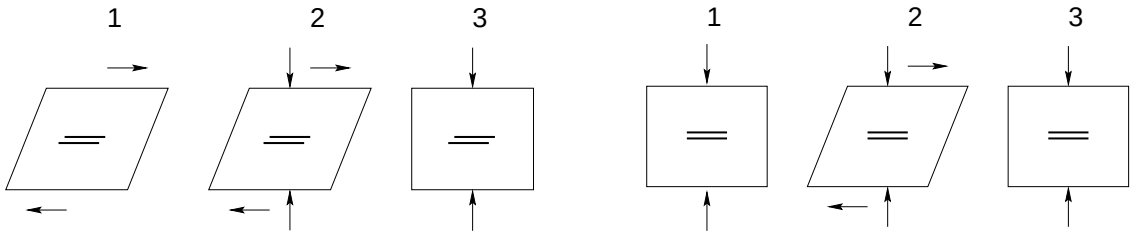

Figure 3.16: Single-crack specimen subject to different loading paths: application of shear traction followed by superposed compressive load produces non-zero shear opening displacement (left), whereas reversing the sequence produces smaller displacement or no displacement at all (right).

According to Krajcinovic [48], an accurate assessment of the magnitude of the friction coefficient (which basically reflects the roughness of the crack faces) "is an absolutely crucial prerequisite for the determination of the effective moduli" of materials in a state of compression. In the present formalism, the movement of contacting grain surfaces is assumed to be governed by a simple friction law: for a compressive load t^{n} normal to the contact surfaces, the tangential friction load $t^{\mathrm{s}}_{\mathrm{friction}}$ is given by

$$|t^{\mathrm{s}}_{\mathrm{friction}}| = \mu_m \, |t^{\mathrm{n}}| \tag{3.44}$$

in sliding friction, and

$$|t^{\mathrm{s}}_{\mathrm{friction}}| = \mu_s \, |t^{\mathrm{n}}| \tag{3.45}$$

in static friction (sticking friction, 'stiction'). As a rule, the coefficient μ_s of static friction is higher than the coefficient μ_m of sliding friction. The macroscopic coefficients of friction for ceramics typically assume values in between 0.05 and 0.5 [29].

Incremental crack opening displacement. Compared to eq. (3.29), the change $\Delta\langle \mathbf{b}_k \rangle$ of crack opening displacement due to an incremental change $\Delta \mathbf{t}_k$ of traction on the crack must be written here as follows:

$$\begin{bmatrix} \Delta\langle b_k^{\mathrm{n}} \rangle \\ \Delta\langle b_k^{\mathrm{s}} \rangle \end{bmatrix} = \frac{\pi l_k}{2E'} \begin{bmatrix} a_k^{\mathrm{n}} \, (t_{k,\mathrm{mism}}^{\mathrm{n}} + \Delta\langle t_k^{\mathrm{n}} \rangle \,) \\ a_k^{\mathrm{s}} \, (t_{k,\mathrm{mism}}^{\mathrm{s}} + \Delta\langle t_k^{\mathrm{s}} \rangle \,) \end{bmatrix} \tag{3.46}$$

The fundamental, nonlinear equation (3.46) introduces two additional parameters: The *activity factors*, which are collected for the k-th crack in the vector array

$$\mathbf{a}_k = \{a_k^{\mathrm{n}} \; a_k^{\mathrm{s}}\}, \tag{3.47}$$

and the *(shear) traction mismatch*, which reads in vector form:

$$\mathbf{t}_{k,\mathrm{mism}} = \{t_{k,\mathrm{mism}}^{\mathrm{n}} \; t_{k,\mathrm{mism}}^{\mathrm{s}}\} \tag{3.48}$$

These two parameters characterize the instantaneous kinematic condition of each crack and will be described in the following:

Shear mismatch. Due to the nonlinear effects of closure and friction, the opening displacement $\mathbf{b}_k$ of the crack is not necessarily proportional to the acting traction $\mathbf{t}_k$ (see the illustrative example in fig. 3.17). Since the present model is inherently based upon *tractions*, it is straightforward to introduce an 'active traction' $\mathbf{t}_{k,\mathrm{active}}$, which is defined to be proportional to $\mathbf{b}_k$ (corresponding to eq. 3.29):

$$\langle \mathbf{b}_k \rangle \approx \frac{\pi l_k}{2E'} \mathbf{t}_{k,\mathrm{active}} \tag{3.49}$$

Then, as a matter of course, the incremental formula

$$\Delta\langle \mathbf{b}_k \rangle \approx \frac{\pi l_k}{2E'} \Delta\mathbf{t}_{k,\mathrm{active}} \tag{3.50}$$

holds as well. Comparing eq. (3.50) and eq. (3.46), the explicit definition of the change of active traction must read

$$\Delta\mathbf{t}_{k,\mathrm{active}} \;=\; \begin{bmatrix} a_k^{\mathrm{n}} \, (t_{k,\mathrm{mism}}^{\mathrm{n}} + \Delta\langle t_k^{\mathrm{n}} \rangle \,) \\ a_k^{\mathrm{s}} \, (t_{k,\mathrm{mism}}^{\mathrm{s}} + \Delta\langle t_k^{\mathrm{s}} \rangle \,) \end{bmatrix} \tag{3.51}$$

The current 'mismatch' between the actual, effective traction $\mathbf{t}_k$ on the crack and the traction $\mathbf{t}_{k,\mathrm{active}}$ proportional to the actual displacement of its faces is thus given as

$$\mathbf{t}_{k,\mathrm{mism}} = \mathbf{t}_k - \mathbf{t}_{k,\mathrm{active}}. \tag{3.52}$$

For small increments Δt_k^{n}, the mismatch in normal direction can be neglected[13]:

$$t_{k,\mathrm{mism}}^{\mathrm{n}} = 0 \tag{3.53}$$

What remains in eq. (3.46) is a 'shear mismatch' $t_{k,\mathrm{mism}}^{\mathrm{s}}$:

$$\begin{bmatrix} \Delta\langle b_k^{\mathrm{n}} \rangle \\ \Delta\langle b_k^{\mathrm{s}} \rangle \end{bmatrix} = \frac{\pi l_k}{2E'} \begin{bmatrix} a_k^{\mathrm{n}} \, (\qquad\qquad \Delta\langle t_k^{\mathrm{n}} \rangle \,) \\ a_k^{\mathrm{s}} \, (t_{k,\mathrm{mism}}^{\mathrm{s}} + \Delta\langle t_k^{\mathrm{s}} \rangle \,) \end{bmatrix} \tag{3.54}$$

[13](The case $t_k^{\mathrm{n}} < 0$ is not of interest here, since $a_k^{\mathrm{n}} = 0$ if $t_k^{\mathrm{n}} < 0$.)

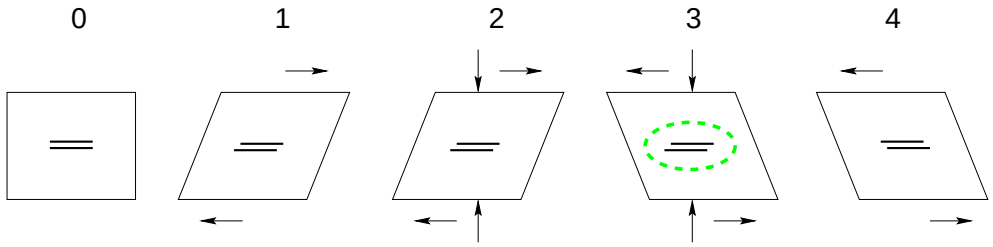

Figure 3.17: Example for a transiently 'locked' shear displacement ('mismatch' between effective traction on the crack and opening displacement): The normal load on a crack with shear opening displacement is changed from tensile to compressive, and thus temporarily 'locks' the displaced crack faces (step 3). The shear mismatch is emphasized by the dashed ellipse.

Activity factors. The activity factors $\mathbf{a}_k$ describe whether (and to which extent) a certain 'mismatch traction' $(\mathbf{t}_{k,\mathrm{mism}} + \Delta\mathbf{t}_k)$ on the crack faces results in a change of crack opening displacement $\Delta\mathbf{b}_k$.[14] For unconstrained crack opening $a_k^{\mathrm{n}} = 1$, $a_k^{\mathrm{s}} = 1$, whilst $a_k^{\mathrm{n}} = 0$ and $0 \le a_k^{\mathrm{s}} \le 1$ for the closed crack.

Just as the shear mismatch, the activity factors depend on the current state of local stress; in the numerical algorithm, both parameters are stored and updated continuously.

The following list gives a detailed description of the crack activity factors and its determination in the numerical algorithm.

1. If the normal traction t_k^{n} is positive (tensile), then the crack is 'fully active', and both the 'normal activity' and 'shear activity' are equal to 1:

$$a_k^{\mathrm{n}} = 1 \quad , \quad a_k^{\mathrm{s}} = 1 \tag{3.55}$$

   In this case, there are currently no closure or friction effects of the respective crack. The crack is open, and an incremental change of load results in a corresponding change of crack opening displacement.

2. Cracks under normal compression are closed in normal direction. The special properties of closed cracks may be summarized as follows:

   (a) The *normal* displacement is zero, and an incremental change of load results in no change of normal opening displacement. The crack transmits the normal compression just as the compact material. For this reason, the crack is called 'passive' in the normal direction, and the 'normal activity factor' a^{n} is set equal to zero:

$$a_k^{\mathrm{n}} = 0 \tag{3.56}$$

   (b) Regarding the *shear* activity, two cases have to be distinguished depending on the friction of the crack faces:

      i. If the shear 'mismatch' $t_{k,\mathrm{mism}}^{\mathrm{s}}$ on the crack is lower than the static friction $\mu_s|t_k^{\mathrm{n}}|$ hampering the sliding of the crack faces, then there is no variation in crack shear displacement. The crack is in a 'fully passive' state:

$$a_k^{\mathrm{s}} = 0 \tag{3.57}$$

[14] Note: The present definition of crack activity is different from Krajcinovic's definition ([48]).

ii. If the shear 'mismatch' $t^{\mathrm{s}}_{k,\mathrm{mism}}$ on the crack is higher than the static friction $\mu_s|t^{\mathrm{n}}_k|$ hampering the sliding of the crack faces, then the crack faces will move until a force equilibrium is reached:

$$|t^{\mathrm{s}}_{k,\mathrm{mism,new}}| = |\mu_m t^{\mathrm{n}}_k| \tag{3.58}$$

The associated change in shear crack opening displacement is given by eq. (3.54) if the simple expression

$$a^{\mathrm{s}}_k = \frac{|t^{\mathrm{s}}_{k,\mathrm{mism}}| - |\mu_m t^{\mathrm{n}}_k|}{|t^{\mathrm{s}}_{k,\mathrm{mism}}|} \tag{3.59}$$

is assumed. The associated state is called a 'reduced shear activity'.

3. The case of a zero normal load is 'critical', just as the case $|t^{\mathrm{s}}_{k,\mathrm{mism}}| = \mu_s|t^{\mathrm{n}}_k|$ is 'critical' at negative normal load. The crack opening displacement will undergo a change only if the incremental load-to-be-applied has the appropriate sign ($\Delta t^{\mathrm{n}}_k > 0$ resp. $|t^{\mathrm{s}}_{k,\mathrm{mism}} + \Delta t^{\mathrm{s}}_k| > \mu_s|t^{\mathrm{n}}_k|$).

Assuming vanishing friction ($\mu_s = \mu_m = 0$), the model can be significantly simplified: Cracks are always active with respect to the shear mode ($a^{\mathrm{s}} = 1$), whereas they may be active ($a^{\mathrm{n}} = 1$) or passive ($a^{\mathrm{n}} = 0$) with respect to the normal mode, as before. 'Mismatches' in shear tractions ('locked' shear loads resp. displacements) are not present.

3.5.2 Incremental determination of the effective load on a crack

Assessment of the 'activity' of a crack k requires the determination of the effective load $\mathbf{t}_k$ acting on it. To this end, the approach outlined in section 3.4.3, which accounts for interactions between the cracks in a deterministic arrangement, may serve as a starting point. Again, the nonlinear effects of crack closure, friction and structural changes enforce an incrementation of the formalism. Furthermore, the increments $\Delta\langle\mathbf{t}_k\rangle$ of the effective load are directly entering the expression for the crack opening displacement (eq. (3.54)).

Compared to eq. (3.41), the change of effective traction $\Delta\langle\mathbf{t}_k\rangle$ during a step of the loading loop comprises in the presence of crack closure, friction and possible structural changes several contributions:

$$\begin{aligned} \Delta\langle\mathbf{t}_k\rangle = \quad & \Delta_{(\mathrm{l})}\mathbf{t}^0_k \;+\; \boldsymbol{\Lambda}_{ki}\;\Delta\mathbf{t}_{i,\mathrm{active}} \\ + \; & \Delta_{(\mathrm{s})}\mathbf{t}^0_k \;+\; \Delta\boldsymbol{\Lambda}_{ki}\;\mathbf{t}_{i,\mathrm{active}} \end{aligned} \tag{3.60}$$

The meaning of the individual terms is:

basic terms (see also section 3.5.3):	
$\Delta_{(\mathrm{l})}\mathbf{t}^0_k$	change of traction on k due to change of 'basic' load
$\Delta_{(\mathrm{s})}\mathbf{t}^0_k$	change of 'basic' traction on k due to change of geometry of k (i.e., change of length and orientation resulting from a kinked crack extension, see section 4.1.2, p. 97)
interaction terms:	
$\boldsymbol{\Lambda}_{ki}\;\Delta\mathbf{t}_{i,\mathrm{active}}$	change of traction on k due to change of the opening displacement of any crack i
$\Delta\boldsymbol{\Lambda}_{ki}\quad\mathbf{t}_{i,\mathrm{active}}$	change of traction on k due to change of the relative geometric arrangement of k and any crack i; includes effects of crack extension and crack nucleation (additional cracks i) — see Chapter 4

Regarding the interactions, the 'active' load $\mathbf{t}_{i,\text{active}}$ is the key parameter here. The reason is that the disturbance of the stress field due to a certain crack i rather depends on its opening displacement $\mathbf{b}_i$ than on the traction $\mathbf{t}_i$, and $\mathbf{t}_{i,\text{active}}$ is proportional to $\mathbf{b}_i$ (see equations (3.49) and (3.50)).

If $\Delta\mathbf{t}_{i,\text{active}}$ in eq. (3.60) is substituted by eq. (3.51), then a 'self-consistent' system of N equations for the effective traction increments $\Delta\mathbf{t}_i$ is obtained. Collecting the terms which comprise $\Delta\langle\mathbf{t}_i\rangle$, and separating the terms independent on $\Delta\langle\mathbf{t}_i\rangle$ yields

$$(\delta_{ki}\mathbf{I} - \mathbf{\Lambda}_{ki,\text{active}})\ \Delta\langle\mathbf{t}_i\rangle = \Delta\mathbf{t}_k^{\text{sum}} \tag{3.61}$$

where

$$\Delta\mathbf{t}_k^{\text{sum}} = \Delta_{(\text{l})}\mathbf{t}_k^0 + \mathbf{\Lambda}_{ki,\text{active}}\mathbf{t}_{i,\text{mism}} + \Delta_{(\text{s})}\mathbf{t}_k^0 + \Delta\mathbf{\Lambda}_{ki}\mathbf{t}_{i,\text{active}} \tag{3.62}$$

and

$$\mathbf{\Lambda}_{ki,\text{active}} = \begin{bmatrix} (\Lambda_{ki}^{\text{nn}}\ a_i^{\text{n}}) & (\Lambda_{ki}^{\text{ns}}\ a_i^{\text{s}}) \\ (\Lambda_{ki}^{\text{sn}}\ a_i^{\text{n}}) & (\Lambda_{ki}^{\text{ss}}\ a_i^{\text{s}}) \end{bmatrix} \tag{3.63}$$

In analogy to eq. (3.43) for the simple linear conditions, the equation system (3.61) can be solved for the changes $\Delta\langle\mathbf{t}_i\rangle$ of effective crack load by numerical methods (matrix inversion):

$$\Delta\langle\mathbf{t}_i\rangle = (\delta_{ki}\mathbf{I} - \mathbf{\Lambda}_{ki,\text{active}})^{-1}\ \Delta\mathbf{t}_k^{\text{sum}} \tag{3.64}$$

The total effective load on a crack k is then obtained by

$$\langle\mathbf{t}_k\rangle = \langle\mathbf{t}_{k,\text{prev}}\rangle + \Delta\langle\mathbf{t}_k\rangle, \tag{3.65}$$

where the subscript "prev" indicates the traction in the previous step of the loading loop. Based on these effective loads $\langle\mathbf{t}_k\rangle$, the current activity factors $\mathbf{a}_k$ for all cracks can be determined.

3.5.3 Accounting for pore-crack interactions and internal pressure

The present subsection specifies the 'basic' load $\mathbf{t}_k^0$ on a crack k, which comprises all effects that are not associated with the other cracks $i \neq k$. Namely, it comprises the direct impacts of an externally applied load $\boldsymbol{\sigma}$ on crack k and possibly of a pressure P acting in crack k, and the stress disturbances 'transmitted' from pores to the crack k.

In general, the change of $\mathbf{t}_k^0$ may be attributed to changes of load (indicated here by subscript 'l'), and to changes of the geometry of the respective crack k (indicated here by subscript 's'):

$$\Delta\mathbf{t}_k^0 = \Delta_{(\text{l})}\mathbf{t}_k^0 + \Delta_{(\text{s})}\mathbf{t}_k^0 \tag{3.66}$$

Changes of the geometry of k may be due to a successive, kinked extension of k (see section 4.1.2, p. 97).

Both contributions may be considered as a superposition of four different portions (the summations extend over all pores p):

$$\begin{aligned} \Delta_{(\text{l})}\mathbf{t}_k^0 \ = \quad & \mathbf{\Lambda}_{k\infty}^{(\sigma)}\ \Delta\boldsymbol{\sigma} \ + \ \textstyle\sum_p \mathbf{\Lambda}_{kp}^{(\sigma)}\ \Delta\boldsymbol{\sigma} \\ + \ & \mathbf{\Lambda}_{k\infty}^{(P)}\ \Delta P \ + \ \textstyle\sum_p \mathbf{\Lambda}_{kp}^{(P)}\ \Delta P \end{aligned} \tag{3.67}$$

$$\begin{array}{rcccc} \Delta_{(\mathrm{s})}\mathbf{t}_k^0 & = & \Delta\boldsymbol{\Lambda}_{k\infty}^{(\sigma)}\,\boldsymbol{\sigma} & + & \sum_p \Delta\boldsymbol{\Lambda}_{kp}^{(\sigma)}\,\boldsymbol{\sigma} \\ & + & \Delta\boldsymbol{\Lambda}_{k\infty}^{(P)}\,P & + & \sum_p \Delta\boldsymbol{\Lambda}_{kp}^{(P)}\,P \end{array} \tag{3.68}$$

The transmission coefficients $\boldsymbol{\Lambda}_{k\infty}^{(\sigma)}$ denote the direct change of load on crack k due to a unit change of external stress $\boldsymbol{\sigma}$. In a matrix notation (Voigt notation),

$$\Delta\mathbf{t}_k = \begin{bmatrix} \Delta t_k^{\mathrm{n}} \\ \Delta t_k^{\mathrm{s}} \end{bmatrix} = \boldsymbol{\Lambda}_{k\infty}^{(\sigma)} \begin{bmatrix} \Delta\sigma_{xx} \\ \Delta\sigma_{yy} \\ \Delta\sigma_{xy} \end{bmatrix} \tag{3.69}$$

with

$$\boldsymbol{\Lambda}_{k\infty}^{(\sigma)} = \begin{bmatrix} \sin^2\theta_k & \cos^2\theta_k & -2(\sin\theta_k)(\cos\theta_k) \\ -(\sin\theta_k)(\cos\theta_k) & (\sin\theta_k)(\cos\theta_k) & \cos^2\theta_k - \sin^2\theta_k \end{bmatrix}, \tag{3.70}$$

where θ_k is the orientation angle of crack k (see equations 3.35 and 3.36, p. 72).

The transmission coefficients $\boldsymbol{\Lambda}_{k\infty}^{(P)}$ denote the direct change of load on crack k due to a unit change of internal pressure P:

$$\begin{bmatrix} \Delta t_k^{\mathrm{n}} \\ \Delta t_k^{\mathrm{s}} \end{bmatrix} = \boldsymbol{\Lambda}_{k\infty}^{(P)}\Delta P \tag{3.71}$$

with

$$\boldsymbol{\Lambda}_{k\infty}^{(P)} = \begin{bmatrix} m_k \\ 0 \end{bmatrix}, \tag{3.72}$$

where m_k indicates whether crack k is under pressure ($m_k = 1$) or not ($m_k = 0$). Self-evidently, crack-internal pressure is equivalent to an additional normal tensile load.

The transmission coefficients $\boldsymbol{\Lambda}_{kp}^{(\sigma)}$ relate the change of external stress $\boldsymbol{\sigma}$ on pore p to the change of load on crack k, i.e. they represent the pore→crack transmission coefficients. Correspondingly, the $\boldsymbol{\Lambda}_{kp}^{(P)}$ relate the change of pressure P inside pore p to the change of load on crack k. Each of these coefficients can be numerically determined from the analytical stress solutions presented in section 3.3.

3.5.4 Local stress analysis

The basic load $\mathbf{t}_f^0$ on any line element f located in the solid structure can be determined in exact analogy to the basic load $\mathbf{t}_k^0$ on a crack k as outlined in the previous subsection 3.5.3. In fact, the situation is easier here since a selected line element will not change its geometry, so that the second term ($\Delta_{(\mathrm{s})}\mathbf{t}_k^0$) in eq. (3.66) vanishes.

The complete traction on the line element f is composed of the basic load $\mathbf{t}_f^0$ and the load 'transmitted' from the cracks:

$$\langle\mathbf{t}_f\rangle = \mathbf{t}_f^0 + \boldsymbol{\Lambda}_{fk}\mathbf{t}_{k,\mathrm{active}}, \tag{3.73}$$

where $\boldsymbol{\Lambda}_{fk}$ denotes the transmission factors [crack k] → [line element f], and $\mathbf{t}_{k,\mathrm{active}}$ is associated with the actual opening displacement of crack k (see eq. (3.49)).

Equation (3.73) is suitable for two points: On the one hand, the line element f may refer to a facet, so that the loading conditions on the network of grain boundaries are determined. On the other hand, one may cover the solid phases of the material structure with a mesh of small horizontal and vertical line elements; determination of $\langle\mathbf{t}_f\rangle$ for any of these line elements then yields a numerical representation of the complete local stress field in the material.

3.5.5 Determination of macroscopic elastic properties

Overall strain. In extension to eq. (3.30), the average strain over a representative area A may be decomposed into the contribution of the compact solid material ($\boldsymbol{\epsilon}_0$), the contributions of each individual crack ($\boldsymbol{\epsilon}_k$), and the contributions of each individual pore ($\boldsymbol{\epsilon}_p$):

$$\boldsymbol{\epsilon} = \boldsymbol{\epsilon}_0 + \sum_k \boldsymbol{\epsilon}_k + \sum_p \boldsymbol{\epsilon}_p \tag{3.74}$$

The summations extend over all cracks k and pores p located in the range of A. The determination of the strain contributions $\boldsymbol{\epsilon}_0$ and $\boldsymbol{\epsilon}_k$ has already been described in section 3.4.2. Accounting for crack closure and friction requires, however, to replace the actual tractions $\mathbf{t}_k$ by the 'active' tractions $\mathbf{t}_{k,\text{active}}$, since the latter are proportional to the crack opening displacement (eq. 3.49):

$$\boldsymbol{\epsilon}_k = \frac{\pi}{2AE'}\, l_k^2\, (\mathbf{n}_k \mathbf{t}_{k,\text{active}} + \mathbf{t}_{k,\text{active}} \mathbf{n}_k) \tag{3.75}$$

The contributions of the pores may be due to prescribed stresses $\boldsymbol{\sigma}$ as well as prescribed internal pressure P:

$$\boldsymbol{\epsilon}_p = \mathbf{C}_p\, [\boldsymbol{\sigma} + P\, \mathbf{I}] \tag{3.76}$$

$\mathbf{C}_p$ denotes the contribution of pore p to the compliance tensor; it can be determined from the cavity compliance tensors mentioned in section 3.2.3 (p. 58).

If there is a gradient of pressure across the considered area A, or if some of the pores are not under pressure (closed porosity), then a pore-specific pressure P_p can be introduced.

Effective elastic compliance. For the nonlinear systems involving crack closure, friction and structural changes, the effective elastic compliance $\mathbf{C}$ is a function of current load and the history of applied load. Consequently, the constitutive law must be formulated incrementally:

$$\Delta\boldsymbol{\epsilon} = \mathbf{C}\ (\Delta\boldsymbol{\sigma}) + (\Delta\mathbf{C})\boldsymbol{\sigma} \tag{3.77}$$

In the discrete numerical algorithm, one may assume the increment $\Delta\boldsymbol{\sigma}$ of prescribed stress to be sufficiently small so that $\Delta\mathbf{C}$ is momentarily equal to zero. The current effective compliance can then be decomposed into the contribution of the compact solid material ($\mathbf{C}_0$), the contributions of each individual crack ($\mathbf{C}_k$), and the contributions of each individual pore ($\mathbf{C}_p$):

$$\mathbf{C} = \mathbf{C}_0 + \sum_k \mathbf{C}_k + \sum_p \mathbf{C}_p \tag{3.78}$$

While the contributions $\mathbf{C}_0$ and $\mathbf{C}_p$ are not difficult to find, the particular task here is to determine the crack contributions $\mathbf{C}_k$. This can be accomplished with the incremental version of eq. (3.75):

$$\Delta\boldsymbol{\epsilon}_k = \frac{\pi}{2AE'}\, l_k^2\, (\mathbf{n}_k \Delta\mathbf{t}_{k,\text{active}} + \Delta\mathbf{t}_{k,\text{active}} \mathbf{n}_k) \tag{3.79}$$

The components of the respective crack contribution $\mathbf{C}_k$ to the compliance tensor can be found from eq. (3.79) if $\Delta\mathbf{t}_{k,\text{active}}$ is substituted by eq. (3.51), $\Delta\langle\mathbf{t}_k\rangle$ is then substituted by eq. (3.64), $\Delta\mathbf{t}_k^{\text{sum}}$ is then substituted by eq. (3.62), and $\Delta_{(\text{l})}\mathbf{t}_k^0$ is finally substituted by eq. (3.67): In the end, a relation between $\Delta\boldsymbol{\epsilon}_k$ and $\Delta\boldsymbol{\sigma}$ is obtained, and the individual coefficients establish the elements of $\mathbf{C}_k$. The explicit terms are completely implemented in the computer program and are thus accounted for in the numerical calculations.

3.6 On the significance of cavity interactions

The micromechanical models presented in sections 3.4 and 3.5 account for crack↔crack interactions, and the nonlinear micromechanical model presented in section 3.5 additionally accounts for the impact of pores on cracks ('pore→crack interactions'). It is assumed that the presence of cracks does not affect appreciably the deformation behaviour of the pores: 'crack→pore interactions' are completely neglected.

The effect of the interactions between micro-cavities depends on their respective locations and orientations, on the specific loading conditions, the cavity density, the cavity shapes, and on the relative cavity sizes. It is important to distinguish the impact of the interactions on the macroscopic elastic properties and the impact of the interactions on the microscopic stresses: The macroscopic effects may remain negligible, while at the same time fluctuations of the microscopic stresses can be considerably intensified. The consequences of those microscopic fluctuations for the damage behaviour of the material may be substantial, but this point is to be discussed later (in Chapter 4).

'Biased' cavity distributions. Compare a model structure where cavity interactions are present, and the same model structure when the cavity interactions are absent. As soon as the locations and orientations of the cavities (in particular, cracks) tend to form a parallel and 'stacked' arrangement (widely separated stacks of closely located parallel cracks), the presence of the interactions enhances the material stiffness perpendicular to the arrangement. On the other hand, if the arrangement is more 'columnar' (widely separated rows of closely located collinear cracks), then the presence of the interactions reduces this stiffness. [43]

The computational model has been utilized to illustrate this phenomenon. As an example, fig. 3.18 (left) shows two specimens of equal size, either of them including 20 parallel cracks of equal length. A uniaxial tension perpendicular to the crack faces has been applied to the specimens. In a calculation without interactions, the stiffness of the specimens reduced by 35 % with respect to the undamaged material, independently on the explicit crack arrangement. In contrast, the reduction of stiffness amounted to 19.5 % for the 'stacked' arrangement of the cracks, and to 40 % for the 'columnar' arrangement of the cracks. Similar observations have been made for configurations including both cracks and pores (see fig. 3.18, right).

An important fact to point out here is that the presence of pores may locally reverse the mode of applied load: Figure 3.19 illustrates how a crack in the vicinity of a pore may be under compression while the pore is under external tension, and vice versa. This issue can be understood with the aid of the stress field plots for pores (section 3.3). For the particular configuration, the stress disturbance 'transmitted' by the pore is the only load acting on the crack.

Random cavity distributions. The impact of crack-crack interactions on the effective stiffness in a random crack distribution is controversely assessed in the literature. In the effective continuum theories such as the self-consistent scheme and the differential scheme, interactions generally augment the reduction of stiffness, a result which is confirmed by more extensive approaches by Ju and Chen (see eq. (3.13)) or Huang et al. [31], and by percolation theory. In contrast, there are second-order models which predict that "the

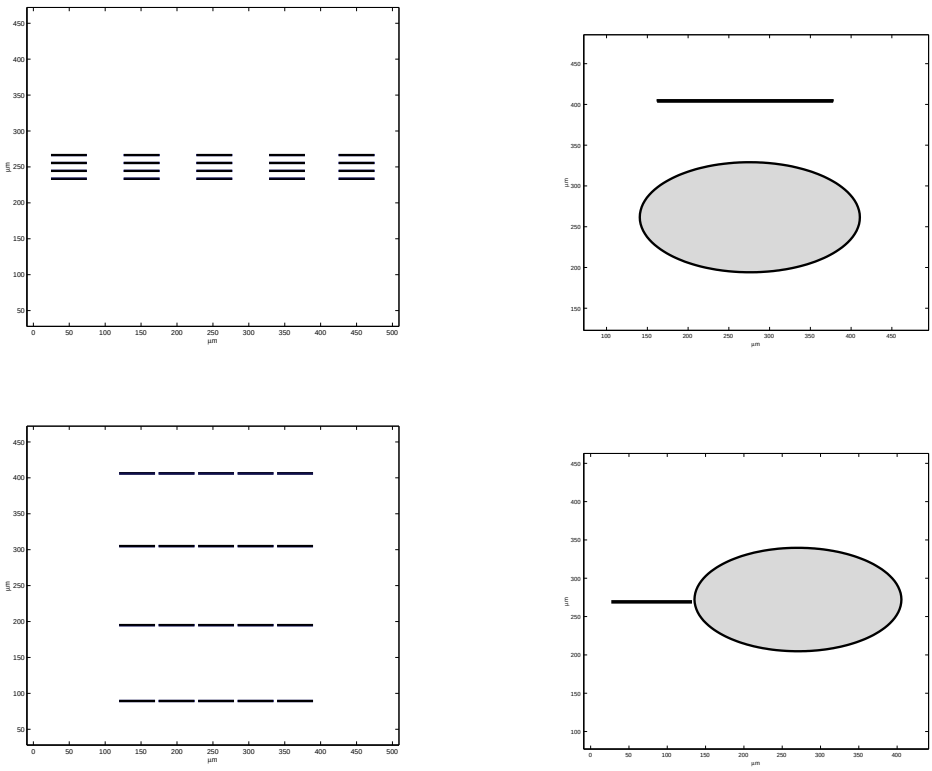

Figure 3.18: Interactions in a 'stacked' arrangement of cracks or cracks and pores (above) reduce, interactions in a 'columnar' arrangement of cracks or cracks and pores (below) enhance the influence of the cracks on the overall elastic moduli.

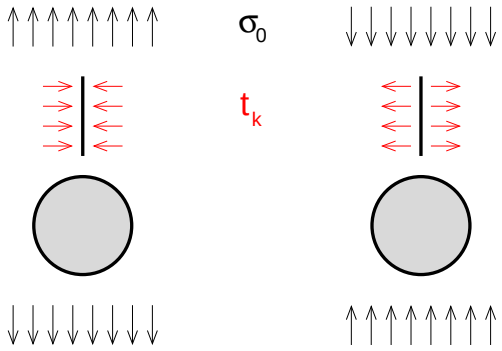

Figure 3.19: A simple pore/crack configuration where an external vertical tension results in a horizontal compression on the crack (left), and where an external compression results in a horizontal tension on the crack (right).

effect of interactions on the effective stiffness is on the balance amplifying" (as reported by Krajcinovic [48])!

On the other hand, it seems reasonable that in a perfectly random crack distribution the competing effects of stress shielding and stress amplification due to direct crack interactions "cancel each other out rendering the results of the computer simulations practically indistinguishable from the dilute concentration estimates" [48]. This point of view is supported by a number of extensive computer experiments (cf. [41]), and it is in ac-

cordance with Mori-Tanaka's scheme, too (see section 3.2.2). Kachanov [43] ascertains the approximation of non-interacting cracks to remain accurate up to high crack densities ($\rho \to 0.35$).

A *perfect* randomness is the prerequisite here. Placing slight constraints on the spatial crack distribution — e.g., if crack centers are not allowed to be inside the circles drawn around the other cracks — suffices to cause a 'bias' of the crack model and to make the approximation of non-interacting cracks inappropriate [43]. But it is important to note that a perfect randomness of the crack locations is "not always the case in naturally occuring crack systems" [43]. For example, crack arrangements resulting from uniaxial external tension are anything but random (see Chapter 4).

The semi-numerical model introduced in the present thesis has been employed to calculate the impact of interactions of cracks randomly distributed in a 'distorted honeycomb facet grid' (fig. 3.20, left). The computations show that the interactions slightly reduce the effective stiffness of the material (fig. 3.20, right). This result indicates that the crack distribution is slightly 'biased' towards a columnar arrangement. The crack distribution is not perfectly random in the experiment, since the cracks are constrained to the honeycomb facet grid.

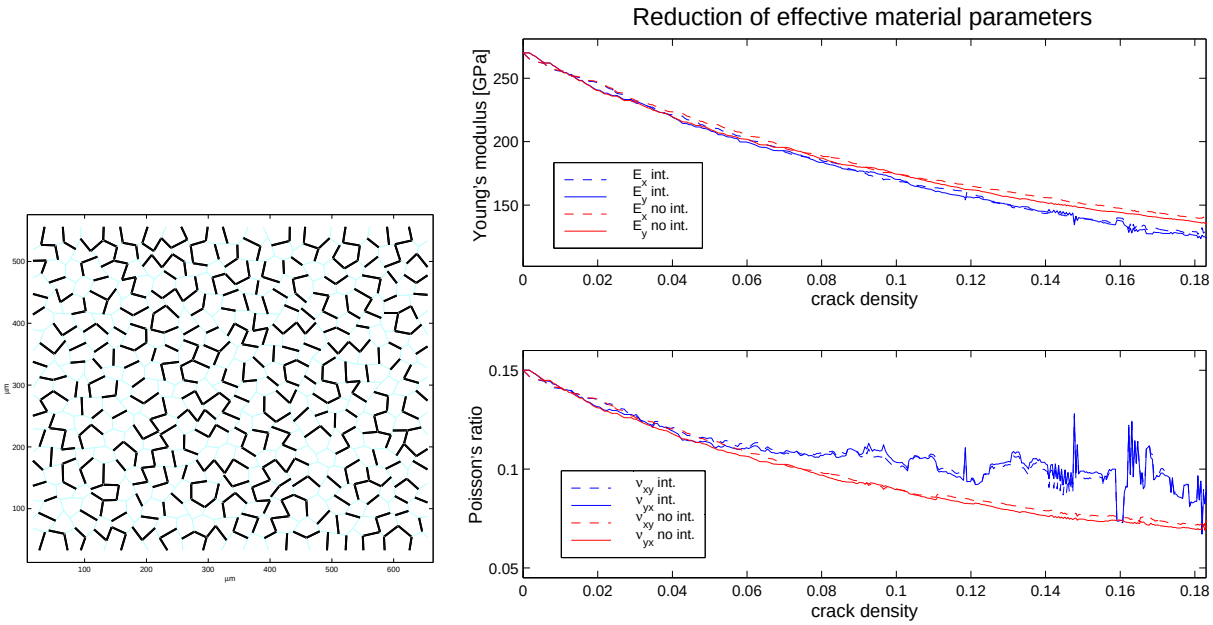

Figure 3.20: Left: ultimate, 'random' crack structure resulting from a model computation. Each line is regarded as an individual crack. It is assumed that there are only fully active cracks (as appearing under biaxial tension). Right: evolution of Young's modulus and Poisson's ratio with increasing crack density.

A numerical study with fluid pressure. To take another example, consider a large section of a material with pores, subject to internal fluid pressure (fig. 3.21, left). The material specimen exhibits a pattern of distributed cracks which might have originated in the presence of a chemically aggressive (corrosive) fluid. The cracks are emanating from the pores. In order to study the effects of cavity interactions, the geometric structure is simplified: for the stress analysis, the pores and pore-crack combinations are substituted

by simple cracks (fig. 3.21, right). This approach leads to a coarser flaw pattern where the micromechanical model introduced above can be employed.

Applying an internal fluid pressure of $P = 150$ MPa, extensive computations based upon the full stress solutions for cracks (fig. 3.6) yield the local stress distributions illustrated in fig. 3.22. What differentiates the calculations with cavity interactions from those without is the local fluctuation of stress, as mentioned above: The plots for stress interactions clearly show areas of higher tensile, compressive and shear loads. Mention should also be made of the fact that in the interactive calculation 15 % of the cavities are under compression (i.e., 'closed'), whereas the non-interactive calculation naturally cannot display this effect.

Regarding the macroscopic parameters, it appears that the interactions enhance the material stiffness: The horizontal stiffness amounts to $E_x = 130.8$ MPa for interactions and $E_x = 125.7$ MPa for no interactions, while the vertical stiffness amounts to $E_y = 123.3$ MPa for interactions and $E_y = 121.7$ MPa for no interactions.

The overall strain components are:

	ϵ_{xx}	ϵ_{yy}	ϵ_{xy}
with interactions	0.0007	0.0008	0.0006
without interactions	0.0006	0.0007	0.0003

Obviously, neglection of interactions leads to an underestimation of the strains in the present example.

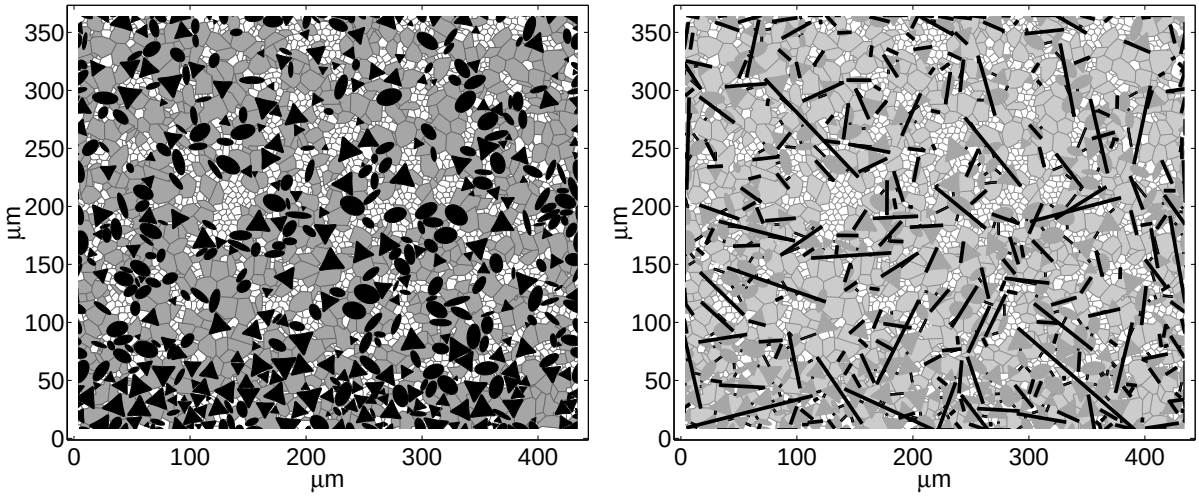

Figure 3.21: An extensive microstructure in the undamaged state (left), and with a multitude of microcracks (right; crack density $\rho = 0.38$). The pore-crack combinations in the figure on the right are approximated by single larger cracks, respectively.

Conclusion. As for the effective stiffness and overall strain, the impact of cavity interactions is negligible if the cavities are randomly distributed. If the cavities exhibit a preferred orientation and the mutual positioning of the cavities is 'biased' at the same time, then the effect of the interactions may be of an augmenting or of a degrading type.

As for the microscopic stresses, the cavity interactions are generally important, since they intensify the local fluctuations.

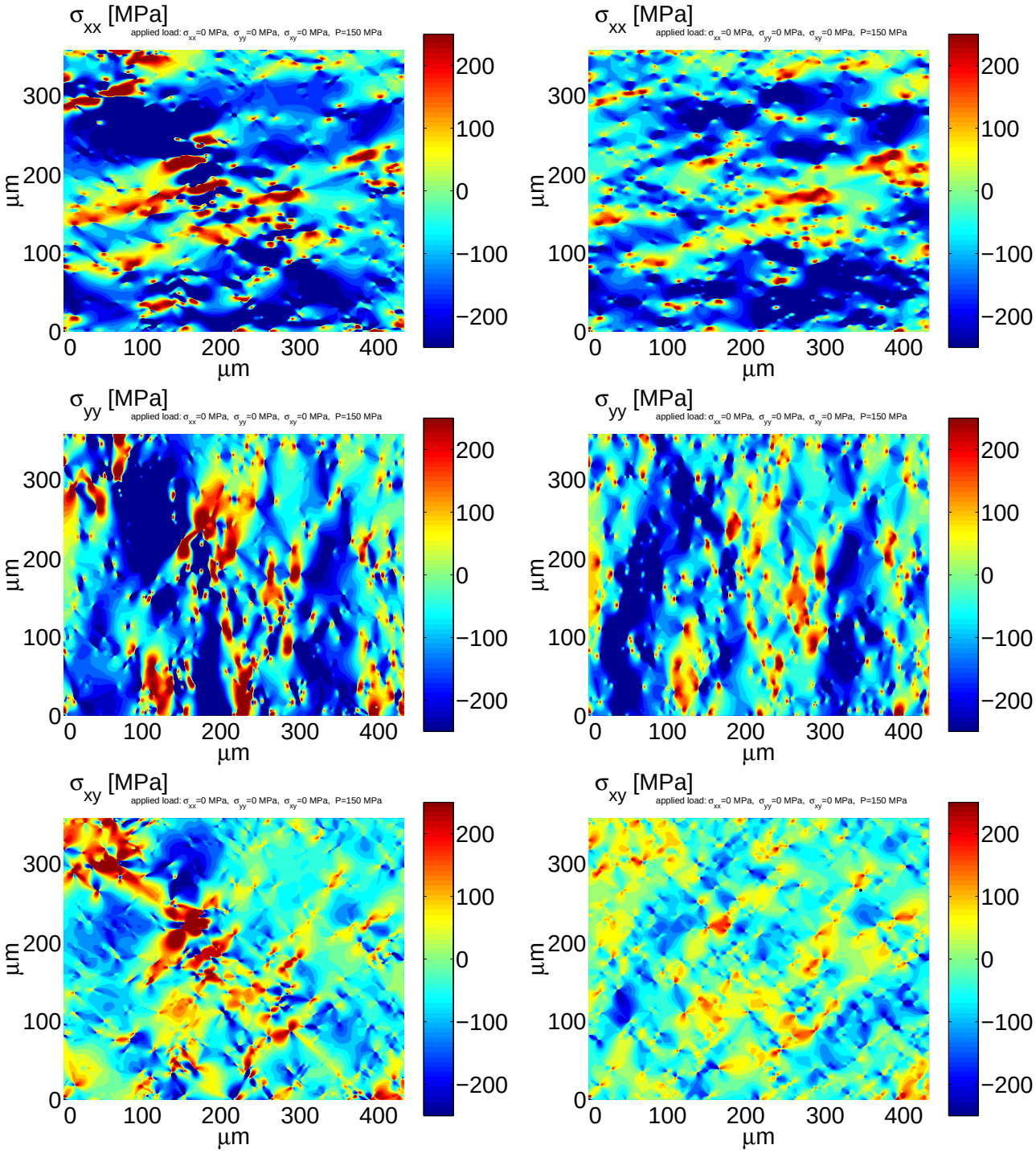

Figure 3.22: Local stress distribution in the microstructure with flaws (approximated by cracks) under internal pressure $P = 150$ MPa (fig. 3.21, right). Left column: calculation with interactions. Right column: calculation without interactions.

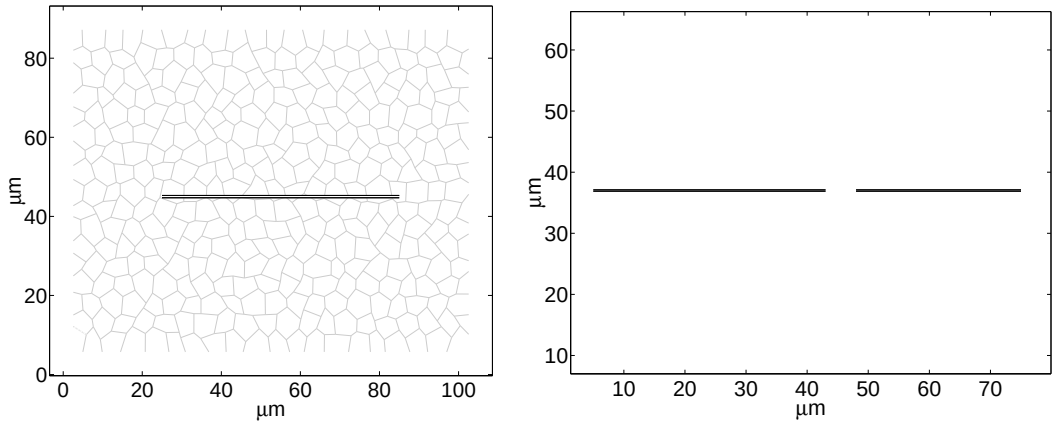

Figure 3.23: Simple model specimens comprising one resp. two facets or cracks.

3.7 Selected studies on the stress-strain response

As another application of the micromechanical theory introduced in the present chapter, the stress-strain behaviour of some exemplary structures under tension, shear and compression is to be examined now. Even if the structures are absolutely simple (comprising just one or two cracks), they reveal nevertheless a great variety of features in the context of crack closure and friction. For obvious reasons, the present studies already include the issue of fracturing: The occurence of crack nucleation represents another nonlinear effect which can clearly be monitored in the stress-strain diagrams, and it thus completes the current account.[15]

At the same time, the numerical studies help to check for the correct implementation of the background theory within the computer algorithm. It has been observed that the considered loading cycles are very sensitive to errors in the program code. A main condition to be preserved is that the stress-strain curves return to the origin as soon as the applied load is removed, no matter how complex the loading cycle and how large the number of incremental steps in the computer algorithm. (This condition holds since the model does neither account for permanent interlocks nor for thermal residual stresses.) Generally, the area enclosed by closed loops in the σ-ϵ-space equals half of the total elastic energy per unit volume, which is lost by frictional sliding and irreversible rearrangements of the structure.

The first example, presented in fig. 3.24, addresses the effect of fracturing on the stress-strain response, and the significance of interactions on the overall strain. The model specimen initially comprises two horizontally aligned facets (fig. 3.23, right), which successively fail under a tensile load (step 1). The initially high slope of the curve reduces to a much weaker slope in the damaged specimen. According to the 'columnar' arrangement of the facets/cracks, the crack interaction promotes the fracturing and augments the overall strain. The weaker slope of the stress-strain curve is maintained until the tensile load decreases to zero.

A similar study has been performed on a more complex microstructure where many microcracks arise in the course of step 1. Figure 3.25 shows the stress-strain diagram

[15] Concerning the theoretical fundamentals for crack nucleation, see the next chapter (section 4.1).

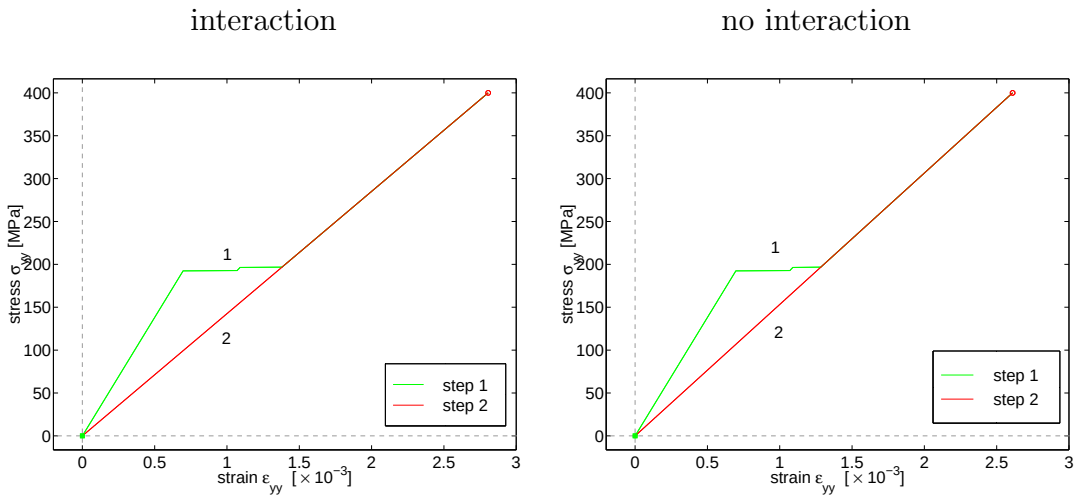

Figure 3.24: Stress-strain diagram of a two-facet specimen (fig. 3.23, right), subject to external vertical tension (step 1). The cracks arise in the course of step 1; step 2 corresponds to release of external tension. Left chart: calculation with interactions (crack→facet, crack↔crack). Right chart: calculation without interactions.

where step 2 not only releases the tensile load but alternates to a compressive one. At the point where the origin is traversed, the modulus of the damaged material is restored to the undamaged value. A strong enhancement of the compressive load during step 2 may lead then to *damage in compression* and a nonlinear curve even in the range of negative stress/strain, but this is not shown here.

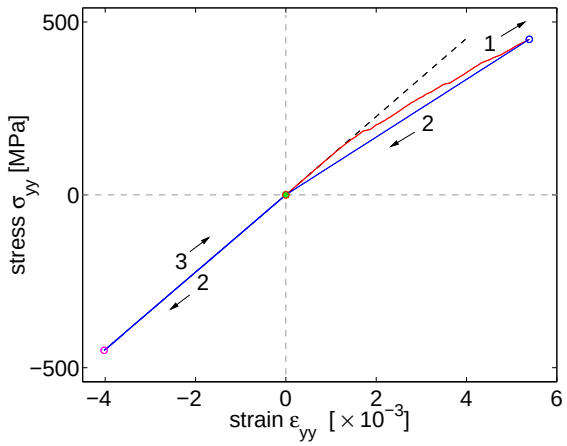

Figure 3.25: Nonlinear stress-strain curve of a complex microstructure, progressively fracturing under tension: step 1 increases the tensile load, step 2 changes from tensile to compressive load, step 3 removes the loading (relaxation). The dashed line refers to the pristine material under tension (absence of fracturing).

The remaining part of the subsection is dedicated to a more extended stress-controlled loading cycle (fig. 3.26) imposing shear load and compression, so that the 'mismatch' effect (i.e., temporarily locked microcracks) is encountered.

The loading cycle is first applied to a single-facet specimen (fig. 3.27): The facet

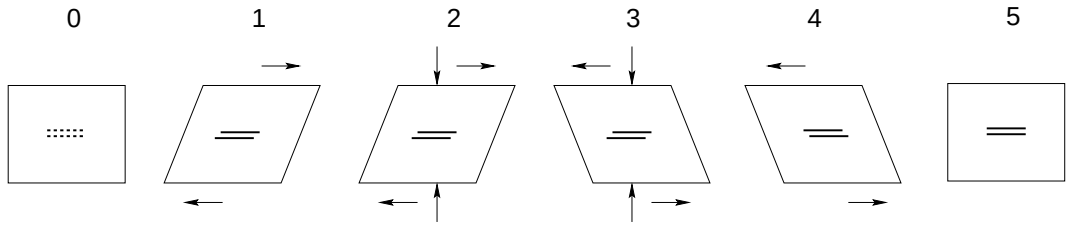

Figure 3.26: Illustration of the shear/compression loading cycle underlying the studies in figures 3.27 to 3.31.

fails under the shear load applied in step 1. Superposition of a normal compressive load (step 2) provides that the shear opening mode of the crack is retained when the shear load is removed and reversed (step 3). Step 3 comes along with an increasing mismatch between crack opening and load acting on the crack; the value of static friction ($\mu_s|t^n|$) decides on the maximum mismatch that can build up. If the maximum is exceeded, then the crack faces yield to the shear: under the present *quasistatic* conditions, they abruptly start to slide and thus reduce the mismatch. The sliding stops right afterwards when the mismatch and the sliding friction ($\mu_m|t^n|$) are in equilibrium again. For a moderate friction, several such processes string together in the course of step 3, leading to a remarkable staircase-like curve (fig. 3.27, left).[16] In case of very high friction (i.e., large compression and/or high coefficient of static friction), the moving of the crack faces is totally suppressed until the compressive load is released in step 4 (fig. 3.27, right).

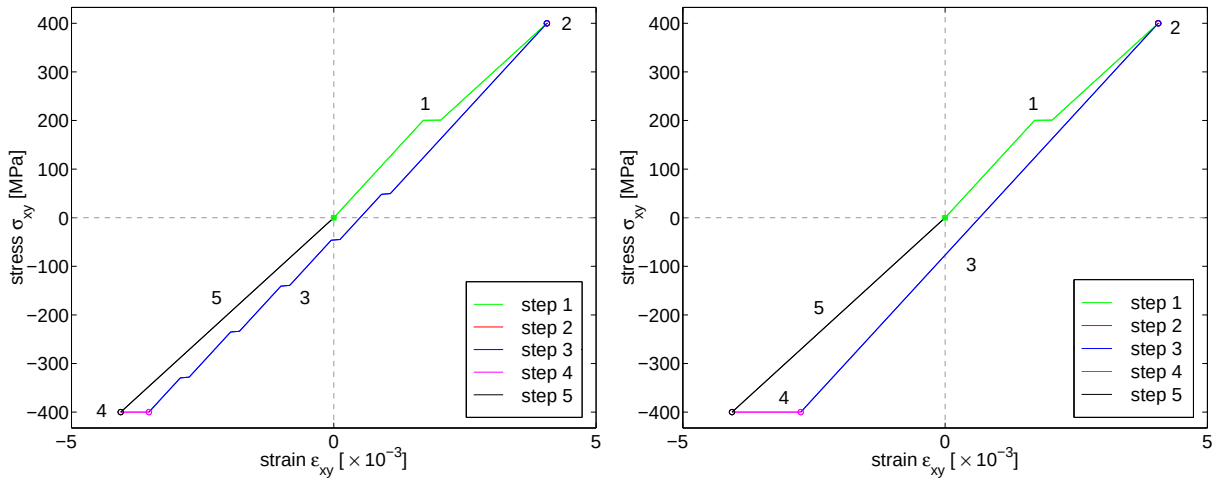

Figure 3.27: Single facet specimen (fig. 3.23, left) subject to the shear/compression cycle illustrated in fig. 3.26. The facet cracks in the course of step 1. Left: stress-strain response in case of moderate friction (the crack faces start moving in the course of step 3). Right: stress-strain response in case of high friction (the crack faces do not move throughout step 3).

Similar observations can be made for a two-facet specimen, including interaction effects (fig. 3.28). A variation of the friction coefficients points out here that the uneasy course of

[16] It should be emphasized that the staircase-like course at step 3 does not depend on the width of the load increments.

step 3 is indeed a consequence of the discrepancy in the coefficients of static friction and sliding friction: If both coefficients are assumed to be equal, then the mismatch vanishes immediately when it exceeds the friction. The figure also illustrates that no mismatch will arise in case of zero friction, while in case of very large friction the mismatch reaches its maximum at the end of step 3.

Figure 3.29 confirms that the model works for a specimen comprising two oblique facets as well, and fig. 3.30 illustrates the same for complex defect configurations comprising crack↔crack and pore→crack interactions. As intended, the model calculations end in a zero strain when the applied stresses are removed. Regarding fig. 3.30, corresponding calculations neglecting the interactions showed no observable effects at this scale; this is in accordance to the random locations of the defects. Figure 3.31 supplements the macroscopic stress-strain diagrams in fig. 3.30 by plots of the microscopic stresses σ_{xy} at the end of the individual loading steps.

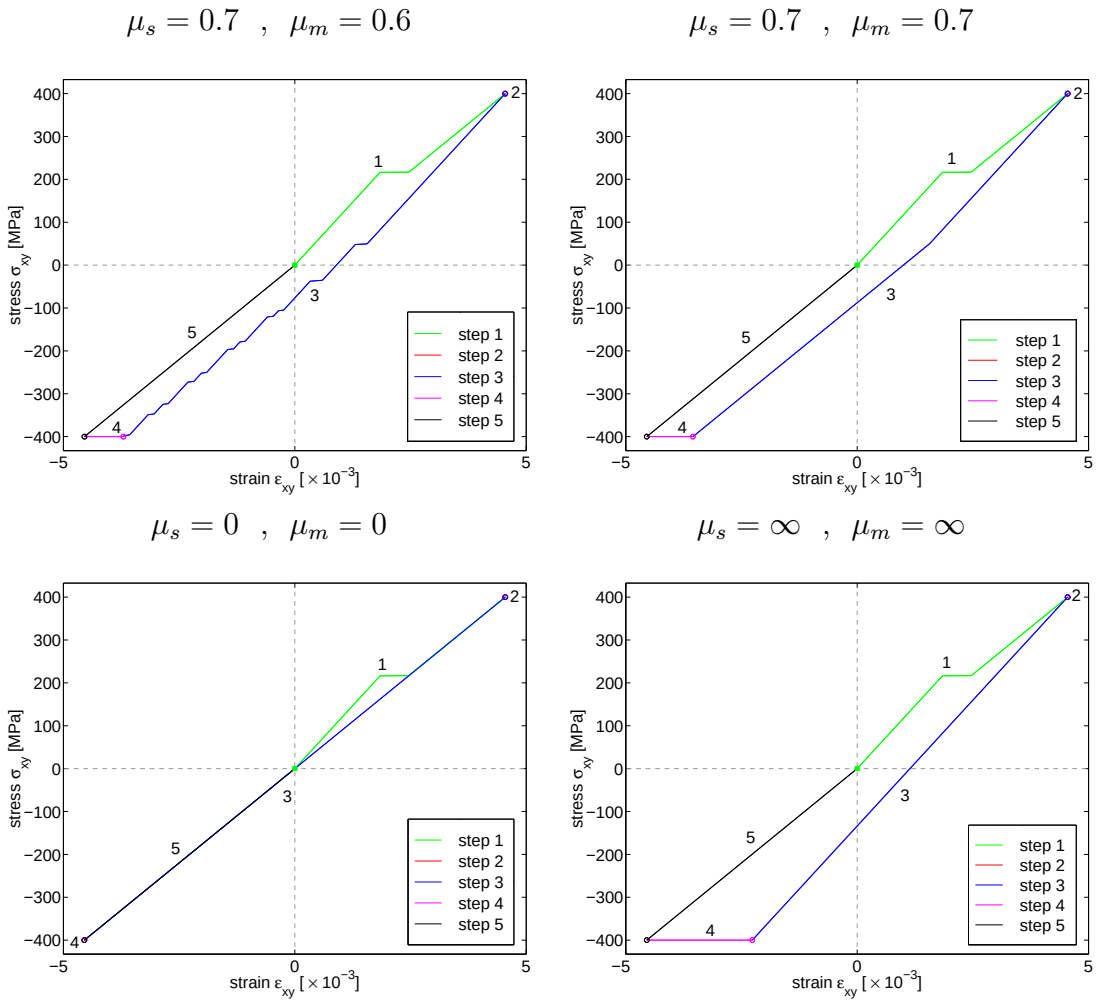

Figure 3.28: Two-facet specimen (similar to fig. 3.23, right), subject to the shear/compression cycle illustrated in fig. 3.26. Investigation of friction conditions: moderate friction ($\mu_s = 0.7$, $\mu_m = 0.6$; above, left), moderate friction ($\mu_s = 0.7$, $\mu_m = 0.7$; above, right), zero friction (below, left), sticking (below, right).

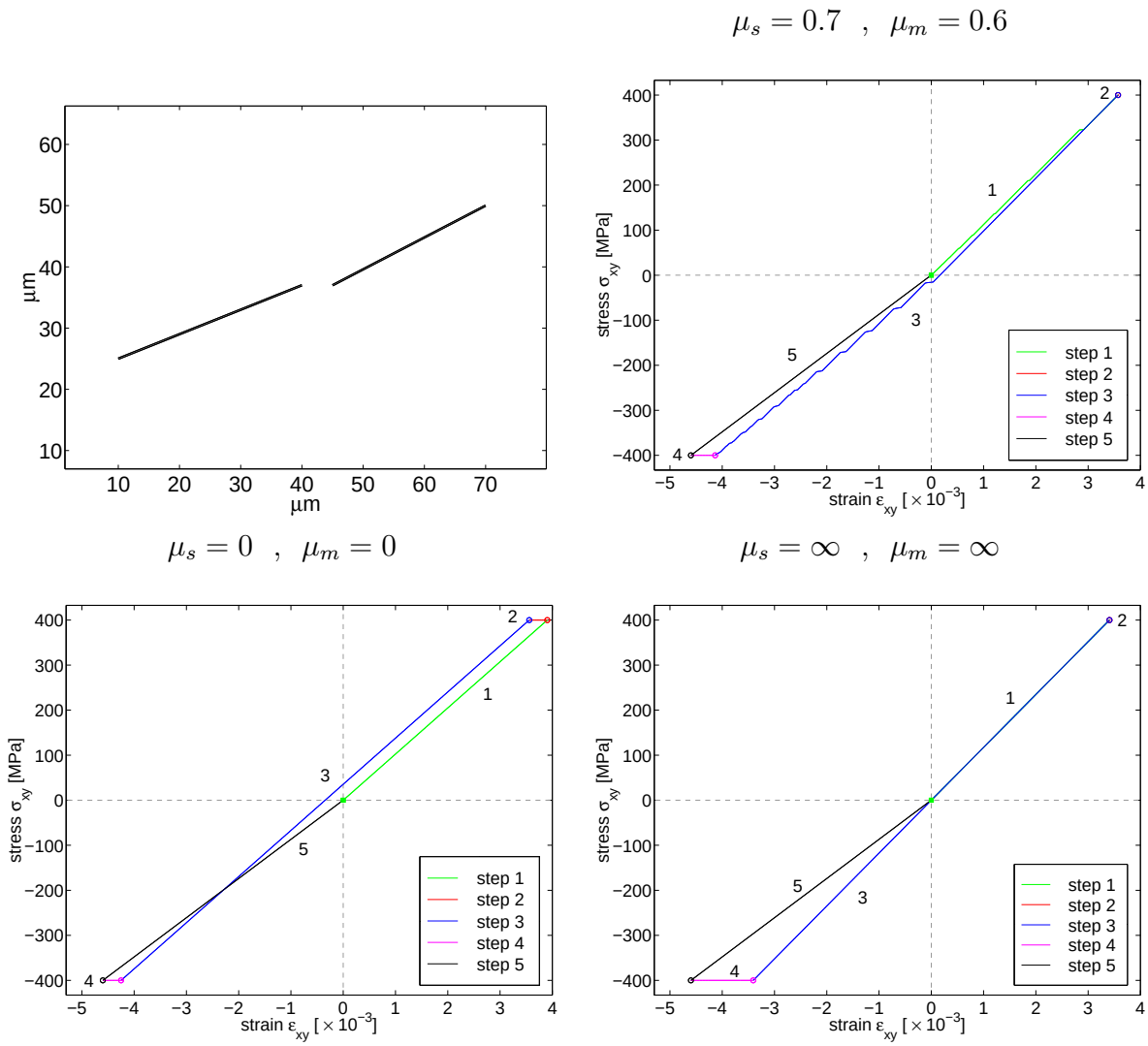

Figure 3.29: Model specimen comprising two oblique cracks, subject to the shear/compression cycle illustrated in fig. 3.26. Investigation of friction conditions: moderate friction (above, right), zero friction (below, left), sticking (below, right). In the latter example, the cracks do not arise until step 4 (shear upon release of compression).

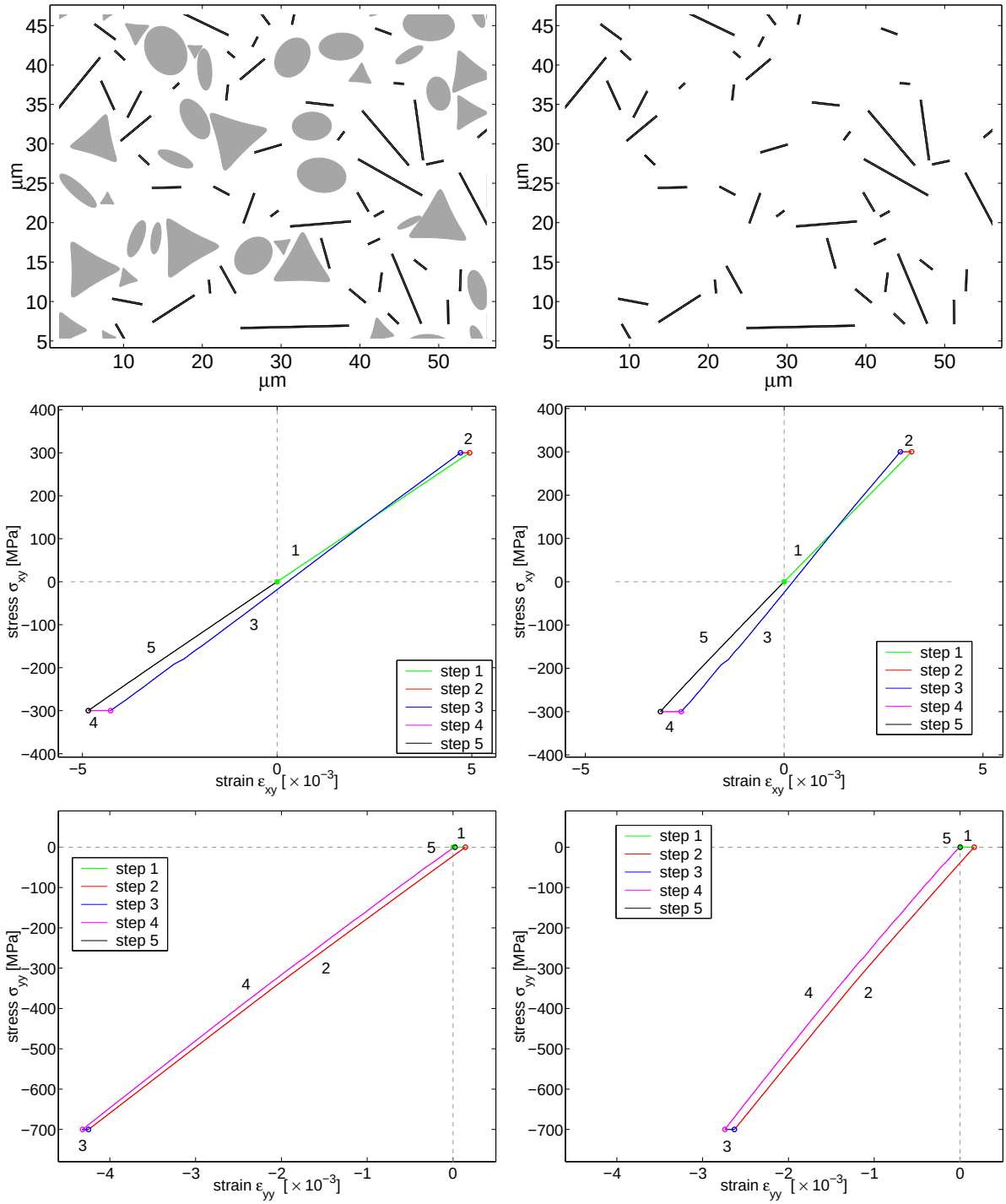

Figure 3.30: Stress-strain response of a microstructure with pores and cracks (left column) and microstructure with cracks only (right column) when exposed to the shear/compression cycle illustrated in fig. 3.26. Moderate friction.

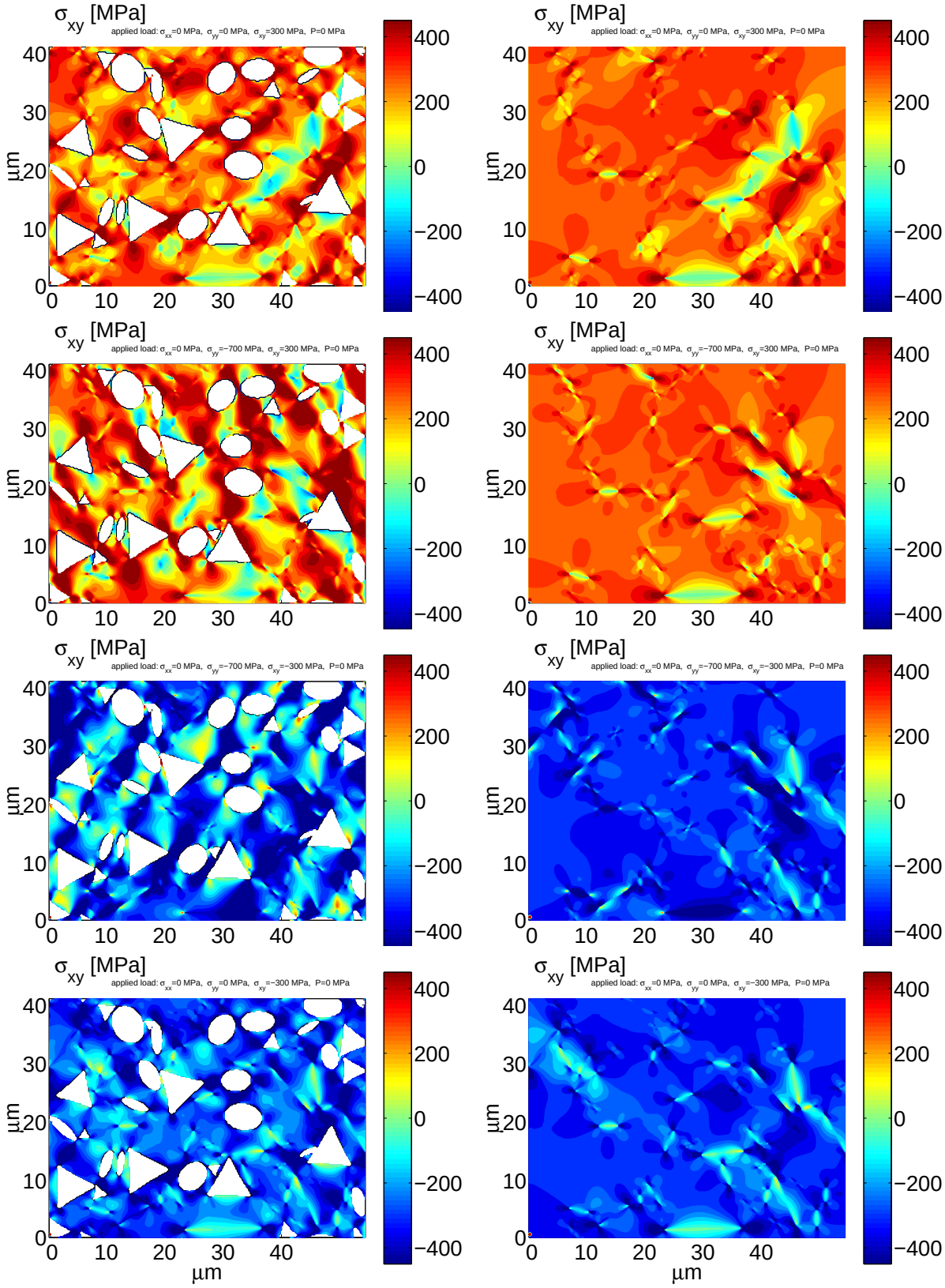

Figure 3.31: Corresponding to fig. 3.30: Local σ_{xy} stresses in a microstructure with pores and cracks (left column), and in a microstructure with cracks only (right column) when exposed to the shear/compression cycle illustrated in fig. 3.26. Upper row: stresses at the end of step 1. Second row: stresses at the end of step 2. Third row: stresses at the end of step 3. Lower row: stresses at the end of step 4.

Chapter 4

Microcrack nucleation and progressive damage in compact solids

The non-local formalism for the microscopic stress fluctuations established in the previous chapter is of fundamental importance now where the simulation of crack nucleation and damage progression is addressed. For it is obvious that averaged properties and macroscopic parameters cannot suffice to describe the evolution of microcracks from the very beginning. The actual local stress distributions are needed instead, together with the local strength of the solid-phase texture.

As elaborated in the previous chapter, the local stresses are governed by the disturbance fields of existing, interacting cavities and cracks. On the other hand, the local material strength is dominated by microscopic inhomogeneities associated with the disorder of the grain structure. To be exact, crack initiation and evolution is assumed to be dictated by the grain *boundaries*. This assumption bases on several facts:

Firstly, grain boundaries are interfaces between two differently-oriented systems. Along the interfaces, the atoms are in irregular positions, and the cohesive forces between them deviate from those in the interior of the grains. The specific surface energy between two grains reduces with increasing difference in the orientation angle of the crystallographic planes. Hence it usually is easier to cause *inter*granular ruptures than transgranular cleavages [29] (*intra*granular cracks).

Secondly, it has been observed that during sintering, the impurities on the surface of the powder move into the boundaries of the grains. "The impurities tend to gather in the grain boundaries where they form amorphous films which are fractured more easily than the crystalline grains" [29].

Another important point is the discrete nature of fracturing in a granular structure, which emerges from experimental experience. The observation refers to both nucleation and extension of defects at the microscopic level. In order for an existing defect (pore or crack) to propagate, "it is not sufficient that the stress reaches the critical value σ_c at the tip of the indentation, but it must exceed this value over a certain minimum distance, for example the length of a grain" [29]. Due to this insight, the present simulations assign the smallest unit of microcracking to the facet length.

The present chapter is concerned with microcracking in compact granular structures. The tentative restraint on compact structures enhances the tractability and clarity of the exploration here, whereas microcracking in the presence of pores involves essential

peculiarities and thus calls for modified strategies (see the subsequent Chapter 5).

First of all, section 4.1 introduces the basic fracture criterion employed in the model, which relies on energy considerations. The criterion is first formulated for the simple case of tensile or shear load on a single facet, then extended with respect to compressive load, friction effects, kinked crack extension and coalescence of cracks.

Section 4.2 provides some general considerations on the modes of damage evolution, which are somewhat characteristic for the different loading conditions. The manifestations of damage comprise a wide spectrum in between unstable propagation of a single defect and quite distributed, stable microcracking. Moreover, it will be demonstrated how interactions are responsible for the phenomenon of localization encountered at high stresses.

Section 4.3 concentrates on the stochastic features of microcracking in ensembles of macroscopically identical specimens. A brief introduction to some fundamental terms in statistics is followed by test series from different points of view. These Monte Carlo simulations illustrate the effect of microscopic disorder on the scattering and the expectation values of the individual tests. Emphasis is on microcracking under compressive loads.

The chapter is concluded by an attempt to establish a continuum model for evolutionary damage (section 4.4). The formalism utilizes the basic, micromechanical approaches on fracture (section 4.1) and homogenization (section 3.4.2), but does not demand a numerical, discrete input information on the structure.

4.1 Energy criterion for damage nucleation and progression

The formation of a new crack (crack nucleation) or the lengthening of an existing crack (crack extension) involves transformation of elastic energy to surface energy: The release of strain energy stored in the material is associated with an increase of surface energy. A crack will not propagate or nucleate if the elastic energy released by its growth is less than the energy required to create the pair of new surfaces.

In the numerical simulation, fracturing is assumed to occur in discrete steps: individual grain facets fail at once. Accordingly, crack nucleation as well as crack extension are measured in terms of facet lengths. Interpreting Griffith's energy criterion [33], it is assumed that a facet of length l_f fails and forms a crack of the same length if the elastic energy released by this transition exceeds the energy required for the creation of the new surfaces [23]. Formally,

$$\underbrace{\int_{l_f} G \, \mathrm{d}l}_{\text{reduction of strain energy}} \geq \underbrace{2\gamma_f \, l_f}_{\text{increase in surface energy}} , \tag{4.1}$$

where G denotes the energy release rate of the loaded system during crack extension (energy released per unit crack area), and γ_f is the specific surface energy of the considered facet (energy per unit crack surface). Here, the crack area is $l_f \cdot 1$ and the crack surface $2l_f \cdot 1$, the unity referring to the thickness of the specimen.[1]

[1] In order to turn from the two-dimensional consideration into real *energy* terms, the equations should be multiplied by the length ('depth') h of the facet/crack in the third dimension instead.

Subsections 4.1.1, 4.1.2 and 4.1.3 summarize the energy expressions for nucleation and extension of isolated cracks. The theory will be extended in Chapter 5 (subsection 5.2.1) to pore–crack combinations.

4.1.1 Energy expressions for straight crack extension and crack nucleation

In order to establish an energy condition of failure on an individual facet, consider first the familiar case of infinitesimal extension of a straight crack under normal tension [76]:

$$G\ \mathrm{d}l = \frac{\pi\ l\ t^2}{2E'}\ \mathrm{d}l\ \geq\ 2\gamma\ \mathrm{d}l\ , \tag{4.2}$$

where l is the length of the existing crack, $\mathrm{d}l$ is an infinitesimal virtual extension of the crack, t is the applied tension, E' is Young's modulus of the elastic compact matrix[2], and γ is the specific surface energy of the material.[3]

For fracturing of a facet, an integrated form of eq. (4.2) is needed: For straight crack extension,

$$\int_{l_0}^{l_0+l_f} G\ \mathrm{d}l = \int_{l_0}^{l_0+l_f} \frac{\pi\ l\ t^2}{2E'}\ \mathrm{d}l\ \geq\ 2\gamma_f\ l_f\ , \tag{4.3}$$

and thus,

$$\frac{\pi\ t^2}{4E'}(l_0+l_f)^2 - \frac{\pi\ t^2}{4E'}\ {l_0}^2\ \geq\ 2\gamma_f\ l_f\ , \tag{4.4}$$

where l_f is the length of the considered facet f, and l_0 is the length of an already existing crack touching f. Crack *nucleation* is covered by setting l_0=0. A graphical representation of the net energy profit $\Phi_f = \int_{l_f} G\mathrm{d}l - 2\gamma_f l_f$ for crack nucleation is shown in fig. 4.1. The evolution of the 'critical' load for crack nucleation and crack extension as a function of facet resp. crack length is shown in fig. 4.2: the higher the length, the sooner will the failure of a facet or the unstable growth of a crack occur.

It is worth noticing that, generalizing, the quantity t is the magnitude of the traction acting on the crack/facet system, which can consist of tensile and shear components, and comprises contributions from the pressure of an intruding fluid (see sections 3.5.2 and 3.5.3).

So far, the energy release rate G associated with crack extension could be given in terms of the applied load. Usually, under more general conditions one encounters in the literature rather expressions for the crack tip stress intensity factor K. For the above interior crack under normal tension (mode I condition), the stress intensity factor reads

$$K_I(l,t) = \sqrt{\pi\ l/2}\ t\ , \tag{4.5}$$

and use in the energy criterion of eq. (4.2) leads to

$$G\ \mathrm{d}l = \frac{{K_I}^2}{E'}\ \mathrm{d}l\ \geq\ 2\gamma\ \mathrm{d}l\ . \tag{4.6}$$

[2] $E' = E/(1-\nu^2)$ for plane strain conditions, whilst $E' = E$ for plane stress conditions

[3] Extensions of the Griffith equation by a 'plastic work' have been proposed to account for the plastic deformation observed near the crack tips. These extended conditions predict thus a higher critical load on the materials; see, e.g. [72]. For an extended description of the plastic zones around cracks, see [29].

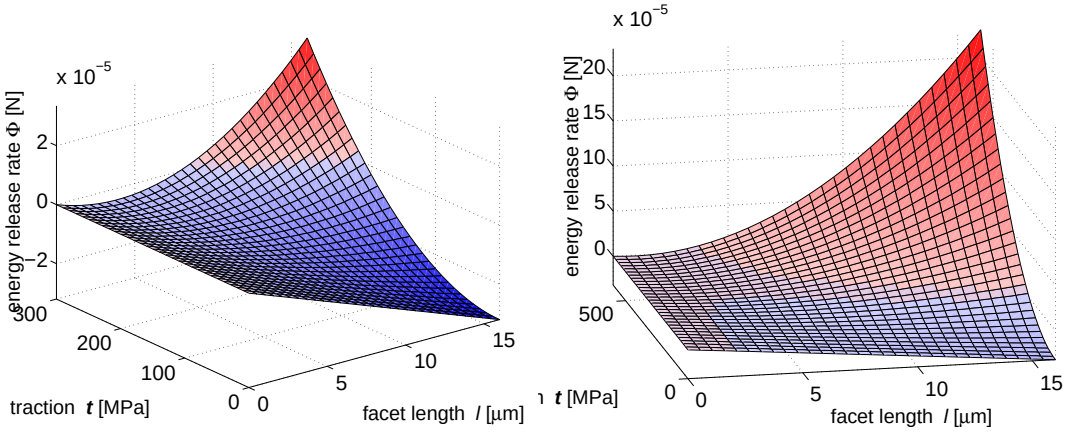

Figure 4.1: Net energy profit $\Phi_f = \int_{l_f} G\mathrm{d}l - 2\gamma_f l_f$ *associated with crack nucleation, as a function of facet length* l_f *and local (tensile) traction* $\mathbf{t}_f$*. The energy release is positive (red-coloured range) if the facet length or the traction exceeds a certain critical value. For* $\Phi_f \geq 0$*, the slope of the* $\Phi_f(l_f)$ *and* $\Phi_f(\mathbf{t_f})$ *functions is generally positive. For* $\Phi_f < 0$*, the slope of the curve exhibits a non-monotoneous behaviour. (Calculations have been performed with* $E' = 276.2$ *GPa,* $\gamma_f = 1$ Jm^{-2}*).*

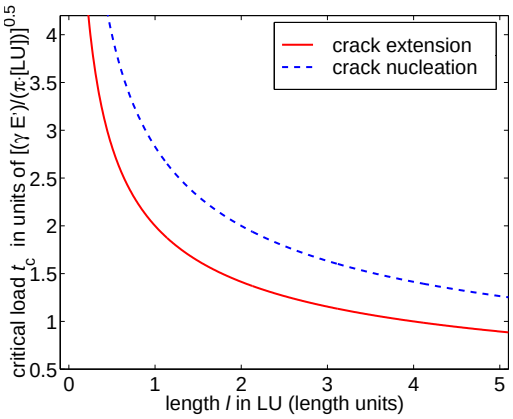

Figure 4.2: Critical load on a facet (→ crack nucleation) or crack (→ crack extension) as a function of facet or crack length, respectively. (Nondimensional representation.) The graph illustrates how microcracking is grain size dependent: Microcracks arise sooner at the boundaries of larger grains than at the boundaries of smaller grains.

More generally, following [33], a relationship between the strain energy release rate and the stress intensity factors for in-plane crack extension (modes I and II; the out-of-plane shear mode III is not relevant for the present two-dimensional analysis) may be given as

$$G = \frac{1}{E'}(K_I{}^2 + K_{II}^2) = \frac{K^2}{E'} \ . \tag{4.7}$$

The definition of the above compound stress intensity factor K is obvious. For the interior crack in the elastic plane the stress intensity factors K_I and K_{II} differ only with respect to the value of the loading component and thus K has the same form as eq. (4.5) but $t = \sqrt{t^{(\mathrm{n})2} + (t^{\mathrm{s}})^2}$ then denotes the magnitude of the traction vector, which possesses components normal (t^{n}) and tangential (t^{s}) to the crack line.

By eq. (4.7), fracturing of a facet requires that

$$\int_{l_0}^{l_0+l_f} G \, \mathrm{d}l = \int_{l_0}^{l_0+l_f} \frac{K^2}{E'} \, \mathrm{d}l \;\geq\; 2\gamma_f \, l_f \;, \tag{4.8}$$

which is an alternative expression of the energy criterion of eq. (4.3). It is interesting to consider transition from the energy concept of fracture to a stress intensity factor concept [8]: With a generalized K in eq. (4.6), the *local* criterion for crack extension is deduced as

$$K \geq \sqrt{2\gamma E'} = K_c \;, \tag{4.9}$$

where K_c represents a critical value (often called the 'fracture toughness' or 'modulus of cohesion' of the material).

4.1.2 Kinked crack extensions

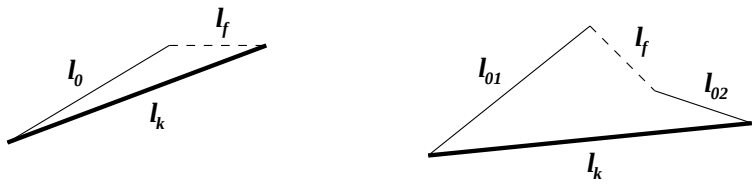

Figure 4.3: Modelling of kinked crack extension and unification of two cracks (failure of a facet bridging two existing cracks): The kinked crack is approximated by a straight line (bold).

In the numerical model, the path of a crack composed of several failed facets is approximately represented by a straight line connecting the two end points of the path (fig. 4.3). By this approach, kinked crack extension as well as formation of a kinked path by the failure of a bridging facet relies on the following form of the energy criterion:

$$\left(\int G \, \mathrm{d}l\right)_{\mathrm{pot}} - \left(\int G \, \mathrm{d}l\right)_{\mathrm{anc}} \;\geq\; 2\gamma_f \, l_f \;, \tag{4.10}$$

which substitutes the strain energy term for crack *extension* by the difference of two corresponding terms for crack *nucleation*. Integration for the *pot*entially new crack is over the artificial length l_k whereas the *anc*estor crack refers to the length l_0 (in the case of bridging $l_0 = l_{01} + l_{02}$: fig. 4.3, right). The surface energy is associated with the length l_f of the facet in question.

If the cracking facet touches no existing cracks, then $\left(\int G \, \mathrm{d}l\right)_{\mathrm{anc}} = 0$. Generally, application of the energy criterion on a facet requires determination of the crack structure for an assumed event of failure of this facet.

4.1.3 Cracking under compression and friction

So far, the case of a compressive normal load and the impact of friction has not been considered in the energy relations. This is accomplished by replacing the actual ('effective') load $\mathbf{t}_k$ acting on the potential crack k by the *active* load $\mathbf{t}_{k,\text{active}}$ as introduced in section 3.5.1. Moreover, in the presence of friction, crack formation under normal compression comes along with a heat loss of energy[4],

$$W_{k,\text{fric}} = \left\{ \begin{array}{cc} \frac{\pi(l_k)^2}{4E'} \left(|t^{\text{s}}_{k,\text{active}}| \cdot \mu_m |t^{\text{n}}_k| \right) & \text{if } \; t^{\text{n}}_k \leq 0 \\ 0 & \text{if } \; t^{\text{n}}_k \geq 0 \end{array} \right\} \tag{4.11}$$

which may be set off against the reduction of strain energy:

$$\int_{l_k} G \; \mathrm{d}l = \frac{\pi(l_k)^2}{4E'} (\mathbf{t}_{k,\text{active}})^2 - W_{k,\text{fric}} \tag{4.12}$$

Eq. (4.12) is the general expression for the energy available to build new surfaces while nucleating a single crack k.

4.2 Progressive microcracking: general considerations

The energy criterion is employed now for some general considerations on crack initiation and propagation, starting with quite simple microstructure specimens. The first part of the present subsection addresses the identification of critical locations in a microstructure, i.e. locations where crack nucleation may occur (section 4.2.1). The second part deals with damage progression under tensile load, and the difficulties in simulation and assessment of failure in the micromechanical model (section 4.2.2). The third part finally focuses on the special characteristics of microcracking under external compression (section 4.2.3).

4.2.1 Critical locations in a simple structure

Prior to simulation of any structural changes, the energy criterion allows for an identification of locations in the microstructure where nucleation and successive growth of microcracks has to be expected. Such a description in terms of the potential energy release goes beyond the classical stress analysis as presented in Chapter 3 since it accounts for the local properties of the grain phases, too.

To illustrate this, fig. 4.4 emphasizes those facets within a simple microstructure whose failure would become energetically possible at various levels and modes of externally applied load. It turns out that the orientation of the potential cracks is close to the direction of external load in case of compression, whereas it is perpendicular to the direction of external load in case of tension. In simple terms, larger facets are more 'critical' than smaller ones, but the decisive quantity is in fact the *projection* of the facet length onto the direction of applied load.

In addition to the length and orientation of the facets, the third important quantity is the specific surface energy of the grain boundaries. Figure 4.5 refers to a specimen comprising two different grain phases, namely a mixture of TiO_2 and Al_2O_3 grains. Since the specific surface energy is lower at the inter-phase boundaries, the most critical locations are observed right there rather than in between the TiO_2 grains.

[4] for an isolated crack: $W_{k,\text{fric}} = \langle b_k \rangle (\mu_m t^{\text{n}}_k \cdot l_k)$ with $\langle b_k \rangle = \frac{\pi l_k}{2E'} t^{\text{n}}_{k,\text{active}}$

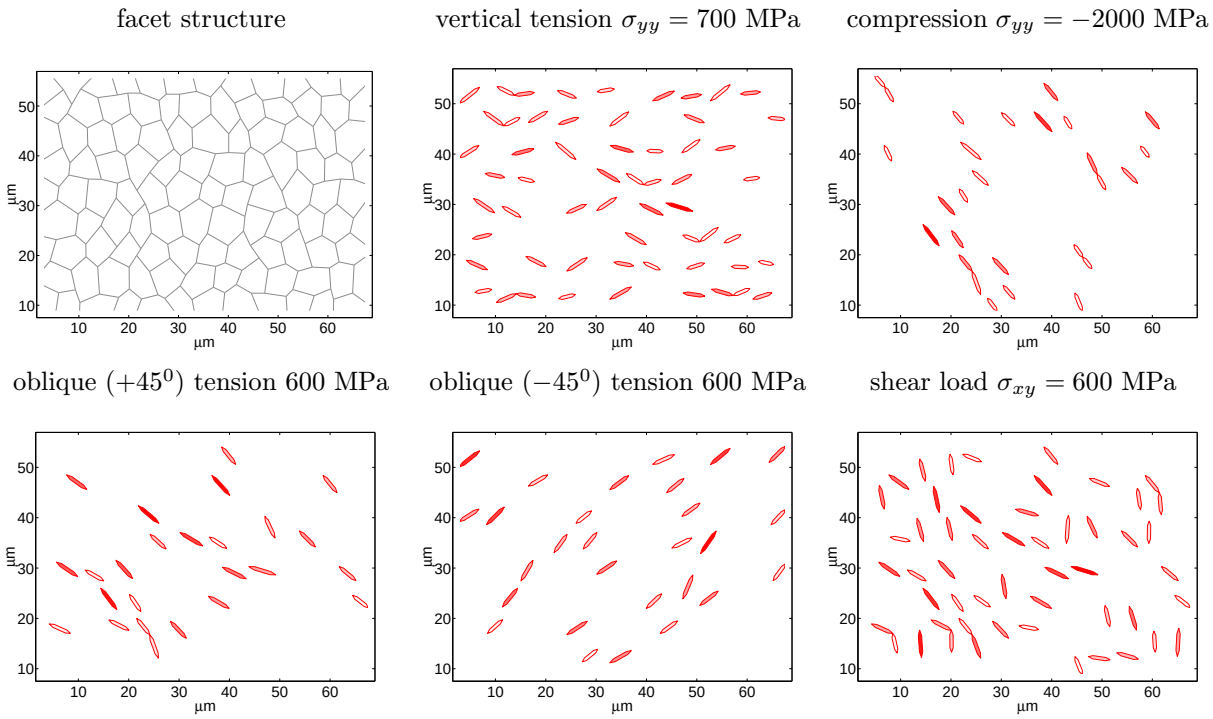

Figure 4.4: 'Critical locations' in a simple microstructure under various loading conditions. Assuming $\gamma_f = 2$ Jm^{-2} for the specific surface energy, the red-colored facets would have failed under the respective loading condition.

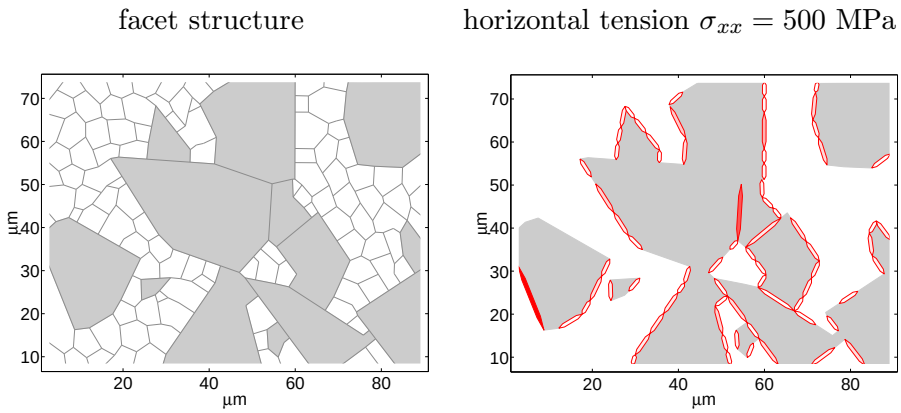

Figure 4.5: 'Critical locations' in a microstructure comprising two grain phases (TiO_2 in white, Al_2O_3 in gray) under horizontal tension. Assuming $\gamma(TiO_2/TiO_2)$=2 Jm^{-2}, $\gamma(Al_2O_3/Al_2O_3)$=1 Jm^{-2}, and $\gamma(TiO_2/Al_2O_3)$=0.5 Jm^{-2} for the specific surface energies, the red-colored facets would have failed under $\sigma_{xx} = 500$ MPa.

4.2.2 From microcrack initiation to simulation of failure

Consider now the process of crack nucleation and damage progression in a simple, one-phase structure under external uniaxial tension. Both the structure and the loading mode promote a brittle behaviour of the specimen.

The typical scenario of fracturing in the numerical simulation begins with the nucleation of a first microcrack at the most critical location. Due to the disturbance of the

local stresses by the first microcrack, one or more additional microcracks will then nucleate in the vicinity. The microcracks finally coalesce to an unstably growing (macro-)crack separating the specimen (fig. 4.6). It is straightforward to associate the resulting pattern with the failure of the specimen. More precisely, the percolation of a specimen (i.e., a crack extending from one border of the specimen to the opposite border) may be defined as its failure.

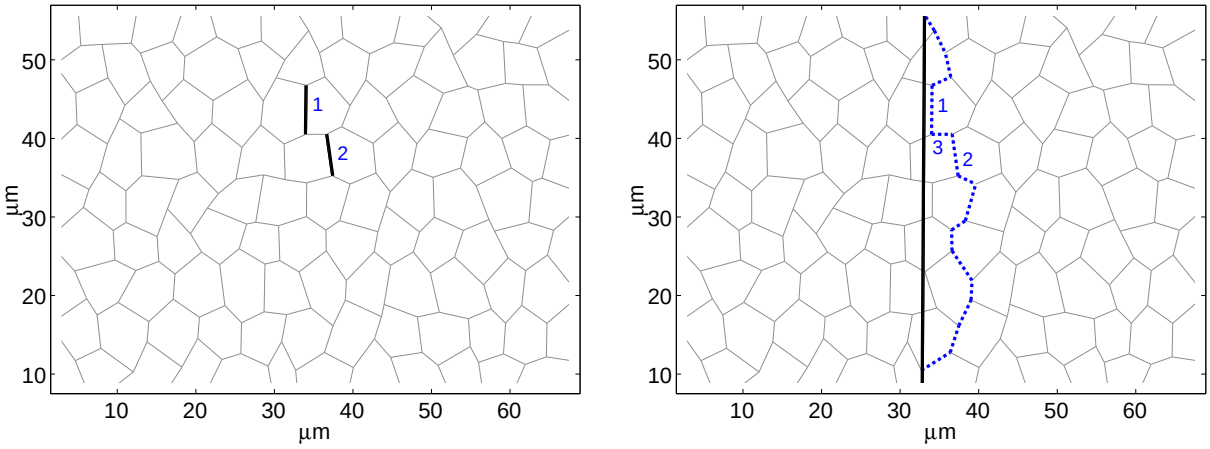

Figure 4.6: Crack nucleation and evolution under external horizontal tension. The second, smaller crack in the left figure propagates unstable, 'swallows' the first crack, and percolation of the specimen is reached in the end (figure on the right).

The situation encountered in modelling, however, is not always that clear. Since the structures are neither perfectly homogeneous nor distinctly heterogeneous (but just *granular*), the growth of a defect may be blocked at the irregular kinks of the grain boundaries, and the group of closely located microcracks may coalesce only partially: The cooperative phenomenon leading to *localization* (see section 1.1.1 in the introductory chapter) arises, which is difficult to catch or describe in a quantitative way (see fig. 4.7). The situation is further complicated if the unstable growth of a defect is stopped into one direction only, so that the growing crack runs into one border of the specimen only. Since the damage does not reach the percolation level, no failure of the specimen is recorded, and continued calculations will be dominated by boundary effects (see fig. 4.7, too). Especially if the specimen is not assumed to be isolated, but embedded in a larger structure, then the calculations may go well beyond the validity of the model. As a matter of course, the point where the simulation starts to diverge from the actual behaviour of a brittle granular structure is hard to define. An automatized finishing of the simulation algorithm would require a very sophisticated failure criterion. Defining a limit in terms of a 'critical' crack density is not adequate since this quantity does not include any information on whether the crack growth is stable or not.

This observation only goes to show that the crack patterns resulting in the simulations have to be permanently assessed with respect to their rationality. If necessary, the simulations must be restricted to lower crack densities or lower loads in order to avoid model artifacts. The current chapter does not deal with percolation and failure. Moderate levels of stably growing damage are considered instead, as encountered under compressive loading conditions.

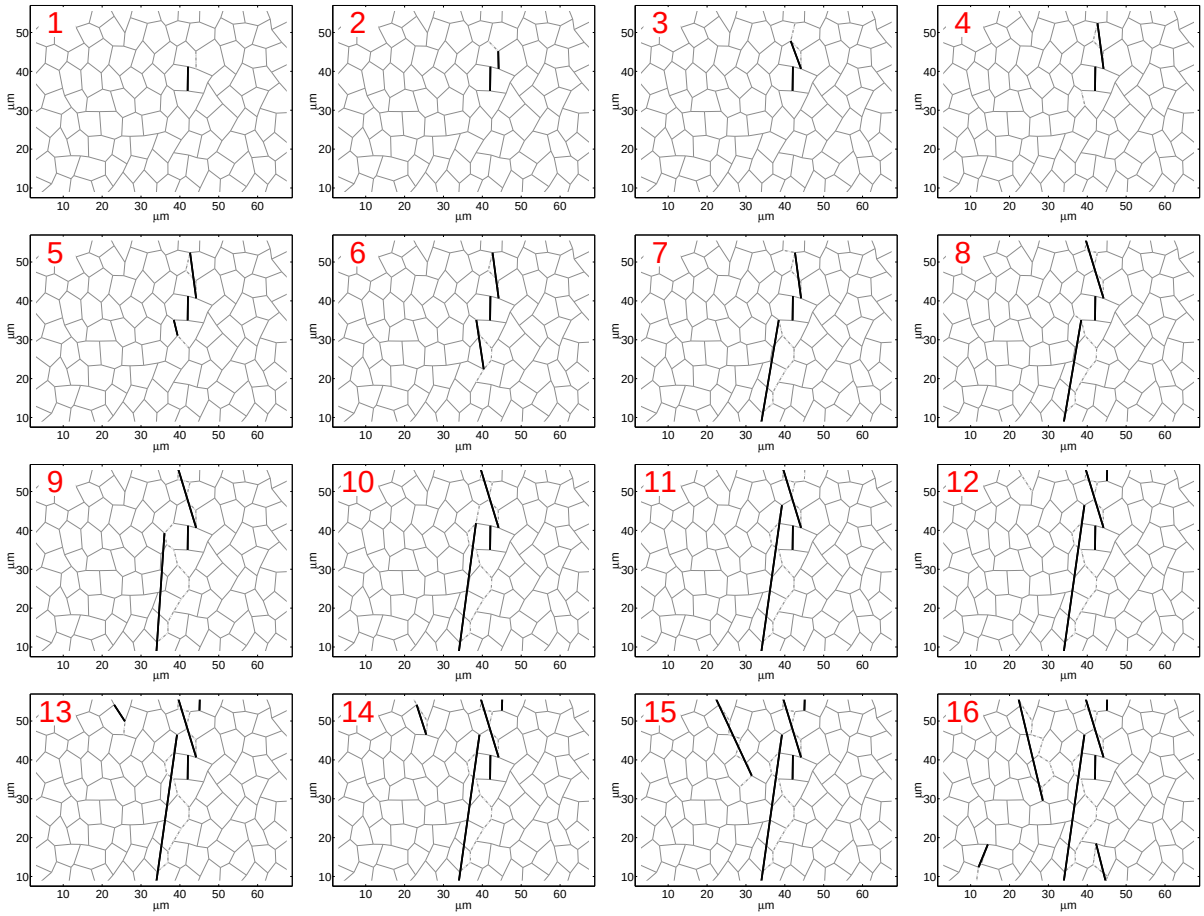

Figure 4.7: Crack nucleation and evolution under external horizontal tension. The crack pattern (which does not depend on the specific surface energy γ) grows within a narrow band and represents the phenomenon of localization. After step 8, the model calculations are dominated by boundary effects and must be assessed with increased prudence.

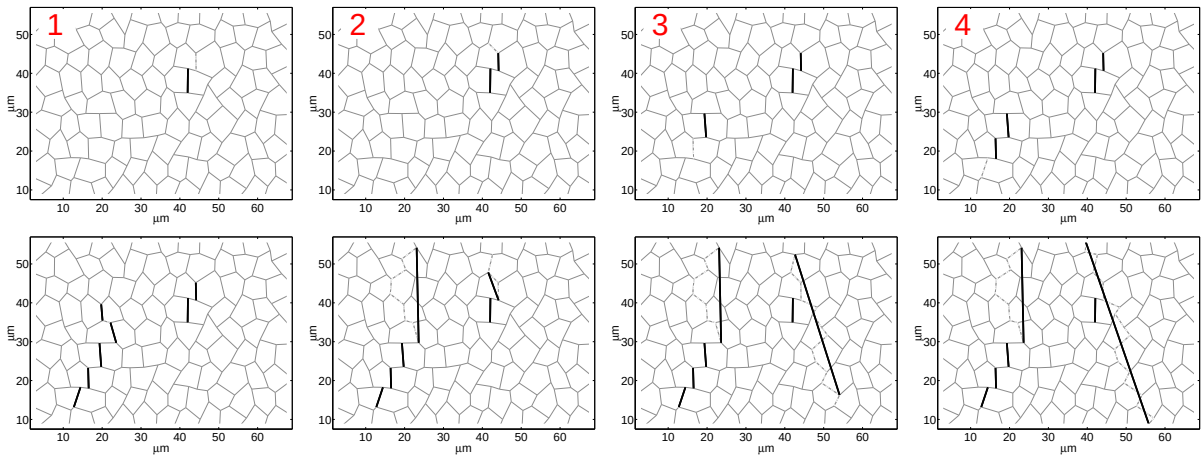

Figure 4.8: Crack nucleation and evolution under external horizontal tension. Neglection of the local stress disturbance due to the cracks (neglection of crack–facet interactions). The resulting crack pattern is quite different from fig. 4.7; the fact that no distinct localization occurs underlines the importance of the local stresses.

4.2.3 Microcracking under external compression

In contrast to the more unstable growth of cracks in specimens under tension (see also the localization phenomenon in fig. 4.9, left), a rather distributed pattern of stable microcracks is observed in materials under compressive load. This can be explained as follows: A tendency to unstable crack growth is given if an existing crack entails intense disturbances of the local stress field and has thus a violent impact on its environment. This situation is given if the crack exhibits a large opening displacement (COD). Under compressive load, however, the opening displacement is repressed due to crack closure and friction effects. Accordingly, the unstable crack growth is favored under tension, whereas a distributed crack pattern is more likely to occur under compression. Besides, the phenomenon of distributed microcracking is promoted by more heterogeneous structures (consisting of two grain phases, see e.g. fig. 4.9, right).

The expected orientation of microcracks arising under external uniaxial compression has already been demonstrated in fig. 4.4. The next step is to consider the further evolution of microscopic damage under particular circumstances. To this end, some mechanisms will be described from a phenomenological point of view, and the reflections will be supplemented by selected numerical simulations.

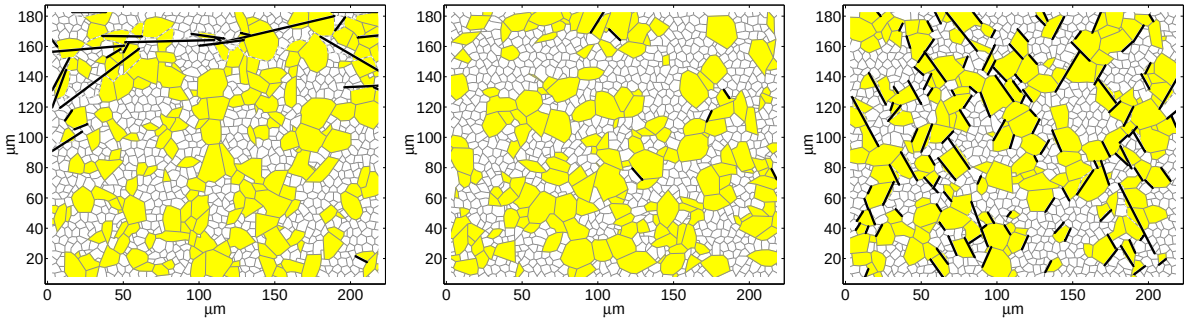

Figure 4.9: Left: crack pattern in a specimen under vertical tension ($\sigma_{yy} = 250$ MPa); a strong localization of the damage (and boundary effects as well) is clearly visible. Middle: crack pattern (crack density 0.004) in a specimen under vertical compression ($\sigma_{yy} = -650$ MPa). Right: crack pattern (crack density 0.152) in a specimen under higher vertical compression ($\sigma_{yy} = -900$ MPa). As for the specimens under compression, the microcracks are rather uniformly distributed.

Preexisting flaws. Though the evolution of damage from *preexisting* flaws is not concerned here, some points are worth mentioning in that context: Preexisting micro- or macro-flaws (cavities, cracks, inclusions) represent sources of local tensile stresses and, thus, tensile microcracks, even if the applied loads are compressive (see fig. 3.19, p. 82). In experiments, ensuing 'tension cracks' ('tension wings', see e.g. [79] or [48]) are observed to emanate from flaws of elongated shape, to curve toward the direction of (maximum) compression, and to grow with increasing compression, eventually orientating parallel to this loading direction. Under these conditions, the crack growth initially is stable. (This behaviour is in contrast to the initially unstable growth of cracks emanating from circular pores under vertical compression, see [67].)

The presence of a slight lateral tension ($4\% - 8\%$ of the applied compression), can

render the crack growth unstable: As soon as a critical crack length is attained, the crack grows spontaneousely, leading to axial splitting of the specimen [62].

Lateral tension. The study presented in fig. 4.10 shows the microcrack patterns and the damage evolution due to increasing vertical compression in a specimen under variated lateral tension. Obviously, the uniform distribution of microcracks for low tensile loads gives way to a strongly localized crack band if the lateral tension σ_{xx} exceeds a value of about 140 MPa. This means that high values of σ_{xx} reduce the crack initiation level for vertical compression σ_{yy} and promote the brittle failure of the material. (For comparison: The crack initiation level under a single uniaxial tension would be at about 200 MPa.)

Confinement. If the axial compression is accompanied by a lateral *confinement* (moderate levels of lateral compressive stresses, typically $25 - 30\%$ of the peak stress), then the growth of larger cracks is certainly arrested. The macroscale response of the material is stabilized. However, a region of high-density microcracks may emerge, the so-called 'shear band', spanning an angle between 10^0 and 30^0 [62] (15^0 and 25^0 [48]) with respect to the direction of maximum axial compression. The shear band is a consequence of the cooperative effect (localization) of the microscopic flaws; it finally represents the failure plane.

On the other hand, sufficiently high confining pressures (exceeding $20\% - 25\%$ of the applied compression) promote a "more or less uniform distribution of microcracks within the specimen" [62]. At this stage, brittle failure is suppressed (no shear band emerges), and one can speak of a brittle-ductile transition.

Significance of friction. The compressive resistance of the specimens is increased if the material has high static and sliding friction coefficients (μ_s, μ_m). Regarding the graphical analysis, changing the friction coefficients shifts the damage curves along the axis of applied load, but the critical locations and the resulting crack patterns seem — by and large — not to be affected. These observations are illustrated by fig. 4.11.

Evolution of effective parameters. Figure 4.12 shows the stress-strain response of a specimen under vertical compression σ_{yy}. Vertical compression results in a negative vertical strain ($\epsilon_{yy} < 0$) and in a positive lateral strain ($\epsilon_{xx} > 0$). The linearity of the stress-strain curves is lost at the point where the first microcrack is nucleated (here: at about $\sigma_{yy} = -500$ MPa). Nucleation of microcracks results in a loss of stiffness and an increased (negative resp. positive) strain of the specimen. Due to the simple uniaxial loading mode, the variation of the shear strain is very weak; the oszillations around $\epsilon_{xy} = 0$ reflect the random sign of the orientation angle of the nucleating microcracks.

The loss of material stiffness as a function of increasing external compression is represented in fig. 4.13. As outlined in the previous chapter (section 3.5.5, eq. 3.77, p. 80), the compressive loading conditions cause the stiffness to be a function of the current load (and of the load history), relating increments of stress and strain. Due to the preferred orientation of the microcracks (rather parallel to the direction of uniaxial compression), the lateral component of Young's modulus (E_x) is stronger affected by the progressive damage than the vertical component (E_y). The contribution of the cracks predominantly results from their *shear* compliance, since the majority of them is under normal compression, i.e. inactive with respect to the normal mode.

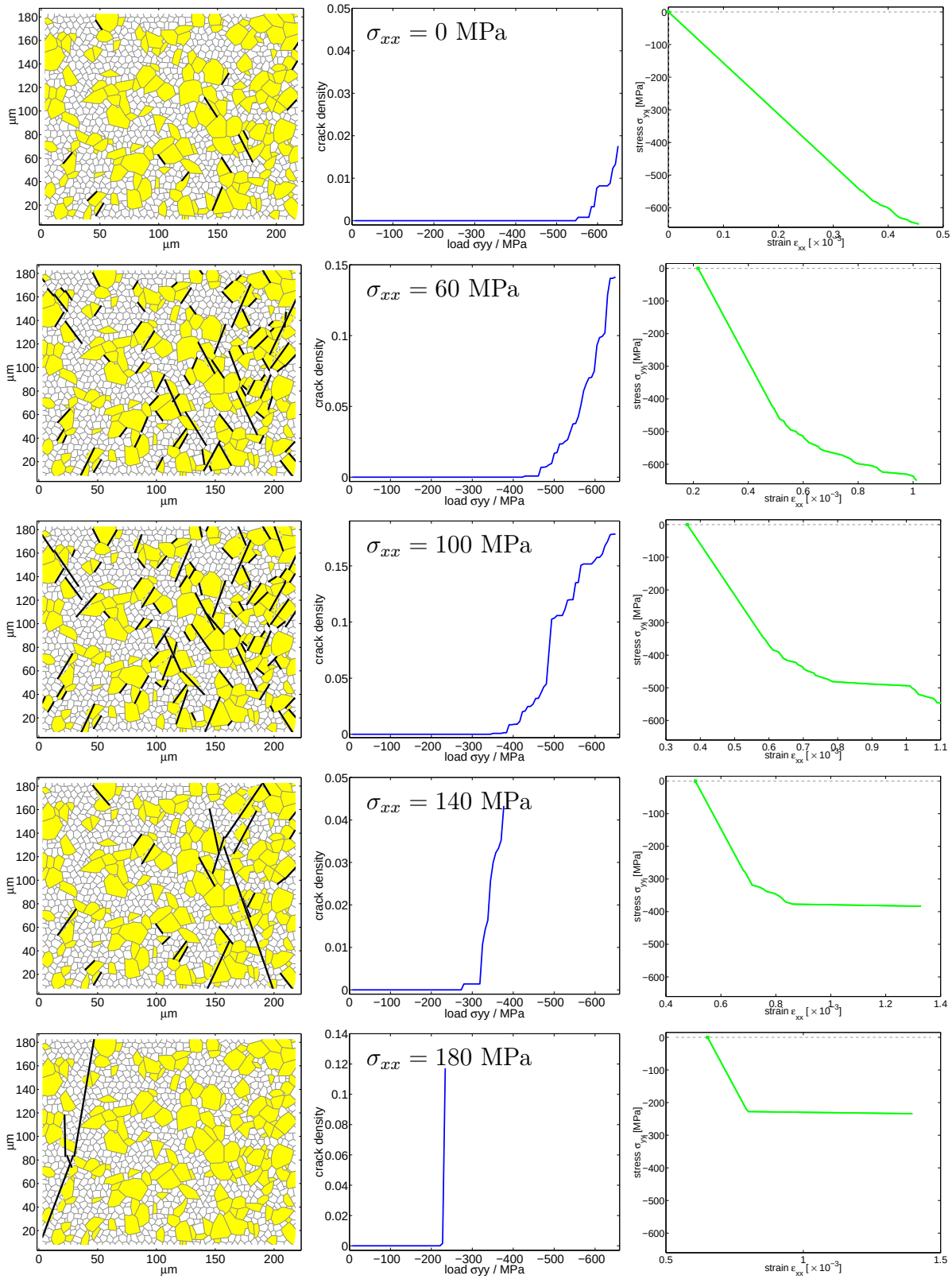

Figure 4.10: Microcracking under lateral tension σ_{xx} (applied first) and vertical compression σ_{yy} (applied afterwards). The tension σ_{xx} amounts to 0 MPa (first row), 60 MPa (second row), 100 MPa (third row), 140 MPa (fourth row), 180 MPa (fifth row), and is – on its own – not sufficient to cause any damage. Microcracking starts if the tension is supplemented by a vertical compression: the graphs in the middle show the crack density as a function of σ_{yy}, while the diagrams on the right show the evolution of lat. strain ϵ_{xx}.

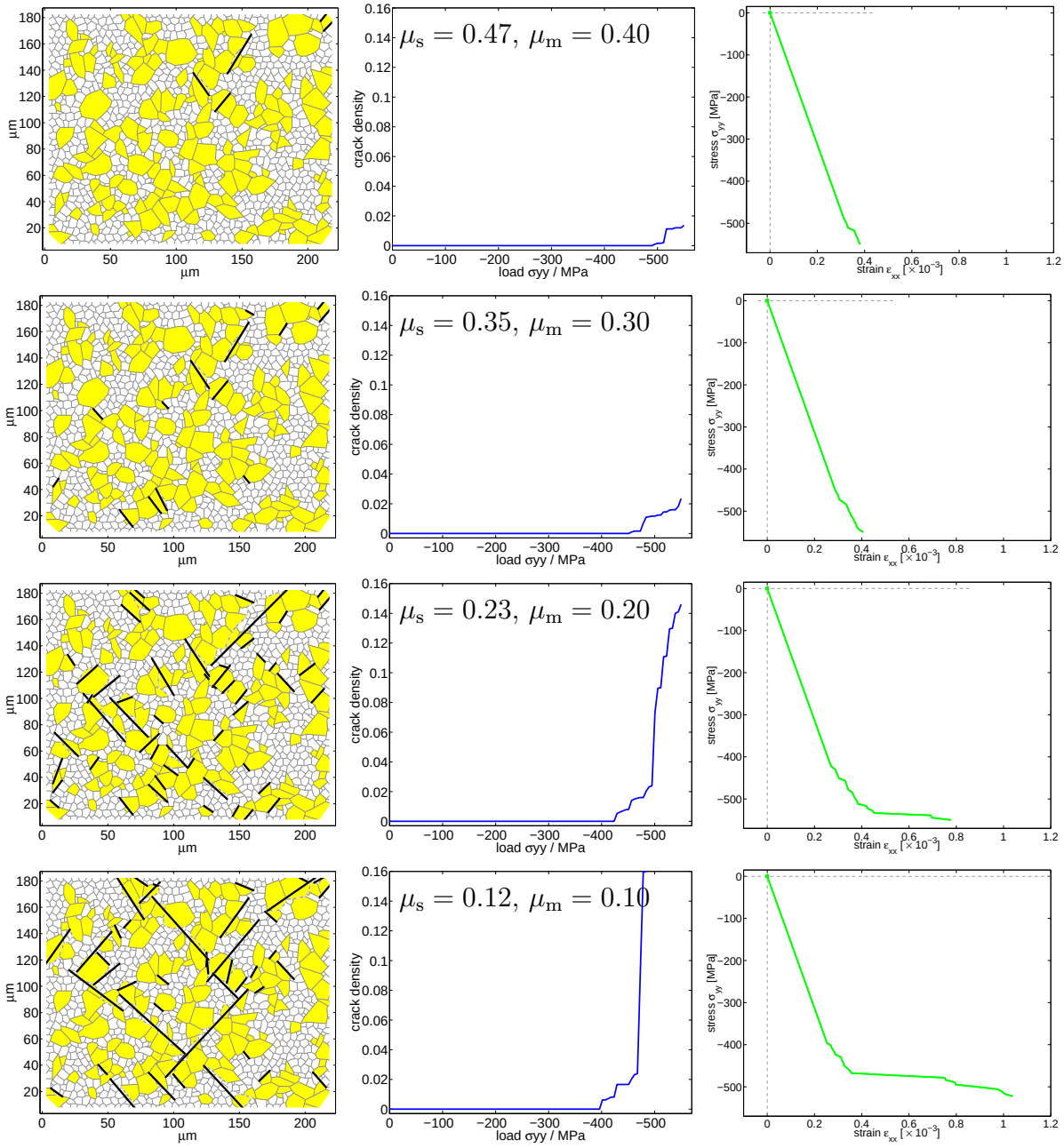

Figure 4.11: Studying the effect of friction on microcracking in a specimen under vertical compression $\sigma_{yy} = -550$ MPa. The setting of the friction coefficients μ decreases from the upper to the lower row. (First row: 100 %, second row: 75 %, third row: 50 %, fourth row: 25 %). The static friction μ_s exceeds the sliding friction μ_m by 17 %, respectively.

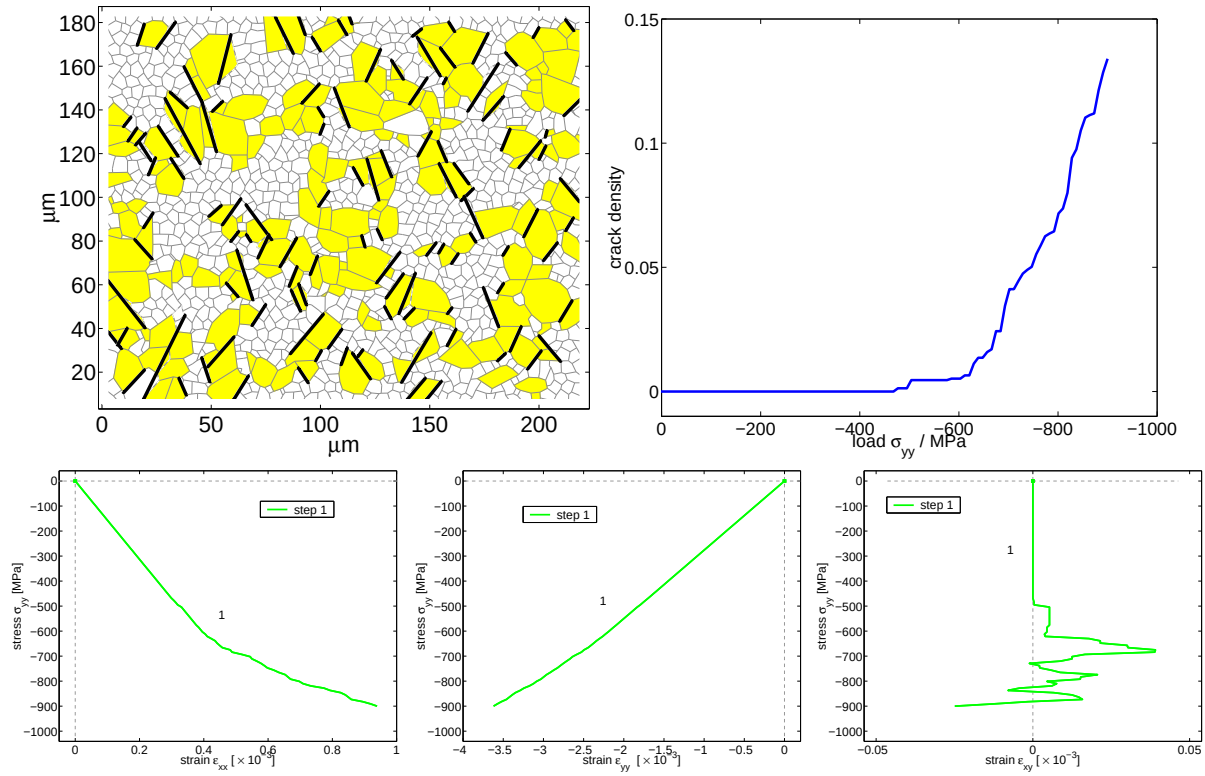

Figure 4.12: Specimen under a vertical compressive load which is increased to $\sigma_{yy} = -900$ MPa. The diagrams show the evolution of crack density, and the strain response (ϵ_{xx}, ϵ_{yy}, ϵ_{xy}) as a function of σ_{yy}.

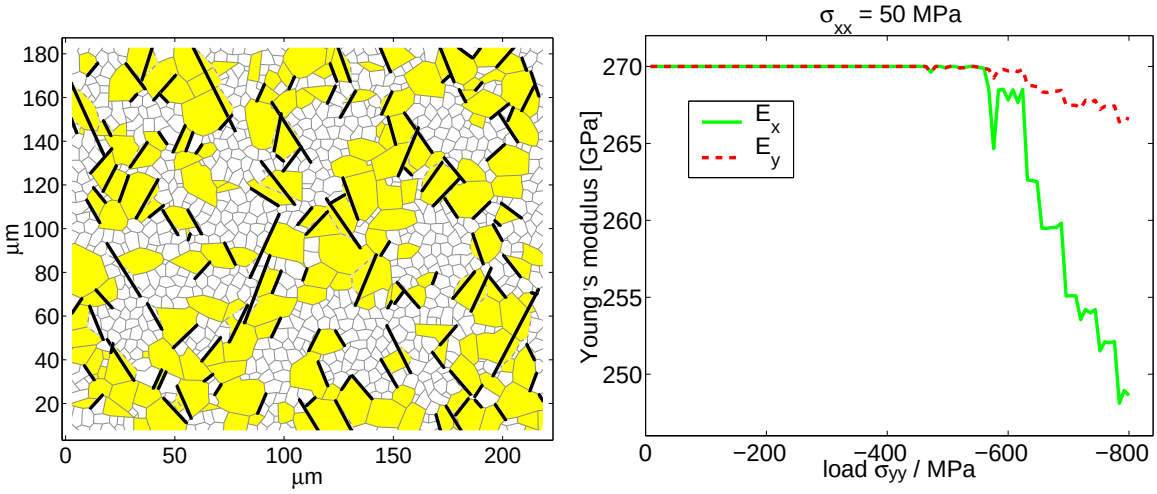

Figure 4.13: Evolution of Young's moduli in a microcracking specimen under lateral tension $\sigma_{xx} = 50$ MPa (applied first), as a function of increased vertical compression σ_{yy}. Anisotropy of the material stiffness: in the final loading state, the vertical stiffness is higher than the lateral stiffness. 91 % of the cracks are under compression (negative normal traction).

4.3 Statistical studies on compact materials under compression: effect of structural disorder

The following considerations are dedicated to the stochastic behaviour of damage evolution in compact microstructures as revealed by Monte Carlo simulations. The investigations aim at an exploration of statistical trends attributable to certain intrinsic and extrinsic conditions. The complex subject necessitates some introductory accounts (subsection 4.3.1), before several explicit numerical studies will be presented in subsection 4.3.2.

4.3.1 Fundamental remarks

This section is first to outline some basic terms in statistics, and to summarize those statistical quantities that are employed in the rest of the current chapter and in the following Chapter 5. Then, some reflections on the appropriate observable in the numerical simulations are added. The last part is on the statistical input for the simulations, i.e. on the microstructure parameters and their variation.

4.3.1.1 Some terms and definitions in statistics

Applying the language of statistics to the issues of the present thesis, a *statistical sample* (or *statistical ensemble*) comprises the total number of events subject to observation, while the single realization of the material microstructure (and its response under specified conditions) is termed a specimen representing a single *member of the ensemble*, or simply a *test*. The observations on the multitude of tests focus in one or more selected physical quantities y, respectively. The first two moments of the statistical distribution of these *observables* represent the main output parameters of the statistical studies: firstly, the *mean value* $\bar{y}$ of a set of n observations (*sample* mean), which reads

$$\bar{y} = \frac{1}{n} \sum_{i=1}^{n} y_i \ , \tag{4.13}$$

and, secondly, the *standard deviation* for a set of n observations (*sample* standard deviation), which is defined as

$$s_y = \sqrt{\frac{\sum_{i=1}^{n}(y_i - \bar{y})^2}{n-1}} \ . \tag{4.14}$$

The square of the standard deviation is called the *variance*, which represents the average squared deviation of the values of y from the mean, indicating the extent of scatter in the variable.

Another useful quantity is the standard error (deviation) of the mean:

$$s_{\bar{y}} = \frac{s_y}{\sqrt{n}} = \sqrt{\frac{\sum_{i=1}^{n}(y_i - \bar{y})^2}{n(n-1)}} \ , \tag{4.15}$$

which is a measure for the accuracy of the statistical test results — it indicates the range of confidence for the mean.

The *population* mean (also called 'expected value'), which is defined as the mean of all possible values of y, is denoted as μ_y (not to be confused with the friction coefficient

introduced in Chapter 3). The corresponding standard deviation of the population is denoted as σ_y (not to be confused with the similarly called stress) [22].

Some considerations address the relationship between two variables k and l, say one input parameter and one observable (output parameter). A meaningful indicator in this context is the *correlation coefficient* of the statistical sample:

$$r_{kl} = \frac{s_{kl}}{s_k s_l}, \tag{4.16}$$

where s_{kl} denotes the mutual *covariance* of the variables and indicates their tendency to stay on the same side of the mean (see, e.g., [22] for a detailed description). For a visual assessment of the correlation, 'scatter plots' are a suitable tool; they show the pairs of values as points in an orthogonal coordinate system (see, e.g., fig. 4.14).

For the presentation of the distribution of an observable y over the individual observations, histogram plots are employed (see, e.g., fig. 4.18): the whole range of y is subdivided into intervals of equal width (Δy), and the frequency of tests exhibiting a value of the observable lying in the respective range is assigned to these intervals. In the limit of an infinitesimal interval width dy and an infinite number of tests, one would get to the *probability*

$$p_{D_0}(y)\ \mathrm{d}y \tag{4.17}$$

of finding the observable in the range between y and $y + \mathrm{d}y$ (for a specimen of size D_0). The parameter $p_{D_0}(y)$ represents the *probability density* as a function of y. The probability density is to be distinguished from the *cumulative probability* (see eq. 5.6, p. 139).

In the simulations, random sampling will be continued until the mean of the observable is stabilized (see the curves representing the evolution of the mean with increasing number of tests, e.g. in fig. 4.21, right).

4.3.1.2 On the appropriate damage observable

The proper choice of the observable in the context of progressive damage is sometimes an objective of research by itself, but some remarks should be sufficient here. Ideally the observable should reflect both the actual structural changes in the material and the significance of these changes on the macroscopic response of the material. This is a difficult demand since the macroscopic response depends on the active defects only, and thus on the loading conditions, the load history, etc. Certainly there is no generally suitable damage parameter, instead it must be selected with respect to the present material properties, loading conditions, failure modes, and with respect to the observation scale. Last but not least, a damage parameter should be measurable by experiment. Some possible candidates for the damage parameters will be discussed in the following.

Damage parameters at the microscale. At the microscale, the observable is a *damage parameter* in the actual sense since it refers to the structural properties rather than to the mechanic or elastic behaviour. In defect-sensitive materials, the size of the largest defect will be of importance, especially in weakest-link theories (see Chapter 5, section 5.5.1.2). For distributed defects, recording the total length of cracked grain interfaces or the additional internal surface energy introduced by the microcracks may be more appropriate.

The most prominent damage parameter is doubtlessly the *crack density*. If the microcrack distribution is approximately isotropic (random), then it can be characterized by a scalar damage variable (see eq. 2.3, p. 36). The isotropic distribution is a special case which is rather rarely encountered in nature but extensively assumed by analysts because of the easy tractability. In a general case, the microcrack distribution is characterized by a varying degree of anisotropy. An orthotropic microcrack distribution (which may result from uniaxial loading conditions) which induces an orthotropic behaviour of the macroscopic material properties is a frequently encountered situation. This class of microcrack distributions may be adequately represented by a second order damage tensor.[5]

The detection of microcracks and the determination of the mentioned damage parameters is difficult or even impossible in actual experiments. In the simulations, however, these quantities are easy output parameters.

Observables at the macroscale. In typical laboratory experiments on actual material specimens, the *stiffness* is easily accessible and therefore a reasonable (if not the most appropriate [48]) candidate for the observable at the macroscale. With respect to progressive damage, the *change* of the effective stiffness is to be favored, since the initial damage is seldom known. In typical cases, the effective stiffness allows a rough estimation of the microcrack density, and the course of the stiffness expresses the thresholds of the intrinsic failure modes (localization, percolation). Recording the effective stiffness is useful but rarely sufficient for the prediction of the macroscopic failure threshold. Unfortunately, the stiffness is not appropriate under compressive loading conditions, because it is strongly coupled to the activity status of the cracks — passive cracks are completely ignored (see fig. 4.15, fig. 4.16).

An alternative to the stiffness is the overall *strain* at a certain load, or – strictly speaking – the additional strain due to the damage. Even though strains are strongly dependent on the loading conditions, too, they nevertheless have the advantage that passive cracks may contribute by means of locked shear displacements.

Depending on the scope of the respective studies, other possible observables may be the rupture strength resp. failure threshold of the specimens (see Chapter 5).

Damage parameter in the model simulations. As already noted, the above microscopic parameters have no general and immediate impact on the macroscopic response of the material. Nevertheless, analysis of the test results shows that — for the compressive load and the associated distributed microcracks patterns — the scalar crack density is highly correlated to the overall strains (fig. 4.14 and fig. 4.15 reveal an approximately linear relationship). Thus, the crack density seems to be representative for the change in strain, i.e. for the macroscopic response of the material.

For convenience, the crack density will therefore be employed as the principal observable. Most of the statistical studies will address the crack density at a certain value of applied load, while a different setting concerns the load required to cause a certain crack density. The latter is approximately equivalent to the load required for exposing the material to a certain strain.

[5] In principle, higher accuracies can be reached by applying higher order damage tensors, but it seems that the second order tensor representation of damage satisfies all rational criteria of accuracy for the approximation of effective properties [41].

Figures 4.15 (lower row) and 4.16 illustrate that the elastic stiffness (Young's modulus) is definitely not suitable for an assessment of microscopic damage under compression.

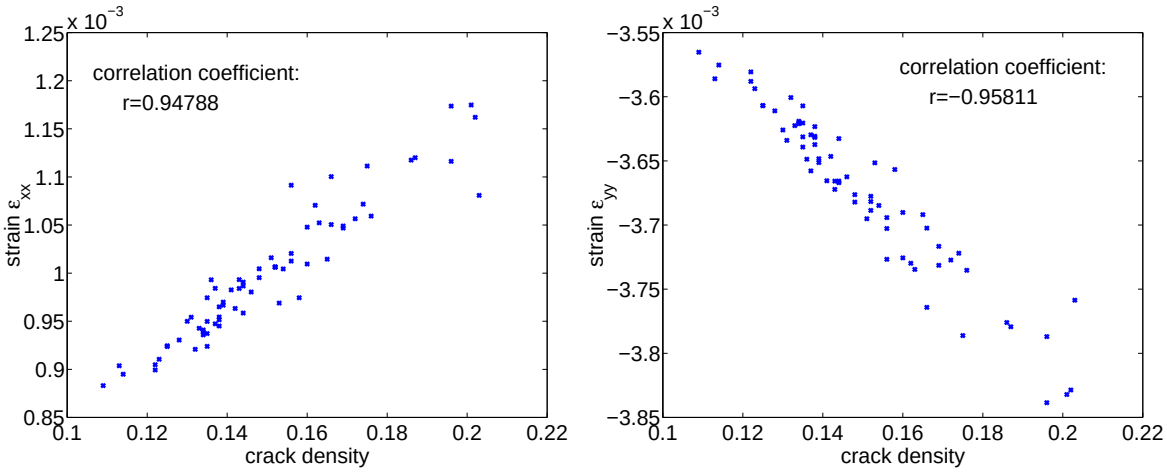

Figure 4.14: Scatter plots for investigation of two-parameter correlations. Correlation of crack density and overall strain for specimens under a compressive load $\sigma_{yy} = -900$ MPa. A strong correlation is seen for the ϵ_{xx} and ϵ_{yy} strain components. (In contrast, there is no significant correlation for the shear strain ϵ_{xy}: $r = 0.27$)

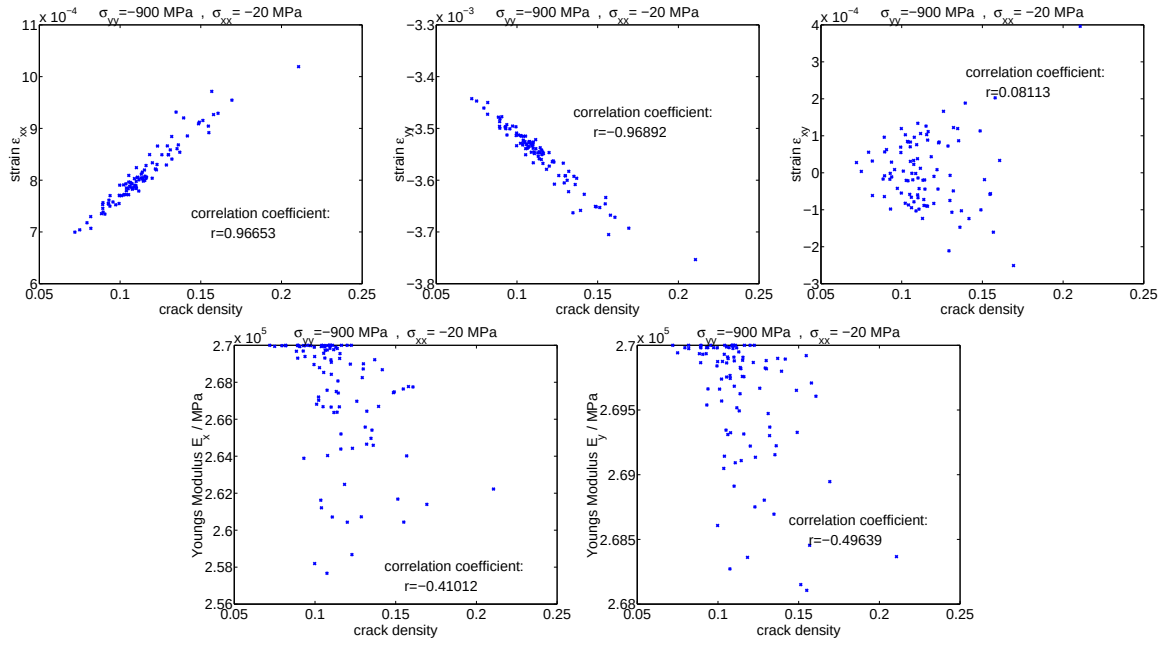

Figure 4.15: Scatter plots for investigation of two-parameter correlations. Correlation of crack density and overall strain (above), and of crack density and Young's moduli (below) for specimens under a lateral compressive load $\sigma_{xx} = -20$ MPa (applied first) and a vertical compressive load $\sigma_{yy} = -900$ MPa. A strong correlation is seen for the ϵ_{xx} and ϵ_{yy} strain components.

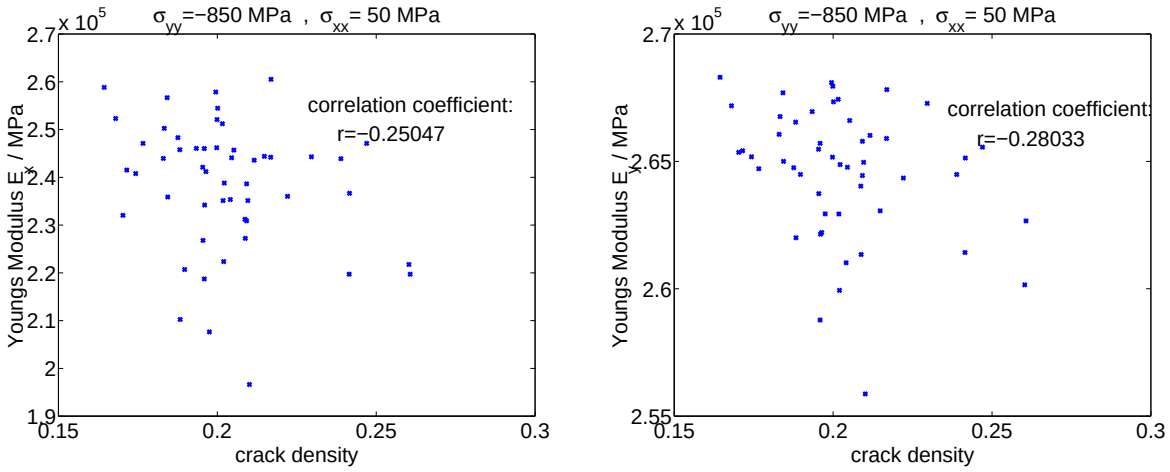

Figure 4.16: Investigation of the correlation between crack density and Young's moduli for specimens under a lateral tensile load $\sigma_{xx} = 50$ MPa (applied first) and a vertical compressive load $\sigma_{yy} = -850$ MPa.

4.3.1.3 Statistical input in the simulations

The studies refer to compact heterogeneous structures comprising two phases of grains (Al_2O_3, TiO_2). The majority of tests is performed on specimens of size $D = 37905\ \mu m^2$, which are exposed to an external vertical compression. The default values for the friction coefficients are $\mu_s = 0.7$, $\mu_m = 0.6$.

A local statistical disorder is obtained by randomly determining the sizes, shapes and positions of the individual grains according to uniform distributions within certain bounds (see Chapter 2). In addition, the global parameters 'area density' and 'specific perimeter' fluctuate among the individual members of the ensemble as well. The mean values of the global parameters of the second grain phase in the specimens are: area density $A_A(Al_2O_3) = 0.43$, specific perimeter $L_A(Al_2O_3) = 103$ mm/mm^2. It is seen that the fluctuations in the global parameters have no direct correlation to the respective damage resistance (see fig. 4.17).

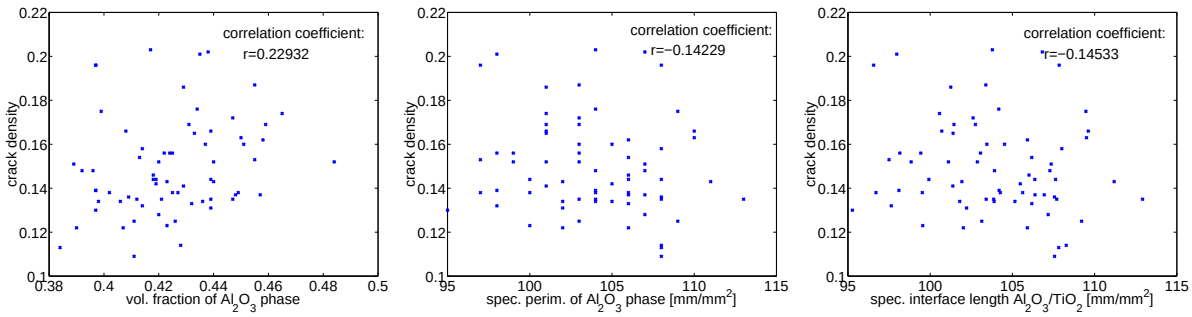

Figure 4.17: Scatter plots for investigation of two-parameter correlations. Correlation of crack density and structural parameters for specimens under a compressive load $\sigma_{yy} = -900$ MPa. Similarly low correlations are observed for crack density and specific interface TiO_2/TiO_2, and for crack density and specific interface Al_2O_3/TiO_2.

4.3.2 Selected studies

The subsequent studies refer to four selected issues: confinement, friction, crack interactions, and specimen size. The particular scope of the first two studies is to illustrate the evolution of the mean and of the scatter (standard deviation) of the crack density as a function of load and friction.

Vertical compression, and significance of lateral stresses. A series of tests on microcracking has been performed for specimens under biaxial stress: a predominating vertical compression, accompanied by a weak lateral tensile or compressive load. The crack density distributions for variated levels of vertical and lateral load have been recorded, and are displayed in fig. 4.18.

For loading states moderately exceeding the crack initiation level, fig. 4.19 (left) indicates that the mean of the crack density increases roughly linear with the vertical

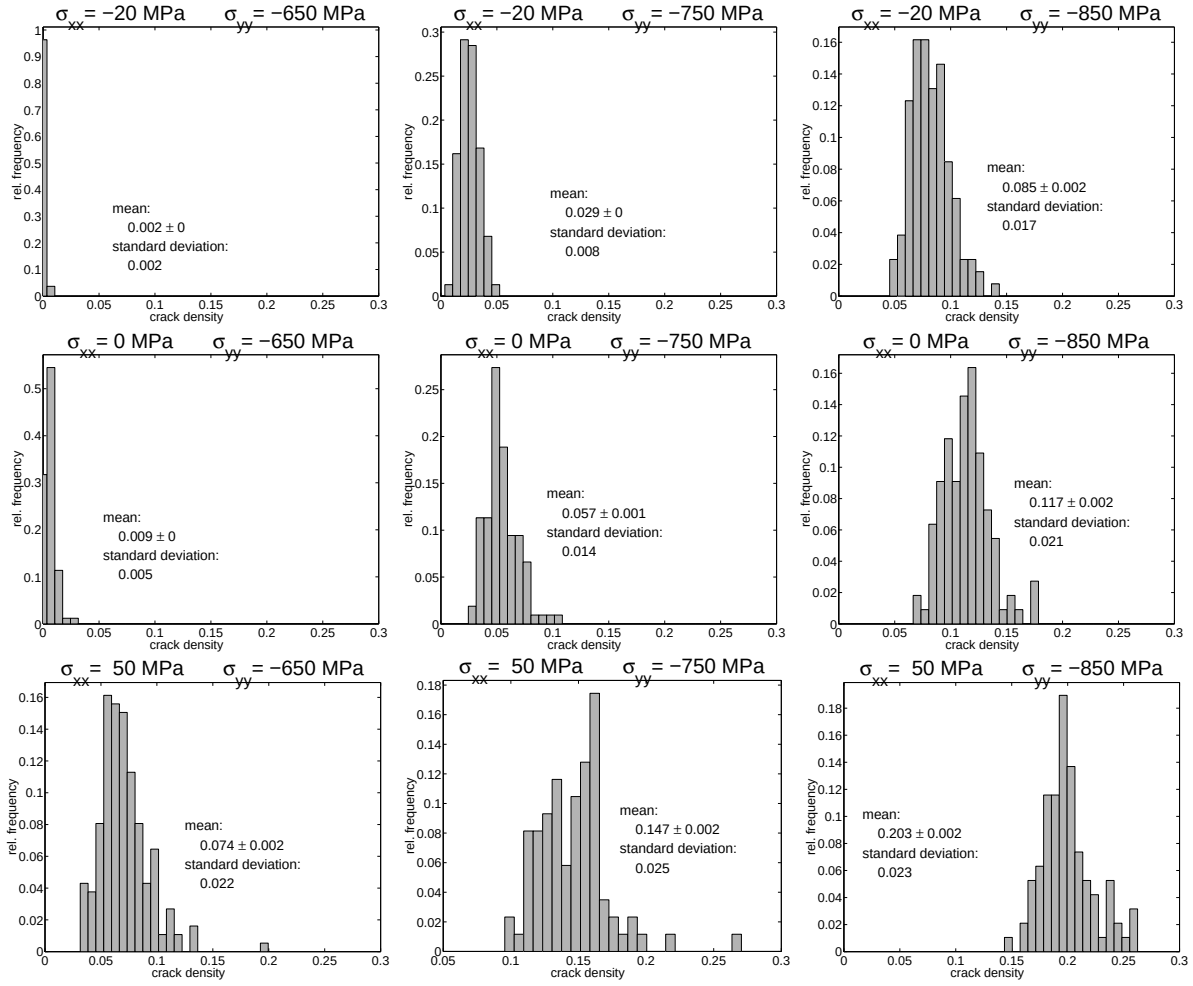

Figure 4.18: Studies on the crack density in specimens under lateral stress (applied first) and vertical compression (applied afterwards). The lateral stress amounts to $\sigma_{xx} = -20$ MPa (upper row), $\sigma_{xx} = 0$ MPa (middle), $\sigma_{xx} = 50$ MPa (lower row). The compression is increased to $\sigma_{yy} = -650$ MPa (first column), $\sigma_{yy} = -750$ MPa (second column), $\sigma_{yy} = -850$ MPa (third column). Each statistical series relies on 100 tests minimum.

compression σ_{yy} and the lateral load σ_{xx}. As for the lateral load, the linear course of the function seems to be not affected by a transition from negative to positive values.

The results suggest that the *absolute* scatter of the damage parameter increases with increasing load. This may be explained as follows: Increasing load enables the evolution of larger cracks. From the micromechanical point of view, evolution of larger cracks depends on the respective spatial arrangement of *several* grains. In contrast, the nucleation of small cracks is affected by the immediate vicinity of a single grain only. The correlation of an increasing number of grains makes the situation more and more complex. The drastically growing 'number of degrees of freedom' is reflected in the scatter of the damage parameter.

The *coefficient of variation* (standard deviation devided by the mean), however, clearly decreases with increasing load (fig. 4.19, right).

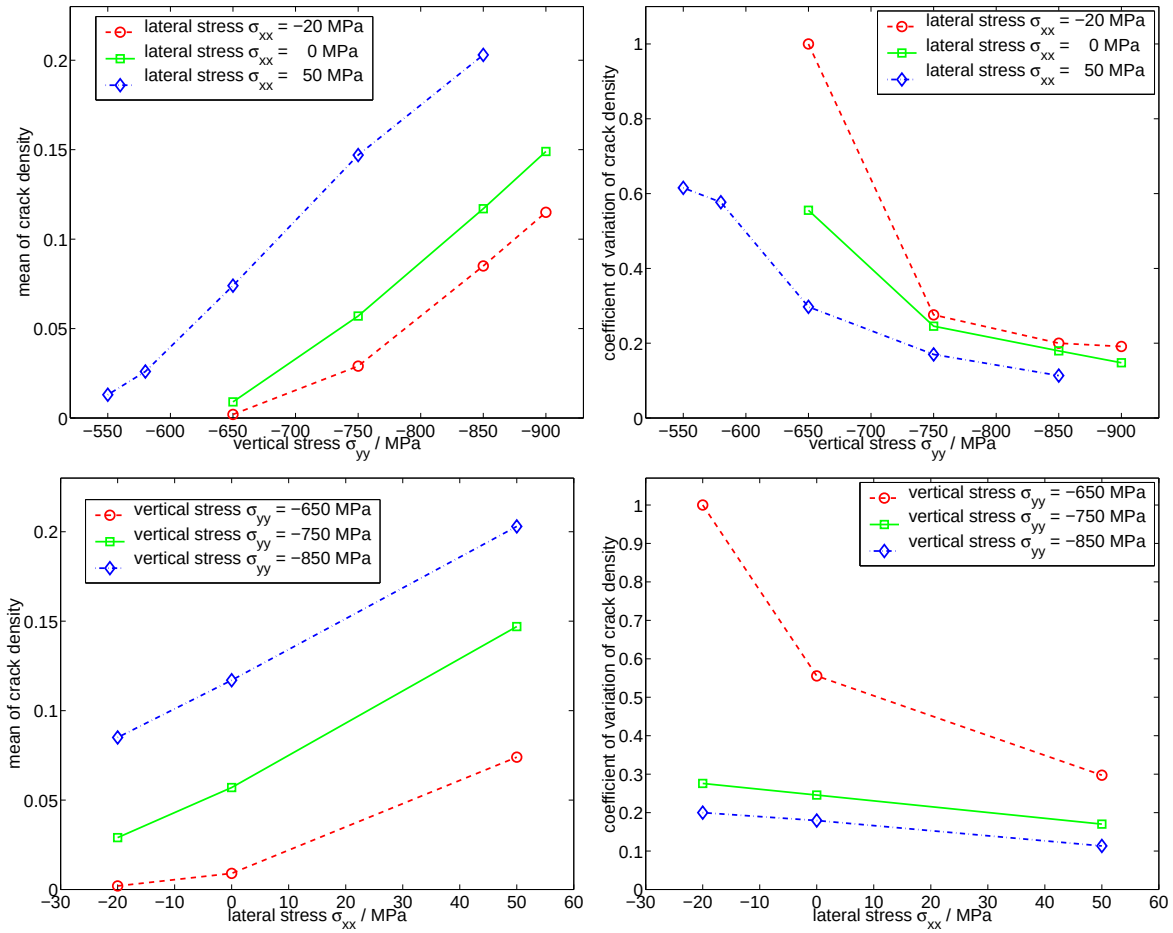

Figure 4.19: Evolution of the mean value (left) and coefficient of variation (right) of the crack density as a function of vertical compression (above) and of lateral stress (below). The plots summarize the results presented in fig. 4.18, and contain further calculations.

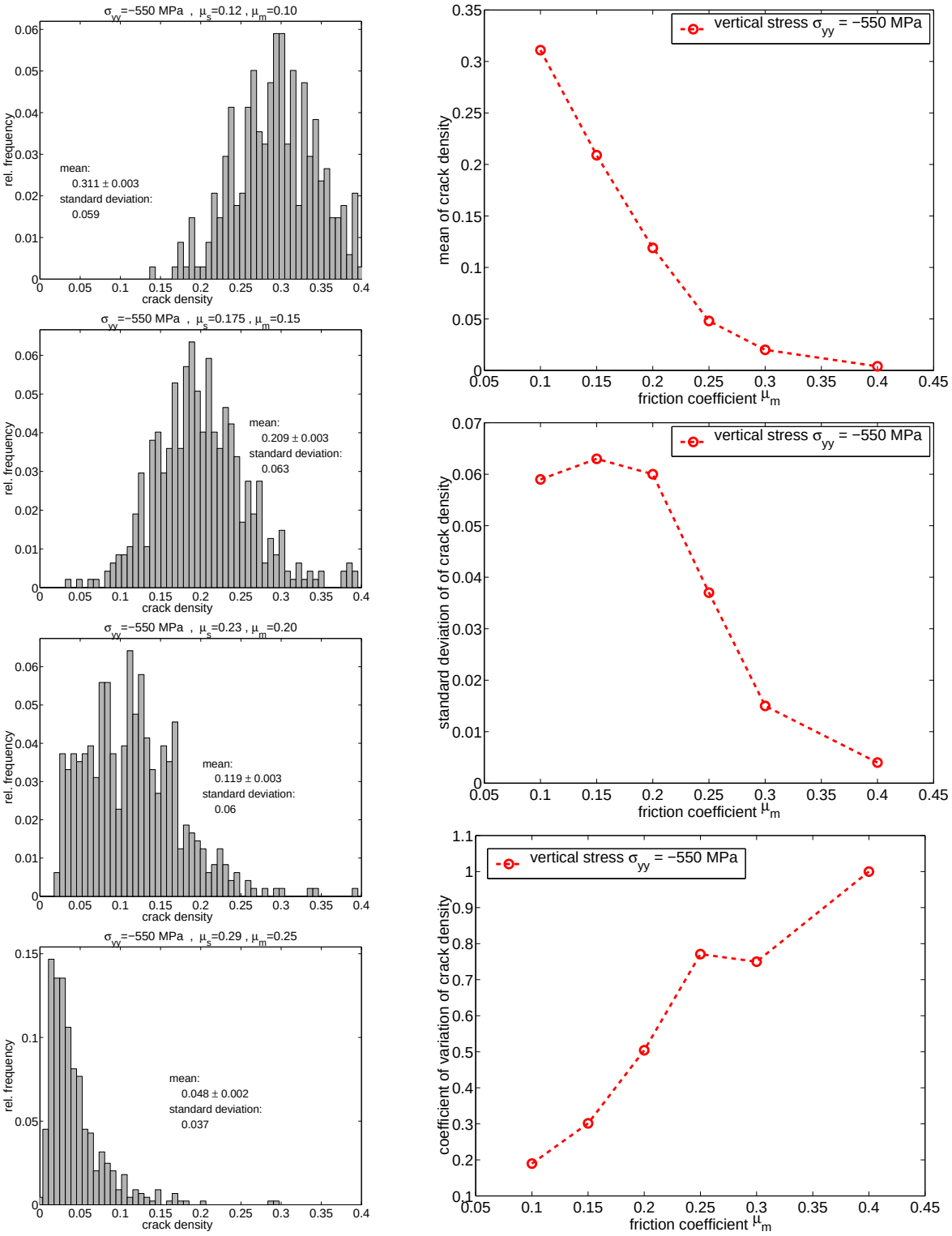

Figure 4.20: Statistical investigations on the effect of friction in specimens (size 37905 μm^2) under uniaxial compression $\sigma_{yy} = -550$ MPa. Left column: the observed distribution of crack density shifts towards zero when the values of the friction coefficients are increased. (The static friction μ_s exceeds the sliding friction μ_m by 17 %, respectively.) The diagrams on the right refer to the mean, the absolute standard deviation, and the coefficient of variation of the crack density as a function of friction.

Significance of friction. As has been illustrated in fig. 4.11, a sufficiently strong friction within a material may suppress the evolution of damage under compression. Figure 4.20 now shows how the mean — and, at the same time, the absolute scatter — of the crack density tends towards zero with increasing values of the friction coefficients. It turns out that there is no sharp 'friction threshold' above which no microcracks occur, but the transition from a linear decrease to zero damage is rather smooth. As above, the coefficient of variation of the damage parameter decreases with increasing overall damage.

Significance of local stresses around cracks. According to the theoretical framework outlined in Chapter 3, the numerical simulations account for local stress disturbances by means of explicit crack↔crack interactions and crack→facet interactions. Comparison of the structure images in fig. 4.7 and fig. 4.8 above (p. 101) demonstrates the importance of these interactions for the deterministic crack patterns, and for the occurrence of the localization phenomenon.

The statistical significance of these interactions is to be checked now for specimens under uniaxial vertical compression. The observable is the load required to produce a crack density $\rho = 0.07$. In the first series of computational tests, the interaction effects have been included (as throughout the present chapter). In the second series of tests, however, the local stress disturbances have been neglected. The results, which are presented in fig. 4.21, reveal that the mean value of required load is significantly higher in the second test series than in the first test series (814 MPa to 779 MPa). The logical conclusion is that the local stress fluctuations must not be neglected. If cracks have nucleated under certain loading conditions, and if these loading conditions are retained, then the local stress disturbances due to these cracks promote the nucleation of further cracks.

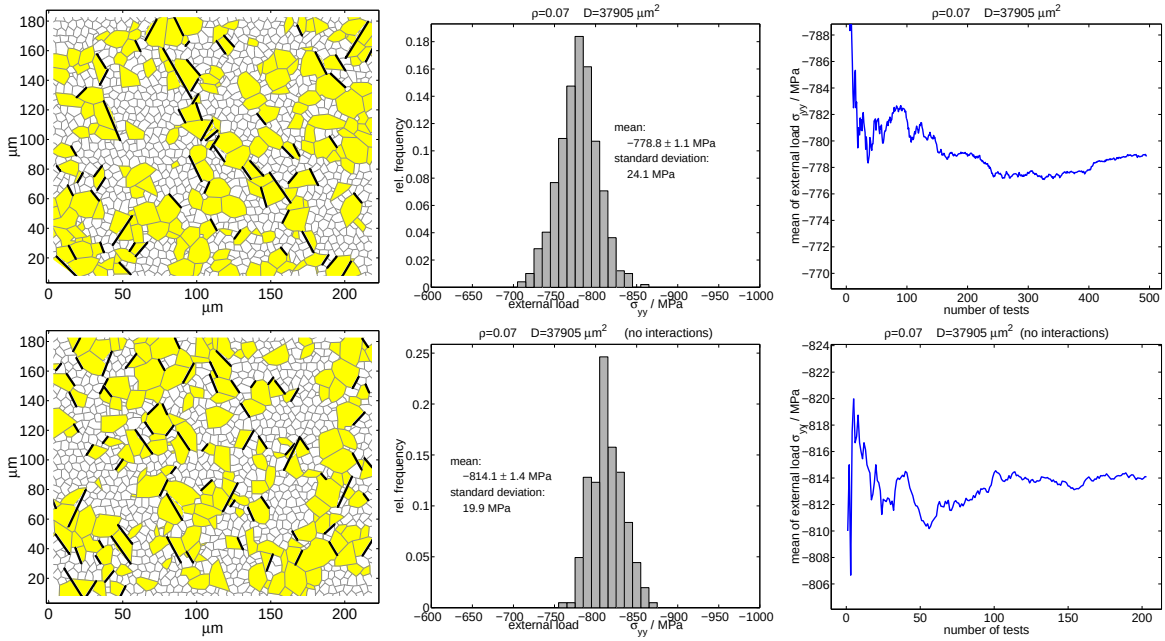

Figure 4.21: Studies on specimens (size 37905 μm^2) under compression. The compression is increased until the crack density reaches a value of $\rho = 0.07$. The figures on the left represent exemplary specimens of each test series. Above: calculation with interactions (crack↔crack, crack→facet). Below: calculation without interactions.

Significance of specimen size. Figure 4.22 shows a test series performed on specimens sized 57% larger than the other specimens of the current section. The results are to be compared with those presented in fig. 4.21 (first series, above). It is seen that the average resistance is higher for the larger specimens than for the smaller specimens (819 MPa to 779 MPa). One must suppose that this obvious effect is due to the reduced boundary effects in the larger specimens. Indeed, the specimen borders act as barriers for microcrack expansion, and the interaction between cracks located inside a specimen and cracks located outside are completely disregarded. These shortcomings are coupled to the specimen size and must not be ignored.

Another point to mention here concerns the size of the representative volume element: In the course of damage progression, the length over which the cracks are correlated increases, and the RVE grows in size. In this context, smaller specimens will sooner cease to be statistically homogeneous than larger specimens.

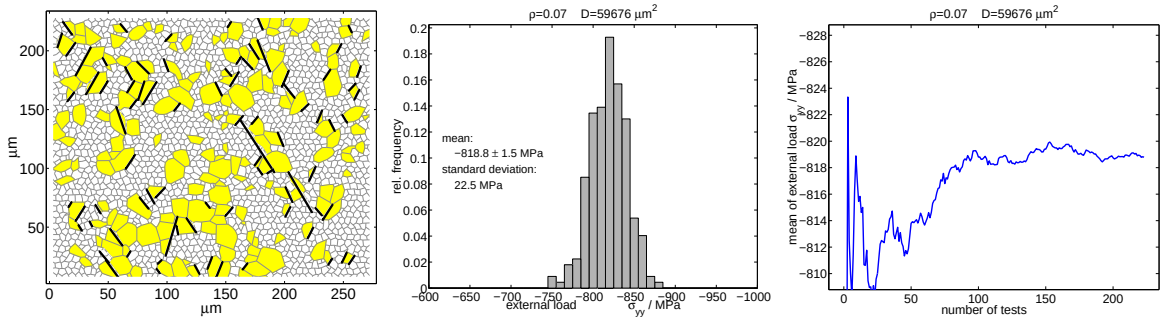

Figure 4.22: Studies on specimens (size 59676 μm^2) under compression. The compression is increased until the crack density reaches a value of $\rho = 0.07$. The figure on the left shows an exemplary specimen of the test series.

4.4 Stochastic analytical approaches on progressive fracturing

The previous section has demonstrated how the numerical model can be employed in Monte Carlo simulations to obtain expectation values for 'global' parameters such as the crack density, or macroscopic material properties such as the overall strain. In principle, the results for deliberate test series could be collected and concentrated into macroscopic expectation laws for the material behaviour.

To round off the considerations on progressive damage in compact materials, the present section tries to outline an alternative, more elementary way to deduce a continuum law for the progressively fracturing material from the background micromechanical theory. Typically for such 'evolutionary' continuum damage models, the present approach aims at the change and evolution of the effective moduli as a function of applied load. The formalism is intended to be throughout analytical, a demand which necessitates a transition from the previous discrete system to a continuum, namely from the discrete facet and crack arrangement to a continuous facet and crack distribution. To this end, the statistical input information must be available in terms of distribution functions or probability density functions.

The presented formalism restricts to crack nucleation under simple conditions. Crack interactions and effects of crack closure are not accounted for. In the second part of the section, a different approach will be sketched which deals with crack extension (but not crack nucleation), and accounts for crack interactions and crack closure.

Establishing an elementary analytical approach. In general, the effect of damage on the response of the material is a degradation of its elastic stiffness and, inversely, an enhancement of its elastic compliance. To establish a continuum law for this phenomenon, the micromechanical equation (3.37) (p. 72) in the previous chapter serves as a starting point; it expresses the contribution $\mathbf{C}_{\text{cracks}}$ of a discrete ensemble of non-interacting cracks to the total compliance $\mathbf{C}$ of the two-dimensional structure.

If the density of microcracks is high and the distribution of crack lengths and orientations is considered continuous, then the summation can be replaced by an integration over the entire range of crack lengths and crack orientations ([48], [62]). A crack density function $\rho_c(l,\theta)$ can be introduced such that $\rho_c(l,\theta)\ \mathrm{d}l\ \mathrm{d}\theta$ represents the number of microcracks per unit area with lengths in the range $[l, l+\mathrm{d}l]$ and orientations in the range $[\theta, \theta+\mathrm{d}\theta]$ (fig. 4.23).[6] If the structural information on the respective specimen is not exactly known, the density distribution function ρ_c may possibly be given by a probability density function p in the sense of eq. (4.17) (p. 108):

$$\rho_c(l,\theta) = \frac{N}{A}\ p(l,\theta)\ , \tag{4.18}$$

where N/A denotes the total number of cracks per area.

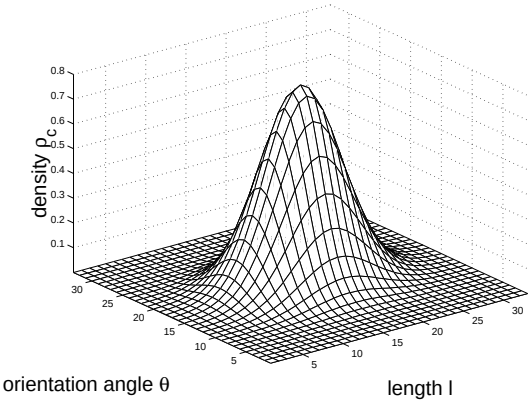

Figure 4.23: Normal distribution as an example for the crack (or facet) density function $\rho(l,\theta)$.

Using this quantity, the contribution of the continuous crack ensemble to the effective compliance can be expressed as follows:

$$\mathbf{C}_{\text{cracks}} = \frac{\pi}{2E'} \int_{\theta} \int_{l_{\min}}^{l_{\max}} l_c^2\ \mathbf{N}_\theta\ \rho_c(l_c,\theta)\ \mathrm{d}l_c\ \mathrm{d}\theta\ , \tag{4.19}$$

[6] The crack density distribution function $\rho_c(l,\theta)$ must be strictly distinguished from the crack density parameter ρ (eq. 2.3, p. 36).

where the integrations have to be performed over the entire distribution range of the variables l and θ, respectively.[7]

The next step is the case of progressive fracture. The scope is to determine the change $\mathrm{d}\mathbf{C}(\boldsymbol{\sigma}) = \mathrm{d}\mathbf{C}_{\mathrm{cracks}}(\boldsymbol{\sigma})$ of the compliance due to microcracking when the applied stress is enhanced by an infinitesimal step from $\boldsymbol{\sigma}$ to $\boldsymbol{\sigma} + \mathrm{d}\boldsymbol{\sigma}$. Obviously, one has to deal here with the density function $\rho_f(l, \theta)$ of the *potential* cracks instead of a crack density function ρ_c. Following the assumptions of the present thesis, ρ_f represents a *facet* density function. Substituting ρ_c in eq. (4.19) by ρ_f, and accounting for only those facets of orientation θ which have — at the current load $\boldsymbol{\sigma}$ — the 'critical' length $l_{(\boldsymbol{\sigma},\theta)}$, one obtains

$$\mathrm{d}\mathbf{C}(\boldsymbol{\sigma}) = \frac{\pi}{2E'} \int_\theta \left(l_{(\boldsymbol{\sigma},\theta)}\right)^2 \ \mathbf{N}_\theta \ \rho_f(l_{(\boldsymbol{\sigma},\theta)}, \theta) \ \frac{\mathrm{d}l_{(\boldsymbol{\sigma},\theta)}}{\mathrm{d}\boldsymbol{\sigma}} \mathrm{d}\boldsymbol{\sigma} \ \mathrm{d}\theta \ . \tag{4.20}$$

The 'critical' length $l_{(\boldsymbol{\sigma},\theta)}$ is the crucial term here; facets with orientation angle θ and length $l_{(\boldsymbol{\sigma},\theta)}$ will fail as soon as the applied stress assumes a value $\boldsymbol{\sigma}$. The function $l_{(\boldsymbol{\sigma},\theta)}$ thus denotes the 'fracture surface' (compare [24]) in the l-θ-$\boldsymbol{\sigma}$-space.

An explicit expression for $l_{(\boldsymbol{\sigma},\theta)}$ can be deduced from the energy criterion introduced in section 4.1. In the 'critical' case of energy balance, eq. (4.3) reads

$$\frac{\pi \ {l_{(\boldsymbol{\sigma},\theta)}}^2 \ |\mathbf{t}(\boldsymbol{\sigma}, \theta)\,|^2}{4E'} = 2\gamma \ l_{(\boldsymbol{\sigma},\theta)} \ , \tag{4.21}$$

so that one finds

$$l_{(\boldsymbol{\sigma},\theta)} = \frac{8\gamma E'}{\pi |\mathbf{t}(\boldsymbol{\sigma}, \theta)\,|^2} \ . \tag{4.22}$$

The explicit components of the traction vector $\mathbf{t}(\boldsymbol{\sigma}, \theta)$ can be directly adopted from equations (3.35) and (3.36) (p. 72).

Ultimately, integration of the increments $\mathrm{d}\mathbf{C}$ in eq. (4.20) along the stress path $\boldsymbol{\sigma}$ yields the desired continuum evolution law for the compliance.

[7] If one can assume that the crack lengths and orientations are independently distributed, then the density function admits the multiplicative decomposition [48]:

$$\rho_c(l, \theta) = \rho_c(l)\rho_c(\theta) \ ,$$

where the individual density functions have to be normalized such that

$$\int_{l_{\min}}^{l_{\max}} \rho_c(l) \ \mathrm{d}l = \frac{N}{A}$$

and

$$\int_{\theta_{\min}}^{\theta_{\max}} \rho_c(\theta) \ \mathrm{d}\theta = 1.$$

The contribution of the crack ensemble to the effective compliance is then:

$$\mathbf{C}_{\mathrm{cracks}} = \frac{\pi}{2E'} \left[\int_{l_{\min}}^{l_{\max}} (l_c)^2 \rho_c(l) \ \mathrm{d}l\right] \left[\int_{\theta_{\min}}^{\theta_{\max}} \mathbf{N}_\theta \ \rho_c(\theta) \ \mathrm{d}\theta\right].$$

A different approach from the literature. Most of the evolutionary damage models available in the literature either neglect the crack interactions (which means they restrict to small crack densities) or account for them in a quite simplified manner, e.g. by means of the self-consistent method (see [38] for literature informations). On the other hand, the strong microcrack interaction models (see [38] for literature informations) usually restrict to deterministic and *stationary* crack arrays and thus do not belong to the class of *evolutionary* damage models.

As an example for a formalism which includes damage evolution, statistical input, explicit crack interactions and even crack closure, mention can be made of the approach by Ju and Chen [39], which is an extension of the stationary model outlined in section 3.2.2.4 (p. 56). The underlying ideas of 'pairwise' interactions and 'ensemble averaging' have already been described there.

The approach by Ju and Chen to damage evolution accounts for the growth of *pre-existing* microcracks in the course of loading. The growth is described in a rather simplified manner: Once the local fracture energy is reached, the microcrack length changes instantaneously from an initial value to a previously specified final value (which can be associated with a full facet length, for example). Multiple crack extensions, kinked crack extensions, coalescence of cracks etc. are not considered. The fracture criterion employed by Ju and Chen is a function of the stress intensity factors of the initial crack. With respect to the pairwise crack interactions, sometimes extensive case distinctions have to be performed in order to assess whether the second of the two cracks has still initial or already extended length.

Depending on the external loading conditions and the respective crack orientation angle, the set of all cracks has to be permanently divided into 'process domains' of active, unstable cracks and domains of stable, closed cracks.

The common feature of all 'strong interaction' models, including that by Ju and Chen, is the high numerical computational effort required to get closed-form solutions.

Chapter 5

Progressive damage under internal pore pressure

The present chapter focuses on microcracking in porous ceramics under pressure acting inside the pores. This loading mode, typically transmitted by a fluid, is dominant under service conditions in filtration equipments.

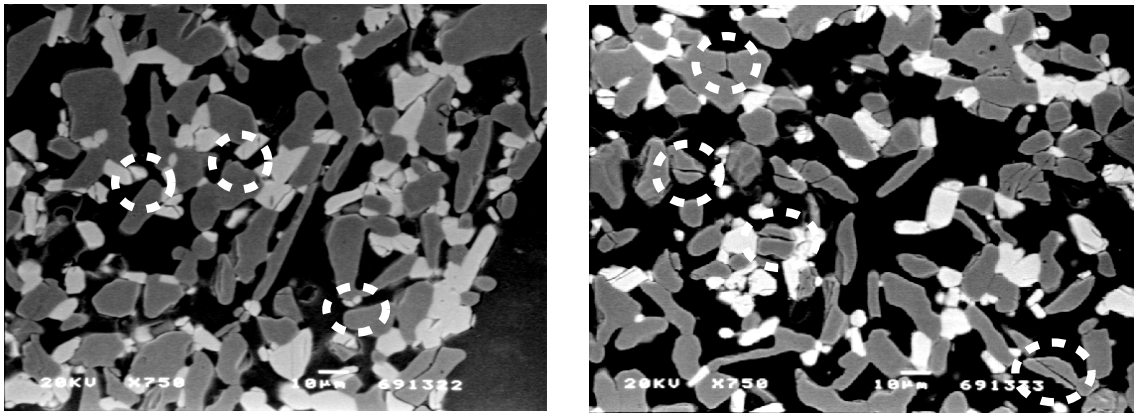

Figure 5.1: Scanning electron micrograph of a porous ceramic (TiO_2 *and* Al_2O_3 *grains, porosity* 0.4*) after industrial use as a filter support [64]. Left: Specimen from the vicinity of a flow channel. Microcracks are observed within the agglomerates of* TiO_2 *grains as well as in the* Al_2O_3 *grains. Right: Far from the channels, microcracks are observed primarily between or within* Al_2O_3 *grains. Some cracks are pointed out by the dashed circles.*

The particular mode of loading by internal pressure raises some crucial tasks which necessitate an adjustment of the background numerical approach. A first idea of the subject is gained when one considers the local stress distribution in the model images (section 5.1): Locations critical to damage are observed in the immediate vicinity of pores, especially in narrow solid ligaments between pores. This feature corresponds to crack patterns detected by scanning electron microscopy in industrial filter supports (fig. 5.1).

In contrast to cracking far from or in absence of pores, description of crack formation at these locations involves a first fundamental difficulty: Applying the fracture criterion introduced in the previous chapter to decide on failure of grain facets requires knowledge of the stress distribution around cracks emanating from pores. The availability of analytical stress solutions is restricted to very simple geometries, and extrapolation to arbitrary

configurations is necessary. The associated theory, which is outlined in section 5.2, allows for the identification of 'critical facets' in explicit grain structure models (section 5.3).

A second essential problem, subject of section 5.4, is ensuing from damage progression: patterns of local pore–crack networks have to be recognized since the maximum extent of such connected flaws is decisive in assessing the actual state of damage; common parameters as the crack density lose their meaning here where cracks are connected to pores. The limiting state of a flaw chain separating the specimen (percolation) is considered as failure of the material. In addition, analytical stress distributions do not suit with the complex shape of pore–crack networks. Therefore, in a simplified treatment the flaw networks are modelled as larger cavities, and fracturing is effectively considered at the extremities of the flaw network, thus assuming that the intrusion of a fluid in the solid via microcracking is driven by the tips of the flaw network.

Finally, the performance of the damage model under the specified conditions is investigated for selected test cases in section 5.5. A number of statistical studies addressing effects of specimen size and of pore phase properties on the strength of the material is presented and evaluated. The connection to failure in weakest-link theories is discussed.

5.1 Local stresses in porous microstructures under internal pressure

Accounting for the location and orientation of the pores in the microstructure model, superposition of the stress solutions for the individual pores under internal pressure (section 3.3.3, p. 68) leads to a complex distribution of the stresses (fig. 5.2). The simulation relies on a dilute approximation, which means that the pores are considered isolated and the interactions between them are neglected.

The local stress fields clearly reveal the sectors in the solid material phase which are exposed to the highest load: locations in the vicinity of strongly curved pore borders, and even more where two of these pore 'tips' are close together. Regarding the simulation of progressive damage, this makes clear that the attention must be directed to the ligaments between the pores.

As has already been sketched in Chapter 2 (fig. 2.5, p. 38), the consideration of the material bounding the respective specimen is restricted to a certain margin. Stresses induced by pores located within the margin are accounted for within the specimen. Figure 5.3 illustrates for the present mode of internal pressure that those pores located remotely outside the specimen can indeed be disregarded; the stresses from pores within the margin represent sufficiently the effect of the surroundings.

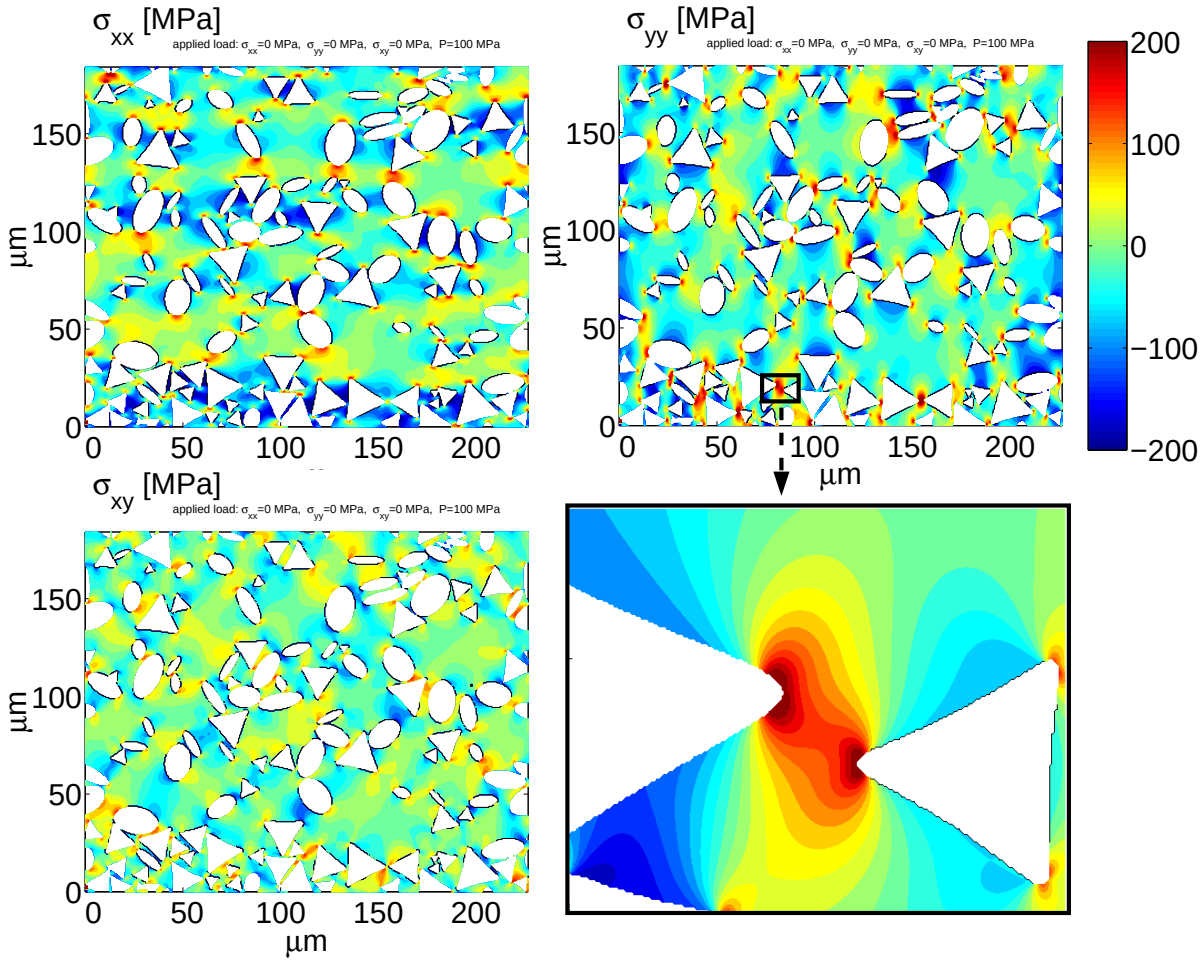

Figure 5.2: Local stress distribution in a porous microstructure (in the absence of microcracks) under internal pressure. The enlarged detail of the σ_{yy} field demonstrates that narrow solid ligaments between pores are most critical to damage.

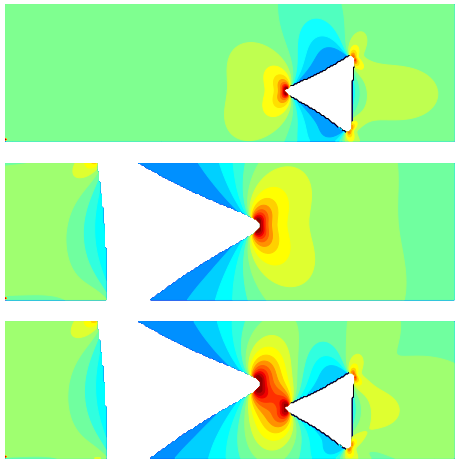

Figure 5.3: Local σ_{yy}–stress field induced by single pores under internal pressure (above and middle). In a superposition approach (below), the respective stress disturbance obviously is negligible beyond the neighbouring pore.

5.2 Elastic description of cracks emanating from pores

Since stress concentrations are encountered in the vicinity of pores, the microcracks are expected to start from the border of the existing cavities. Therefore, the energetical description of crack nucleation from pore boundaries and of subsequent crack extension is a main topic of the current chapter.

In the following, a suitable analytical solution is presented for the stress concentration at a crack which emanates from a pore, and it is outlined how the solution is employed in the numerical model: in the fracture criterion, and for determination of the strain contribution.

Without exception, the considerations in the current chapter refer to the loading conditions of internal pressure.

5.2.1 Stress concentration at cracks emanating from pores

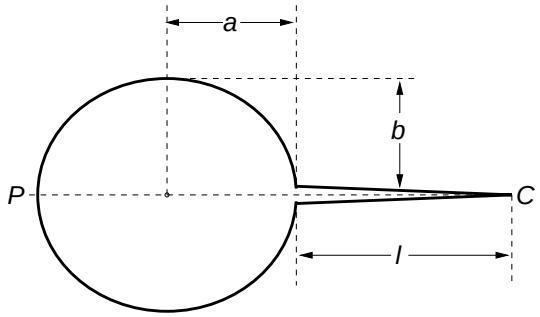

Figure 5.4: Crack emanating from an elliptical pore in the direction of a semi-axis.

An essential situation encountered in structures with pores under pressure concerns cracks emanating from a pore or connecting two pores. The most comprehensive analytical stress solution found in the literature is given by Berezhnitskii [7] and refers to cracks in the elongation of the axes of elliptical pores (fig. 5.4).

According to this solution, the internal pressure P or

$$t = \frac{K}{\pi}\sqrt{\frac{1}{a+\frac{l}{2}}}\sqrt{\frac{\left[1-\frac{m}{(1+l/a)^2}\right]\left[1+\frac{m}{1+l/a}\right]}{\left[1-\frac{1}{(1+l/a)^2}\right]\left[1+\frac{1}{1+l/a}\right]}}, \tag{5.1}$$

where a and b denote the semi-axis lengths of the elliptical pore, and l is the length of the crack (see configuration in fig. 5.4); $m = (a-b)/(a+b)$ is a shape parameter of the elliptical pore. A graphical representation of the stress intensity factor is given in fig. 5.5. (A similar relation corresponding to eq. (5.1) for *uni*axial tension can be found in [44]. Relations for cracks emanating from hypocycloid cavities[1] are presented in [7] also.)

Equation (5.1) has to be appropriately extrapolated for arbitrary crack–pore configurations regarding the position of the crack, the relative orientation of crack and pore semi-axes, and the different shapes of the pore. Figure 5.6 illustrates the way of extrapolation. Triangular pores are approximated by circular pores of equal area (since both triangular and circular cavities are isotropic inhomogeneities).

[1] cavities with concave borders and sharp corners

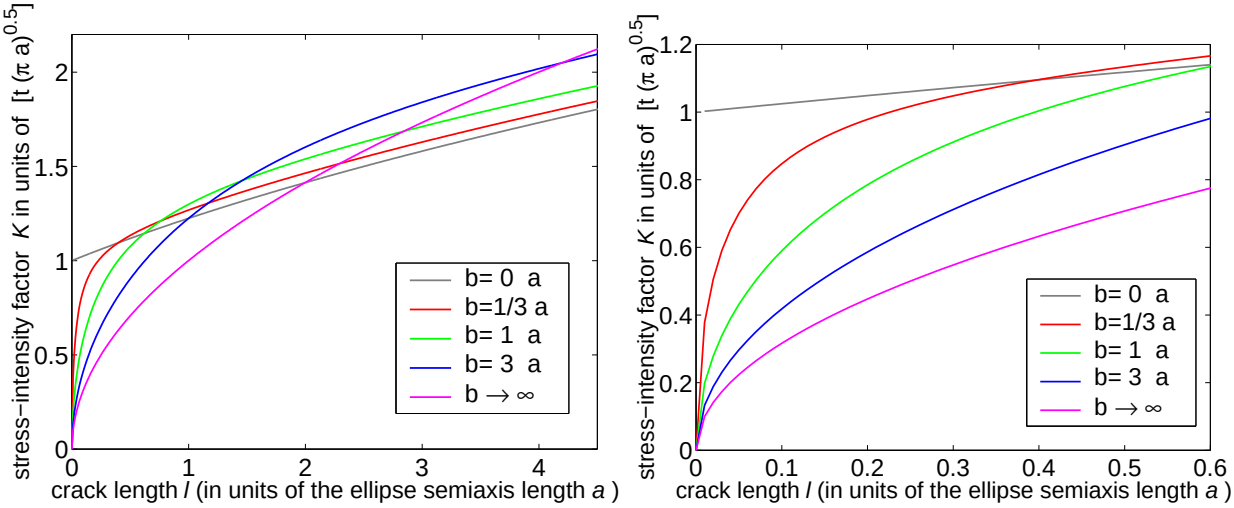

Figure 5.5: Stress intensity factor for a crack emanating from an elliptical pore (see fig. 5.4), as a function of normalized crack length and for various shapes of the pore, following the analytical results by Berezhnitskii [7].

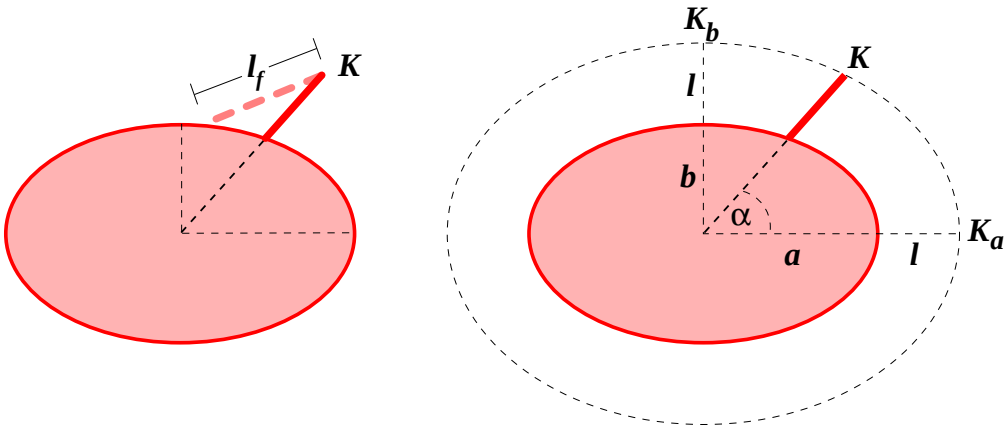

Figure 5.6: Left: Regarding the stress intensity factor, a crack with arbitrary orientation to the pore (dashed bold line) is treated as emanating 'radially' from the pore (solid bold line). Regarding the surface of the crack, the pristine (actual) facet length l_f is stored. Right: Approximation of the stress intensity factor K of a crack emanating in an arbitrary way from an elliptical pore: $K = K_a + \alpha/\left(\frac{\pi}{2}\right)\ (K_b - K_a)$

5.2.2 On the strain energy release

Equation (5.1) enters the strain energy term in the fracture criterion. For straight extension of a crack (length l_0) along a grain facet of length l_f, the stress intensity factor K can be directly employed in eq. (4.8) (see section 4.1, p. 94):

$$\int_{l_0}^{l_0+l_f} G \, \mathrm{d}l = \int_{l_0}^{l_0+l_f} \frac{K^2}{E'} \, \mathrm{d}l \ \geq \ 2\gamma_f \, l_f \ ; \tag{5.2}$$

the case $l_0 = 0$ refers to crack formation from the elliptical pore. The complicated expression for K from eq. (5.1) necessitates numerical evaluation of the integral in eq. (5.2).

Figure 5.7 shows plots of the critical loads for both crack extension and crack nucleation, as a function of relative crack length and of pore shape (ratio of semi-axes).

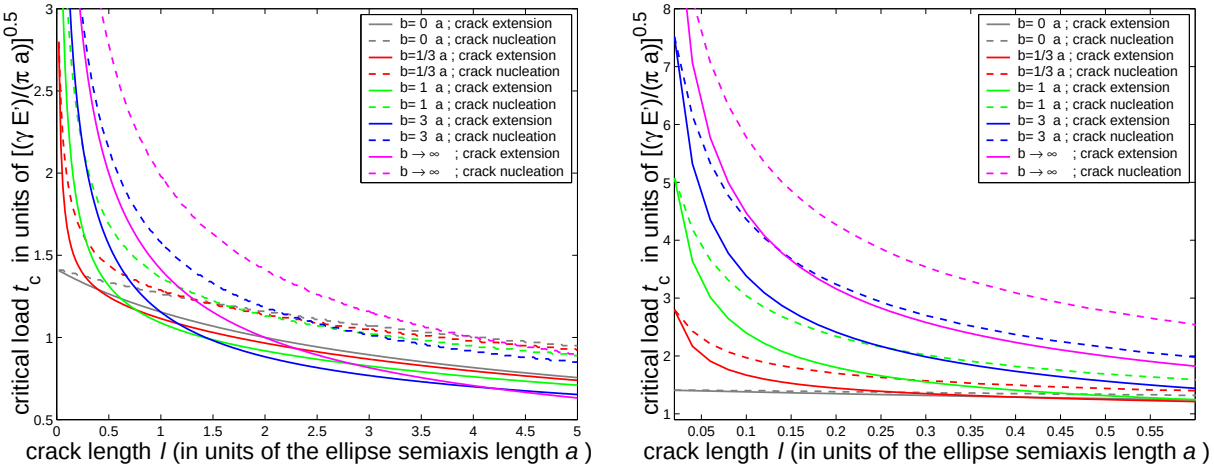

Figure 5.7: Critical biaxial tension resp. critical internal pressure on the pore–crack combinations (fig. 5.4), as a function of normalized crack length for various shapes of the pore. It can be concluded that for short cracks (length l/a), the stability of the system reduces with decreasing pore semi-axis b/a, while for long cracks the stability reduces with increasing semi-axis b/a. The solid-line curves refer to the critical load for unstable crack extension (as a function of crack length), while the dashed curves refer to the load necessary for crack nucleation (as a function of facet length).

For a determination of the individual contribution to the overall strain, an important quantity is the average opening displacement $\langle \mathbf{b} \rangle$ of the crack emanating from the pore. It can be determined from the reduction of strain energy in the material due to formation of the crack, which reads

$$\int_0^l G \, \mathrm{d}l = \int_0^l \frac{K^2}{E'} \, \mathrm{d}l \ . \tag{5.3}$$

By assigning the total amount of strain energy release ($\int_0^l G \, \mathrm{d}l$) to a work *on the crack only*, a relation can be established as follows:

$$\frac{1}{2} \langle \mathbf{b} \rangle (\mathbf{t} \cdot l) = \int_0^l \frac{K^2}{E'} \, \mathrm{d}l \ , \tag{5.4}$$

where $\mathbf{t}$ denotes the load on the crack (internal pressure P or biaxial tension). Due to the particular loading mode, the shear components of $\langle \mathbf{b} \rangle$ and $\mathbf{t}$ can be assumed to vanish, so that a scalar expression for the normal crack opening displacement (note that $t^{\mathrm{n}} = P$) is obtained:

$$\langle b^{\mathrm{n}} \rangle = \frac{2}{t^{\mathrm{n}} \, l} \int_0^l \frac{K^2}{E'} \, \mathrm{d}l \tag{5.5}$$

This expression for the opening displacement can be employed in eq. (3.31) (p. 71) to deduce the strain contribution of the crack in question.

Another important point to mention concerns the strain release associated with failure of a *bridging* facet between two pores. The approximation model separates the pore-crack-pore combination into two individual pore-crack combinations (see fig. 5.8 for illustration), and sums up three terms: the strain energy released by an isolated crack (length l equal to the facet length), the additional strain energy release due to the fact that the crack opens into the one pore, and the additional strain energy release due to the fact that the crack opens into the second pore. The actual strain energy release, however, is underestimated to some extent by this approach.

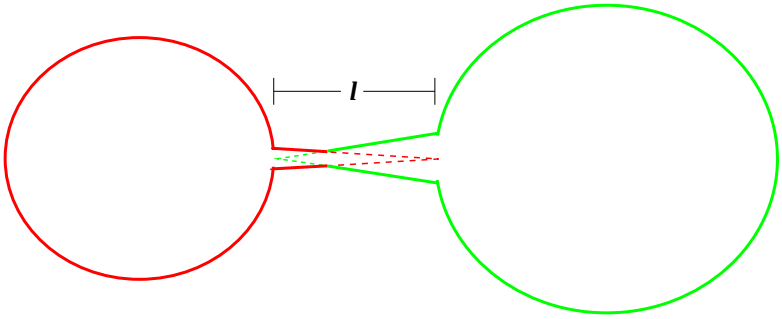

Figure 5.8: Model approach for the failure of a bridge facet (length l) between two pores: the pore-crack-pore combination is virtually separated into a pore-crack combination (on the left) and a crack-pore combination (on the right).

5.3 Critical locations for microcracking

As a first step, the fracture criterion may be applied for an identification of critical locations in the microstructure, i.e. locations where nucleation and successive growth of microcracks has to be expected. (The present section corresponds to section 4.2.1 for compact materials).

In extension of the observations in section 5.1, which reflect the effect of the porous phase only, the present consideration accounts for the local properties of the grain phases, too. In particular, the length, orientation, and specific surface energy of the grain boundaries is playing an important role now.

Figures 5.9 and 5.10 illustrate those facets within a simple microstructure whose failure would become energetically possible at a certain level of the pore pressure.

The driving force for facet failure is not exclusively the local load transmitted by the solid material around pores under internal pressure (fig. 3.12, fig. 3.13, fig. 3.14). To this one has to add the impact of a pressure acting inside the *potential* new crack. The latter must not be neglected in the energy criterion, which compares the energetical states of the material before and after cracking.

On the other hand, fig. 5.10 reveals that the energy criterion is not sufficient for deciding on microcrack nucleation: The interpretation of several facets located at the flat parts of the triangle border as 'critical' is due to the consideration of pressure inside the *potential* crack, but this does not match with reality since the normal compression acting on the facet prevents its failure (consider fig. 3.14, p. 69).

This observation leads to the conclusion that a *hierarchy* of conditions is needed to decide on facet failure under internal pressure: the first one claiming the load on a candi-

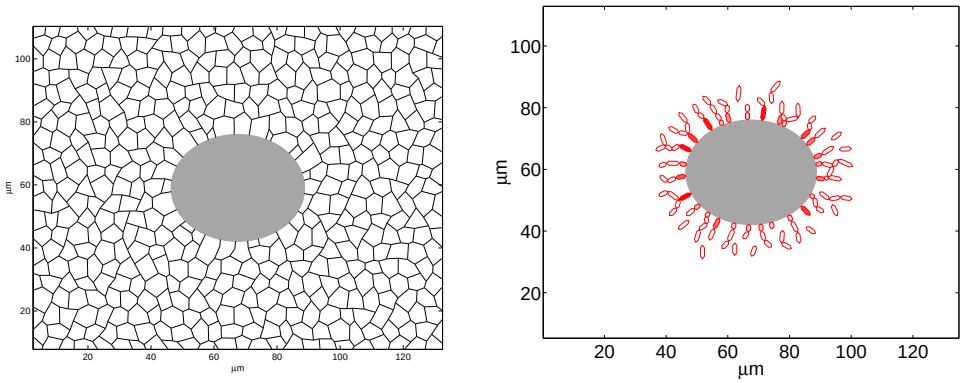

Figure 5.9: Left: a single elliptical pore surrounded by a grid of grain boundaries (network of potential cracks). Right: 'Critical locations' (identified by the energy release due to facet cracking) under internal pore pressure. Assuming $\gamma = 2$ Jm^{-2} for the surface energy, the indicated facets would have failed at a pressure $P = 1500$ MPa.

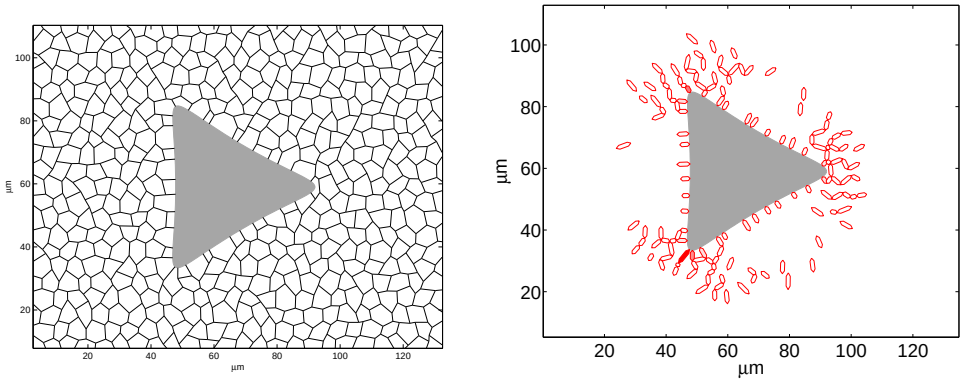

Figure 5.10: Left: a single triangular pore surrounded by a grid of grain boundaries (network of potential cracks). Right: 'Critical locations' (identified by the energy release due to facet cracking) under internal pore pressure. Assuming $\gamma = 2$ Jm^{-2} for the surface energy, the indicated facets would have failed at a pressure $P = 1500$ MPa. (Note: The interpretation of the single facets located at the flat parts of the triangle border as 'critical' is due to the consideration of pressure inside the potential crack (see section 4.1); this approach is obviously not appropriate in the current example, since these facets are under external compression (fig. 3.14).)

date facet to be not negative, the second one claiming a lower energy state of the cracked configuration.

Figure 5.11 finally shows critical locations in a complex microstructure. Even if the process of fracture is not yet considered at the moment, the sensitivity of ligaments between closely located pores to cracking becomes obvious. The calculations presented in the following sections will confirm that unstable damage progression mostly starts with the failure of a bridge facet.

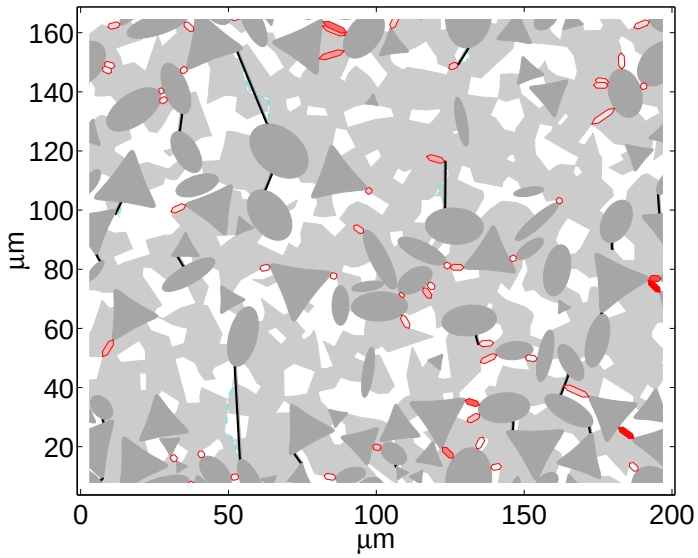

Figure 5.11: Porous microstructure containing already several cracks (black lines): Potential energy release identifies critical locations due to internal pressure in the pores.

5.4 Formation of flaw networks and percolation

The next step addresses the flaw patterns which result from coalescence of the pores by microcracks. They require extended efforts with respect to the geometric assessment (subsection 5.4.1) and to the stress analysis (subsection 5.4.2).[2] A look at some single simulations at the microscopic level (subsection 5.4.3) will provide deeper insight into the features of progressive damage under pore pressure.

5.4.1 Assessment of damage

From all the observations in the preceding sections, there is an obvious tendency in porous microstructures under internal pressure to connect pores by microcracks. Regarding the damage simulation, this suggests the transition from the original grid of grain boundaries to a coarser lattice which restricts to direct paths between neighboured pores. Beyond that, there is a need to detect the formation of local pore–crack networks, and to treat these connected flaws as single large flaws. While the classical crack density parameter has no meaning in this context, a different, equally simple parameter is desirable for an assessment of the state of damage in the structure: In order to assess the significance of an individual pore–crack network, its largest linear extent is recorded here (fig. 5.12); in order to assess the overall damage in a specimen, the length of the largest flaw group is recorded, which ultimately indicates percolation. Percolation, i.e. the appearance of a flaw network (a cluster of interconnected defects) which separates the rectangular specimen by extending from one boundary to the opposite boundary, is considered as failure of the material.

[2] The present approach has a certain affinity to that of Jeulin (see, e.g., [36] or [35]), which deals with cracking paths minimizing the energy consumption in porous meshes under uniaxial tension. The present approach, however, goes beyond that by considering the entire flaw chain for the strain release, and by imposing much less restrictions on the possible crack pattern.

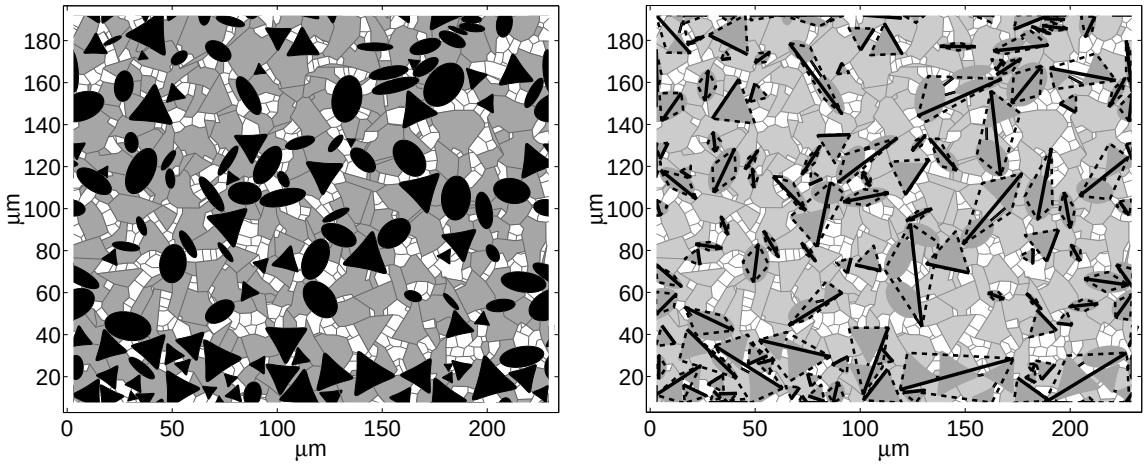

Figure 5.12: Left: undamaged microstructure. Right: After formation of some microcracks, flaw combinations (connected pores) have been recognized, and each individual flaw group is represented by a simple geometry.

5.4.2 Simulation of damage progression

The arbitrary, complex shapes of arising pore–crack networks cannot be handled by analytical stress solutions. In order to apply the available solutions in the way suggested in section 5.2, the damage simulation is confined to extension of existing flaws (i.e., pores or pore–crack networks), and the flaw networks are approximated by larger, elliptical cavities (figures 5.13 and 5.14); thus the respective extent of the flaw is accounted for in the stress analysis (section 5.2.1).

Nucleation of isolated microcracks not adjacent to pores is considered of secondary importance, and it is disregarded in view of uncertainties concerning the stress distribution. For the same reason, interactions between the individual defects (flaw combinations) are neglected.

Thus, evolution of damage is exclusively attributed to the spread of pressure from the extremities of a flaw.

5.4.3 Some general considerations

Before turning to studies on statistical samples, a consideration of some stand-alone tests should help to elucidate some phenomena.

Firstly, fig. 5.15 illustrates how the propagation of a pore/crack flaw chain may be stopped by a grain representing an energy barrier, or by the borders of the specimen. Since only a flaw chain extending from one border to the opposite border is defined as percolation and causes the simulation algorithm to stop, the case of a flaw running across a corner of the specimen involves an inevitable boundary effect.

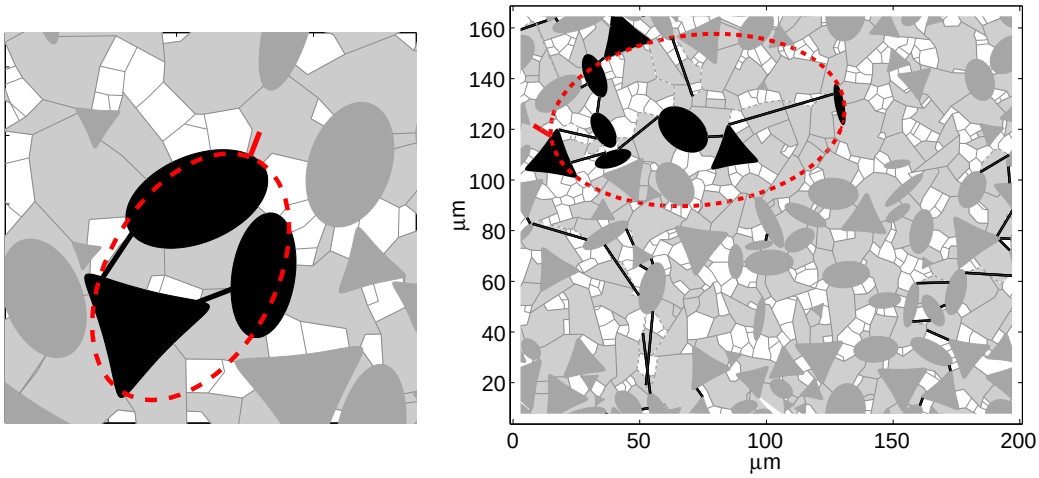

Figure 5.13: For the determination of the critical load on a facet or crack (red-coloured stroke), the pore–crack network is approximated by an elliptical cavity.

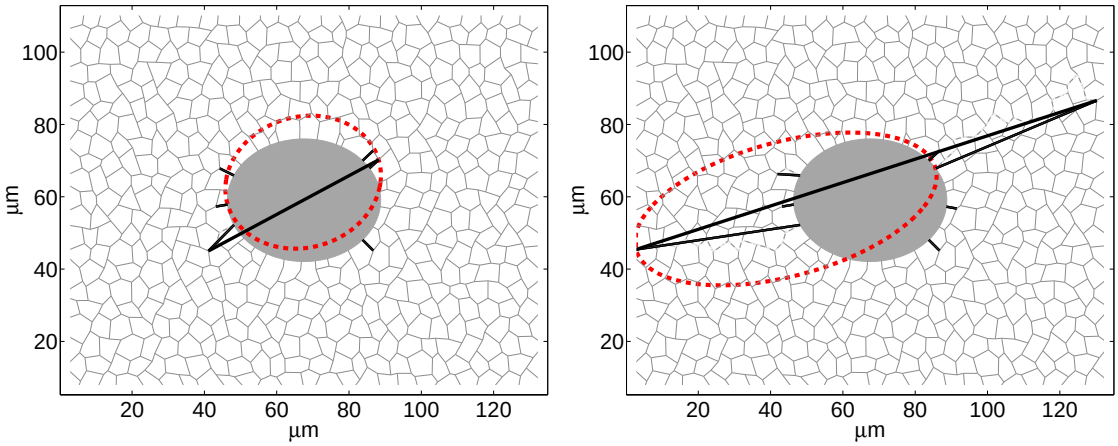

Figure 5.14: Damage progression under internal pressure in a 'solitary' pore: unstable crack growth starts (left) and finally leads to percolation (right). The bold black line indicates the maximum linear extent of the flaw.

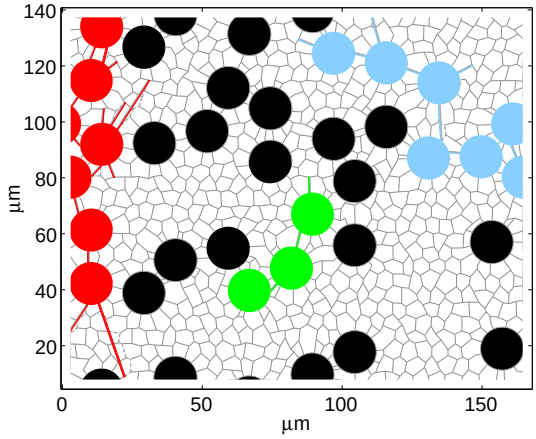

Figure 5.15: Damage propagation may be stopped by a grain (center of the specimen; green) or by the specimen border (right above, and left). The flaw chain on the left (red) is defined as percolation.

The trapping of the propagating crack by a grain is a rather rare feature in the present simple microstructures; the dominant mode is *unstable* propagation. Figure 5.16 demonstrates for four specimens of a statistical ensemble that neither the direction of the splitting paths nor the respective ultimate load can be predicted from the global parameters. A common fact is, however, that the spatial correlation of the pores significantly reduces the failure load in comparison to solitary pores: Microcracking generally starts with the failure of a *bridge* facet contacting two pores.[3]

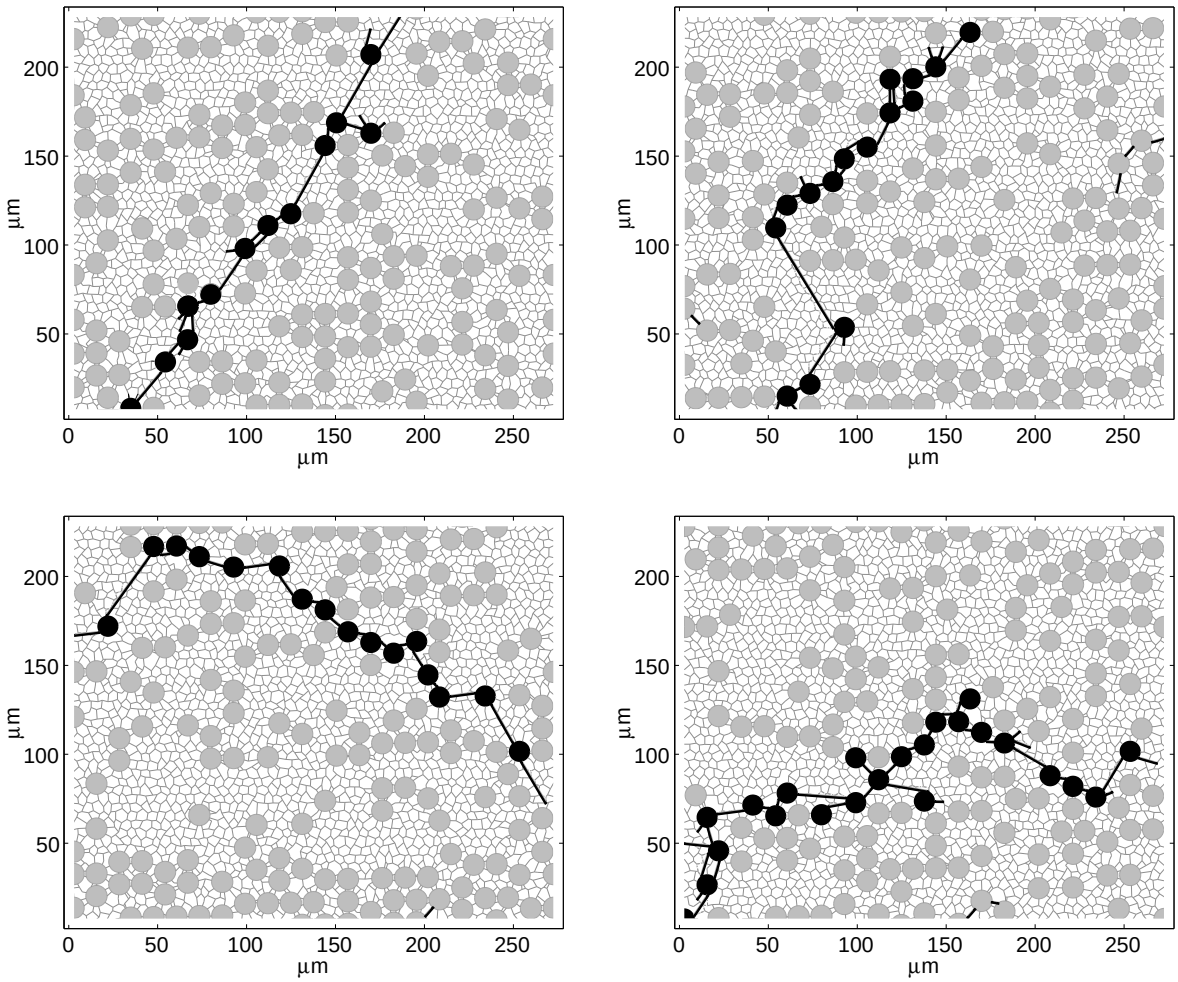

Figure 5.16: Patterns of percolation in four specimens of equal size $D = 59676\ \mu\text{m}^2$, porosity ($A_A = 0.30$), and specific perimeter of the porous phase ($L_A = 101\ \text{mm/mm}^2$). Ultimate load is 171.6 MPa, 205.4 MPa, 174.2 MPa, 187.2 MPa, respectively.

The effect of the progressive damage on some (scalar) 'damage parameters' is shown in figures 5.17 and 5.18. The diagrams in fig. 5.17 refer to the evolution of the overall strain components, i.e. to a macroscopic 'damage parameter'. The structures under consideration are rather heterogeneous, comprising several grain phases. The studies reveal a 'quasi-brittle' behaviour of the first specimen, and an almost perfectly brittle failure of the second specimen. The difference may be traced back to a slightly more inhomogeneous

[3]For a quantitative comparison, see fig. 5.28 (p. 147).

(disordered) grain structure in the first specimen; in the second specimen, the propagating flaw finds a path of rather equally-sized facets.

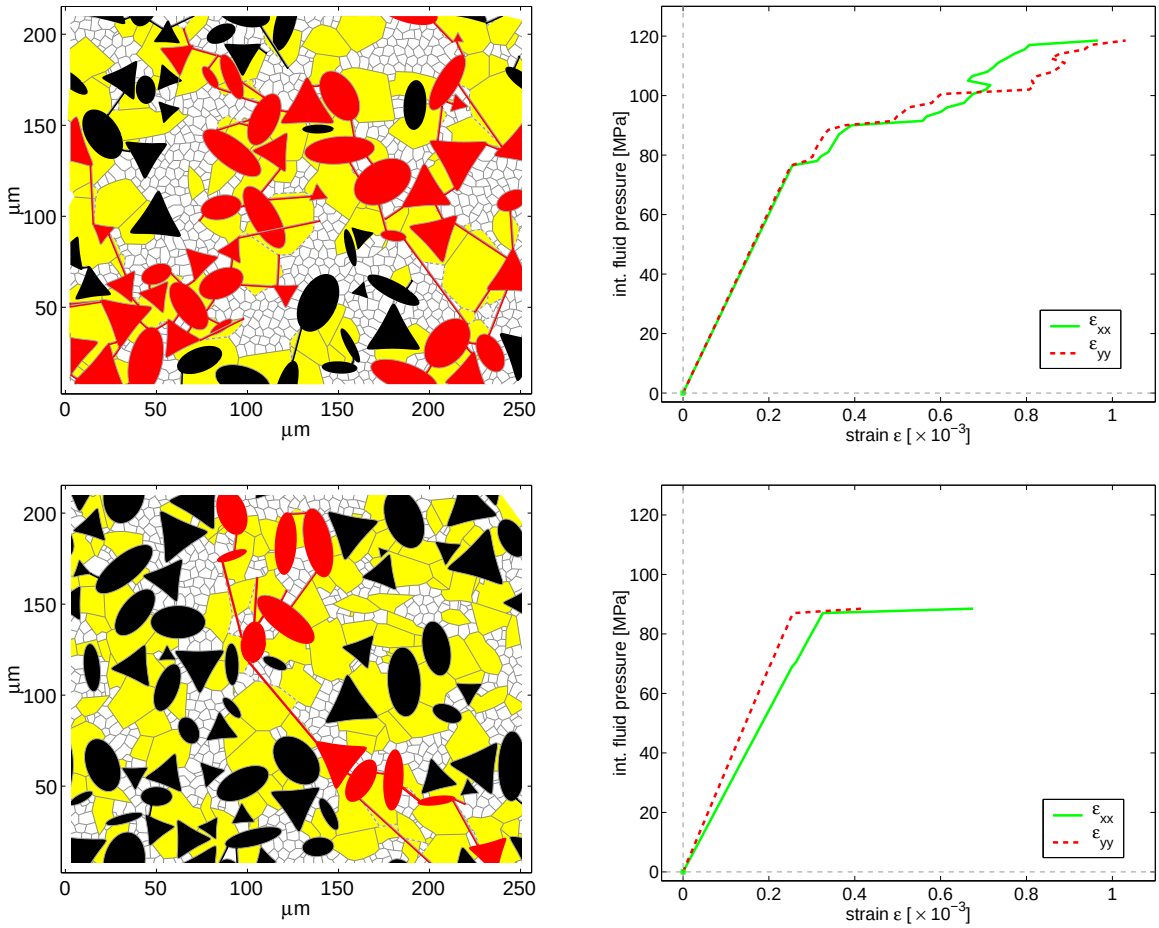

Figure 5.17: Examples of 'quasi-brittle' failure (above) and 'perfectly brittle' failure (below) under pore pressure, reflected by crack patterns and evolution of strain. (The set of pores is equal in both specimens, but the pores are randomly distributed. The grain phase parameters are different: Above: $A_A(Al_2O_3) = 0.36$, $A_A(TiO_2) = 0.31$*; below:* $A_A(Al_2O_3) = 0.40$, $A_A(TiO_2) = 0.27$.*)*

The diagrams in fig. 5.18 refer to the additional internal surface energy produced by the microcracks, and to the linear extent of the largest flaw chain. It is obvious that initiation of microcracking is immediately followed here by total failure: the considered material exhibits a rather brittle failure.

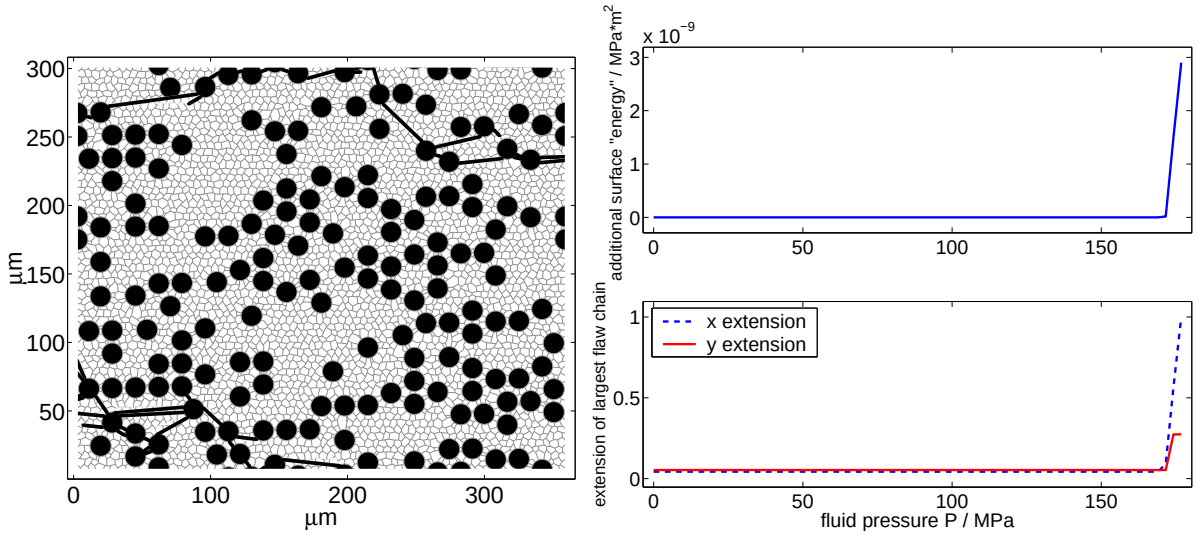

Figure 5.18: Damage evolution as a function of increasing load for a typical specimen. The upper graph shows the increase of internal surface energy due to microcracking, while the lower graph shows the length of the largest flaw chain in relation to the specimen size (x-/y-projections, a value of "1" indicates percolation).

5.5 Statistical studies on the failure of brittle microstructures under pore pressure

Now the studies will be directed to the failure of statistical samples as obtained by Monte Carlo simulation. The investigations in section 5.5.1 aim at the specimen-size effect, i.e. the scaling law, whereas section 5.5.2 explores the significance of pore-phase and grain-phase parameters. In view of the complex interrelations, the considerations restrict here to quite elementary model classes: two-phase structures, the porous phase consisting of circular resp. elliptical pores, randomly distributed within a single grain phase. In each study, basically one structure parameter is varied. Throughout the current section, the observed quantity y is the critical internal pressure ('rupture strength') P_c which causes the microstructure to fail by percolation.

The observations are fluctuating among the different units of a statistical sample. The statistical fluctuations are due to the microstructural disorder, which basically refers to the sizes, shapes and mutual positions of the pores. These 'individual' parameters represent the *characteristics* of a single specimen. On the other hand, the 'global', averaged structural parameters (specific areas, specific perimeters, size distributions, shape distributions) are equal in each specimen of a statistical sample, in fact equal to the statistical mean.[4]

For a review on the fundamental statistical terms and quantities appearing in the current section, see section 4.3.1.1 (p. 107) in the previous chapter.

[4]This means that the linear size of the specimen volume is presumed to be larger than the fluctuation length of the parameters ('mean field model', compare [48]).

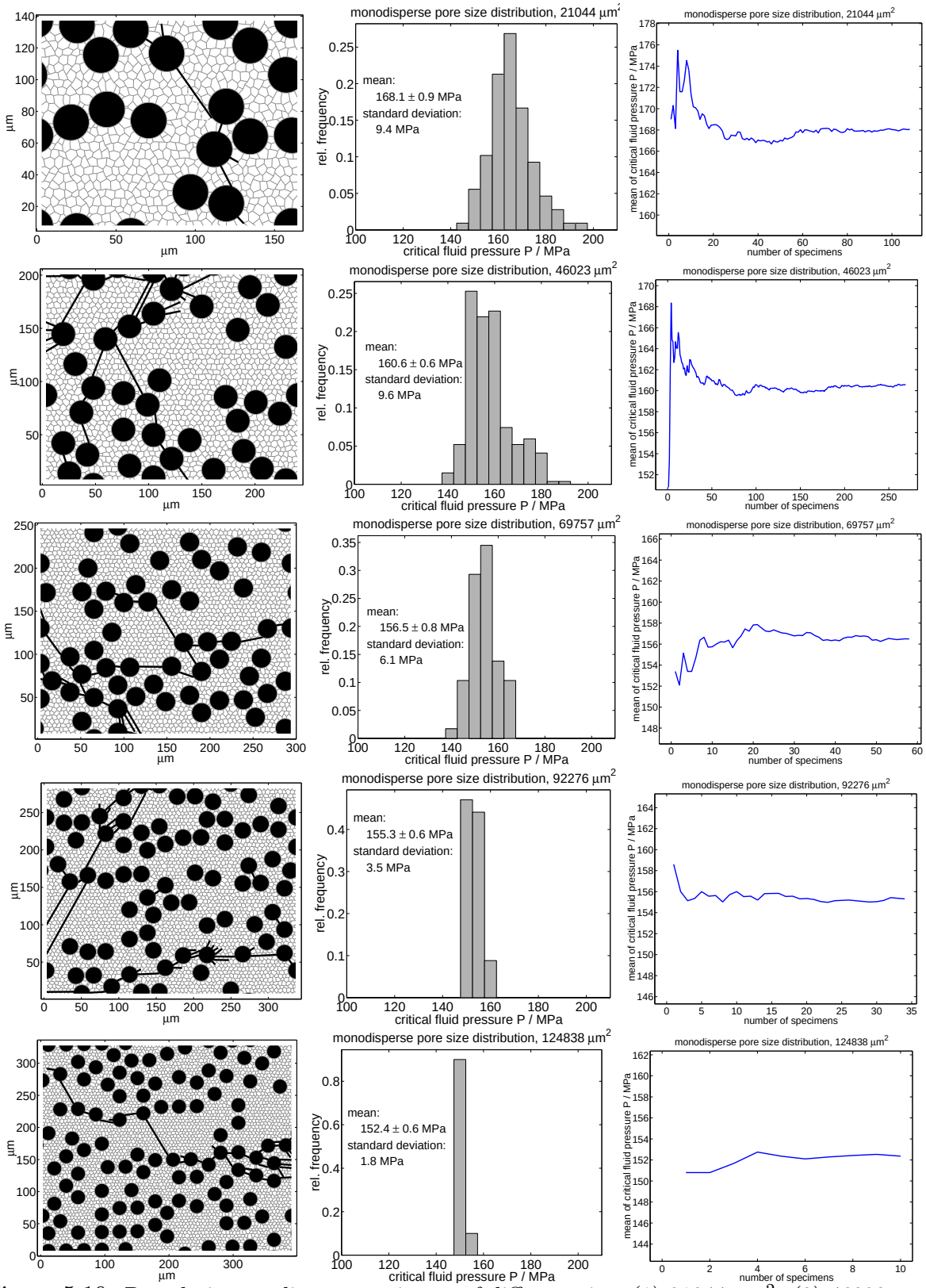

Figure 5.19: Percolation studies on specimens of different size: (1) 21044 μm^2, (2) 46023 μm^2, (3) 69757 μm^2, (4) 92276 μm^2, (5) 124838 μm^2 . The structure includes a monodisperse pore size distribution, porosity A_A(po) = 0.33, pore diameter 23.0 μm. The left column shows an exemplary specimen of each test series. The histogram plots in the middle show the relative frequency (probability) of failure for the resp. interval of internal pressure. The right column illustrates the convergence of the mean of the critical pressure with increasing number of tests.

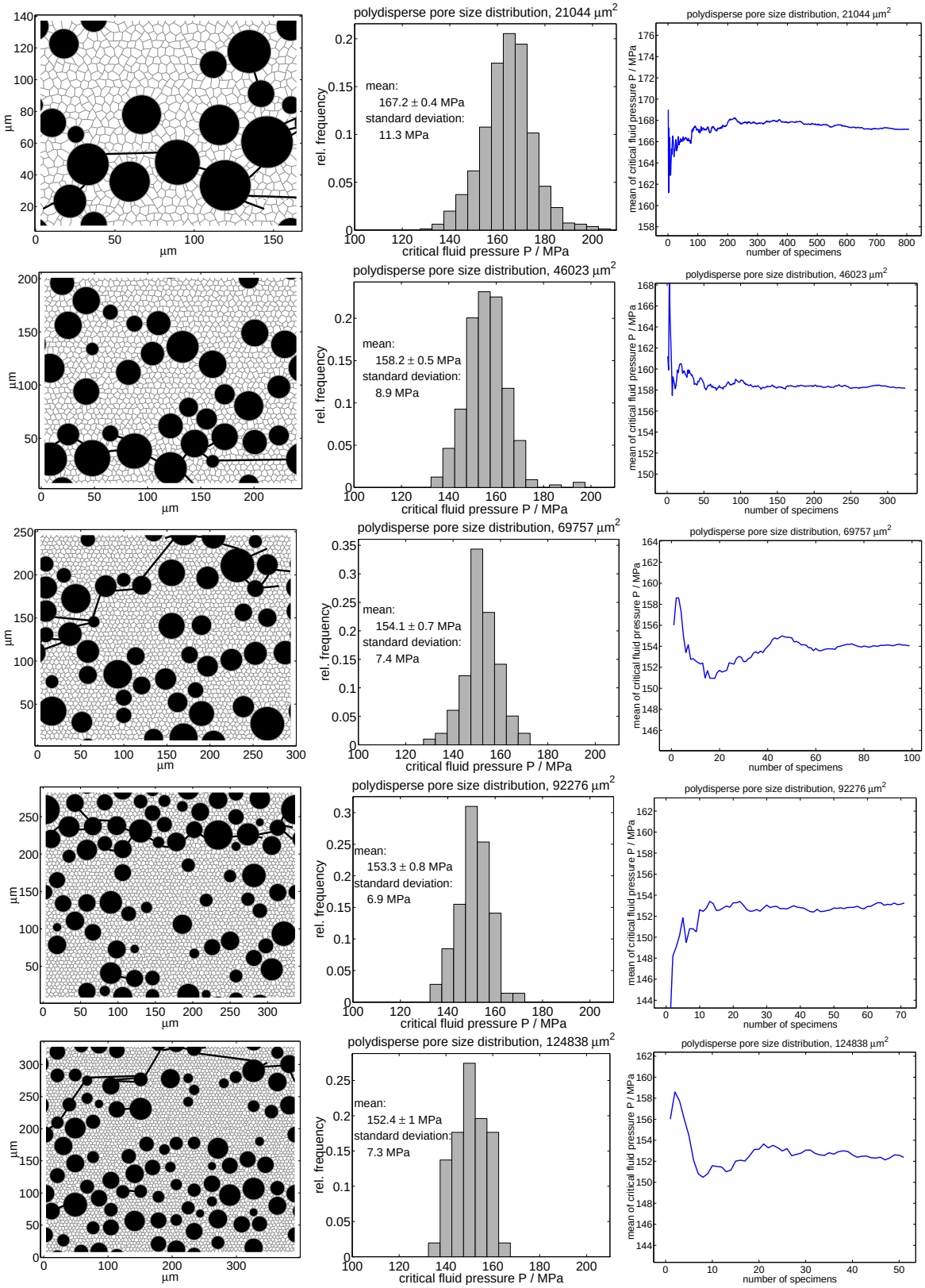

Figure 5.20: Percolation studies similar to fig. 5.19, but on specimens with polydisperse pore size distribution: the pore sizes conform to a Gaussian normal distribution (mean: 23 μm, standard deviation: 5 μm; allowed range of pore diameters: 3 μm to 40 μm; pore sizes exceeding these limits have been set equal to these limits). The porosity is $A_A(\mathrm{po}) = 0.33$. The average size of the grains is 5.4 μm.

5.5.1 Effect of specimen size

As mentioned in section 2.2, the scatter of the *structural parameters* (porosity, specific perimeter) is a function of the specimen size, whereas the mean values remain unaffected. In contrast, the present section will outline that the mean of the *strength* of the specimens is indeed a function of specimen size — an effect which is due to the statistical disorder in brittle materials, important to consider in both computational and experimental analyses.

Statistical size effects associated with fluctuating boundary conditions (as mentioned in section 3.2.3.3) do not occur in the present studies since interactions between the defects are assumed negligible. In addition, it is facilitating here that the loading conditions are not specified at the specimen boundary but at the boundaries of the defects.

Figures 5.19 and 5.20 show exemplary calculations on the specimen size effect in a material with monodisperse circular pores and in a material with polydisperse circular pores, respectively. The corresponding test results, which are summarized in fig. 5.21, serve as a basis for the subsequent detailed discussions: A brief description of the observed phenomena (5.5.1.1) is followed by approaches on an appropriate scaling law (5.5.1.2). Remarks on the existence of an RVE are added in subsection 5.5.1.3.

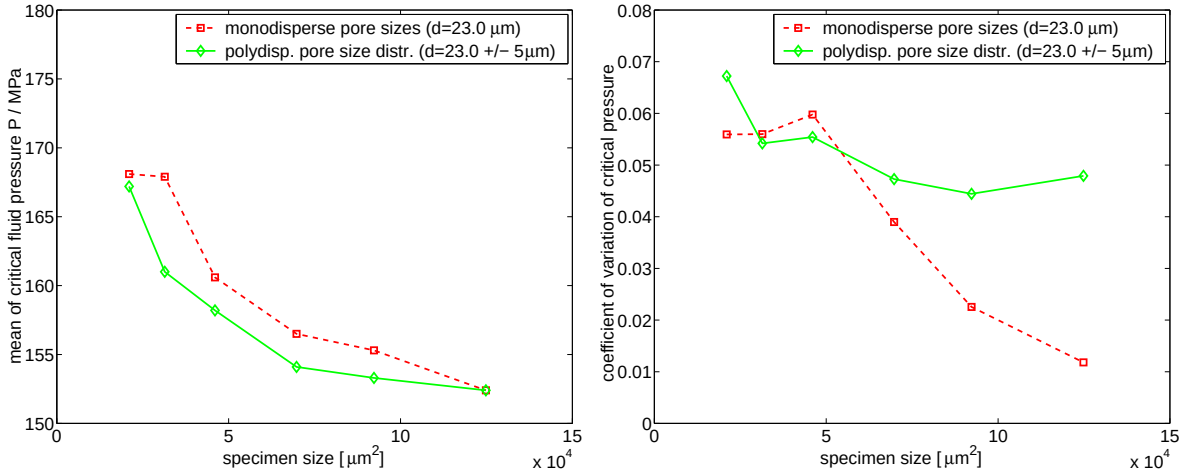

Figure 5.21: Summary of the test results in fig. 5.19 ($A_A = 0.33$, $d = 23$ μm), and fig. 5.20 ($A_A = 0.33$, $d = 23 \pm 5$ μm).

5.5.1.1 Qualitative description of the test results

The numerical studies presented in figures 5.19 and 5.20 (as well as in figures 5.28 to 5.30 below) illustrate a significant correlation of specimen size and average rupture strength: The mean of the maximum internal pressure reduces with increasing specimen size.

In order to explain this, one should recall that brittle failure of a specimen is governed by the weakest location inside, since the weakest location is seen as the source of damage nucleation and unstable crack growth. In the model structures under consideration, critical locations are formed by closely neighboured pores. As mentioned in section 5.4.3, the most critical location is where a facet of maximum length contacts two pores of maximum size. It is obvious that the probability to encounter a very critical location in a specimen increases with its size.

Fig. 5.21 indicates that the asymptotical limit of the average critical load in the model simulations is different from zero. This observation is a consequence of the fact that upper (and lower) bounds in both grain size distributions and pore size distributions are defined here. This step results in a limitation of the most critical situation possible — if the specimen size exceeds a certain value, then the most critical location is present in nearly each specimen. At the same time, upper (and lower) bounds on the maximum rupture strength are established. This property of the model structures should be in rational accordance with actual industrial specimens.

It remains to mention that the number of observations required for getting a stable result of the mean critical internal pressure decreases with increasing specimen size. Computational results on a different material (porosity: 0.30) are illustrated in fig. 5.22.

Pursuant to the decreasing number of specimens needed for convergence of the mean, it is seen that the scatter of the maximum internal pressure from specimen to specimen decreases with increasing specimen size.

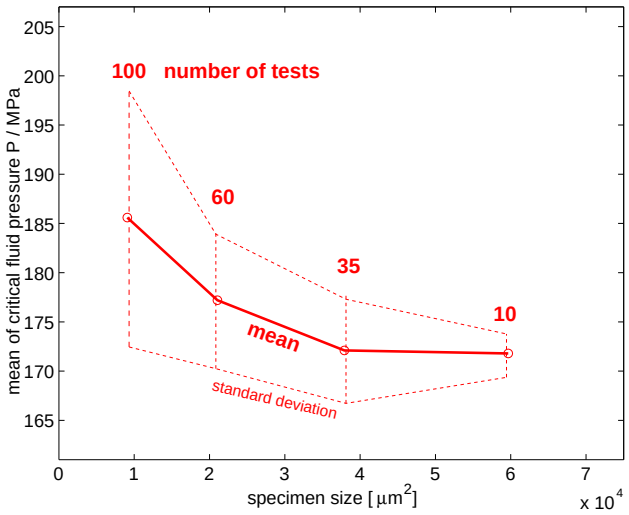

Figure 5.22: Evolution of the mean and of the standard deviation of the critical load, and of the number of tests needed for stable results in statistics. (Extracted from studies on a material with porosity $A_A = 0.3$.)

5.5.1.2 Quantitative analysis of the test results

The ultimate goal is to establish a scaling law appropriate for the considered model situations. To this end, the computational test data will first be analyzed with the aid of Weibull theory, an engineering standard approach for determination of the rupture strength of brittle materials with heterogeneous microstructure. The emphasis is on the scaling law involved therein, which follows from simple probability theory.

As will become clear, the original Weibull scaling law is not quite appropriate here, and therefore an alternative description is presented, too.

Basics of Weibull theory. [5] Consider material specimens of equal size D_0 which have a cumulative failure probability $\Pi_{D_0}(y)$ when subjected to an externally applied stress (or, in the context of the current chapter, an internal pressure) y. The cumulative failure probability function, which is generally defined as

$$\Pi_{D_0}(P_c \leq y) = \int_0^y p_{D_0}(y)\ \mathrm{d}y, \tag{5.6}$$

represents the probability that a specimen of size D_0 will fail until a load $P_c = y$ is reached (in other words: the probability that the strength of a specimen is lower than the applied load y). The parameter $p_{D_0}(y)$ represents the probability *density* at load y (see also eq. 4.17, p. 108).

Vice versa, the survival probability $U_{D_0}(y)$ of a specimen for an applied load y is

$$U_{D_0}(y) = 1 - \Pi_{D_0}(y). \tag{5.7}$$

If the specimens are pieces of a larger object of size D, and if failure of any piece results in failure of the object as a whole, then the survival probability $U_D(y)$ of the large object is given by multiplication of the survival probabilites of the pieces:

$$U_D(y) = [U_{D_0}(y)]^\lambda = [1 - \Pi_{D_0}(y)]^\lambda\,, \tag{5.8}$$

with a size factor $\lambda = D/D_0$. For very large values of λ (i.e., if the large object incorporates many pieces), or for very low cumulative failure probabilities $\Pi_{D_0}(y)$ (which holds for practical applications [3]) an elementary mathematical relation yields

$$U_D(y) = \exp\left[-\lambda\ \Pi_{D_0}(y)\right], \tag{5.9}$$

or, vice verca, for the cumulative failure probability of the large object:

$$\Pi_D(y) = 1 - \exp\left[-\lambda\ \Pi_{D_0}(y)\right] \tag{5.10}$$

For the cumulative failure probability $\Pi_{D_0}(y)$ of the pieces, an empirical power law can be assumed:

$$\Pi_{D_0}(y) = \left(\frac{y - y_\infty}{y_s}\right)^m \tag{5.11}$$

This so-called *Weibull distribution* involves the two Weibull parameters m and y_s: m (always positive, usually much larger than 5) is the Weibull shape parameter (Weibull modulus, Weibull exponent) of the material, which gives an idea of the dispersion of the specimen strengths (see eq. 5.18 below); the *characteristic strength* y_s approaches (with increasing specimen size) the mean rupture load $\bar{y}$.

The classical Weibull law in general involves a load threshold[6] y_∞ below which the failure probability is zero (eq. 5.11). For the sake of simplicity and reliability of the data fitting, in practical applications this lower threshold is almost always taken as zero: $y_\infty = 0$ (see [26], [3], [29]). Then, putting eq. (5.11) in eq. (5.10) yields

$$\Pi_D(y) = 1 - \exp\left[-\lambda\ \left(\frac{y}{y_s}\right)^m\right]. \tag{5.12}$$

[5] The present expositions follow roughly the presentation in [48], but contain important additions, and a treacherous error has been removed.

[6] sometimes called 'location parameter' [58]

The failure probability *density* function $p_D(y) = \mathrm{d}\Pi_D(y)/\mathrm{d}y$ is obtained by differentiation of eq. (5.12):

$$p_D(y) = \frac{m}{y_s}\lambda \left(\frac{y}{y_s}\right)^{m-1} \exp\left[-\lambda \left(\frac{y}{y_s}\right)^{m}\right] \tag{5.13}$$

Using eq. (5.13), the expected value for the mean of the rupture strength $\bar{y}(\lambda)$ of a material of size $D = \lambda\, D_0$ can be derived as

$$\mu_y(\lambda) = \int_0^\infty y\; p_D(y)\; \mathrm{d}y = y_s\; \lambda^{-1/m}\; \Gamma\left(1 + \frac{1}{m}\right), \tag{5.14}$$

where Γ denotes the Gamma function. Since y_s and Γ are not functions of λ, one may write:

$$\mu_y(\lambda) \propto \lambda^{-1/m} \tag{5.15}$$

as well as

$$\mu_y(D) \propto D^{-\frac{1}{m}}. \tag{5.16}$$

Finally, the power law in eq. (5.16) is the scaling formula for the average rupture strength (critical load) predicted by Weibull theory. The parameter D represents the volume (in three dimensions), area (in two dimensions), or length (in one dimension) of the specimen.

Following [48], the variance of the rupture strength, $(\sigma_y)^2$, can be deduced from eq. (5.13) as

$$(\sigma_y)^2 = \sqrt{\frac{\Gamma(1+2/m)}{\Gamma^2(1+1/m)} - 1}\;, \tag{5.17}$$

which for large values of m reduces to

$$(\sigma_y)^2 \propto \frac{1}{m}\;. \tag{5.18}$$

Equation (5.18) predicts that the dispersion is higher for lower values of m.[7] In contrast to eq. (5.18), one should expect the variance to be a function of the specimen size D.

Summarizing, Weibull-type analysis accounts for statistical size effects due to the random spatial distribution of material strength, not for deterministic size effects. The principal assumptions underlying the approach are firstly the *independence* of the 'scaled down specimens' (neglection of spatial correlations), and secondly the sensitivity of the whole structure to its parts: failure of a part will result in failure of the whole (which is certainly valid for one-dimensional structures such as a *chain* of links or a long fiber under tension; moreover, it should apply to *perfectly* brittle materials where the origin of a very small crack suffices to cause an overall failure.). Both assumptions might approximately be applicable to microstructures under internal pressure as studied in the current chapter (since the failure is mostly driven by immediate unstable growth/merging of flaws, see fig. 5.18, p. 134).[8]

[7] Following [58], the relative scatter in strength ('coefficient of variation') is for $m > 5$ approximately

$$\frac{s_y}{\bar{y}} \approx \frac{1.2}{m}. \tag{5.19}$$

[8] Theoretical considerations ([26], [3]) reveal that a power-type size effect as in eq. (5.16) only applies

Application to the test data. Weibull analysis basically consists of three successive steps: firstly performing tests, then fitting of the test data, and finally upscaling of the results:

1. A series of tests on scaled down laboratory specimens is needed. The specimen size D_0 must be *constant* in the experiments. In the following, several of the numerical test series presented in figures 5.19 and 5.20 will be used.

2. The two Weibull parameters m and y_s must be determined so that the experimental data fit best to the Weibull distribution law presented in eq. (5.11). Presuming a zero threshold ($y_\infty = 0$), the procedure for application of the linear regression method is as follows: First, the cumulative probability of failure ($\Pi_{D_0}(y)$, see eq. 5.6) is represented by a graph of $\ln\ln\left[1/\left(1-\Pi_{D_0}(y)\right)\right]$ against $\ln y$. Then, the relation between Π_{D_0} and y following from the algebraic Weibull distribution law (eq. 5.11) and the assumptions discussed above claim that Weibull's theory is applicable if the points lie on a straight line. The slope of the line gives the Weibull exponent m, whereas the intersection of the line with the abscissa gives Weibull's characteristic strength y_s.

   Figures 5.23 and 5.24 show the Weibull plots for the numerical test series. It comes

to materials which have — at the observation scale in question — no characteristic length. Thus, Weibull theory might be unrealistic for structures on the microscopic level where characteristic lengths (or distributions of characteristic lengths), which are provided by the material inhomogeneities (grain boundary sizes, distances between micro-defects, diameters of cavities etc.), are apparent. In any case, it is clear that Weibull theory is inapplicable to quasi-brittle materials [26].

For this reason, Bazant [2] proposed an adaptation of Weibull theory which applies to quasi-brittle structures (e.g. concrete) involving a characteristic length. The size effect predicted by this non-local theory reads

$$\mu_y \propto \left[\left(\frac{D}{D_0}\right)^{\frac{2}{m}} + \frac{D}{D_0}\right]^{-\frac{1}{2}}, \tag{5.20}$$

D_0 being the size of a reference structure. According to this formula, the Weibull-type statistical size effect is approached for sufficiently small sizes, while the statistical size effect asymptotically disappears for large structure sizes, leading to a size effect of purely mechanical, deterministic origin:

$$\mu_y \propto D^{-\frac{1}{2}} \tag{5.21}$$

Instead of the power-type Weibull distribution, the probability of a single specimen failure is sometimes assumed to be an exponential function of the applied load (Gumbel distribution), which leads to a scaling behaviour like [48]

$$\mu_y \propto (\ln D)^{-\gamma}, \tag{5.22}$$

where γ is a material parameter.

Equations (5.16), (5.20), (5.21), (5.22) predict that the mean stress of rupture asymptotically approaches zero with increasing specimen size. The essential difference is related to the damage evolution mode: Weibull distribution is favoured in the case when crack growth is the dominant process (and, thus, rupture depends on the extreme tail end of the defect size/'strength' distribution), while Gumbel distribution should be more appropriate when the crack propagation mode is crack nucleation dominated. Nevertheless, "the difference between the two distributions (Weibull and Gumbel) is, in view of the substantial scatter of experimental data, often indistinguishable" [48].

out that the tests on the smaller specimens fit fairly well (fig. 5.23), and the tests on the larger specimens fit even better to straight lines (fig. 5.24). Furthermore, the Weibull plots in fig. 5.23 illustrate that the characteristic strength y_s of the specimens decreases with increasing specimen size (see also fig. 5.25, right).

The observation that the fluctuations of the maximum internal pressure from specimen to specimen decrease with increasing specimen size (fig. 5.22) is correctly reflected in the slopes of the Weibull plots of the test series (fig. 5.23, and fig. 5.25, left).

3. The studies at constant specimen size must be extrapolated (scaled up) according to eq. (5.16) in order to predict the strength of larger specimens or prototypes. Using the data from specimens of size $D_0 = 21044\ \mu\text{m}^2$, and the data from specimens of size $D_0 = 69757\ \mu\text{m}^2$, the results are presented in figure 5.26. For moderately larger specimen sizes, the prediction of Weibull theory is close to the test results, but it exhibits a tendency different from the simulations: The Weibull scaling law ultimately approaches a zero critical load, while the asymptotical limit of the average critical load in the model simulations is a *non-zero* value: $\lim_{D\to\infty} \bar{y} = y_\infty > 0$.

The overall picture shows that the 'standard' Weibull analysis (with the assumption of a zero threshold $\lim_{D\to\infty} \bar{y} = y_\infty = 0$) is not adequate to predict the size effect, whereas an extended analysis with $y_\infty \neq 0$ (which is fundamentally more difficult) could be.

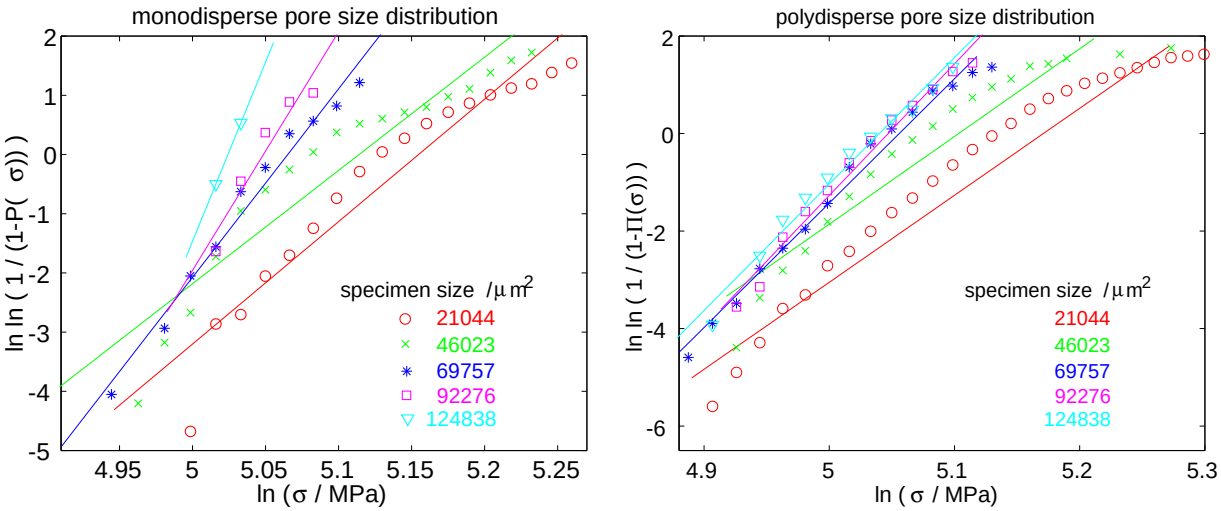

Figure 5.23: Determination of the Weibull parameters: Weibull plots for the tests on the material structures with monodisperse (fig. 5.19) and polydisperse (fig. 5.20) pore size distribution, respectively. The slope becomes steeper (Weibull exponent m increases) and the curves move towards the left (characteristic strength y_s decreases) with increasing specimen size: see fig. 5.25.

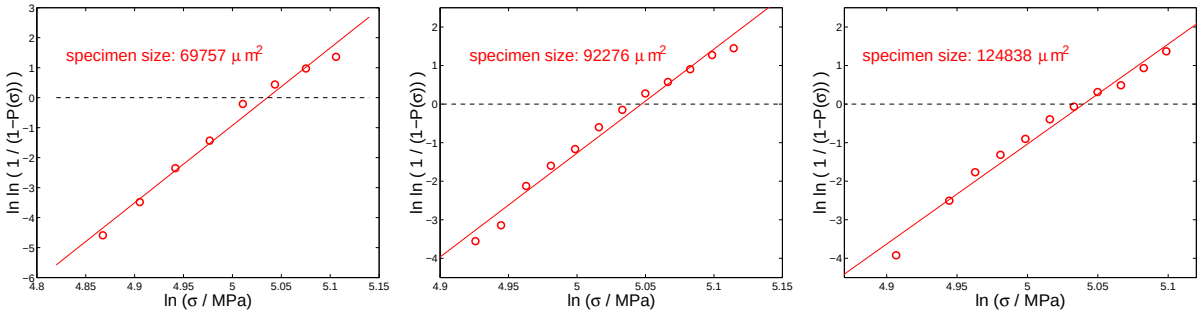

Figure 5.24: Determination of the Weibull parameters: Weibull plots for the tests on the material structure with polydisperse pore size distribution (fig. 5.20). The plots refer to the larger specimen sizes, where the test data lie close to a straight line.

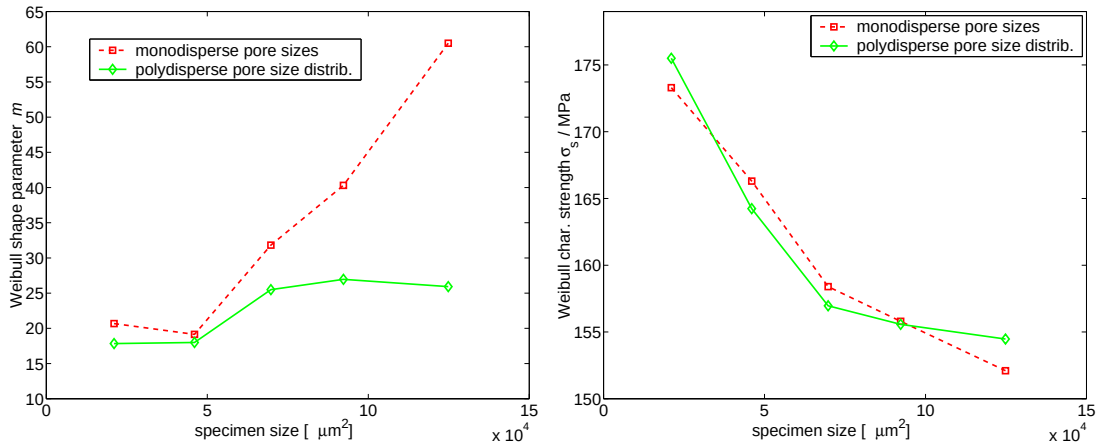

Figure 5.25: Evolution of the Weibull parameters as a function of specimen size. Left: Weibull exponent m. Right: characteristic strength y_s.

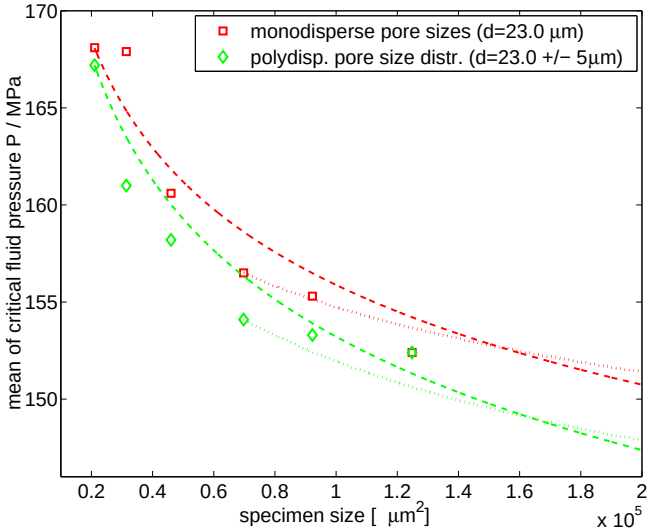

Figure 5.26: Upscaling with Weibull theory, and comparing with results from tests on specimens of different sizes (fig. 5.19 and fig. 5.20). The dashed lines are based on Weibull analysis of the test results at specimen size 21044 μm^2, the dotted lines are based on Weibull analysis of the test results at specimen size 69757 μm^2.

Proposal of a more appropriate scaling law. An alternative approach may be to combine the presence of a non-zero asymptotical limit and the power-type scaling behaviour into one concise scaling law. Proposing

$$\mu_y(D) - y_\infty \quad \propto \quad D^{-\frac{1}{r}} \tag{5.23}$$

suggests itself and fits quite well to the various test results (fig. 5.27, left; see also fig. 5.31 at p. 150). Concerning the material structures investigated in the current chapter, the numerical simulations yield for the parameter r values in between 0.5 and 1.6. It turns out that with increasing specimen size, the mean of the observable approaches its asymptotic limit y_∞ sooner for higher values of r.

It is important to be aware that these parameters entering eq. (5.23) are determined from a genuine study of size effects, i.e. from studies on specimens of different sizes, while the Weibull parameters deduced above inherently result from studies on specimens of constant size.

Corresponding to the scaling law for the mean as introduced above (eq. 5.23), a power law may be proposed for the size effect on the *variance* (square of the standard deviation) as follows,

$$\sigma_y(D) \quad \propto \quad D^{-\frac{1}{r}}. \tag{5.24}$$

Herewith, fitting of the results in fig. 5.19 and fig. 5.20 yields for the parameter r values in between 0.3 and 1.9 (see fig. 5.27, right); these values are roughly in accordance to the results for r from the fittings of the means.

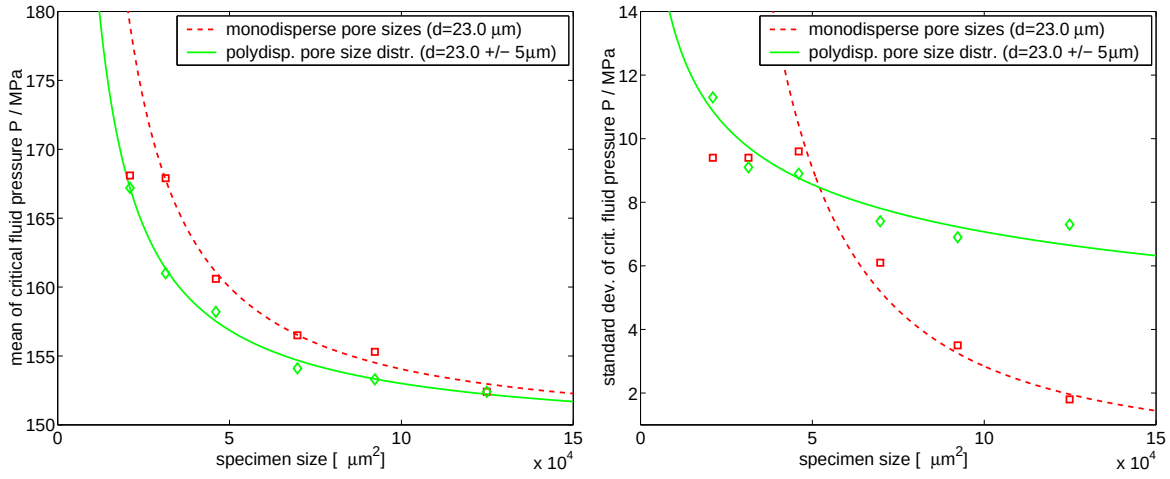

	fitting of the mean values $\bar{y}$	fitt. of the variances $(s_y)^2$
monodisperse, $d = 23.0$ μm	$y_\infty = 149.5$ MPa , $r = 0.84$	$r = 0.35$, $r = 0.30$
polydisperse, $\bar{d} = 23.0$ μm	$y_\infty = 149.0$ MPa , $r = 1.04$	$r = 1.86$

Figure 5.27: Nonlinear least squares curve fittings according to the scaling formulas in eq. (5.23) and eq. (5.24) have been added to the test results (fig. 5.21). The values of the fitting parameters are listed in the table below. The accordance of fitting curve and test results is better for the mean values than for the standard deviations.

5.5.1.3 Remarks on the existence and size of the RVE

Strength usually is considered to be an *extrinsic* property of brittle solids [48], which means that it not only depends on the material but also on the specimen size and shape. For extrinsic properties, a representative volume element (RVE) does not exist at all.

The standard assumption of a zero threshold in Weibull analysis is in accordance to the extrinsic property of the strength: It means that no upper bounds on the size distribution of the individual material constituents do exist, which — at the same time — means that there are no lower limitations on the rupture strength of a specimen. Any specimen of sufficient size contains a 'fatal' defect (e.g., a huge pore).

In the simulations of the present investigation, the strength may *appear* to be an extrinsic parameter since it is changing with the respective specimen size. The fact that upper bounds are put on the size distribution of the cavities renders, however, the critical load to an *intrinsic* structure property, i.e. to a genuine *material* property (which is independent of the specimen size and shape). Thus, one may assume that — with respect to the rupture strength — an RVE does exist for the structures under study.

It has been shown that with increasing specimen size the variance of the observable asymptotically approaches zero and the mean asymptotically approaches a certain value above zero, therefore a specimen can be 'sufficiently representative' even at a moderate size — the size depends on the accuracy with which this observable should be satisfied. Roughly speaking, the size of the RVE is equal to the specimen size where the scatter of the observable vanishes and the observable (as a function of specimen size) converges to the ultimate value. Regarding the parameter r introduced in eq. (5.23), it can be stressed that the size of the RVE is smaller for comparable materials with higher r.[9]

5.5.2 Significance of structure parameters

The specimen size effect outlined in the previous section has to be accounted for now where the sensitivity of the rupture strength to some 'global' characteristics of the material phases is to be investigated. The studies presented below refer predominantly to the porous phase, and are concluded by a brief consideration of the grain-size effect.

5.5.2.1 Significance of pore-phase parameters

In the following, the attention will be directed to the impact of

- the *size distribution* of the pores
  (monodisperse/polydisperse: see figures 5.19, p. 135, and 5.20, p. 136)
- the *specific perimeter* ('fineness') of the porous phase
  (high/low: see figures 5.28, p. 147, and 5.29, p. 148)
- the *shape* of the pores
  (circular/elliptical: see figures 5.29, p. 148, and 5.30, p. 149) .

Each comparative pair of structures is designed so that only one property is different, while the others — especially the porosity — are approximately equal.

[9] 'Comparable materials' means 'materials with equal porosity': see fig. 5.27 (porosity: 0.33) or fig. 5.31 (porosity: 0.30).

The importance of accounting for the specimen size effect becomes clear if one compares the test series presented in figures 5.28 and 5.30: even though the structures with elongated (elliptical) pores turn out to be less resistant than the structures with circular pores *at each specimen size under study*, upscaling of the results according to eq. (5.23) leads one to assume a reversed situation for the asymptotic limits. This amazing feature (see the red and green curves in fig. 5.31), which cannot be predicted by standard Weibull analysis, is due to the different values of the parameters in the scaling function. It should be further investigated by simulations on larger specimens.

The studies try to elucidate how the above parameters affect the respective size of the RVE, the asymptotic limits y_∞ of the mean values, and the scatter of the results. The values for r and y_∞ come out of analyses of the numerical tests, using the fitting function introduced in eq. (5.23).

Size of the RVE. Comparing the tests on materials with high specific perimeter (pore diameter: 12.0 μm) and materials with low specific perimeter (pore diameter: 15.5 μm), it is seen that for the material with larger pores, the RVE is larger (size: not below $D = 80,000\ \mu\text{m}^2$) than for the material with smaller pores (size: not below $D = 40,000\ \mu\text{m}^2$; see fig. 5.31). Obviously, the size of the RVE increases with the size of the *largest* influential components in the structure: for materials with even larger pores such as in the tests on monodisperse/polydisperse pore size distributions presented above (pore diameter: 23 μm), the RVE expands to significantly higher sizes ($D > 150,000\ \mu\text{m}^2$, see fig. 5.27).

Asymptotic mean of the rupture strength. For structures with given porosity and pore shape (circular), it is observed that the asymptotic limit of the average strength descends with the value of the specific pore perimeter: Reducing the specific perimeter by 22 % may reduce the critical load by 9 % (fig. 5.31). This not only holds for monodisperse pore size distributions, but also for the tests on monodisperse/polydisperse pores: The lower average strength is attributed to the polydisperse structure (see fig. 5.27), which has a lower specific perimeter than the monodisperse structure (this becomes clear when the mean values of the specific perimeter of the model specimens are compared). Since the specific perimeter is related to the 'fineness' of the respective phase, one may — as a rule — say that a monodisperse distribution is finer than a polydisperse distribution, and the 'finer' material has a higher strength.

These observations can be explained as follows: The 'coarser' material, i.e. the material with lower specific perimeter of the porous phase, involves the larger cavities. It has been repeatedly mentioned that these *extremes* are decisively diminishing the damage resistance. The most critical locations are found in the vicinity of the largest pores, since the largest pores come along with the most extended ranges of high local stresses.

A striking point is that with increasing specimen size (below RVE), the mean values of the critical load are diverging for the monodisperse/monodisperse tests (red and green curves in fig. 5.31), whereas they are rather converging for the monodisperse/polydisperse tests (fig. 5.27).

As for the significance of the pore *shape*, the simulations on structures with similar porosity, specific pore perimeter, and equal area of the individual pores (figures 5.29 and 5.30) clearly demonstrate that the circular pore shape is the most stable one; elongating the pores to ellipses (aspect ratio: $b/a = 0.56$) results in a reduction of the critical

load by 6.5 %.

For materials with given specific pore perimeter, monodisperse pore sizes and shapes (circular), the significance of the *porosity* should be obvious: Increasing porosity comes along with larger pores and, consequently, decreasing material resistance. This assertion is supported by the tests presented in fig. 5.32, even though these tests have been performed at one specimen size only.

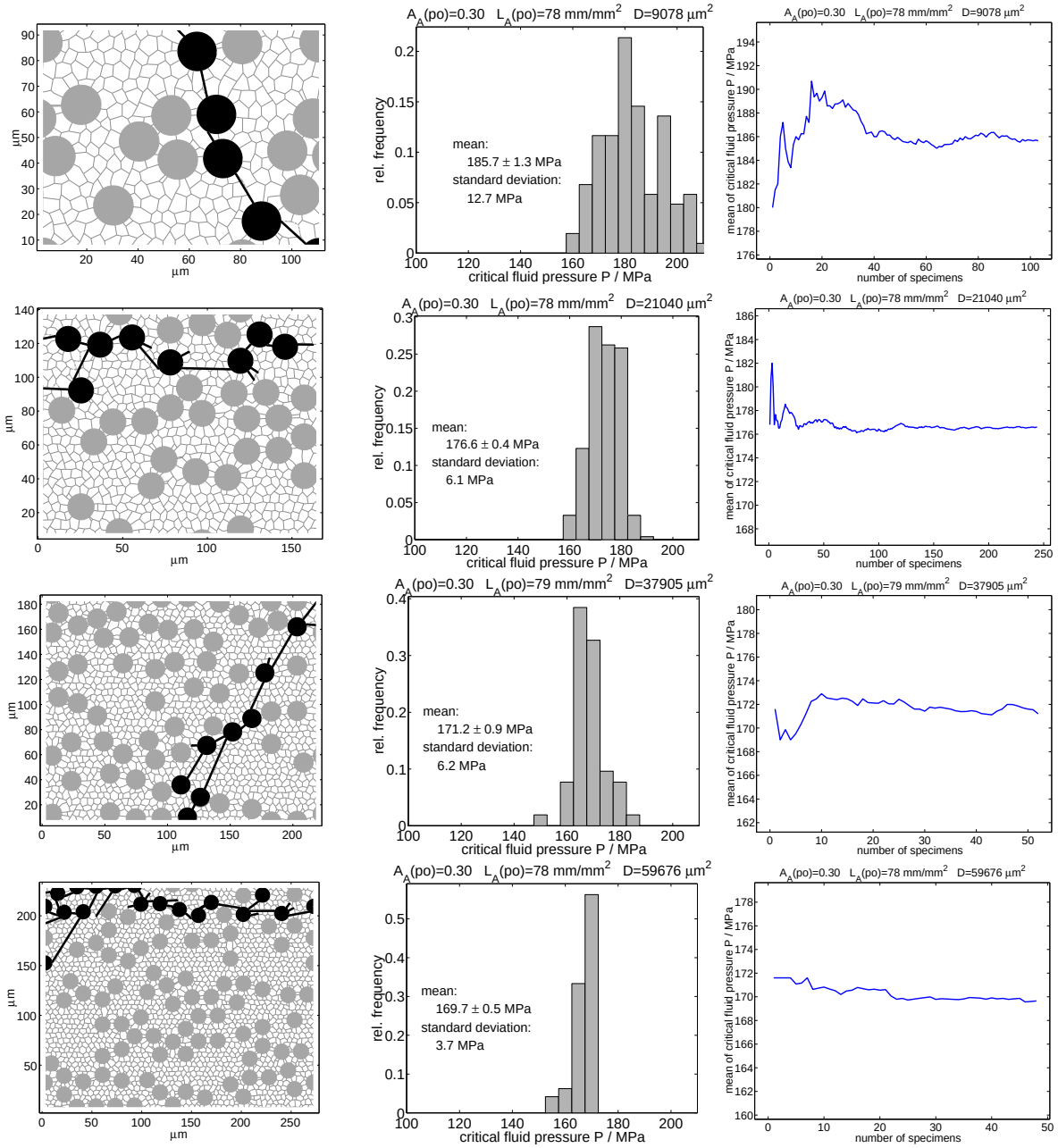

Figure 5.28: Tests on specimens with low specific perimeter of the porous phase (L_A = 79 mm/mm^2). The porosity is $A_A = 0.30$. The diameter of the pores is 15.5 μm, while the average size of the grains is 5.4 μm. If there would be no coalescence of cavities (isolated pores — no awareness of spatial correlation), then the critical load would not be below 225 MPa in any specimen.

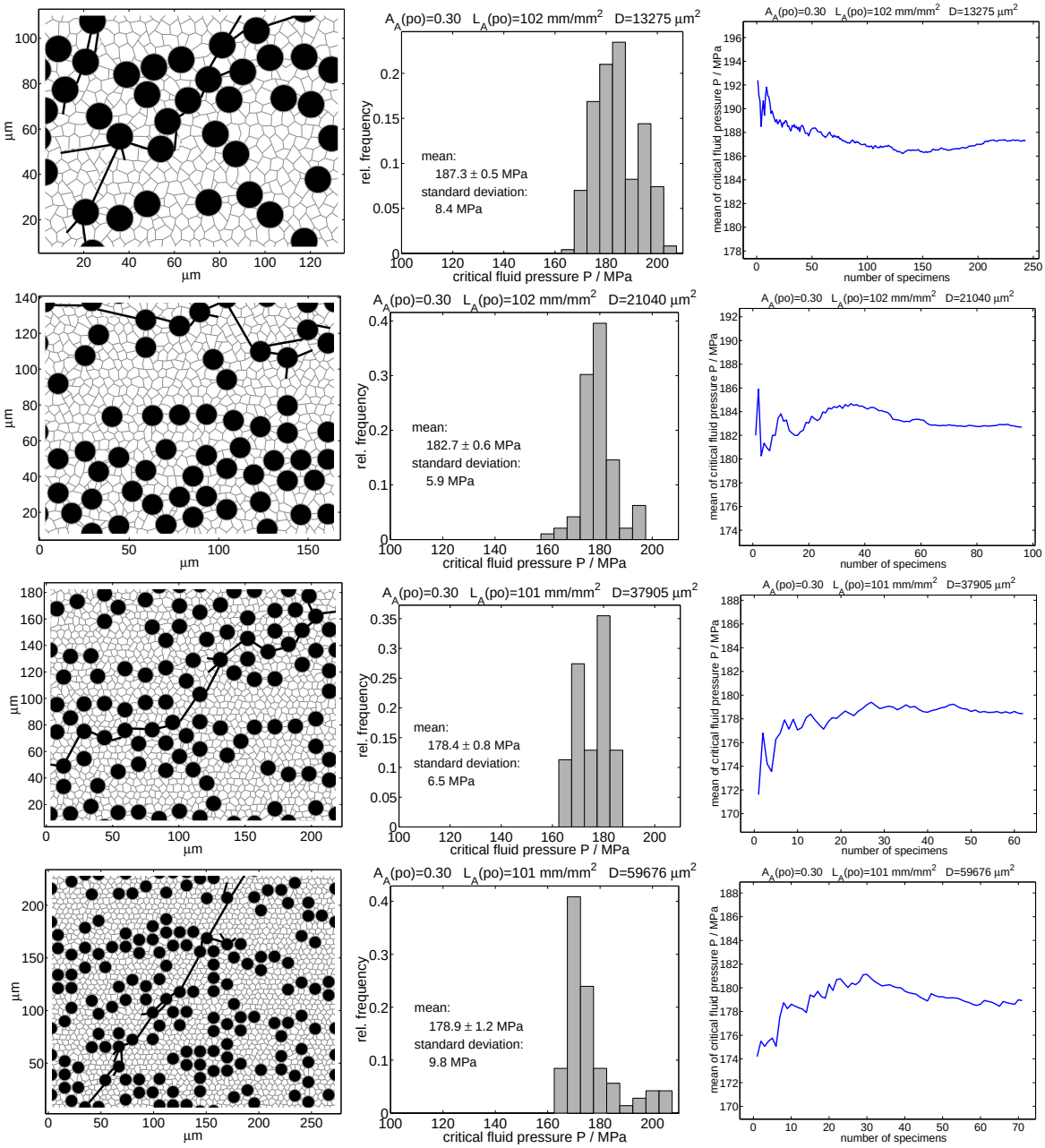

Figure 5.29: Tests on specimens with high specific perimeter of the porous phase (L_A = 101 mm/mm^2). The porosity is $A_A = 0.30$. The diameter of the pores is 12.0 μm, while the average size of the grains is 5.4 μm.

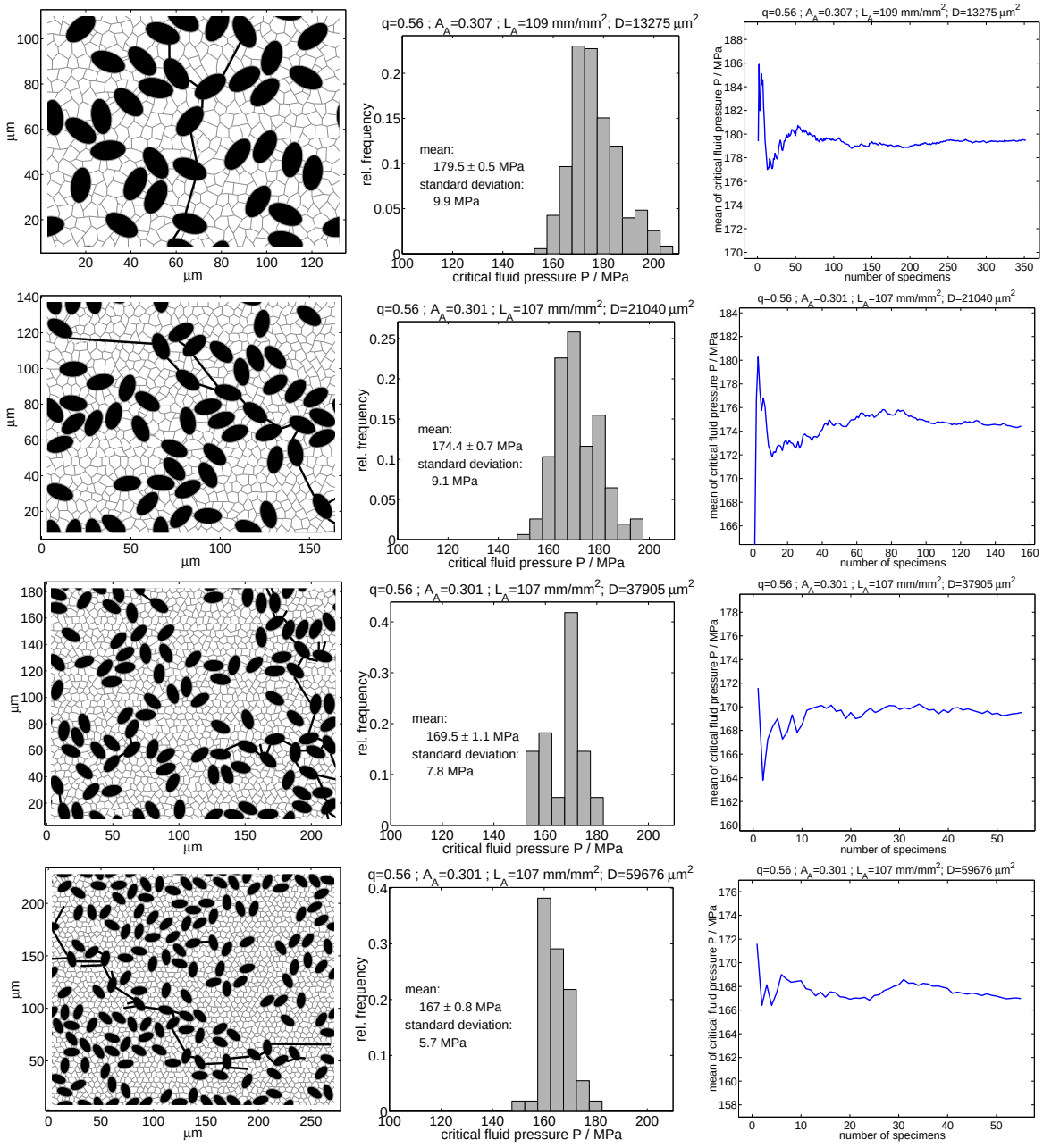

Figure 5.30: Tests on specimens with high specific perimeter of the porous phase (L_A = 109 mm/mm^2) and elliptical pore shape. The porosity is $A_A = 0.307$, the aspect ratio of the elliptical pores is $b/a = 0.56$ (semiaxis lengths: 16.0 μm and 8.5 μm). The area of a single pore is equal to the area of a circular pore as in fig. 5.29. The average size of the grains is 5.4 μm.

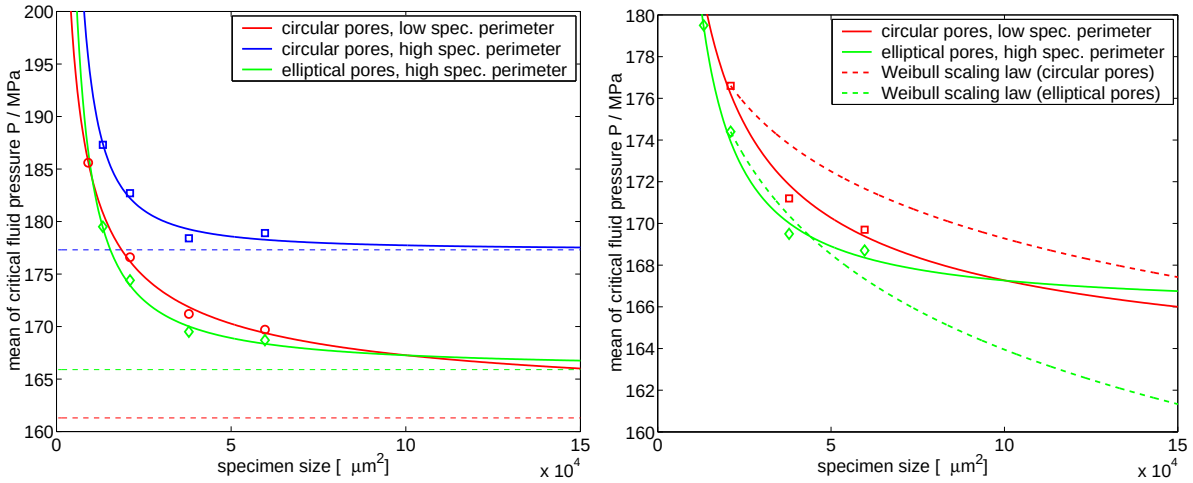

			fitting of the mean values $\bar{y}$
circular pores,	low spec. perimeter	(fig. 5.28)	$y_\infty = 161.3$ MPa , $r = 0.58$
circular pores,	high spec. perimeter	(fig. 5.29)	$y_\infty = 177.3$ MPa , $r = 1.56$
elliptical pores,	high spec. perimeter	(fig. 5.30)	$y_\infty = 165.9$ MPa , $r = 1.13$

Figure 5.31: Left: Summary of test results on specimens of porosity $A_A = 0.30$, supplemented by fitted scaling curves according to eq. (5.23). The dashed lines indicate the asymptotic limits y_∞ of the average critical load for very large specimens. Comparing the two lower-resistant materials, it appears that the strength of structures with elliptical pores (green curve) is higher for very small specimens ($D < 1\times10^4$ μm^2) and for very large specimens ($D > 10\times10^4$ μm^2), while the structure with circular pores (red curve) is more resistant for moderate specimen sizes (1×10^4 μm^2 $< D < 10\times10^4$ μm^2)! Right: For the two lower-resistant materials, upscaling the results at specimen size $D = 21040$ μm^2 with Weibull theory (dashed curves) does not reflect the actual, reversing scaling behaviour (solid curves).

Variance/scatter of the results. It is expected that the scatter of the observable for specimen sizes below RVE increases with the 'number of degrees of freedom' in the respective structure. A certain degree of freedom common to all model structures under study is related to the random positioning of the pores. Another degree of freedom may be the orientation of the pores, which is significant only for the elongated pore shapes. Comparing the tests on circular pores and the tests on elliptical pores in fig. 5.29/fig. 5.30 or in fig. 5.32, one finds indeed that the scatter of the results is wider for the specimens with elliptical pores.

A non-monodisperse size distribution of the pores represents another possible degree of freedom. The test results illustrated in fig. 5.27 confirm that the standard deviation of the observable decreases much sooner for the monodisperse pore sizes than for the polydisperse distribution, a characteristic which is clearly reflected in the parameter r of the respective fitting curves.

Another overall picture of the tests is that the number of observations needed to provide stable results of the mean increases with the number of degrees of freedom.

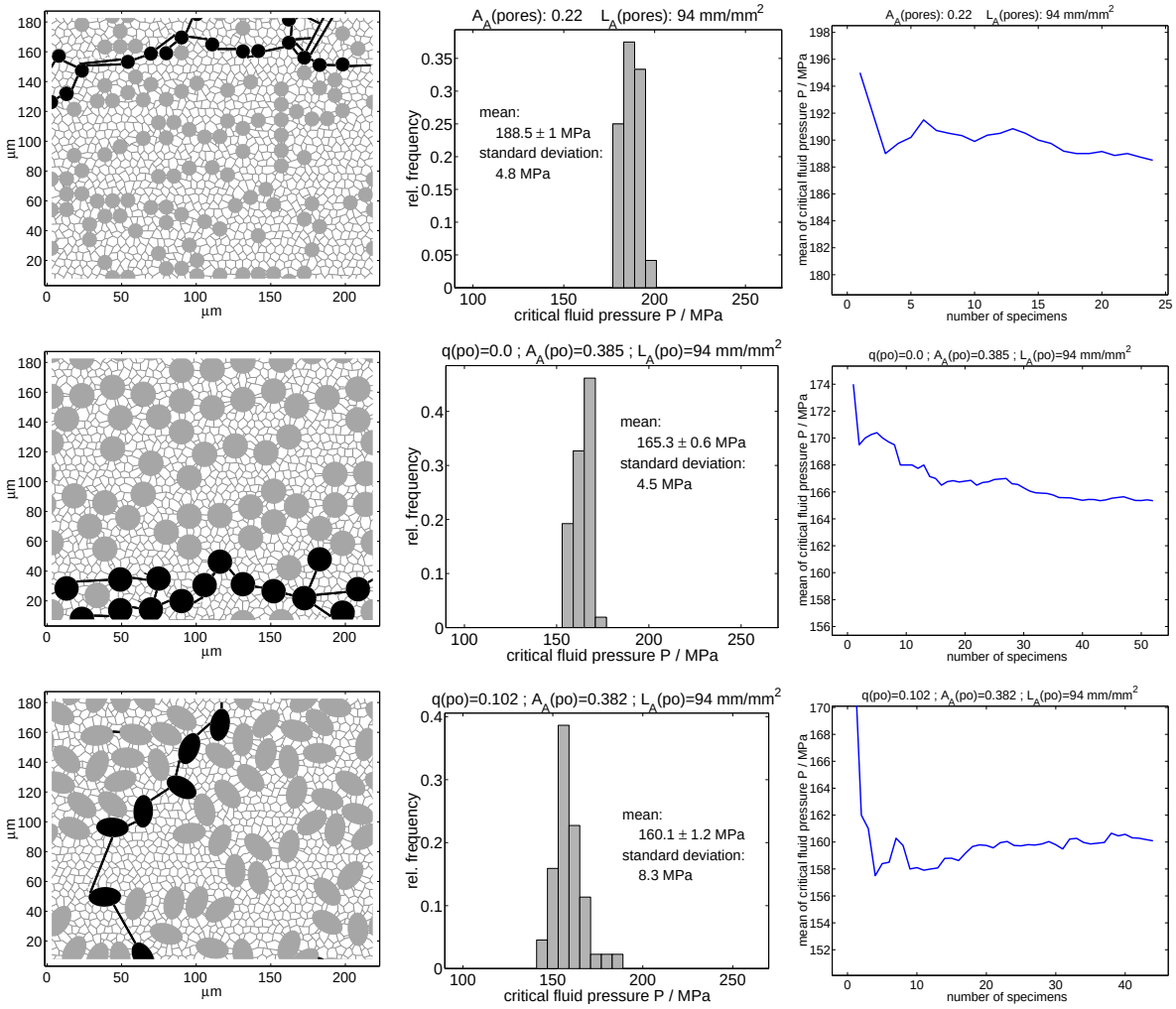

Figure 5.32: Above and middle: percolation studies on specimens with equal specific perimeter of the porous phase ($L_A = 94$ mm/mm^2), but different porosity (above: $A_A = 0.22$, middle: $A_A = 0.385$). Middle and below: percolation studies on specimens with equal porosity ($A_A = 0.38$) and specific perimeter of the porous phase ($L_A = 94$ mm/mm^2), but different ratio of the pore semiaxes (middle: $b/a = 1$, below: $b/a = 0.73$); a higher eccentricity of the pores results in a lower average failure load, but causes a higher scatter of the results.

5.5.2.2 Significance of the grain size

So far, the investigations have confirmed that the critical pressure becomes higher for a finer pore distribution. To some extent, the result can be applied to the grain phase as well: In the exemplary calculations of fig. 5.33, a reduction of the average grain diameter by 28 % achieved an increase of the average strength by 10 %. The observation that material strength benefits from a fine granularity is a consequence of the energy criterion introduced in Chapter 4, which favors the failure of the larger facets (see fig. 4.2, p. 96), and agrees to the empirical knowledge of material scientists.

In actual ceramics, there are several reasons for the increased damage resistance of the fine-grained structures. To mention one of them, one should recall that the process of sintering can never be perfect; some tiny voids will always remain, which then act as generators of stress concentrations. If, however, the fineness of the powder before sintering is increased, then both the size of the grains and the size of the voids will be smaller. Consequently, the stress concentrations are reduced, and the breaking strength of the ceramic is higher in materials with smaller grains [29].

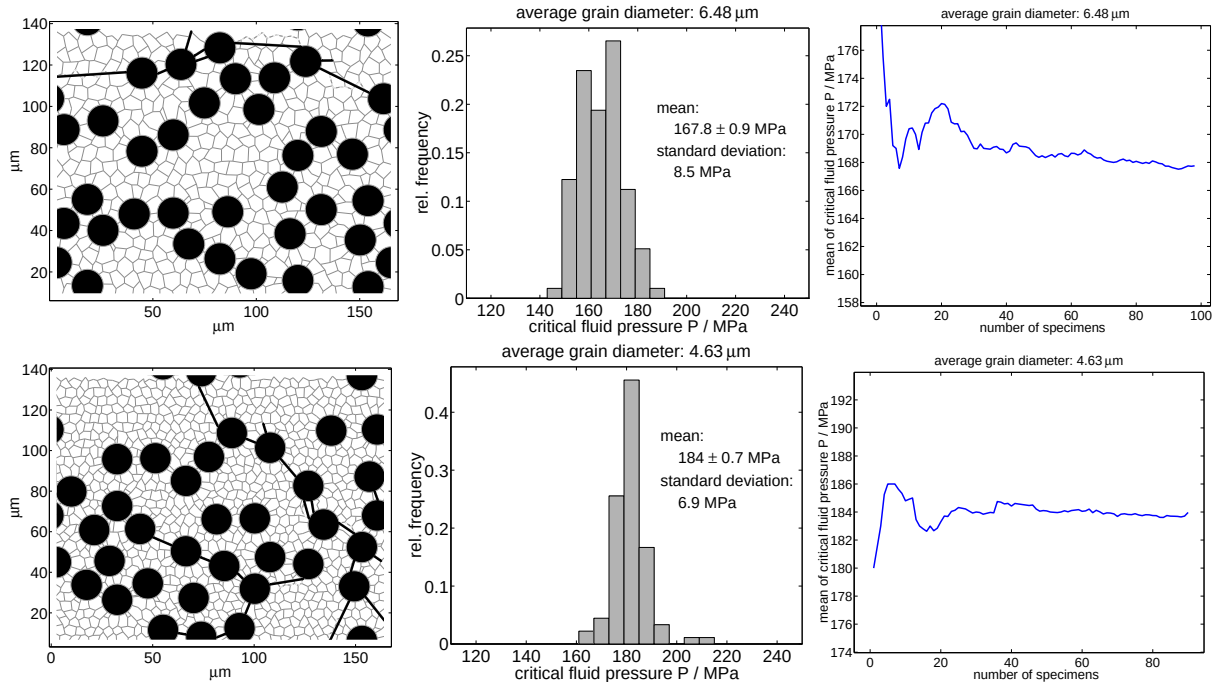

Figure 5.33: Percolation studies on specimens of equal size (20900 μm^2), porosity ($A_A = 0.30$) and specific perimeter of the porous phase ($L_A = 80$ mm/mm^2), but different average grain size (above: 6.48 μm, below: 4.63 μm). The left column shows one specimen of each test series.

Chapter 6

Summary and conclusions

This final chapter provides a concluding survey of the ideas and the assets and drawbacks of the presented work (section 6.1), a brief summary of the basic results, including references to figures and text passages (section 6.2), and it suggests possible extensions and further discussions (section 6.3).

6.1 General assessment

A computational model has been presented which describes the nucleation and evolution of microcracks in granular material structures, and accounts for the impact of cavities (pores and cracks) on the local stress distributions and on the effective elastic properties. With the aid of this model, various subjects in the field of damage mechanics have been investigated.

The presented approach differs from the existing ones in that it combines concepts of the 'micromechanical' models, which are rather analytical in nature, and of the 'mesh' models, which are numerical in nature. The idea was to generate geometrical sampling images of actual microstructures, reduced to the mesh of grain boundaries, on the one hand, and to the cavities, on the other hand. In the simulations, stress analysis was then founded on analytical solutions for the cavities, which disturbe the otherwise homogeneous stress field in the solid material phases. The mesh of grain boundaries was subject to discrete, spontaneous fracturing in the course of loading, supervised by an energy criterion.

The stress analysis from the perspective of pores and cracks allows for a general, compact formalism applicable to tensile and compressive, linear and nonlinear conditions. (Nonlinearity results from structural changes, crack closure and frictional sliding of the crack faces.) Different from pure micromechanical models, the presented approach accounts for spatial correlations of the arbitrarily distributed defects and is thus non-local. In contrast to finite element methods, the computational effort (finite element representation of microdefects, matrix inversion etc.) is reduced since the interacting system is the ensemble of cracks, not the complete set of solid-phase mesh links. The meshing of the solid phases into a disordered grid of grain boundaries fits to the damage behaviour observed in actual materials and is thus more flexible than the regular meshes of standard finite element techniques.

The analytical description of stress disturbances enforces, though, a rough approximation of the defects by simple shapes (elementary cavity geometries, straight crack lines). In particular, the arising networks of connected pores and cracks must be substituted.

Another shortcoming is due to the averaging of tractions along the crack lines for the determination of local stresses and defect interactions. This technique is accurate rather for distributed cracks of similar size. In certain situations, however, interactions may be disregarded.

The presented attempt is certainly no substitute to the various models existing in the literature, but it proved to work fine in many situations and may thus serve as an alternative. It reflects a number of key features in the context of brittle and quasi-brittle damage, internal friction and statistical disorder, spanning the full bandwidth from microcrack nucleation to overall failure, including the intermediate range. Many parts of the presented theory and results are applicable to diverse brittle materials such as ceramics, ceramic composites, rocks and concrete. Extensions can be made with respect to thermal residual stresses, stress corrosion cracking, fatigue cracks. Cooperation with macroscopic approaches (e.g., finite element models) is very conceivable, although these are often displacement-driven, whereas the presented model relies on prescribed stresses.

Even the process of developing the model and suiting it to particular problems has elucidated several core points, for example the 'cooperative' behaviour (localization) of defects, or the coalescence of pores by means of cracks. Further comprehension of the material behaviour was gained by applying the model in a number of computational studies, the results of which will be summarized in the following section 6.2. Randomness of the microstructural configuration, introduced by distortion of the grain mesh and variability of pores and grains, was seen to influence the results. The statistical explorations were based upon Monte Carlo simulations of simply defined models. Scaling effects were observed, revealing the significance of boundary conditions and specimen size.
The studies at the microscopic level ultimately aimed at the effects at the macroscale. To this end, homogenization has been performed to obtain effective elastic and damage parameters where possible. In a series of studies, where averaging was meaningless, the transition from microscopic damage to macroscopic failure has been demonstrated via the crack patterns.

However, it cannot be ignored that the model at the current stage may get into trouble concerning the *quantitative* prediction of the material response. To give an example, the actual internal pressure in industrial applications amounts to $P = 1 - 5$ MPa in contrast to the damage thresholds exceeding 100 MPa for the test structures in Chapter 5. This is a high discrepancy which must not only be traced back to the neglection of thermal, chemical and cyclic impacts, or to the restriction to one grain phase (titanium oxide). The reasons should also be searched at a more fundamental level of the model:

Firstly, there is a conceptual limitation due to the rough geometrical approximation of the cavities. In contrast to the smoothed shapes of the model cavities, actual pores have edges and even tips. Actual pores thus involve higher stress concentrations within the material which significantly facilitate the initiation of microcracks. Accounting for these stress singularities would require an artificial variation of the stress intensity factors in the model. Moreover, the bandwidth of the pore sizes has been chosen too small until now — actual material specimens exhibit an *open* porosity which becomes noticeable by some very extended pores observed in the two-dimensional material sections. The latter have been neglected in the present thesis (see e.g. fig. 2.10 below, p. 44), but are essential for a quantitative prediction.

Another conceptual limitation is due to the two-dimensional consideration. One must

be aware of the fact that a restriction to two dimensions cannot be sufficient, but it seems that a comprehension of the problems in 2-D is suitable before approaching the much complexer situations in 3-D. Essential parts of the formalism are – in principle – applicable to 3-D situations as well, but the implementation in a computer algorithm would be extremely extensive. Forthcoming studies should therefore aim at a rather phenomenological discussion of the 2-D/3-D correlation of the fundamental issues, as started in section 6.3 below.

As for the quantitative validity, the results of Chapter 4 are expected to be closer to reality than the results of Chapter 5. The reason is that Chapter 4 restricts to compact, i.e. pore-free materials, whereas the conceptual limitations mentioned above mainly come to light by the pores. But already the compact grain structure model can be improved by a better-adjusted input. This holds for structure properties such as the accurate grain sizes and the nature of the interfaces, as well as for material parameters such as the specific surface energy or the elastic constants, and for the specimen boundary conditions. A great deal is demanded here of the experimentalists, too; in particular, detailed informations on 3-D structure characteristics are lacking at the moment.

Anyhow, it seems that chasing after an exact picture of the reality by a computational model has never been a promising track. The benefit of the presented approach is given by its clarity to show qualitatively the phenomena, not by any quantitative, numerical accuracy. Accordingly, restricting the studies to elementary situations turned out to be a rational principle here.

6.2 Review of the individual results

In the following, some important issues from each of the preceding chapters are briefly recapitulated, and reference is given to selected figures illustrating the most appealing results.

Chapter 1. A rough categorization of the numerous approaches to damage modelling in the literature has been proposed (fig. 1.1, p. 20). At the microscale, two contrary model types have been distinguished: micromechanical models based upon analytical solutions for the defects, and mesh models based upon numerical calculations for the discretized matrix material.

The approach underlying the present study has been introduced and classified in between these major model types.

Chapter 2. As a prerequisite for the new model approach, generation of the two-dimensional microstructure images has been outlined, and the input informations obtained by stereological analyses of actual materials have been discussed. Since stereological data are not sufficient, additional assumptions on the 'local' characteristics of the structure elements have been described. A respectable visual accordance of the model images and the experimental micrographs in two dimensions has been achieved (e.g. fig. 2.10, p. 44).

Chapter 3. The available analytical stress solutions for cracks and various pores (i.e., single cavities in an infinitely extended homogeneous medium) have been evaluated and

utilized in a computational framework. Visualizations of the elementary stress fields have been presented in section 3.3.

In order to investigate the delicate behaviour of elastic solids with cracks, a complete formalism for determination of local stresses and displacements has been established. The associated homogenization technique aims at the effective compliance tensor and the overall strain (sections 3.4.2 and 3.5.5). It has been demonstrated that the nonlinear effects of crack closure, friction and structural changes (due to microcracking) involve a history dependence of the material response, and necessitate the incrementation of the computational algorithm as well as a complex set of case distinctions.

The key formula established for the single-crack characteristics under compression and frictional sliding is eq. 3.54 (p. 75); it makes use of two important quantities which describe the current crack state: these are the *activity factors* and the *shear mismatch*.

An interesting application of this formalism pointed to the constrained motion of crack faces under a quasistatic shear/compression cycle. The stress-strain response exhibits here a conspicuous, jerky course, and thus illustrates the significance of both the shear mismatch and the crack activity (fig. 3.27, p. 88).

The formalism has been extended to direct micromechanical interactions between the cracks by means of a superposition technique and solution of a self-consistent equation system. The significance of the interactions has been discussed and investigated firstly regarding the local stresses. It turned out that the interactions promote the strength of local stress concentrations (e.g., fig. 3.22, p. 85). Concerning averaged macroscopic parameters such as overall strain and effective stiffness, the computations confirmed the well-known fact that the parameters may be enhanced or degraded, depending on the tendency of the cavities to form rather a 'stacked' or a 'columnar' arrangement.

Chapter 4. The simulation of progressive fracturing at the microscale has been founded on the meshing of the matrix material: An energy balance equation for any facet between two grains establishes the microscopic fracture criterion. Equation 4.3 (p. 95), expressed in terms of average traction, first refers to crack nucleation, whilst eq. 4.8 (p. 97), in terms of the stress intensity factor, inherently refers to crack extension. The model has been designed for crack nucleation, extension and bridging; crack branching (bifurcation) is disregarded.

In a compact material structure, the model simulations reproduced the fundamental modes of damage; these were seen to depend on the loading conditions and on the heterogeneity of the structure. Recording exemplary crack patterns showed up both the brittle failure mode (fig. 4.6, p. 100) and the quasi-brittle damage behaviour (fig. 4.9 right, p. 102; fig. 4.10 above, p. 104). The occurrence of the *localization* of several cracks (fig. 4.7, p. 101; fig. 4.9 left, p. 102; fig. 4.10 below, p. 104) has been traced back to the 'energy barriers' in the granular structure, in connection with the stress disturbance fields by the cracks.

Moreover, the model simulations illustrated the microcrack-induced degradation of the material stiffness under external compression, and the emergence of an elastic anisotropy (fig. 4.13, p. 106). The overall strain components ϵ_{xx} and ϵ_{yy} have been observed to be strongly correlated to the scalar crack density, even under compression (fig. 4.14, p. 110). For this reason, the scalar crack density could serve as a simple but meaningful damage parameter. The model calculations confirmed that damage is a steady function of vertical compression and lateral stresses, and that it is retarded when internal friction is accounted for.

The statistical fluctuations in the global structural parameters (area density, specific perimeter, interface length of certain grain phases) showed no evident correlation to the damage resistance of the specimens (fig. 4.17, p. 111). This observation confirmed that the fluctuations in material resistance are dominated by the local disorder, i.e. the random distribution of the grains.

Studies on statistical ensembles of specimens aimed at the quasi-brittle damage under a prescribed compression. The distribution of the damage parameter has been recorded in terms of its first two moments: mean value and standard deviation. The absolute scatter of the results increased with the damage level (e.g., fig. 4.18, p. 112), whilst the coefficient of variation decreased at the same time.

The local stress disturbances due to the cracks and their interactions proved to promote the evolution of damage (fig. 4.21, p. 115) and must therefore not be neglected.

As for the significance of specimen size, the mechanical strength of larger specimens appeared to be higher than the strength of smaller specimens. The underlying reasons should be further investigated.

Chapter 5. A particular loading mode, relevant to ceramic filter supports, has been adapted: The stress field in a porous material has been induced here by a pressure acting inside the pores. The highest stress concentrations were thus found in the vicinity of pores, and narrow solid ligaments between pores were prone to cracking (fig. 5.2, p. 123). Consequently, failure would emanate from pore borders. Due to the lack of analytical stress solutions for pore-crack combinations in the literature, stress-intensity factors for certain configurations (eq. 5.1, p. 124) have been employed in the energy fracture criterion. It turned out that the energy criterion is not sufficient here, but must be supplemented by a hierarchy of conditions.

The progression of damage by microcracking proved to connect pores and hence to create flaw networks. Since such defect agglomerates are not suitable for the analysis, they need to be collectively replaced by elliptical cavities (fig. 5.13, p. 131) before the fracturing algorithm is continued, respectively.

For structures sufficiently 'heterogeneous', the simulations reflected a quasi-brittle material behaviour (fig. 5.17, p. 133). For simpler structures, failure is dominated by a sudden, unstable defect growth where the internal pressure splits up the specimens in arbitrary directions by percolating flaw chains (fig. 5.16, p. 132).

The brittle behaviour of the simpler structures suggested a comparison with statistical weakest-link theories (Weibull theory in particular), which hold for perfectly brittle materials. Given the specimen size, Weibull analysis proved to fit quite well to the computational results on statistical model ensembles (fig. 5.24, p. 143). Simulations on differently-sized specimens reflected a clear scaling effect for both the mean and the scatter of the rupture strength (fig. 5.21, p. 137): Increasing the specimen size showed to lower the strength in affinity with the size effect of the weakest link hypothesis. While the scatter of the strength tended to zero, the asymptotical limit of the mean, however, represented a non-zero threshold, so that the standard Weibull scaling law (eq. 5.16, p. 140) turned out to be not appropriate (fig. 5.26, p. 143).

On this account, an alternative scaling law has been proposed, involving a non-zero threshold and a second, exponential parameter (eq. 5.23, p. 144). This alternative law describes quite well the computational results for different specimen sizes (fig. 5.27, p. 144); it may serve for further upscaling, i.e. extrapolation of the experimental or computational

results (as obtained from small specimens) to larger pieces of the material.

The presented simulations advise against drawing conclusions from studies on specimens whose size is chosen too small, because neglection of the respective scaling law may possibly lead to wrong conclusions (see fig. 5.31 left, p. 150). By accounting for the scaling behaviour, the simulations confirm that the size of the 'representative' volume element increases with the size of the largest structural elements. For fairly monodisperse pore size distributions, the average strength descends with the value of the specific pore perimeter, i.e. with the 'fineness' of the phase (fig. 5.31 left, p. 150). Obviously, the strength also decreases with increasing porosity (fig. 5.32, p. 151), and it is lower for elliptical pores than for circular pores. The material strength proved to benefit from the fineness of the grain phase just as from the fineness of the pore phase, although the underlying mechanisms are different.

Another point concerned the scatter of the failure load among the members of the statistical ensemble. As expected, a widening of the scatter has been observed for the more disordered structures: Enhancing the 'number of degrees of freedom' in the structure (by allowing an arbitrary location, size, shape or orientation of the pores) yields a higher scatter of the critical pressure, whereas the mean decreases. These points have emerged from comparison of studies on material structures with circular pores and structures with elliptical pores.

6.3 Still open issues and suggestions for future work

As a matter of course, the present dissertation touches on a multitude of issues that cannot be treated exhaustively; it raises questions that remain to be answered, and ignores topics that would be fundamental for any further assessment and employment. This final section will sketch some points which deserve more attention in future studies.

First, a number of interesting subjects could be investigated without further extension of the model. At the current stage, the computer programs may be employed to calculations on the significance of the volume fraction and granularity of the second-phase (Al_2O_3) grains, and of their size and shape. The simulations of the present thesis, which had mainly been restricted to two-phase structures for reasons of clarity, could be extended to three-phase materials, and a multivariate analysis of the many-parameter correlation could be performed. Moreover, a detailed study of the specimen boundary effects — in modelling as well as in reality — is recommendable for understanding the scaling effect observed in Chapter 4.

Besides that, forthcoming studies should address the following subjects, which require extensions to the computational model (sections 6.3.1, 6.3.2), or should be discussed separately from it (section 6.3.3):

6.3.1 Incorporation of thermal stresses

Due to the high sintering temperature and subsequent cooling-down, most of the ceramics are subject to high temperature changes during fabrication. Since the randomly oriented material constituents may differ in their thermal expansion coefficients, or there may be an anisotropy of the thermal expansion coefficients within the single grains, these temperature changes result in mismatch of thermal strains between the individual grains. The strains in turn give rise to intrinsic microstructural stresses. These so-called *thermal residual*

stresses are self-equilibrating (i.e., the average residual stress components are vanishing), but they have important consequences on the evolution of microcracking.

In the presented model, some of these effects may be included by assigning statistically distributed thermal anisotropy coefficients $0 \leq a_f \leq 1$ to the grain boundary [12], and introducing an additional energy contribution in the fracture criterion (left-hand side of eq. 4.3/eq. 4.8): Following [9], the 'thermal contribution' to the elastic energy release during fracturing of a facet f may be approximated by

$$\left[\int_{l_0}^{l_0+l_f} G \, \mathrm{d}l \right]_{\text{thermal}} = \frac{1}{48} \, E' \, (\Delta\alpha \, \Delta\Theta)^2 a_f^2 \, l_f^2 \, , \tag{6.1}$$

where $\Delta\alpha$ denotes the mismatch of the thermal expansion coefficients, and $\Delta\Theta$ the temperature change. This approach (see also [23]) is to some extent equivalent to a statistical distribution of the specific surface energy γ_f; it should enrich the present model in that the transition from distributed microcrack patterns to damage localization can be simulated.

For a simulation of the strain response in the context of thermal residual stresses, however, a more sophisticated approach is needed. Assigning random main axis orientations to the individual grains (fig. 2.4, p. 37), the theoretical concepts established in [54] or [77] could be exploited here. In loading cycles similar to those of section 3.7, the damaged model specimens should finally exhibit *overall residual strains* when the applied load is removed.

6.3.2 Accounting for stress corrosion cracking

Stress corrosion cracking is a damage phenomenon resulting from the combined actions of an aggressive environment, especially of humidity, and a steady (or cyclic) tensile stress. This kind of fracturing is brittle and to a large part intergranular [29], so that it can be incorporated into the presented model.

Assuming that a grain facet f is touched by a fluid-filled crack at either tip, the impact of the stress corrosion on its failure may be accounted for by an additional term $W_{f,\text{corr}}$ in the energy criterion for crack extension (see eq. 4.8, p. 97):

$$\int_{l_0}^{l_0+l_f} G \, \mathrm{d}l \;\geq\; 2\gamma_f \, l_f - W_{f,\text{corr}} \tag{6.2}$$

$W_{f,\text{corr}}$ denotes a time- and stress-dependent increase of free surface energy in the material, which needs not to be supplied by a reduction of strain energy. From the physical point of view it would be rational to associate the corrosion with a reduction of the specific surface energy parameter ($\mathrm{d}\gamma_f$), but a decrease in facet length ($\mathrm{d}l_f$) should turn out more functional in the present formalism:

$$\mathrm{d}W_{f,\text{corr}} = 2\gamma_f \, \mathrm{d}l_{f,\text{corr}} \, , \tag{6.3}$$

where $\mathrm{d}l_{f,\text{corr}}$ represents a crack growth along the facet due to corrosion. It may be adopted from a common relation in the literature (see [81], [82], [57], [66]):

$$\frac{\mathrm{d}l_k}{\mathrm{d}\tau} = A \, (K_k)^n \, , \tag{6.4}$$

where l_k is the length of the existing crack, τ is the time, K_k is the mode I stress intensity factor at the crack tip, A is a constant characterizing the corrosive environment, and n is a material constant.[1] The fact that there is no crack growth below a certain threshold value of K_k should be taken into account [8]. Modelling of the characteristic three stages of corrosion cracking (as reported e.g. in [57] or [82]) might be accomplished by stress-dependent parameters A and n.

Inserting eq. (6.4) into eq. (6.3) yields the 'equivalent' surface energy due to corrosion on facet f at a time T:

$$W_{f,\mathrm{corr}} \;=\; 2\gamma_f \left(A \int_{T_f}^{T} (K_k)^n \, \mathrm{d}\tau \right), \tag{6.5}$$

where T_f denotes the time instant when the corrosive fluid starts to affect the facet tip. Supplementing the computer algorithm by eq. (6.5), failure of the facet must be triggered as soon as inequality (6.2) is fulfilled.

Some preliminary simulations on the time dependency of damage introduced by corrosion have already been presented in the framework of the BRITE-EURAM project. A question to be debated is whether stress corrosion cracking requires stress singularities (at crack tips) or whether it may start from pore borders as well. The latter case would require a proper adaptation of the corrosion law (eq. 6.4).

6.3.3 Effect of the reduced dimensionality

The following remarks might serve as clues for an extended discussion of the relation between two-dimensional simulation and actual three-dimensional material behaviour. The considerations refer firstly to the micromechanical point of view (stress disturbance and strain contribution of the cavities), and subsequently to the grain structure mesh (relevant for discrete fracturing).

Micromechanical view. From the micromechanical point of view, it must be recalled that the 2-D model works with images of 2-D *sections* of the actual material. 2-D sections would indisputably be sufficient for modelling a 'tubular' structure which does not change in the third dimension. Assuming a tubular pore structure is not quite devious in the actual situation since open channels are required to transport the fluid and to transmit the pressure.

Irrespective of that, it has been sketched in section 2.4 that for a certain phase the area fraction in a 2-D cross-section equals the actual volume fraction, and the specific perimeter in a 2-D section is explicitly correlated (by a multiplication factor $4/\pi$) to the actual specific surface. In a structure with three-dimensional characteristics, however, these global parameters alone are not decisive for the effective elastic properties and for the stresses. The relevant quantities are rather the 'local' parameters here, such as the shape and size of the individual defects. In a sense, 2-D sections mostly 'reduce' the size and/or the shape of the 3-D objects: e.g., a sphere is reduced to a circle of a lower radius, an ellipsoid is reduced to an ellipse of a smaller aspect ratio, or a penny-shaped crack is reduced to a slit-like crack of a smaller 'diameter' (length) in most cases. In other words, the actual spatial

[1] Beside the power-law type eq. (6.4), various exponential forms have been proposed and could be adopted as well.

extent —say the largest diameter— and the shape —say the maximum aspect ratio— are *under*estimated in a 2-D section. Such geometrical reductions are usually associated with lower stress concentrations, a smaller range of the stress disturbance, or a lower strain contribution of the cavities in question.

On the other hand, one is tempted to expect a correspondence between 2-D modelling results and 3-D material properties if there is a 'similarity' of the structure elements in 2-D and in 3-D, for example a circular pore shape in 2-D and a spherical pore shape in 3-D. From this perspective, however, the 2-D modelling will *over*estimate the effect on the elastic properties. To give some examples:

- *stresses in the vicinity of cavities*: The maximum circumferential stress concentration at the border of a circular pore (in 2-D) and a spherical pore (in 3-D) under remote uniaxial tension σ_0 is [59]

$$\text{2-D case:} \quad \frac{\sigma}{\sigma_0} = 3 \qquad\qquad \text{3-D case:} \quad \frac{\sigma}{\sigma_0} \approx 2 \ . \tag{6.6}$$

  Obviously, the stress concentration at a 3-D cavity is lower than at a 2-D cavity of similar shape (cross-section). In other words, a limitation of the cavity extent in the third dimension reduces the stress concentration.

- *stiffness reduction due to cavities*: Consider an isotropic elastic material containing randomly distributed spherical pores. Interactions between the pores are neglected. 2-D sections of this material reduce the problem to circular pores. For prescribed macroscopic stress, as a function of porosity p, Young's modulus is given by[2]

$$E = \frac{E_0}{1+3p} \qquad\qquad E \approx \frac{E_0}{1+2p} \tag{6.7}$$

  for the material with circular pores and spherical pores, respectively. Obviously, the effect of the pores on the effective stiffness is overestimated in a 2-D consideration.

- *stiffness reduction due to cracks*: Consider a material with randomly distributed, non-interacting cracks. In order to compare the stiffness reduction due to slit-like cracks (in 2-D) and penny-shaped cracks (in 3-D), the crack density should be defined in an equivalent way for the 2-D and 3-D cases. Such an 'equivalent' crack density ρ_e may be the relative area (in 2-D) and relative volume (in 3-D) swept by the cracks when they are rotated about their centers (in 2-D) or diameters (in 3-D), respectively [43]:

$$\rho_\mathrm{e} = \frac{1}{A}\sum_k \pi \left(\frac{l_k}{2}\right)^2 \qquad\qquad \rho_\mathrm{e} = \frac{1}{V}\sum_k \frac{4}{3}\pi (a_k)^3, \tag{6.8}$$

  where l_k denotes the length of crack k (in 2-D), and a_k denotes the radius of the penny-shaped crack k (in 3-D). For prescribed macroscopic stress and $\nu_0 = 0.25$, Young's modulus is then given by[3]

$$E = \frac{E_0}{1+\rho_\mathrm{e}} \qquad\qquad E = \frac{E_0}{1+0.42\rho_\mathrm{e}} \ . \tag{6.9}$$

[2]The general expressions are given in [41].

[3]The general expressions are given in [62] and [43].

It is seen that for the comparable crack density ρ_e, the stiffness reduction is substantially weaker in 3-D. Similar conclusions hold for non-randomly distributed cracks, and for interacting cracks [43].

- *stress-intensity factors*: Consider again the simplest representation of a crack in 2-D, a slit-like crack (length l), and in 3-D, a penny-shaped crack (diameter $2a$). The corresponding mode I stress intensity factors are as follows:

$$K_I = \sqrt{\pi\ l/2}\ t \qquad\qquad K_I = \frac{2}{\pi}\sqrt{\pi\ a}\ t \tag{6.10}$$

If the size of the cracks is defined as l resp. $2a$, then the stress intensity factor is higher in 2-D than in 3-D. (Identical K-values are given for $l/2 = 4/\pi^2\ a \approx 0.4\ a$). An equivalent correspondence holds for the Griffith fracture criterion: Under plane strain conditions, the critical load t_c for extension of a 2-D crack (length l) is by a factor $\sqrt{4/\pi^2} \approx 0.64$ smaller than for extension of a penny-shaped 3-D crack (radius $a = l/2$) [59].

Thus it is clear that two contrary effects are present in a 2-D model: a 'reduced' detection of the defect geometries, on the one hand, and an overestimation of the impact of the 2-D defects on the elastic properties, on the other hand. The crucial question is whether the two effects are somewhat balancing themselves out, or which of them is dominant. To find an answer, statistical studies on a number of sections of a 3-D structure (similar to [53]) might be helpful.

'Mesh' view. While the previous ideas concerned the cavities or defects in an otherwise homogeneous material, the discrete two-dimensional meshing of the *grain* structure is the second important point to be analyzed. It is clear that a realistic description of the three-dimensional topology of polyhedral grains represents a non-trivial problem; some geometrical methods to characterize the local (dis)order in polycrystalline structures are outlined in [28].

Different from the pores, which are considered as separated elements distributed in the solid matrix, an underestimation of the grain shapes in 2-D sections is minor, since the grains form a compact mesh of adjacent patches, and they have a narrower size and shape distribution.

Secondly, one should note that a 2-D model implicitly assumes a uniform structure in the third dimension: the energy barriers imposed by grain boundaries in this dimension are completely disregarded. It is to be expected that the complexity of actual 3-D grain structures establishes additional obstacles for the crack propagation. So it seems that the 2-D model here underestimates the material strength. Mention should be made of the work by Kamiya et al. [45], which is based upon a finite element model of crystal grains, emanating from a regular mesh of Voronoi polyhedra. Under combined external load and thermal residual stresses, the studies indicate that an unstable crack propagation observed in a 2-D simulation may give way to a rather stable damage growth when the simulation is performed on a full 3-D grain boundary grid.

Generally, the number of possible loading modes on the grain boundaries is higher in 3-D structures, and the arising crack patterns are complexer than a 2-D simulation can reflect. Terms such as 'percolation' and 'failure' require a much more distinct definition in a 3-D context. Regarding the microscopic damage, it is clear that additional phenomena

are present which cannot be explored without 3-D approaches — the account by Kamiya et al. [45] indicates a possible way here.

Two-dimensional models are nevertheless needed to gain an overall picture of the material behaviour. For they reflect features that appear in the three-dimensional world as well, but are not accessible there with a rational effort in theory, modelling and computational time.

Bibliography

[1] Jacob Aboudi. *Mechanics of Composite Materials – A Unified Micromechanical Approach*. Elsevier, Amsterdam, 1991. 50

[2] Z. P. Bazant and Y. Xi. Statistical size effect in quasi-brittle structures: II. nonlocal theory. *J. Engrg. Mech.-ASCE*, 117 (11):2623–2640, 1991. 141

[3] Z. P. Bazant, Y. Xi, and S. G. Reid. Statistical size effect in quasi-brittle structures: I. is Weibull theory applicable? *J. Engrg. Mech.-ASCE*, 117 (11):2609–2622, 1991. 139, 140

[4] Y. Benveniste. On the Mori-Tanaka's method in cracked bodies. *Mech. Res. Comm.*, 13:193–201, 1986. 56

[5] Y. Benveniste, G. J. Dvorak, J. Zarzour, and E. C. J. Wung. On interacting cracks and complex crack configurations in linear elastic media. *Int. J. Solids Structures*, 25(11):1279–1293, 1989. 22, 62, 73

[6] Clotilde Berdin, Georges Cailletaud, and Dominique Jeulin. Brittle failure prediction of ceramics using a multiscale approach. *J. Am. Ceram. Soc.*, 79 (11):2825–2832, 1996. 21, 27

[7] L. T. Berezhnitskii. Propagation of cracks terminating at the edge of a curvilinear hole in a plate. *Soviet Materials Science*, 2:16–23, 1966. 21, 124, 125

[8] David Broek. Introduction to fracture mechanics. In *Fracture mechanics design methodology*. North Atlantic Treaty Organization, 1978. AGARD Lecture Series No. 97. 97, 160

[9] F. E. Buresch. Bruchmechanische Aspekte beim Einsatz partikelverstärkter keramischer Bauteile. *Materialprüfung*, 29(9), 1987. 159

[10] Ignacio Carol and Carlos M. Lopez. Fracture-based interface model: theory, implementation and applications. In S. R. Idelsohn et al., editors, *Computational Mechanics — New Trends and Applications: Fourth World Congress on Computational Mechanics, Buenos Aires*, Barcelona, 1998. CIMNE. CD-ROM. 24

[11] Ignacio Carol, Pere C. Prat, and Carlos M. Lopez. Normal/shear cracking model: application to discrete crack analysis. *Journal of engineering mechanics*, 123(8):765–773, 1997. 24

[12] R. W. Davidge, J. R. McLaren, and I. Titchell. Statistical aspects of grain boundary cracking in ceramics and rocks. *Fracture Mechanics of Ceramics*, 5:495–506, 1983. 159

[13] R. de Boer. *Theory of Porous Media.* Springer, Berlin Heidelberg New York, 2000. 47

[14] A. Delesse. Pour déterminer la composition des roches. *Annales des Mines Paris*, 4. Ser. 13:379–388, 1848. 47

[15] I. Doltsinis. Issues in modelling distributed fracturing in brittle solids with microstructure. In S. R. Idelsohn et al., editors, *Computational Mechanics — New Trends and Applications : Fourth World Congress on Computational Mechanics, Buenos Aires*, Barcelona, 1998. CIMNE. CD-ROM. 28, 70

[16] I. Doltsinis and R. Dattke. Studies on porous fracturing solids. Keynote lecture. In J. Bento, E. A. e Oliveira, and E. Pereira, editors, *EPMESC VII: Computational Methods in Engineering and Science.* Elsevier, Amsterdam, 1999. 28

[17] I. Doltsinis and R. Dattke. Modelling the damage of ceramics under pore pressure. In S. R. Idelsohn et al., editors, *ECCOMAS 2000 Proceedings, 11-14 Sept. 2000*, Barcelona, 2000. CD-ROM. 46

[18] I. Doltsinis and R. Dattke. Modelling the damage of porous ceramics under internal pressure. *Comput. Methods Appl. Mech. Engrg.*, 191(920010):29–46, 2001. 46

[19] I. St. Doltsinis and R. Handel. Modelling the behaviour and failure analysis of brittle microcracking materials. In *Proceedings, ECCOMAS 96.* John Wiley, 1996. 34

[20] I. St. Doltsinis, R. Handel, and G. Nötzel. On the constitutive modelling of brittle materials undergoing microcracking. Unpublished lecture 'Physical and Mathematical Aspects in Material Theory', GAMM-Fachausschuss: Materialtheorie, Apr. 27 and 28, 1992, Stuttgart University. 28

[21] Ioannis Doltsinis. A constitutive approach to the behaviour of brittle materials undergoing microcracking. Unpublished lecture 'Composite Research in Solid Mechanics', Dec. 5 and 6, 1991, Stuttgart University. 28

[22] Ioannis Doltsinis, editor. *Stochastic Analysis of Multivariate Systems in Computational Mechanics and Engineering.* CIMNE, Barcelona, 1999. 108

[23] Ioannis St. Doltsinis, John Harding, and Maurizio Marchese. Modelling the production and performance analysis of plasma-sprayed ceramic thermal barrier coatings. *Archives of Computational Methods in Engineering*, 5, 2:59–166, 1998. 94, 159

[24] J. W. Dougill. On stable progressively fracturing solids. *Journal of Applied Mathematics and Physics (ZAMP)*, 27:423–437, 1976. 118

[25] A. V. Dyskin and H.-B. Mühlhaus. Equilibrium bifurcations in dipole asymptotics model of periodic crack arrays. In H.-B. Mühlhaus, editor, *Continuum Models for Materials with Microstructure.* John Wiley & Sons Ltd., 1995. 22, 25

[26] Zdeněk P. Bazant. Scaling laws in mechanics of failure. *J. Engrg. Mech.-ASCE*, 119 (9):1828–1844, 1993. 139, 140, 141

[27] J. D. Eshelby. The determination of the elastic field of an ellipsoidal inclusion, and related problems. *Proc. Roy. Soc.*, A 241:376–396, 1957. 52

[28] John L. Finney. Local structure of disordered hard sphere packings. In D. Bideau and A. Hansen, editors, *Disorder and granular media*. Elsevier Science Publishers, 1993. 23, 59, 162

[29] Dominique Francois, Andre Pinau, and Andre Zaoui. *Mechanical Behaviour of Materials*, volume 2. Kluwer Academic Publishers, Dordrecht, 1998. 25, 26, 27, 74, 93, 95, 139, 152, 159

[30] N. R. Hansen and H. L. Schreyer. Damage deactivation. *Journal of Applied Mechanics, Transactions of the ASME*, 62(11):450–458, 1995. 26

[31] Y. Huang, K. X. Hu, and A. Chandra. A generalized self-consistent mechanics method for microcracked solids. *J. Mech. Phys. Solids*, 42(8):1273–1291, 1994. 81

[32] Christian Huet. Coupled size and boundary-condition effects in viscoelastic heterogeneous and composite bodies. *Mechanics of Materials*, 31:787–829, 1999. 59, 60

[33] G. R. Irwin. Fracture. In *Handbuch der Physik*, volume 6, pages 551–590. Springer, Berlin Heidelberg New York, 1958. 94, 96

[34] Jean-Paul Jernot. Analyse morphologique et modélisation du frittage et des matériaux frittés. Technical Report TOME 59, 3^0 fascicule, Ministère de la Défense, Paris, 1985. Sciences et techniques de l'armement; Mémorial de l'Artillerie française. 47

[35] D. Jeulin. On image analysis and micromechanics. *Revue Phys. Appl., Physics Abstracts*, 23:549–5567, 1988. 21, 22, 26, 129

[36] D. Jeulin. Damage simulations in heterogeneous materials from geodesic propagations. *Engineering Computations*, 10:81–91, 1993. 129

[37] Patricia Jouannot and Jean-Paul Jernot. Unbiased estimation of the specific Euler-Poincaré characteristic. *Acta Stereologica*, 15\1:45–51, 1996. 41

[38] J. W. Ju and Tsung-Muh Chen. Effective elastic moduli of two-dimensional brittle solids with interacting microcracks, part 1: Basic formulations. *J. Appl. Mech.*, 61:349–357, 1994. 27, 56, 119

[39] J. W. Ju and Tsung-Muh Chen. Effective elastic moduli of two-dimensional brittle solids with interacting microcracks, part 2: Evolutionary damage models. *J. Appl. Mech.*, 61:358–366, 1994. 27, 57, 119

[40] L. M. Kachanov. Time of the rupture process under creep conditions. *Izv. AN SSR, Otd. Tekh. Nauk*, (8):26–31, 1958. also in *Problems in Continuum Mechanics, Muskhelishvili Memorial Volume*, Philadelphia 1961. 25

[41] M. Kachanov, I. Tsukrov, and B. Shafiro. Effective moduli of solids with cavities of various shapes. *Appl. Mech. Rev.*, 47(1):151–174, 1994. 21, 36, 52, 53, 56, 58, 82, 109, 161

[42] Mark Kachanov. Elastic solids with many cracks: a simple method of analysis. *Int. J. Solids Structures*, 23(1):23–43, 1987. 22, 25, 49, 57, 70, 71, 72, 73

[43] Mark Kachanov. Effective elastic properties of cracked solids: critical review of some basic concepts. *Appl. Mech. Rev.*, 45(8):304–335, 1992. 21, 55, 56, 58, 59, 70, 71, 81, 83, 161, 162

[44] A. A. Kaminskii. Determination of the critical load causing crack propagation near a curvilinear hole. *Soviet Materials Science*, 2:24–30, 1966. 21, 124

[45] S. Kamiya, T. Yamauchi, M. Saka, and H. Abe. Three dimensional structure model of damage in brittle polycrystalline materials. In A. Carpinteri and C. A. Brebbia, editors, *Damage and Fracture Mechanics — Computer Aided Assessment and Control*. Computational Mechanics Publications, Southampton, UK, 1998. 23, 24, 162, 163

[46] D. G. Karr and S. A. Wimmer. Microcrack induced bifurcation of stress-strain relations for sintered materials. In M. Predeleanu and P. Gilormini, editors, *Advanced Methods in Materials Processing Defects*. Elsevier Science B.V., 1997. 21, 25

[47] G. V. Kolosov. *On the applications of the complex function theory to the plane problem of the mathematical elasticity theory (orig. Russian)*. PhD thesis, University of Yuriew, 1909. 60

[48] Dusan Krajcinovic. *Damage Mechanics*. North Holland, Elsevier, Amsterdam, 1996. 18, 19, 20, 23, 26, 29, 38, 40, 50, 52, 55, 56, 58, 59, 60, 66, 71, 74, 76, 82, 102, 103, 109, 117, 118, 134, 139, 140, 141, 145

[49] E. Kröner. The statistical basis of polycrystal plasticity. In John Gittus, Joseph Zarka, and Siavouche Nemat-Nasser, editors, *Large Deformations of Solids: Physical Basis and Mathematical Modelling*. Elsevier, London and New York, 1986. 26

[50] E. Kröner. Statistical modelling. In John Gittus and Joseph Zarka, editors, *Modelling small deformations of polycrystals*. Elsevier, London and New York, 1986. 23, 26, 27, 50

[51] B. Kubicki. Stress concentration at pores in sintered materials. *Powder Metallurgy*, 38(4):295–298, 1995. 21

[52] Ch. Lantuéjoul. Ergodicity and integral range. *Journal of Microscopy*, 161, 3:387–403, 1991. 38, 41

[53] Vincent J. Laraia, Ioan L. Rus, and Arthur H. Heuer. Microstructural shape factors: Relation of random planar sections to three-dimensional microstructures. *J. Am. Ceram. Soc.*, 78, 6:1532–36, 1995. 47, 162

[54] N. Laws and J. C. Lee. Microcracking in polycrystalline ceramics: elastic isotropy and thermal anisotropy. *J. Mech. Phys. Solids*, 17:603–618, 1989. 37, 159

[55] Y. H. Liu, H. X. Li, and Z. Z. Cen. Limit state analysis of ductile composite materials. In *European Congress on Computational Methods in Applied Sciences and Engineering*, Barcelona, 11-14 September 2000, 2000. ECCOMAS. 51

[56] G. A. Maugin. *The Thermodynamics of Plasticity and Fracture*. Cambridge University Press, Cambridge, UK, 1992. 18, 40, 50, 51

[57] Ronald A. McCauley. *Corrosion of Ceramics*. Marcel Dekker, Inc., New York, 1995. 159, 160

[58] Dominique P. Miannay. *Fracture Mechanics*. Springer, New York Berlin Heidelberg, 1998. 22, 24, 139, 140

[59] Toshio Mura. *Micromechanics of Defects in Solids*. Martinus Nijhoff Publishers, 1987. 50, 52, 161, 162

[60] N. I. Muskhelishvili. *Some basic Problems of Mathematical Theory of Elasticity*. P. Noordhoff, Groningen, 1953. 52, 60, 61

[61] A. Nadai. *Theory of Flow and Fracture of Solids*, volume 1. McGraw-Hill Book Company, Inc., New York, second edition, 1950. 62

[62] Sia Nemat-Nasser and Muneo Hori. *Micromechanics: Overall Properties of Heterogeneous Materials*. North Holland, Elsevier, Amsterdam, 1999. 22, 52, 53, 55, 60, 103, 117, 161

[63] F. Osterstock and O. Vansse, January 1999. Lermat-Ismra, Caen; personal communication. 33

[64] F. Osterstock and O. Vansse, May 2000. Lermat-Ismra, Caen; personal communication. 121

[65] G. Pijaudier-Cabot. Non local damage. In H.-B. Mühlhaus, editor, *Continuum Models for Materials with Microstructure*. John Wiley & Sons Ltd., 1995. 25

[66] S. Saito. *Fine Ceramics*. Elsevier, 1985. 159

[67] C. G. Sammis and M. F. Ashby. The failure of brittle porous solids under compressive stress states. *Acta metall.*, 34(11):511–526, 1986. 21, 102

[68] G. N. Savin. *Stress Concentration around Holes*. Pergamon Press, Oxford, 1961. 52, 61, 66

[69] J. Schröder and C. Miehe. Aspects of computational homogenization analysis of polycrystalline materials. In D. R. J. Owen, E. Onate, and E. Hinton, editors, *Computational Plasticity — Fundamentals and applications*, Barcelona, 1997. CIMNE. 40, 50, 51, 52

[70] J. Serra. *Image analysis and mathematical morphology*. Academic Press, London, 1982. 38

[71] Igor Sevostianov and Mark Kachanov. Plasma sprayed ceramic coatings: anisotropic elastic and conductive properties in relation to the microstructure. cross-property correlations. 2000. submitted to J. Mater. Sci. Eng -A. 36

[72] G. C. Sih. Introduction to a series on mechanics of fracture. In G. C. Sih, editor, *Mechanics of fracture 1: Methods of analysis and solutions of crack problems.* Noordhoff, Oxford, 1973. 95

[73] Jacek J. Skrzypek and Artur Ganczarski. *Modeling of Material Damage and Failure of Structures.* Springer, Berlin Heidelberg, 1999. 26, 41

[74] A. C. Stevenson. Complex potentials in two-dimensional elasticity. In *Proc. Roy. Soc.*, volume 184 of *A*, pages 129–179, 1945. 61, 62, 65

[75] Hiroshi Tada, Paul C. Paris, and George R. Irwin. *The Stress Analysis of Cracks Handbook.* Paris Productions Inc. (and Del. Research Co.), St. Louis, Missouri, second edition, 1985. 21

[76] S. Timoshenko and J. N. Goodier. *Theory of Elasticity.* McGraw-Hill Book Company, Inc., second edition, 1951. 22, 68, 95

[77] Viggo Tvergaard and John W. Hutchinson. Microcracking in ceramics induced by thermal expansion or elastic anisotropy. *J. Am. Ceram. Soc.*, 71 [3]:157–166, 1988. 37, 159

[78] E. E. Underwood. *Quantitative Stereology.* Addison Wesley Publ., Reading, PA, 1970. 38

[79] George Z. Voyiadjis. *Damage mechanics in engineering materials.* Elsevier, Amsterdam, first edition, 1998. 102

[80] J. Wang and C. Huet. A numerical model for studying the influences of pre-existing microcracks and granular character on the fracture of concrete materials and structures. In C. Huet, editor, *Micromechanics of concrete and cementitious materials*, pages 228–240. Presses Polytechniques et Universitaires Romandes, Lausanne, 1993. 24

[81] S. M. Wiederhorn. Subcritical crack growth in ceramics. In R. C. Bradt, D. P. H. Hasselman, and F. F. Lange, editors, *Fracture Mechanics of Ceramics*, volume 2. Plenum Press, New York - London, 1974. 159

[82] S. M. Wiederhorn. Subcritical crack growth. In R. J. Brook, editor, *Concise encyclopedia of advanced ceramic materials.* Pergamon Press, Oxford, first edition, 1991. 159, 160

[83] Stephanie A. Wimmer and Dale G. Karr. Compressive failure of microcracked porous brittle solids. *Mechanics of Materials*, 22:265–277, 1996. 21, 22, 25

[84] Han Xueli and Wang Tzuchiang. Interacting multiple cracks with complicated crack surface conditions. *International Journal of Fracture*, 82:R53–R57, 1996. 22

[85] O. C. Zienkiewicz. *The Finite Element Method in Structural and Continuum Mechanics.* McGraw-Hill Publishing Company Limited, London, 1967. 24

Index

Danksagung

Sehr herzlich danke ich

Herrn Prof. Dr. Bernd Kröplin für die freundliche Bereitschaft zur Betreuung der Arbeit und die Übernahme des Hauptberichts,

Herrn Prof. Dr. Christian Miehe für die Übernahme des Mitberichts,

Herrn Priv.Doz. Dr. Ioannis Doltsinis für seine wegweisende Personalentscheidung im Mai 1997 und die stete Betreuung und Unterstützung in den darauffolgenden Jahren,

Herrn Dr. Frederic Osterstock, Herrn Dr. Jean-Paul Jernot und Herrn Dr. Olivier Vansse vom Materialforschungsinstitut ISMRA-LERMAT in Caen für die gute Kooperation,

den Mitarbeitern der ehemaligen Zentralen Projektgruppe des Instituts für Computeranwendungen für die ausgesprochen herzliche und freundschaftliche Arbeitsatmosphäre und die vielfältigen Hilfestellungen,

meiner Ehefrau und meiner Familie für ihre Geduld und den jederzeit verlässlichen Rückhalt.

R. D.